STUDIA
UNIVERSITATIS BABEŞ-BOLYAI

CHEMIA

1-2

1994

CLUJ-NAPOCA

ANUL XXXIX **1994**

STUDIA
UNIVERSITATIS BABEŞ-BOLYAI

CHEMIA

1-2

Redacţia. 3400 CLUJ-NAPOCA, str. M. Kogălniceanu, 1 ● Telefon 19 43 15

SUMAR — CONTENTS — INHALT — SOMMAIRE

In memoriam

Recenzii — Book Reviews — Comptes rendus — Buchbesprechungen . . . .

STUDIA UNIV. BABEŞ-BOLYAI, CHEMIA, XXXIX, 1–2, 1994

ASPECTS IN SURFACE ENHANCED RAMAN SPECTROSCOPY

I. MARIAN, T. ILIESCU, M. CARAGIU, S. GHIZDAVU, S. CÂNTĂ

ABSTRACT. Raman spectra are used to be very weak especially in diluted solution. In Surface Enhanced Raman Scattering (SERS) the intensity is larger of 10^6 fold as compared with normal Raman spectra. In this way, SERS is a useful analytical technique.

This paper presents some aspects of SERS such as: the mechanism of enhancement, the preparation of SERS active surface. Some comparison between normal Raman spectra and SERS are reported.

From different techniques to obtain SERS surface, the paper reports especially electrochemical aspects.

I.1. General features of SERS. In 1974 Fleischmann et al. [1] have been observed first time a Raman spectrum of the pyridine molecules adsorbed on a specially prepared silver electrode.

Fig. 1 presents Raman spectra of pyridine molecules (ring valence vibrations) obtained in different conditions.

Silver electrode was prepared by 150 oxido-reduction cycles (ORC) between +200 and −300 mV.

The 1025 cm^{-1} band was assigned to chemisorbed pyridine by nitrogen one pair electrons. The other bands 1036 and 1008 cm^{-1}, similar to solution bands, were assigned to physisorbed pyridine on the electrod-electrolit interface through water molecules. The peak positions of these two bands are slowly changed at different potential by the changing of pyridine and water molecule positions in double electric layer.

Jeanmaire and Van Duyne [2], Albrecht and Creighton [3] was found that the strong Raman bands are obtained by one ORC with triangle pulse. An enhancement factor at 10^4—10^6 from the absorbed molecules was obtained by comparison with the signal of bulk solution. This phenomenon is defined as SURFACE ENHANCED RAMAN SCATTERING (SERS)

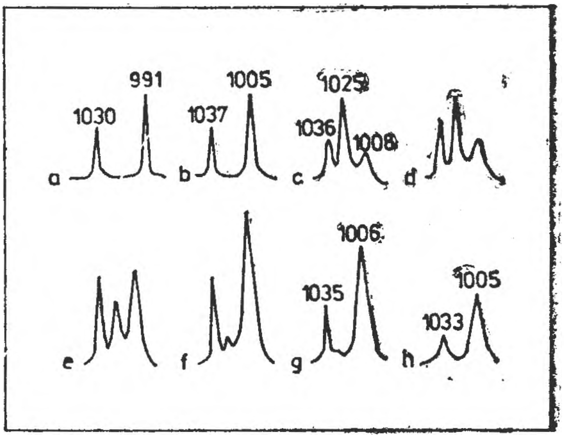

Fig. 1. Raman spectra of pyridine in solution and on Ag electrode. a) pure pyridine; b) 0.05M water-pyridine solution; c) Ag-electrode in 0.1M KCl/0.05 pyridine at 0.0 V (SCE); d) −0.2V (SCE); e) −0.4V (SCE); f) −0.6 V (SCE); g) −0.8V (SCE); h) −1.0 V (SCE).

SERS studies were performed for metal/gas, colloid/liquid and solid/solid interfaces (tunnel jonction configuration).

An intense SERS phaenomenon have been reported on different metals like: silver, copper and gold. For other metals, like platinium, nickel, aluminium, alkalis and some semiconductors, the SERS spectra are present but with low enhancement factor. It is remarcably that the SERS observations onto metals like Ag, Au and Pt in electrochemical studies have a particular significance because this metals are used for getting the electrodes construction. Ag has a big superpotential for reducing the hydrogen ion and Au and Pt have a good resistance to corrosion.

SERS effect has been demonstrated onto several hundreds of molecular-species. Pyridine and heterocyclic-nitrogen compounds, like methyl-pyridine [4], pyrasine [5], cyanopyridine [6], amino-nitro-pyridine [7] were studied. In some conditions, there were observed SERS effect on organic compounds without nitrogen, like C_6H_6 [8], ethylene [9], and also inorganic species [10], metallic complexes [11] and biochemical compounds [12].

Up to now there were crystalised some conclusions concerning SERS:

1. There are small differences between normal Raman (NR) and SERS frequencies.

2. SERS is going on a variety of molecules adsorbed on the metallic surfaces wich have a strong reflection in visible domain (effect of dielectric constante of the metal).

3. A surface roughness with features of submicrometric dimension (10—200 nm) and/or an atomic scale roughness (adatoms) are required.

4. SERS is an interface sensitive technique. The adsorbed molecules in the first layer at the surface show the largest enhancement. However, the enhancement also has a long-range aspect with molecules separated from the surface by several nanometers showing some enhancement.

5. The Raman bands are completely depolarised and have non-Lorentzian line shape. The intensity of the bands decreases when the vibrational frequency is increasing.

6. The SERS active surfaces have a continuous, weak innelastic background scattering and they are very effective in quenching fluorescence.

7. Both vibrational bond frequency and SERS intensities are function of the applied electrode potential.

Generally, there was accepted that there are two mechanism which can explain the SERS phenomena. One of them is the electromagnetic mechanism (EM) which results from the influence of the electric local field produced by the incident radiation. The other one is a chemical mechanism. In this case a charge-transfer between adsorbed molecules and metal can explain SERS effect. The EM mechanism is due to an enormous local electromagnetic field in interaction with the dipole-moment of the molecules. The chemical mechanism is caused by the resonance states which appear between molecule and metal by charge-transfer.

I.2. **Theoretical aspects.** The Raman scattering intensity which can be detected in a scattering volume V, may be written as [13]:

$$I = \frac{8\pi}{9} \cdot \left(\frac{\omega_s}{c}\right)^4 \cdot I_L \cdot N \cdot V \cdot K_e \Sigma \, |\alpha_{\sigma\rho}|^2 L^2(\omega_L) L^2(\omega_S) \tag{1}$$

with: $I_L = cE_0^2/8\pi$

where I_L is the intensity of the incident radiation with cross sectional area A; c = the speed of the light; E_0 = electric field of the incident radiation; N = the molecular density in molec/cm^3; ω_S = Raman scattering frequency; ω_L = the incident light frequency; L^2 = the square of the ratio of the local electric field strenght to that of the incident field (the EM enhancement factor) $\alpha_{\sigma\rho}$ = a component of the polarizability tensor with σ and ρ as polarizability direction; K_e = a factor including the multiplicative parameters like solid angle, the efficience of detection, and the transmission coefficient of the monochromator.

For scattering Raman surfaces, V is replaced with A and the molecular density is gived in molecules/cm^2.

The surface enhancement is in both L^2 electromagnetic term and α term, the effective polarizability.

Since Raman scattering is a two photons process which involves the "absorbtion" of the incident photon and the emission of the scattered photon, there are two EM enhacement terms; one is $L(\omega_L)$ for the effect of the metallic surface in the incident field and the other is $L(\omega_S)$ for the effect of the metallic surface on the scattered field. For a smooth surface, the Fresnel reflection equation showes that L can be as la rgeas 2 for an incident field and the same value for the scattered field. The maximum total effect of the smooth surface on the intensity via the electric field effect is a factor of 16. However much larger EM enhancement come out via the coupling of the excited light to geometrically localized metallic plasmon excitaions [14], leading to very large values of L^4 such 10^3 and larger.

It should be noted other EM interactions which also affect the local average electric field felt by the scattering molecule such as the molecular dipoles imaging in the metal surface. This is, anyway, a second-order effect compared to the localized surface plasmon effect on the electric field magnitude.

The chemical enhancement mechanism is included in equation (1) through the molecular polarizability $\alpha_{\sigma\rho}^{IF}$. Here, the superscript I, F indicates the initial and final vibronic states of Raman transition.

The Kramers—Heisenberg dispersion formula can be used to express the polarisability tensor as:

$$\alpha_{\alpha\rho}^{IF} = \sum \left(\frac{\langle I | \mu\sigma | K \rangle \langle K | \mu\rho | F \rangle}{E_K - E_I - h\omega_L - i\Gamma} \right)$$

where σ, ρ refers to the direction coordonates (x, y, or z), $\langle I|$, $\langle K|$ and $\langle F|$ are the initial, intermediary and final vibronic states, respectively; $i\Gamma$ is a damping term.

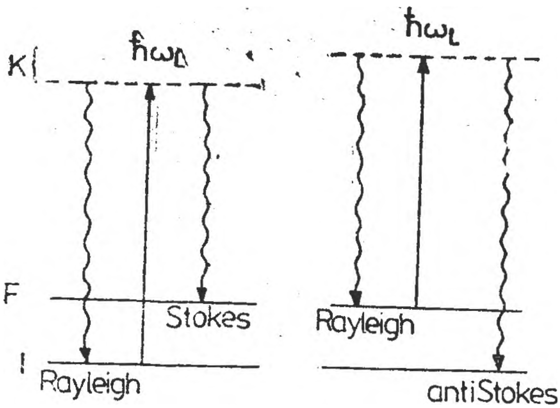

Fig. 2. The energetic dyagram for the scattering processes.

The Raman transition is from the initial vibrational level I of the ground electronic state with energy E_I to the excited vibrational leve F of ground electronic state with energy $E_F = E_I + \hbar\omega_F$, which is called Stokes-Raman scattering (Fig. 2a). In this case the exciting photon loses energy $\hbar\omega_F$, while in the case of anti-Stokes Raman scattering where the transition is from F to I the photon gain the energy $\hbar\omega_F$ (Fig. 2b).

If a molecule is chemisorbed at the surface of a SERS active electrod, then intermediate electronic state may be a metal state and it must be involved in the summation over intermediate states in the polarizability tensor equation. Thus a new type of resonance is possible, giving an aditional SERS enhancement.

II. SOME EXPERIMENTAL ASPECTS IN SERS

II.1. **Comparison between NR and SERS spectrum.** The frequencies of the majority of the bands in SERS spectra are slightly shifted from those in NR spectra of the same molecule. Therefore the energy of the vibrational modes are not influenced very much by adsorbtion. There are weak bonds between the adsorbed molecules and the metallic surface atoms. The relative intensities of the band are attired to a large extend in SERS spectra. In spite of the change in relative intensities, the SERS and NR spectra are similar enough, so the molecule can be easily identified. This is showed in Fig. 3.

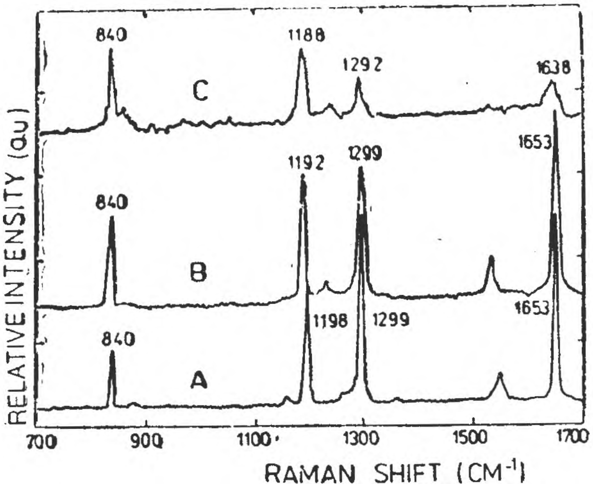

Fig. 3. Comparison between RAMAN spectra of the methylviologen dication species MV^{2+}. (A) NR spectrum of $MVCl_2$ solid; (B) NR spectrum of $MVCl_2$ in solution; (C) SERS spectrum of 10^{-3} M $MVCl_2$ in p.1M KCl at an ORC roughned electrode.

For the four stronger bands in the domain 700—1700 cm^{-1} in NR and SERS spectra, a good coincidence appears. The largest shift is of 15 cm^{-1} in NR band from 1653 cm^{-1} to 1638 cm^{-1} in SERS spectrum.

II.2. **The influences of different metal substrates.** Ag is the most used in SER scattering for its largest enhancement. The first scattering experiment on Cu [15] with green laser exciting light was very weak. It was found later that red laser exciting light allowed well-defined SERS spectra for both Cu and Au electrodes.

Pettinger and Wenning [16] reported that when the laser wavelenght was tuned from 457 to 647 nm, a 200-fold increase enhancement factor for the breathing vibration in pyridine-Au and pyridine-Cu systems was observed whereas only 20-fold increase was obtained for the pyridine-Ag system. It was reported an enhancement factor of 10^6 for Ag, 10^5-10^6 for Cu and 10^4-10^5 for Au [17].

SERS intensities for nonpolar molecules such as benzene, ethylene and CO on gold were higher than those on silver [18].

Other metallic substrate like Pt, Ni, Al, Li, Na were investigated. However the enhancement of those metal is relatively low. For example Bradley and Arunkumar [19] established that the enhancement for carbonoxide on Ni is only 70—100. In addition, SERS spectrum on these metals show a strong intensity dependence on excitation wavelenght.

Yamada and Yamamoto [20] demonstrated that SERS spectra of pyridine-Ni and pyridine-Pt systems can be observed with 514 nm excitation laser light but not with 600 nm light. Other metals like Hg, Cd do not support SERS [21, 22].

There were also the attempts at surface enhancement employing In, Pb, Sn, [23] but without results.

II.3. **The surface roughness.** It is remarcable that the roughned silver surfaces can provide an enhancement factor of about 6 orders of magnitude, whereas a mycroscopically smooth silver surface produce an enhancement factor of around 400 [24]. Different roughening methods are used for different systems. In an electrochemical system, the electrode surface is generally roughened with an oxidation-reduction cycle (ORC). During ORC, the electrode is submitted to a double-potential step or triangular sweep potential. During ORC-many factors can affect the SERS intensity.

The SERS intensity can be related to the extent of charge passed in the anodization process of ORC [25]. The laser illumination of the electrode during the ORC increase the intensity by up to an order of magnitude that produced by an ORC performed in the dark [26]. The ORC is usually carried out in the presence of an adsorbate in the solution. Althought the presence of adsorbate in the solution during the ORC is not necessary rather where Raman intensity is obtained when the adsorbate is added after ORC. Moreover it comes up that changing the potential on the electrode toward the domain of rapid evolution of Hydrogen before performing an ORC can result in SERS intensity greater of about an order of magnitude than that for an electrode submitted to one ORC treatement [27].

It was noticed that electrochemical ORC is not strictly necessary to observed SERS phenomena in electrochemical systems [28]. Mechanically roghned electrodes present also SERS effect, but the enhancement factor of them is at least two order of magnitude less than that for electrochemically roughened electrode [29]. Other rough substrates which presents SERS effect are metallic colloidal particles [30], metallic clusters [31], roughened surfaces of a monocrystal under high vacuum (UHV) [32] tunnel-junction structure [33]. Recently it was demonstrated that chemical prepared silver thin film on glass presents a strong SERS effect [34].

It seems to exist three degree of roughness. The first is macroroughness with the dimension of the particles between 200 and 5000Å, the second is submicroscopic roughness, the particles having between 50 and 200 Å and the third is the atomic scale microroughness, having the order of atomic dimension for particles.

Many experiments have been concluded that the macroroughness is the best in SERS effect [35, 36, 37]. The roughness with the average particle size around 1000 Å for Ag and 500 Å for Cu show the largest enhancement. But other investigation concluded that submicroscopic roughness, adatoms, clusters and surface defect are the most important types of surface roughness and are required to obtain the largest enhancements [38, 39]. It seems to be necessary a combination of roughness scales for the total enhancement effect.

II.4. **Coverage Effects.** The dependence of the enhancement factor with the distance on the metallic surface can be used to evaluate the contribution of short-range and long range mechanisms to the overall enhancement.

The study of the dependence of SERS on coverage in the submonolayer region can provide information on the chemical interaction of the scattering molecules on the surface. The dependence of SERS on coverage is better observed in the UHV system because here the dosing of absorbate can be controlled [32 40]. Anyway, the results are different and this may be due to treatements of the metal surface or to methods for coverage measurement. Some research [32, 40] showed that the SERS signal, beyond the first adsorbed monolayer is unenhanced, so there is an effect of long-range enhancement. Other research groups [41, 42] concluded that the SERS signal is mainly enhanced within the first monolayer.

There are some evidence which show that the scattering from the molecule beyond to the first monolayer in electrochemical systems is enhanced [43]. In the monolayer region, the dependence of SERS intensity on coverage is nonlinear.

Seki and Philipott [44] proposed that the giant enhancement occurs only for some fraction of the first monolayer and the molecules adsorbed only on special sites — named active sites — produce the greatest part of the SERS signal (in fact this concept of "active sites" is usually developed in electrochemical systems).

A very small underpotential coverage of deposited Tl about 3% or Pb leads to the complete quenching of SERS signal from pyridine on silver electrode and this quenching is irreversible [45].

Silver covered by a 0.1 Cu monolayer leads to shift in the pyridine spectra typical of an Ag surface, to that of a Cu surface [46].

In many systems, the SERS signal is irreversible quenched by the negative potentials of about — 1.2 V, vs. SCE (saturated calomel electrode). When the SERS signal is quenched by the negative potential, other ORC treatements are necessary to establish the enhancement effect.

I.5. **Depolarization and the lineshape.** One of the most characteristic phenomenon associated with SER scattering is an depolarization effect.

SERS reports [47] indicated that the majorities SERS spectra are depolarised and the depolarization ratio for totally symmetric and non-totally symmetric SERS bands is in the range 0.60—0.75. The depolarizing effect is due to either the roughness of the metallic surface or the orientation of adsorbed molecules.

The band shape in NR spectra follows a Lorentz lineshape function and in a SERS spectrum does not. The lineshape in SERS spectrum is the result of the simultaneous existance of two or more surfaces environments for adsorbed molecules.

In the Raman line of isochinoline adsorbed on silver at —0.6 V (Fig. 4), a lineshape of SERS bands — different by the gaussian or lorentzian lineshape — can be observed [48].

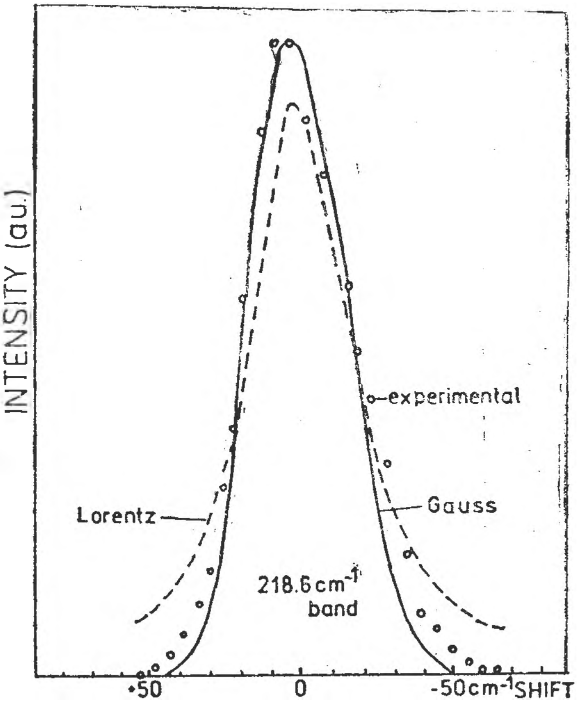

Fig. 4. The SERS band shape from 220 cm^{-1} for 0.01 M isochinoline at -0.6 V$_{SCE}$.

This is probably due to the nonhomogenity of the molecular enviroment, the most important being a distribution in the surface site that is involved in the surface-molecule line interaction.

II.6. **Continuum background** The strong continuum background of the SERS spectrum was demonstrated; he is not due to Rayleigh scattering [29].

The continuum background intensity decreases with the wave number and become flat in the 600—4000 cm^{-1} region, except for a hump between 1100—1700 cm^{-1} [49].

The continuum background has been considered to arise from luminescence except in the 1100—1700 cm^{-1} region, where the continuum has been atributed to surface carbon deposits. [50].

I.7. **The Dependence on the Potential.** The frequency and the intensity of the SERS bands are depending on the potential. This is one of the most important feature of the SER scattering from an electrode surface.

Several studies about the potential dependence have been reported [1, 51, 52, 53]. When the potential is shifted in a negative direction, the frequency of the SERS band moves to lower values. This can be observed for different chemical species such as pyridine, pyrazine, piperidine, p-nitroso-dimethylaniline, chlorides and cyanides.

Fig. 5 shows the shift in the peaks position (Raman shift) of several SERS bands with the change in the silver electrode potential for piperidine, in the $200-1000\ cm^{-1}$ range.

The only band positions who show the shift are Raman lines at $905\ cm^{-1}$ and $217\ cm^{-1}$ which have slopes of $31.2\ cm^{-1}V^{-1}$ and $27.9\ cm^{-1}V^{-1}$ respectively [54]. Since both bands have a roughly equal potential dependence, they were taken to be external vibrations, due to surface species.

The experimental features of potential-intensity profile are:

— The potential-intensity profile is usually bell-shaped and presents a maximum. The potential-intensity profile is similary to that of the differential capacitance vs. potential curve. In this way, the potential-intensity dependence reflects the change in surface coverage with the potential [53].

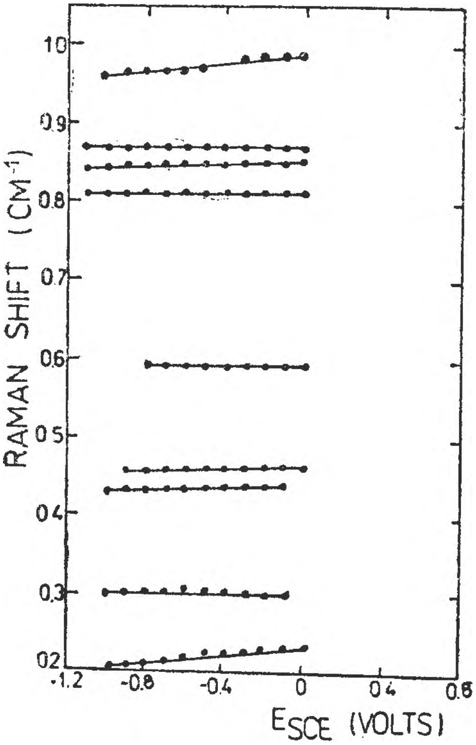

Fig. 5. Raman shifts vs. potential for piperidine bands.

— The potential at which the SERS maximum intensity occurs is different for different vibrational bands in the same spectrum. This is presented in Fig. 6, where the potential-intensity profile for two bands of the pyridine are show [54, 55].

The potential-intensity profile for some adsorbed molecules that can be reduced or oxidized on the electrode, have also been studied.

Farquarson et al. [56] found that there is a correspondence between potential-intensity profile and the cyclic voltammogram in the potential range were electrochemical reactions are going on.

In Fig. 7 we observe the crossing point, at $-0.57\ V\ V_{SCE}$ which is almost identically with the peak potential position of the cyclic voltammogram for the reaction:

$$MV^{2+}(\mathrm{ad}) + e^{-} \rightleftharpoons MD^{+}(\mathrm{ad})$$

where the process on the electrode is an reversible reduction of the adsorbed species.

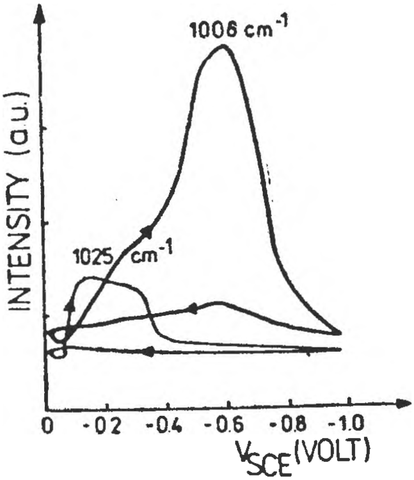

Fig. 6. Variations of SERS band intensities for pyridine on an Ag SERS active electrode, during ORC.

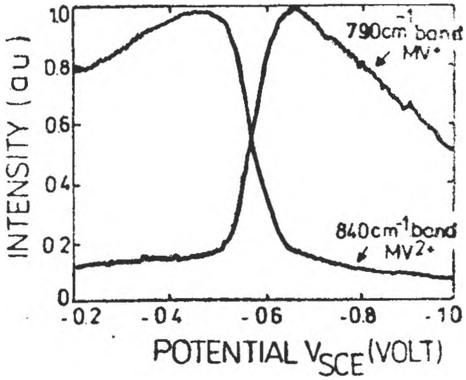

Fig. 7. The relative normalised SERS intensities dependence on potential for the bands at 840 cm^{-1} and 790 cm^{-2} of methylviologen dication MV^{2+} and methylviologen radical cation (MV^{+}).

Thus, the SERS intensities of bands caracteristic for different adsorbed redox states, can be related to the surface concentration of the adsorbed species and they are used to estimate the surface potential of the different adsorbed redox couple.

III. EXPERIMENTAL ASPECTS IN SERS SPECTROELECTROCHEMISTRY

SERS takes a special place in spectroelectrochemical techniques, because of the facilities to obtain data about: the kind and the geometry of SERS active electrode surfaces, surface adsorbed species, the nature of an interaction between adsorbate and electrodic substrate (metal, semiconductor or insulator).

The block-scheme of the SERS spectroelectrochemical system is shown in Fig. 8.

The exciting source can be an argon-ion, Kr, He-Ne laser or even a NdYAG laser [57]. The plasma lines can be eliminated by interferential and holographic filters. The laser light is focussed on the SERS active electrode

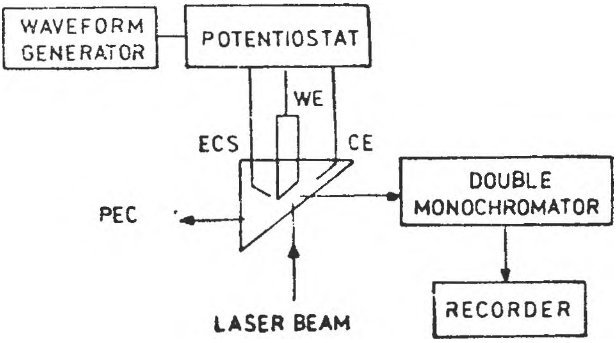

Fig. 8. Block scheme of the SERS apparatus.

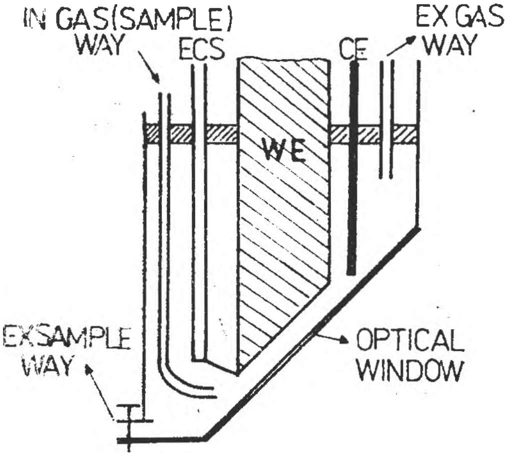

Fig. 9. Crossing section in spectroelectrochemical cell.

from the electrochemical cell. The details of this cell is showed in Fig. 9.

This construction of the cell allows to place the active SERS electrode in the proximity of the optical window to eliminate the Raman scattering and the fluorescence determined by the bulk solution. The oxigen was eliminated from solution by bubbling an innert gase.

The SERS activity of the electrod is obtained by following pretreatments: grinding with abrasive refined pulvers; washing with distilled deionised water; ultrasounding in bidistilled water; ORC in support solutions. Starting from negative potential, which correspond to positive current (Fig. 10), an oxidation of the electrode appears, and metallic surface is covered with a precipitated layer.

In negative current the precipitated layer is reducing, the electrode surface is covered with small metallic structures [48].

The adatoms (metal reduced atoms) are surrounded and immobilised by the anions of the solvent, and by the tested molecules in support solution.

The pretreatement concerns two or three ORC with or without the presence of exciting radiation.

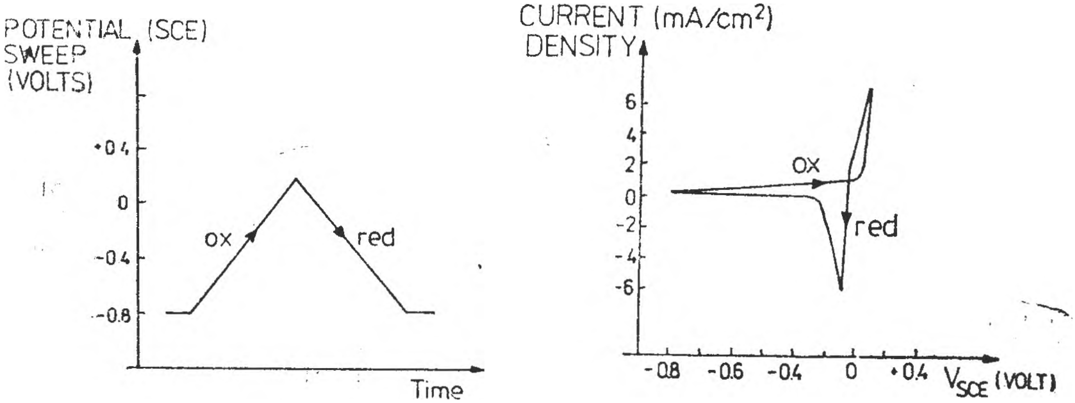

Fig. 10. The current density dependence vs. potential in ORC.

Generally speaking, the SERS spectroelectrochemical experimental observations have a hard reproductibility and, obviously, are conditioned by the purity of the used reactives.

Conclusions: SERS spectra are a useful tool for the study of adsorbed molecules species on Ag, Au and Cu electrode. From the shift of the peak position of the bands by comparison with that from normal Raman spectra, we can conclude about the position of the adsorbed of molecules at metal surface. The electrochemical technique allow the SERS studies of the molecules that can be reduced or oxidized on the electrode.

The large enhancement factor (10^6) in SERS spectra allow the use of this technique as a very sensitive analytical method.

REFERENCES

1. M. Fleischmann, P. J. Hendra and A. McQuillan, J. *Chem. Phys. Lett.* **26,** 163 (1974)
2. D. L. Jeanmarie and R. P. Van Duyne, *J. Electroanal. Chem.* **84,** 1 (1980)
3. M. G. Albrecht and L. A. Creighton, *J. Am. Chem. Soc.* **99,** 3514 (1980)
4. K. A. Bunding, R. A. Durst and M. I. Bell, *J. Electroanal. Chem.* **150** (1–2), 437 (1983)
5. R. Dornaus, M. B. Long, R. E. Benner and R. K. Chang, *Surf. Sci.* **93** (1) 240 (1980)
6. C. S. Allen and R. P. Van Duyne, *Chem. Phys. Lett.* **63** (3), 455 (1979)
7. C. C. Busby and T. A. Creighton, *J. Electroanal. Chem.* **133** (1), 183 (1982)
8. W. Krasser and A. J. Renouprez, *Solid State Commun.* **41** (3), 231 (1982)
9. M. L. Patterson and M. J. Weaver, *J. Phys. Chem.* **89** (23), 5046 (1985).
10. B. H. Loo, *J. Phys. Chem.* **87** (16), 3003 (1983).
11. J. A. Chambers and R. P. Buck, *J. Electroanal. Chem.* **140** (1), 173 (1982).
12. L. A. Sanchez and T. G. Spiro, *J. Phys. Chem.* **89** (5), 763 (1985).
13. *Techniques for caracterization of electrodes and electrochemical Processes*, Ed. R. Varma, J. R Selman, John Wiley and sons, 1991.
14. N. Avram, *Introducere in spectroscopia Raman*, Ed. Facla, Tim. 1982.
15. R. L. Paul, A. J. McQuillan, P. J. Hendra and M. Fleischmann, *J. Electroanal. Chem.* **66,** 248 (1975).
16. B. Pettinget, U. Wenning and H. Wetzel, *Surf. Sci.* **101** (1–3), 406 (1980).
17. C. S. Allen, G. C. Schatz and R. P. Van Duyne, *Chem. Phys. Lett.* **75** (2) 201 (1980).
18. P. Gao, M. J. Weaver, *J. Phys Chem,* **89** (23), 5040 (1985).
19. R. B. Bradley and K. A. Arunkumar, *Spectrosc. Lett.* **15** (2), 113 (1982).
20. H. Yamada and Y. Yamamoto, *Chem. Phys. Lett.* **77** (3), 520 (1981).
21. B. H. Loo, *J. Chem. Phys.* **75** (12), 5955 (1981).
22. R. S. Naaman, S. J. Buelow, O. Cheshovsky and D. R. Herschbach, *J. Phys. Chem,* **84,** 2692 (1980).
23. J. C. Tsang and J. Kirtley, *Solid State Commun.* **30** (10), 617 (1979).
24. M. Udagawa, C. C. Chou, J. C. Hemminger and S. Ushioda, *Phys. Rev.* B: **23** (12), 5843 (1981).
25. S. G. Schultz, M. Janik-Czachor and R. P. Van Duyne, *Surf. Sci.* **104** (2–3), 449 (1981).
26. S. H. Macomber, T. E. Furtak and T. M. Devine, *Chem. Phys. Lett.* **90** (6), 439 (1982).
27. F. Barz, J. G. Gordon, M. R. Philpott and M. J. Weaver, *Chem. Phys. Lett.* **94** (2), 168 (1983).
28. J. E. Pemberton and R. P. Buck, *J. Phys. Chem.* **85** (3), 248 (1981).
29. A. Otto, *Surf. Sci.* **75** (2), L392 (1978).

30. T. Iliescu, I. Marian, R. Mişca, V. Smarandache, *Analyst*, **119**, 567(1994).
31. W. Kasser, U. Kettler and P. S. Bechthold, *Chem. Phys. Lett.* **86** (3), 233 (1982).
32. P. N. Sanda, J. M. Warlaumont, J. E. Demuth, J. C. Tsanq, K. Christmann and J. A. Bradley, *Phys. Rev. Lett.* **45** (18), 1519 (1980).
33. J. C. Tsang, J. R. Kirtley and J. A. Bradley, *Phys. Rev. Lett.* **43**, 722 (1979).
34. D. W. Boo, W. S. Oh, M. S. Kim and K. Kim, *Chem. Phys. Lett.* **120** (3), 301 (1985).
35. Y. Mo, I. Morke and P. Wachter, *Solid State Commun.* **50** (9), 829 (1984).
36. M. Moskovits, *J. Chem. Phys.* **69** (9), 4159 (1978).
37. J. Gersten and A. Nitzan, *J. Chem. Phys.* **73** (7), 3023 (1980).
38. J. G. Bergman, J. P. Heritage, A. Pinczuk, J. M. Worlock and J. H. McFee, *Chem. Phys. Lett.* **68** (2–3), 412 (1979).
39. T. E. Furtak, *Solid State Commun*, **28** (11), 903 (1978).
40. I. Pockrand, *Chem. Phys. Lett.* **92** (5), 509 (1982).
41. I. Pockrand and A. Otto, *Solid State Commun.* **35** (1), 861 (1980).
42. G. L. Eesley, *Phys. Lett.* A 81A (2–3), 193 (1981).
43. B. Simic-Glavaski, S. Zecevic and E. Yeager, *J. Am. Chem. Soc.* **107**, 5625 (1985).
44. H. Seki, and M. R. Philpott, *J. Chem. Phys.* **73** (10), 5376 (1980).
45. J. J. Kester, *J. Chem. Phys.* **78** (12), 7466 (1983).
46. L. Moerl and B. Pettinger, *Solid State Commun.* **43** (5), 315 (1982).
47. T. E. Furtak, *Adv. Laser Spectrosc.* **2, 175** (1983).
48. J. R. Lombardi, R. L. Birke, *Surf. Sci.* **95,** L 259 (1980).
49. R. L. Birke, J. R. Lombardi, J. I. Gersten, *Phys. Rev. Lett.* **43, 71** (1979).
50. J. P. Heritage, J. C. Bergman, A. Pinczur, J. M. Worlock, *Chem. Phys. Lett.* **67** (23), 299 (1979).
51. S. Venkatesan, G. Erdheim, J. R. Lombardi and R. L. Birke, *Surf. Sci.* **101** (1–3), 387 (1980).
52. R. Kotz and E. Yeager, *J. Electroanal. Chem.* **123** (2), 235 (1981).
53. M. Fleiscmann, P. R. Graves and J. Robinson, *J. Electroanal. Chem.* **182** (1), 73 (1985).
54. A. L. Sanchez, R. L. Birke, J. R. Lombardi, *J. Phys. Chem.* **88** (9), 1792 (1984).
55. S. Kruszewski, J. Skonieczny, *Acta Phys. Pol. A* **80** (4), 611 (1991).
56. S. Farquarson, M. J. Weaver, P. A. Lay, R. A. Magruson and H. Taube *J. Am. Chem. Soc.* **105** (10), 3350 (1983).
57. H. J. Goldner, *Res. Development*, **56**, July (1992).
58. R. Christoph, H. Siegenthaler, H. Rohrer, H. Wiese, *Electrochim. Acta* **34,** 1011 (1989).

STUDIA UNIV. BABEŞ-BOLYAI, CHEMIA, XXXIX, 1–2, 1994

AN IMPROVED FIRST-ORDER OPTIMISATION OF THE MOLECULAR STRUCTURE TAKING ACCOUNT OF THE MOLECULAR TOPOLOGY

DRAGOŞ HORVATH, IOAN SILAGHI-DUMITRESCU

ABSTRACT. The classical gradient optimisation procedure used to minimise the molecular energies in the molecular mechanics approach was improved by superposing of the motions defined by the resulting forces acting on the molecular fragments viewed as rigid entities and the individual motions of the atoms defined by the derivatives of the energy with respect to their Cartesian coordinates. A translational and rotational correction accounting for the rigid fragment behaviour were introduced to calculate a better descent direction. The modified algorithm was able to accomplish in about 20 iterations the same drop in the function value obtained in 255 gradient iterations. Supplementary computing time or memory requirements are minimal and negligible in comparison to those employed by a second-order minimisation procedure.

1. Introduction. The modelling of molecular structure by means of computer programs that optimise the potential energy with respect of the atomic coordinates became a widespread tool in theoretical chemistry. No matter how this potential energy is obtained — either in the quantum-chemical or in the empirical force-field approach — it can be viewed as a function of the molecular geometry. Consequently, the potential energy of a molecule will be described in terms of *internal coordinates* (interatomic distances, valence or torsional angles, out of plane bending angles) and additive energetic contributions are assigned directly to these structural elements. The main problem encountered when trying to work on the internal coordinates consists in the fact that these are quite often dependent. Cartesian coordinates offer the advantage of being independent (even if the set of 3N coordinates is still redundant as far as they include the translation and rotation of the whole molecule) and very simple to use while the other way of finding a system of generalized coordinates raises a lot of theoretical and computational difficulties. Therefore, the molecular potential can be regarded as a function of 3N cartesian coordinates and this point of view was adopted by a large number of authors of molecular mechanics [1—10] and quantum chemical calculation programs.

The *optimisation* of a function having such a large number of variables is a challenging attempt for both mathematicians and chemists, but most molecular modelling software available today is based on adaptations of classical minimisation algorithms to this particular problem. The *direct search algorithms* are the most simple but least effective ones, so that we will restrain our discussion to the most widely used optimisation procedures: the *descent methods*. These use the information provided by the *derivatives* of the functions and calculate the best *descent direction* in the conformational hypersurface (the 3N-dimensional space of the cartesian coordinates). *First order* *descent methods* evaluate and use only the first derivatives of the molecular potential $V = V(x_{ij})$ with respect to the coordinates:

$$G = \Delta V = \| \partial V / \partial x_{ij} \|$$

$$\mathbf{g}_{ij} = (\partial V / \partial x_{ij}) / [\sum_n \sum_k (\partial V / \partial x_{nk})^2]^{1/2}$$

The direction g_{ij} is a versor pointing in the opposite direction of the gradient vector $\mathbf{\Delta V}$ and hence shows the direction in which the function decreases most rapidly. Shifting from the point where the gradient was evaluated (x^0) to a point at a distance s in the direction g

$$x_{ij} = x^0_{ij} + g^*_{ij} s \tag{1}$$

should lead to a position with a lower value of the potential if the step lenght s is properly chosen. A good strategy for finding s is to perform an *unidirectional optimisation*[14] of the function along the given direction g. keeping that value of s which leads to the smallest function value accesible within a given iteration. This process is to be continued until the minimum is reached whithin the wanted precission). Of course, there are other procedures using a modified direction basically derived from first-order derivatives.

A superior approach to the minimisation problem consists in using both first and second order derivatives in determining the optimal descent direction. Considering the Taylor expansion of the molecular potential in the vicinity of the point x:

$$V(\mathbf{x} + \Delta\mathbf{x}) = V(\mathbf{x}) + \langle \Delta\mathbf{x} | \mathbf{G} \rangle + \frac{1}{2} \langle \Delta\mathbf{x} | H \Delta\mathbf{x} \rangle + R_3$$

where G and H are the gradient and hessian matrices respectively $(H = = |\partial^2 V / \partial x_{ij} \partial x_{nk}|)$ and neglecting all higher order terms, if the displacement Δx is chosen such that the minimum is in $x + \Delta x$, then we have:

$$G(\mathbf{x} + \Delta\mathbf{x}) = G(\mathbf{x}) + H|\Delta\mathbf{x}\rangle = 0$$

If the function would have been quadratic, the calculation of the needed displacement $\mathbf{\Delta x}$ could have been done in one single iteration: $|\Delta\mathbf{x}\rangle = -\mathbf{H}^{-1}|\mathbf{G}\rangle$, but as this is not true, the direction defined by the vector Δx must be regarded as a descent direction and a suitable step lenght for advance in that direction must be determined in the same manner we already discussed at the first order methods.

Second-order (Newton-Raphson) methods are quadratically convergent, while first order methods do not always have this property. On the other hand, the latter require much less time per iteration because the evaluation of second-order derivatives is a quite tedious task and raises memory management problems as well (for example, the storage of the upper triangle of the Hessian for 1000 atoms requires about 26 Mbytes of memory). Furthermore, the inversion of the Hessian is a problem because, due to the redundance of 6 coordinates this matrix will be always singular. Therfore, the calculation of the descent direction is actually more complicated than described here (the "inversion" of *H* also implies its transformation into an equivalent but nonsingular matrix (see the method described briefly in reference [6], employing the Cholesky factorization or [7—9] for other examples). The *Davidon-Flecher-Powell* method[5] tries to approximate the inverse Hessian by means of two succesive gradient vectors and hence combines the advantages of the fast first order methods and the convergent quadratic Newton-Raphson procedures.

There are few available studies about the relative efficiency of these procedures when applied to molecules [6] but nowadays the second order methods are gaining importance as large and fast computers can support them. Anyway, gradient methods work much faster in bringing distorted geometries close to minimum but they require a much too large number of iterations to converge. Davidon-Flecher-Powell methods also need a quite large number of steps before they can build up a good approximation of the Hessian.

The purpose of this paper is to point out some of the specific, "chemical" properties of the potential function, which are not taken into account when a classical optimisation procedure is implemented. Difficulties in convergence arise because the function is non-quadratical as mathematicians say, but from a chemist's point of view some of these reasons can be easily derived and understood by means of basical knowledge about molecular structure. Furthermore, we have developped a simple first-order optimisation procedure which combines the information provided both by the gardient of the potential function and by the *molecular topology*, having a much better convergency rate while the computational effort required to derive the new descent method from the gradient is practically negligible.

2. **About the convergency of classical methods.** We will use a few examples to stress some of the difficultiess arised when classical methods are applied in molecular modelling. A first problem is encountered if in the initial distorted geometry there are bonds that differ significantly from their final lenght. Looking at the distorted ethane in figure 1.a it is easy to understand why a first-order method will exhibit an oscillatory behaviour.
At the first iteration, there will be atractive forces acting on the carbon atoms, trying to shorten the bond lenght, but *the attached hydrogens do not "feel" this,* since they are not involved in the C—C bond. If the C—H bonds are not streched and the C—C—H angles have their natural values, there will be no force at all acting on the hydrogens (except the van der Waals interactions which are not important in understanding the phenomenon since that type of potential is much weaker than the bond stretching one). Now, the atoms will be moved along the forces acting on them ($F = -\Delta V$) until the

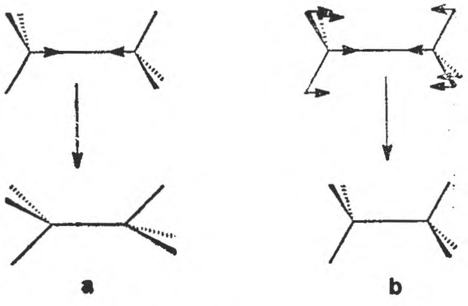

Fig. 1.

gain in energy accomplished by the shortening of the C—C bond will be equaled by the loss produced by the stretching of the C—H bonds and opening of C—C—H angles. Even if the energy lowered, it is difficult to admit that this new structure is indeed *closer to the true minimum* since as a matter of fact it is even more distorted than the first. At the next step, the hydrogens will be "dragged" after the carbons, and then the whole process would repeat, causing oscillations. It is obvious that the *methyls should be moved as bulks according to the forces acting on the C atoms.* Now, second order methods (figure 1b) will perform better because they simulate a "coupling" of the forces acting on different atmos: the second derivatives take account of the fact that the forces in the C—H bonds (zero in the begining) will increas while the C atom is moved. As a result, the hydrogens will be moved even if there is no initial force acting on them, but not as much as necessary — they will still lag behind the carbons. It is clear that the same kind of problems appear with distorted angles or torsional angles. Furthermore, the difficulties increase with the dimension of the fragment to be translated, because the effect of the displacement of the "pilot" atom implied in this distorted structural element can not be "felt" at a distance of p bonds from this until n iterations have been performed. Second-order methods provide a strong coupling between bonded atoms since the bonds are the most rigid structural elements in the molecule and somewhat weaker effect for geminal and vicinal atoms (coupling through angles and torsional angles; in the molecular mechanics approach $\partial^2 V / \partial x_{ij} \partial x_{nk} = 0$ unless there are structural elements including both atoms i and n). Since force fields do not assign potential contributions to fragments larger than 4 atoms (torsional angles and out-of-plane bendings), the coupling between more distant atoms relies completely on the weak nonbonded interactions. On the other hand, the rigidity of the bonds in a real molecule assures a relative stability of the geometry of the fragments. The optimal molecular model can be bracketed by the two extreme approaches: the rigid fragment approach where fragments are treated as bulks and no changes in their internal geometries are allowed and the complete geometry relaxation assumed by the classical optimisation procedures. The rigid fragment approach is widely used in molecular mechanics [10, 12] especially due to its simplicity, but it can be used only for a rough optimisation since most of the structural elements in the molecule are fixed. One could expect to obtain an effective optimisation procedure when combining these two extremes. Principially, it would be a good ideea to simply *alternate* these methods during optimisation [12], but it is even more effective to *use them simultaneously by designing an algorithm which calculates a descent direction as a linear combination of fragment and individual atom movements.* The alternation of total energy optimisation and displacement (translation or rotation) of fragments may indeed show some improvement, but no significant increase in convergence, due to the interdependence existing between the relative position of the fragments and their internal geometry. Yet, if the torsional angles of the starting geometry differ with more than 10 degrees from their final values, the intercalation of a torsional relaxation procedure during the full geometry optimisation leads to an important decrease of the required number of iterations. It is not adviceable to start with the torsional relaxation, because if the starting geometry of the fragments is very distorted, this will lead to artificial torsional minima and the only thing the procedure actually performs is rotating the fragments into unnatural positions.

3. **The fragmentation of the molecules.**. There are many criteria according to wich molecular fragments can be defined. Our workstation uses a single fragmentation procedure, which we have found convenient to use both for structure manipulation and optimisation as well. This procedure generates fragments by breaking of exocyclic bonds between nonterminal atoms and always considering the smallest of the two obtained fragments. As a consequence, there will be atoms contained in more than one fragment and also atoms that are not included in any of these:

$$\boxed{\mathrm{CH_3}}-\mathrm{CH_2}-\boxed{\mathrm{CH_2}-\boxed{\mathrm{CH_3}}}$$

Cycles can not be broken in this manner. In the Turbo Pascal program the fragments are considered as sets of atoms (F_k).

As a consequence of this fragmentation mode, each of the generated fragments are linked through one bond with the rest of molecule. Their motion will be relative to the superior fragment containing them, while the group of atoms that are not included in any fragment are fixed. It is known that the bonds are *the most rigid structural elements* in the molecule and hence it is predictible that under normal conditions, the changes in bond lengths are small compared to the modifications of the other structural elements. Therefore, the displacement directions for the fragments should be mainly orthogonal to the bond "anchoring" the fragment to the rest of the molecule. It is important for our optimisation procedure that a fragment is obtained by breaking of only one bond, although this is not explicitly imposed by the algorithm: a series of tests using a fragmentation procedure that also opens cycles showed no good results. The reason for this behaviour will be discussed later.

4. **Quantitative evaluation of the performance of the minimisation procedures.** The best criterium characterising an optimisation procedure is the time required to reach the optimum. The problem rising here is that various procedures could lead to different minima or get caught in false minima. Furthermore, in most cases the gradient procedure stopped before having finished, because the number of iterations grew too large (>255), so that the only way one can measure the efficiency of a method with respect to the gradient optimisation is the ratio between the number of iterations required by both methods to reach the same function value (usually the best value obtained by the gradient method). This criterium is not a very exact one because it compares the behaviour of the methods far from nimimum, while convergency speed might change dramatically as the optimisation advances. Finally we have chosen the following criteria to characterise the optimisation strategies:

A: total minimisation time;

B: the time needed to minimise a linear chain structure;
C: the time required to minimise non-cyclic molecules with gauche interactions, where large rotations are expected to occur;
D: the time required for the minimisation of cyclic molecules;
E: the total amount of unminimised energy, e.g. the sum of the difference between the lowest energy value obtained for the molecule through the whole series of tests and the energy at which the given method had stopped (if this difference is significant, >0.005 kcal/mol). B, C, D were monitored in order to find if a given strategy has any preference to a certain type of structural problems.

Tests were carried out on a set of randomly chosen molecules with up to 60 atoms, containing both liniar, ramificated, cyclic and polyciclic hydrocarbons and also structures with heteroatoms.

5. **The minimisation algorithm.** We use a simple adaptation of the gradient procedure, changes were made only at the calculation of the descent direction. At each fifth calculation of the gradient an unidirectional search is performed and the optimal advance step is used to make the following 5 steps (during which the variation of the function is no longer monitored), being simultaneously reduced — to simulate the natural tendency of decreasing as the optimisation approaches the minimum. The next unidirectional search will use a step of 0.75 of the previous optimal value and tries to bracket the local function minimum by calculating the molecular potential at 0.5, 1 and 1.5 times this value. The new optimal step is found by parabolic interpolation. The decrease in the function value after two succesive local optimisation is monitored as Δf. A combined termination criterium is used: $\Delta f < 0.002$ and the norm of the gradient must drop under a threshold value calculated as a function of an admissible residual force (0.05) per atom: $0.05\, N^{1/2}$, N being the number of atoms in the molecule. Finally an upper limit for the number of iterations can be imposed. If the ratio of the two succesive Δf values falls under 1.5, then it is assumed that the low convergency is due to the difficulties encountered with the torsional angles, the full geometry optimisation is interrupted and a torsional relaxation is performed.

The torsional relaxation program consists in a succesive search for the optimum torsional status for each torsional axis, reiterated until position of any fragment is no longer significantly influenced by the changes in the all others. Larger fragments are rotated first, because they produce the most important changes in geometry. Since just one fragment is rotated at one time, this procedure does not force symmetry conservation during the optimisation.

The parametrisation used is basically that of MM2[1] but uses Del Re[13] fractional charges (instead of bond moments) in evaluating the electrostatic terms.

6. **The calculation of the improved descent direction.** The procedure presented here can be most easily described in terms of an analogy between the optimisation process and the movement of points under the influence of a force field. The derivatives of the potential with respect to the coordinates are actually the components of the forces acting on each atom, and according

to the laws of dynamics (and considering that the atoms have all the same mass and do not posses any initial velocity) one can write:

$$\Delta x = 1/2 \cdot F/mt^2 \tag{2}$$

Comparing (1) and (2) it is obvious that the advancement step used in the gradient optimisation stands for $1/2t^2$ (since we do not care explicitely for the for the real parameters of the atomic motion *as the molecular dynamics* [14] does). Now we can use this mechanical analogy to write the equations for an improved descent direction: by assuming a rigid behaviour of the fragments, we can calculate the *resulting forces* acting on each of them:

$$\mathbf{G}_{kj} = \sum_{i \in F_k} \mathbf{g}_{ij} \tag{3}$$

where $\mathbf{G}_{kj}$ defines the force exercised by the rest of the molecule on the fragment F_k and all atoms will be translated in this direction, i.e. the all local forces $\mathbf{g}_{ij}$ will be substituted by the same value G_{kj}. If an atom is included in more than one fragment, it will be moved along the sum of the resulting forces on these fragments:

$$\mathbf{g}'_{ij} = \sum_{k, i \in F_k} \beta_k G_{kj} \tag{3'}$$

The ponderation coeficients β_k were taken as empirical functions of sizes s_k of the fragments (defined by the number of atoms in the fragment:)

$$\beta_k = [1 - y \cdot (s_{\max} - s_k)/(s_{\max} - s_{\min})] \tag{4}$$

where $s_{\max}$ and $s_{\min}$ are the maximal and minimal size of the fragments in the molecule. Then the values of these coefficients are normed: $\Sigma\beta_k = 1$. If $s_{\max} = s_{\min}$ then $\beta_k = 1/\text{number of fragments}$.

So far we have completely supressed the individual motions of the atoms, neglecting the *internal forces* in each fragment. In this approach, all structural elements involving terminal atoms are fixed. To allow complete geometry relaxation, we have to compromise between the classical gradient procedure and the rigid fragment approximation, generating a linear combination of the desceny directions given by the two alternatives:

$$\mathbf{g}^{t}_{ij} = \alpha_t \mathbf{g}'_{ij} + (1 - \alpha_t) \cdot \mathbf{g}_{ij} \tag{5}$$

The final problem is now to find an optimal translational rigidity coefficient α_t providing a fast convergency rate. This must also be done empirically and the best strategy we have found is a decreasing dependence of α_t on the norm of the gradient **G**:

$$\alpha_t = \alpha_1 \times \sigma(\sigma + \sigma_{\text{lim}}) + \sigma_2 \tag{6}$$

where σ_{lim} is the threshold value of the gradient norm at which minimisation is considered to be complete. It is surprising that values up to 0.8 perform well, showing that the participation of the rigid fragment approximation is very important. The tests have shown an increasing of the convergency rate —

the final potential value obtained by the gradient method was reached in up to 10 times less iterations especially for linear untorsioned chaines. With molecules having gauche interactions, the improvement was not so striking (only up to 3—4 — fold dropping the number of iterations). It was clear that the structures requiring modifications of torsional angles were still more difficult to optimise, because the algorithm developed until now did nothing to enhance the *rotation of the fragments*. The resulting force $\mathbf{g}_{ij}$ does not completely describe the motion of the rigid body: a resulting *moment* must be added to account for the rotational motion. It is convenient to calculate this moment in the point where a fragment is fixed:

$$\mathbf{M}_k = \sum_{i \in F_k} \mathbf{r}_i \times \mathbf{g}_i \tag{7}$$

where r_i is the position vector of the atom i with respect to the reference point and g_i is the force acting on this atom. The rotation of the fragment occurs around the axis of vector M and not around a torsional axis of molecule because angle bending or nonbonded interactions also tend to rotate it. It is difficult to simulate this rotation as such, but the physical analogy with the motion of a rigid body can be used to calculate the displacement directions for each atom according to the global tendency of rotation of the fragment:

$$\Delta\Phi = \mathbf{M}/(2I_a) \cdot t^2 \tag{8}$$

where $\Delta\Phi$ is the analog of (2), it is colinear to $\mathbf{M}$ and represents the rotation angle of a rigid having an inertial moment I_a subjected to a constant moment M as a function of time t. The inertial moment I_a with respect to the rotational axis defined by the moment M is actually the sum of the squared distances of the atoms in the fragment to this axis since the mass of each atom is not to be taken into account (is equaled to 1). At small $\Delta\Phi$ values, the corresponding displacement of the atoms in the fragment will be:

$$\Delta\mathbf{x}_i = 1/2(\mathbf{M}/I \times \mathbf{r}_i)t^2 \tag{9}$$

which compared to (2) leads to the conclusion that the terms:

$$\mathbf{g}^i_{rot} = \Sigma(\mathbf{M}/I_a \times \mathbf{r}_i)\beta_k \tag{10}$$

are the forces that should be added to the atoms in order to take account of the rotation of the rogid fragment. β are the same ponderation coeficients we previously met for the translational motion. The last step consists in combining the translational and rotational gradients:

$$\mathbf{g}^*_{ij} = \mathbf{g}^t_{ij} + \alpha_r \cdot \mathbf{g}^{rot}_{ij} \tag{11}$$

followed by the normation of g leading to new descent direction. Good values for α_r were found to be in the range 60..70 and are again surprisingly high. The classical gradient method asumes that the displacements of the points are proportional to the forces acting on them, but this is in fact a quite rough approximation because these forces change while the atoms are moved and the method is unable to take account of this changing. Since the applied step lenght is the same for all atoms, one of these will be moved too far (they "jump" over the potential valley) while others could be moved still further because in that direction the potential surface is smooth. It is clear that the movement in a radial direction — implying bond stretching or compression — will meet a sharp potential, while in directions tangential to the bonds the potential varies smoothly and allows larger advance steps. This is exactly what the very large α value accomplishes, amplifying the tangential movement with respect to the movement in other directions and thus empirical knowledge concerning the behaviour of the *second-order derivatives* is transmitted to the program. If the external forces acting on a fragment would also include bond stretching components (except the strain of the anchoring bond, which has no rotational contribution), the rotation of the fragment would also be characterised by sharp potential variations and the method would loose much of its effectiveness. This actually happens if the cycles are broken into multivalent fragments.

The best strategy seems to be the simple use of a constant α of about 70, during the whole minimisation. Of course, an optimal α could be determined for each iteration (searching for that values that allows to reach the smallest function value), but this requires much too many function calls. Another approach consisted in making a change in α ar each unidirectional optimisation, increasing or decreasing it with a value of 10 if this lowered the local minimum (selfadaptive α_r). This requires one or two more function calls for each iteration but does not improve significantly the convergence, and more, the total computation time is generally higher that in the case of a constant α_r.

7. **Results and disscusions.** We have selected a set of 9 optimisation strategies and their performances are listed in Table 1. The characteristics of these strategies are as follows:

— 1: uses an α_t value calculated with function (6) and having $\alpha_1 = 0.6$, $\alpha_2 = 0.2$; α_r is kept constant at 70. Ponderation coefficients β are those according to (4) and γ is fixed at 0.5. The full geometry relaxation transfers the control automatically to the torsional subroutine if there are hints that convergency might be slow (if the ratio of two succesive differences between local minimum function values falls below 2.5). Torsional relaxation can be called only once and then returns control to the full geometry optimisation.

— 2: identical to 1, but with $\alpha_1 = 0.65$ and without calls of the torsional relaxation procedure.

— 3: identical to 2 but uses equal ponderation coefficients (1/nr. of fragments).

— 4: identical to 3 but having $\alpha_1 = 0.6$ as in 1.

— 5: the same as 1, but with $\alpha_1 = 0.65$ and $\gamma = 0.6$.

— 6: α is calculated as in 1, but α is allowed to vary with ±10 at the unidirectional optimisation. No ponderation and no torsional relaxation are employed.

— 7: identical to 3, but torsional relaxation is called after a fixed number (21) of descent iterations.

— 8: as in 1 or 5, but with equal ponderation coefficients and no rotational correction ($\alpha_r = 0$).

— 9: classical gradient procedure.

Table 1

Energies (kcal/mol), minimisation times (seconds) and the number of iterations in 9 selected optimisation strategies.

Molecule	Applied minimisation strategy								
	1	2	3	4	5	6	7	8	9
1 E	9.7804	9.7802	9.7802	9.7804	9.7801	9.7825	9.7808	9.7887	9.9468
time	262 s	311 s	299 s	284 s	285 s	365 s	267 s	972 s	870 s
iterations	75	88	87	81	81	96	67+2	281+3*	255*
2	2.3417	2.3417	2.3417	2.3417	2.3417	2.3417	2.3417	2.3417	2.3417
	27 s	21 s	21 s	26 s	16 s	28 s	31 s	27 s	71 s
	27	21	21	26	17	26	27+1	27	76
3	3.2239	3.2242	3.2242	3.2243	3.2241	3.2242	3.2239	3.2241	3.2278
	22 s	22 s	21 s	21 s	22 s	28 s	32 s	74 s	233 s
	22	22	21	21	22	26	27+1	73+3	255*
4	4.2845	4.2875	4.2844	4.2844	4.2844	4.2844	4.2844	4.2863	4.2866
	49 s	37 s	49 s	60 s	49 s	66 s	74 s	49 s	311 s
	22	17	22	27	22	26	27+1	22	146
5	0.0989	0.0989	0.0989	0.0989	0.0991	0.0989	0.0989	0.0991	0.0992
	23 s	29 s	29 s	23 s	29 s	26 s	42 s	23 s	84 s
	17	22	22	16	22	16	27+1	17	66
6	6.2088	6.2088	6.2088	6.2088	6.2088	6.2088	6.2088	6.2100	6.2120
	103 s	104 s	95 s	77 s	105 s	96 s	132 s	103 s	834 s
	26	26	26	21	27	21	27+1	27	231
7	0.7086	0.7086	0.7086	0.7086	0.7086	0.7086	0.7086	0.7166	0.7921
	33 s	36 s	36 s	42 s	36 s	34 s	44 s	303 s	267 s
	27	32	32	36	32	26	32+1	281+1*	255*
8	9.4118	9.4118	9.4119	9.4119	9.4122	9.4119	9.4118	9.4136	9.4524
	199 s	202 s	198 s	198 s	165 s	224 s	271 s	284 s	1781 s
	26	26	26	26	22	26	27+1	33+1	255*
9	8.0288	8.0246	8.0261	8.0295	8.0231	8.0250	8.0227	8.0260	8.1219
	103 s	186 s	198 s	177 s	92 s	210 s	101 s	204 s	534 s
	37+4	86	91	81	33+4	86	32+5	81+6	255*
10	4.5158	4.5152	4.5164	4.5165	4.5156	4.5175	4.5144	4.5183	4.5864
	69 s	68 s	68 s	79 s	76 s	123 s	89 s	681 s	536 s
	31	31	31	37	35	51	32+2	202+6	255*
11	5.2693	5.2695	5.2696	5.2693	5.2696	5.2693	5.2694	5.2723	5.3146
	60 s	59 s	47 s	59 s	61 s	67 s	73 s	524 s	528 s
	27	26	21	26	28	26	27+1	241+2	255*
12	3.2703	3.2703	3.2703	3.2704	3.2704	3.2704	3.2703	3.2709	3.2752
	37 s	37 s	31 s	31 s	36 s	39 s	44 s	111 s	322 s
	27	27	21	21	27	26	27+1	80+3	255*

(Table 1 continued)

	1	2	3	4	5	6	7	8	9
13	4.0288	4.0287 35 s 28	4.0287 30 s 21	4.0287 37 s 28	4.0288 36 s 27	4.0287 33 s 21	4.0287 44 s 27+1	4.0291 118 s 77+2	4.0310 317 s 255*
14	6.1206 75 s 36	6.1205 61 s 26	6.1208 101 s 46	6.1214 101 s 46	6.1209 72 s 33	6.1210 138 s 56	6.1199 77 s 27+2	6.1239 449 s 201+4	6.241 534 s 255*
15	4.1047 49 s 22	4.1008 59 s 27	4.1010 57 s 26	4.1011 49 s 21	4.1008 48 s 21	4.1010 64 s 26	4.1008 73 s 27+1	4.1024 390 s 179+2	4.1079 523 s 255*
16	7.3910 60 s 27	7.3912 48 s 22	7.3913 48 s 22	7.3910 48 s 22	7.3910 59 s 27	7.3910 66 s 26	7.3921 70 s 27+1	7.3921 322 s 152+1	7.3956 518 s 255*
17	6.4391 235 s 90+7	7.1756 167 s 76	7.1751 240 s 111	7.1752 240 s 111	6.4384 251 s 99+7	7.1773 252 s 106	6.4390 268 s 102+6	6.5967 616 s 281+4*	7.5747 532 s 255*
18	25.726 608 s 107+3	25.725 663 s 121	25.725 740 s 136	25.725 715 s 131	25.725 615 s 107+3	25.725 687 s 116	25.726 631 s 107+3	26.19 1547 s 281+3*	27.581 1357 s 255*
19	7.2369 480 s 281+26	7.2412 432 s 255*	7.2563 430 s 255*	7.2475 430 s 255*	7.2381 484 s 255*	7.2430 468 s 255*	7.2447 479 s 272+2*	7.3503 485 s 281+2*	7.4660 429 s 255*
A	2531 s	2577 s	2738 s	2620 s	2537 s	3014 s	2842 s	7274 s	10581 s
B	411 s	399 s	399 s	403 s	371 s	448 s	552 s	766 s	3264 s
C	747 s	742 s	841 s	842 s	753 s	1020 s	871 s	3489 s	4577 s
D	1350 s	1406 s	1469 s	1429 s	1384 s	1520 s	1377 s	3004 s	2674 s
E	0.0000	0.7400	0.7600	0.7500	0.0000	0.7500	0.0080	0.7600	3.8600

List of symbols:

* optimisation stopped after this number of iterations

1 : e-n-butylcyclohexane
2 : anti-butane
3 : gauche-butane
4 : anti-n-heptane
5 : 2,2-dimethylpropane
6 : anti-n-decane
7 : 3-methoxypropanoic acid
8 : anti-n-pentadecane
9 : 2-ethylpentane
10 : 2-methylhexane (1 gauche interaction)
11 : 2-methylhexane (2 gauche interactions)
12 : 1-methylbutane (1 gauche interaction)
13 : 1-methyl-butane (2 gauche interactions)
14 : 2-methylhexane
15 : 2,2-dimethylpentane
16 : 3,3-dimethylpentane
17 : 2,4-dimethylpentane
18 : 1-sec-buthyl-adamatane
19 : 1,3-dioxane-5-a-carboxylic acid

A : total time (on a PC-AT 386, whitout numerical coprocessor)

B : time for linear anti-conformations (2, 4, 6, 7, 8)

C : time for noncyclic molecules with gauche-interactions (3, 9...17)

D : time for cyclic molecules (1, 18, 19)

E : sum of the unminimised energies, if these exceeded 0.005 kcal/mol

It can be seen from Table 1 that all the methods lead essentially to the same energy minimum for most of the molecules, an interesting exception being 2,4-dimethylpentane (entry nr. 17) where the obtained minimum was dependent on the chosen minimisation strategy. Both minima (at 6.43 and 7.17) showed to be real minima and not artefacts of the torsional minimisation routine (calculations performed with an alternative torsional relaxation procedure which rotates simultaneously all fragments also lead to the lower minimum if applied on the *initial geometry*, but *not* on the geometry of higher minimum. The later is stable with respect to torsional angle optimisation and it is not a false minimum due to incapacity of descent methods to adjust the torsional angles). Hence, the higher energies reported by methods 2, 3, 4 and 6 do not stand for a failure to reach the minimum point, but simply express that different paths lead to different local minima.

The *best methods are certainly* 2 *and* 5 *which "intelligently" combine the descent and torsional procedure*. These methods did not call the torsional procedure at all when minimising untorsioned chains, because they "felt" that convergency is already good. Moreover, it was ignored even in molecules with gauche interactions in which the rotational correction of the gradient could efficiently adjust the torsional angles. The longer time required by 7 is mainly due to unnecessary torsional relaxation calls (this trend is clearly visible when comparing the times for optimising the untorsioned chain structures (B)). Methods 2 and 5 lead always to the minimum while the gradient method usualy had to be aborted because of the too large number of iterations, so that the real time needed by the later to perform a job as good as the first should be significantlly higher. Even so, the improved procedure is about 4 times faster and it required meanly 11..21 iterations to reach a lower energy than the final threshold reached by gradient optimisation in 255 iterations. The ratio of the employed times is even higher for noncyclic structures (about 8 for untorsioned chains and 6 for molecules with gauche interactions) because the improvements made do not apply on the adjustment of ring geometries. The improvement in minimisation is increasing with an increasing number off exocyclic torsional axes (1,3-dioxane-5-a-carboxilic acid — entry 19, where the exocyclic group is small compared to the ring, can be only difficulty minimised by any of the methods. Another starting geometry, containing a preminimised dioxane ring — not listed in Table 1 — performed much better). Nevertheless, the optimisation of the substituted ring systems was still about 2 — times faster in comparison with the gradient optimisation.

Untorsioned chains (except 3-methoxypropanoic acid, entry 7) can be minimised quite well when no rotational correction is used (method 8). On the contrary, this correction is extremly important for molecules with gauche-interactions, or generally speaking for structures where rotations play an important role. Even if no torsions occur, important rotations are required for the adjustment of the valence angles in 3-methoxypropanoic acid, since these were badly reproduced in the initial geometry (the geometry-building program assigned tetrahedral, angles for both carbon and oxygen).

Method 6 is somewhat different because here the empirically chosen α_r is itself a subject of optimisation: the unidirectional search procedure was modified to allow this. Two modified descent directions were calculated with the values $\alpha_r + 10$ and $\alpha_r - 10$, then a step of current length was taken in each of these directions and the molecular potential evaluated in the reached points. The α value generating the direction that lead to a better function value was taken as current α_r. It would have been more rigurously to perform a full unidirectional optimisation on both directions and to select the one showing the best local minimum, but this would have required a much too large number of function evaluations. Even so, one supplementary function call is needed and it is visible that this continuous altering of α does not improve the convergency as much as to compensate for the extra computational effort.

It is important to notice that the number of iterations is practically no longer dependent or at least very weakly dependent on the molecular size, as it is in the gradient optimisation. This is a direct consequence of the "coherence" introduced in the motion of the atoms.

8. **Conclusions.** The simple and intuitive modifications described by eq. 11 can be very easily implemented into all programs using gradient methods, without extending too much the memory requirements. There are also no reasons for which this modification should not work together with other, more performant descent methods, including Newto-Raphson procedures. This effective optimisation method might be very powerful when applied to large chains as proteins.

Acknowledgement. The authors wish to thank dr. Muzsnay Csaba from "Babes-Bolyai" University for the computer access granted for this work.

REFERENCES

1. U. Burkhert, N. L. Allinger, *Molecular Mechanics*, ACS, Washington DC, 1981.
2. G. J. Gleicher and P. R. von Schleyer, *J. Amer. Chem. Soc.* **89**, 582 (1967).
3. M. Bixon and S. Lifson, *Tetrahedron*, **23**, 769 (1967).
4. K. B. Wiberg, *J. Amer. Chem. Soc.*, **87**, 1070 (1965).
5. J. E. Williams, P. J. Stang and P. R. von Schleyer, *Ann. Rev. Phys. Chem.*, **19**, 531 (1968).
6. S. Niketik and K. Rasmussen, *The Consistent Force Field*, Springer Verlag, New York, 1977.
7. A. Warshel and S. Lifson, *J. Chem. Phys*, **49**, 5116 (1968).
8. R. H. Boyd, *J. Chem. Phys.*, **49**, 2574 (1968).
9. C. Altona and G. H. Faber, *Fortschr. Chem. Forsch.*, **45**, 1 (1974).
10. J. Labanowsky, I. Moţoc, C. B. Naylor and R. A. Dammkoehler, *Quant. Struct.-Activity Relat.*, **5**, 138 (1986).
11. In unidirectional optimisation, the computational effort required to locate the minimum must be compensated by the increasing in convergency rate obtained by performing the linear search. This is not always true since in the local minimum the new gradient direction is orthogonal to the previous one, this might lead to a slow convergence.
12. D. Horvath and I. Silaghi-Dumitrescu, *Rev. Roumaine. Chim.*, **37**, 1165 (1992).
13. G. del Re, *J. Chem. Soc.*, **1958**, 4031.
14. J. A. McCammon and S. C. Harvey, *Dynamics of Proteins and Nucleic Acids*, Cambridge University Press, 1987.

STUDIA UNIV. BABEŞ-BOLYAI, CHEMIA, XXXIX, 1–2, 1994

USING NEURAL NETWORKS IN MODELING AND OPTIMIZATION OF THE ION EXCHANGE MEMBRANE ELECTROLYSERS
PART I – ANALYTICAL MODEL

ARPAD IMRE LUCACI, IOANA BUNEA, ŞERBAN AGACHI

ABSTRACT. This paper deals with the implementation of a neural network (NN) model of an industrial electrolyser. In order to have modeling data, from NN point of view, we had to model the electrolyser analytically at the beginning. The main equations of the model and some simulation results are given in the paper. In order to optimize the process, one could have been observed that the using of the analytical model is much too slow for practical purposes in industry. The result, was the idea to use a NN model.

The main procedure used in the manufacturing of chlorine, is the brine electrolysis. This is performed in industrial electrolysers, the best known types being those with amalgam cathode, azbestos diaphragm and ion exchange membrane (IEM) electrolysers. Due to the fact the IEM electrolysers are the most advantageous, from the economic and ecological points of view, it is of great interest, the study of their mathematical modeling having as an ultimate target, the optimization of their work and their proper control.

The construction of an electrolysis cell is given in fig. 1. These cells are assembled in their bipolar way, 50 in a block, and a number of 21 blocks are connected (fig. 2) to a c.c. source or rectifier.

It is desirable, that the process to be operated at optimum, in order to obtain the lowest production cost per ton of NaOH. That's why one needs a steady state mathematical model capable to compute the cost, based on the computed production of chlorine, hydrogen and NaOH, on the consumption of energy and raw materials.

There are many ways to compose an object or scope function subjected to minimization. In this case, we have decided to minimize the expenses on the ton of NaOH (lei/t). The correspondent objective function is the sum of the expenses with the electric and thermal energy, at which the raw materials consumption is added (1).

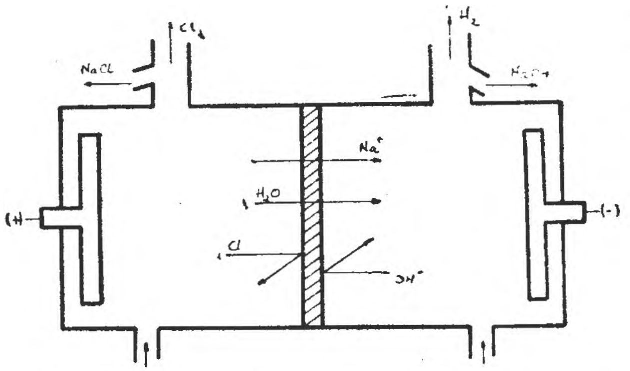

Fig. 1. Schematic diagram of an IEM chlorine cell

$$y = \frac{(C_{curent} + C_{enterm} + C_{matprim}}{Productie} \qquad (1)$$

The way these costs are computed is given in Appendix 1 where

y_1 is the temperature of the cell, T

y_2 — voltage drop on the cell, Tensiune

y_3 — NaOH output flow, F_ec

y_4 — output concentration of H_2O, c_eH_2Oc

y_5 — weight concentration of NaOH.

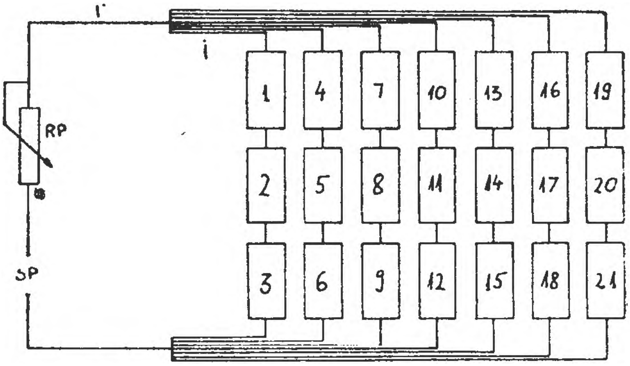

Fig. 2. Connection of the blocks in the electric circuit

Appendix 1

Matlab program for the optimization of the IEM reactor

```
function y = f_ob(X_)
% calculul cheltuielilor minime pe tona de NaOH [lei/t];

% Notații

% C_curent   — cheltuieli cu energia electrică        [lei/s];
% C_matprim  — cheltuieli cu materiile prime          [lei/s];
% C_enterm   — cheltuieli cu energia termică          [lei/s];
% lV         — căldura latentă de vaporizare          [kcal/kg];
% costsar    — costul saramurii                       [lei/t];
% costenel   — costul energiei electrice              [lei/kWh];
% costent    — costul energiei termice                [lei/Gcal];
% CpSar      — căldura specifică saramura             [kcal/kg*K];

% Constante

   lv=525;              %[kcal/kg];
   CIS=304;             %[g/l];
   costsar=2358;        %[lei/t];
```

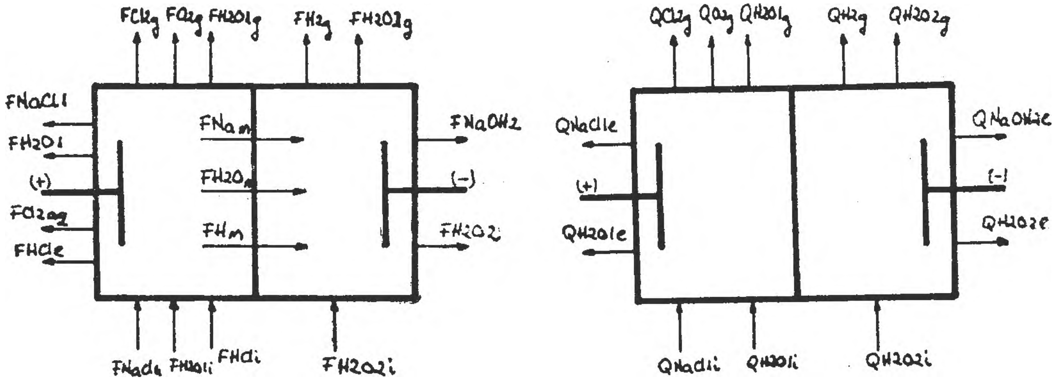

Fig. 3. Diagram with mass and heat balances on an IEM cell

```
   costenel= 101 ;        %[lei/kWh] ;
   costent= 17000 ;       %[lei/Gcal] ;
   MH20= 18 ;             %[kg/kmol] ;
   MNaOH= 40 ;            %[kg/kmol] ;
   MNaCl= 58.5 ;          %[kg/kmol] ;
   Ap= 2.4 ;              %[mp] ;
   DensApa= 1000 ;        %[kg/mc] ;

X_

   Itot = X_(1) ;         %[kA] ;
   Tint = X_(2) ;         %[grd] ;
   FiNaCl = X_(3) ;       %[mc/s] ;

%%%%%%%%%%%%%%%%%%%%
   CIS      = CIS/MNaCl ;                    % [kmol/mc]
   rc       = rc / 100 ;                     % adim.
   id       = Itot/(Ap*1450)*le3 ;           % [A/mp]
   ir       = id ;
   cH20Ci   = DensApa/MH2O ;                 % [kmol/mc]
   roiA     = DSO1NaCl (CIS) ;
   roiC     = DensApa ;
%%%%%%%%%%%%%%
CpSar =4.187*(1-CIS)+CIS*0.837 ;
roiA =DSO1NaCl (CIS) ;
[y1, y2, y3, y4, y5] = fmod(Itot, Tint, FiNaCl) ;
C_curent = y2*Itot*costenel/3600/le3 ;
C_matprim = FiNaCl*CIS*costsar/1000 ;
C_enterm = y3*y4*MH2O*lv*costent/le6+FiA*roiA*CpSar*le3/4.185*(TAlim-TRef)*..
           le-9*costent ;
Producţie = y3*y5*MNaOH/1000 ;

    y = (C_curent + C_matprim + C_enterm)/Producţie
```

All output variables are computed as function of three independent inputs: input temperature (Talim), input brine flow (Falim) and total current (I).

2. Mathematical model of the electrolysis process. The basic equations of the mathematical model are those written for mass and heat balances (fig. 3), voltage balance and electrochemical equations.

The main equations of the model [1] are given bellow:

Mass balance

Anode compartment:

$$F_{Cl^-,1} + F_{Cl^-,M} + X \cdot F_{Cl^-,1i} = F_{Cl^-,1i} \tag{2}$$

$$F_{Na^+,1} + F_{Na^+,M} = F_{Na^+,1i} \tag{3}$$

$$F_{H_2O,1} + F_{H_2O,1}(g) + F_{H_2O,M} + \frac{I \cdot 3600 \cdot (1-\eta)}{2F} = F_{H_2O,1i} \tag{4}$$

$$F_{OH^-,M} - \frac{I \cdot 3600 \cdot (1-\eta)}{F} = 0 \tag{5}$$

$$F_{Cl_2}(g) + F_{Cl_2}(aq) = \frac{I \cdot \eta \cdot 3600}{2F} \tag{6}$$

$$F_{O_2}(g) - \frac{I \cdot (1-\eta) \cdot 3600}{4F} = 0 \tag{7}$$

$$P_{H_2O,1} \cdot [F_{Cl_2}(g) + F_{O_2}(g) + F_{H_2O,1}(g)] - P \cdot F_{H_2O,1}(g) = 0 \tag{8}$$

$$F_{Cl^-,1} - F_{Na^+,1} = 0 \tag{9}$$

$$F_{Cl_2}(aq) - \left(\frac{m_{Cl_2} \cdot 18 \cdot F_{H_2O,1}}{1000}\right) = 0 \tag{10}$$

Membrane :

$$t_{Na^+} + t_{OH^-} = 1 \tag{11}$$

$$F_{H_2O,M} = F_{Na^+,M} \cdot t_{H_2O} \tag{12}$$

Cathode compartment :

$$F_{Cl^-,M} - F_{Cl^-,2} = 0 \tag{13}$$

$$F_{Na^+,M} - F_{Na^+,2} = 0 \tag{14}$$

$$F_{H_2O,M} - F_{H_2O,2} - F_{H_2O,2}(g) = \frac{I \cdot 3600}{F} - F_{H_2O,2i} \tag{15}$$

$$F_{OH^-} + F_{OH^-,M} = \frac{I \cdot 3600}{F} \tag{16}$$

$$F_{H_2}(g) = \frac{I \cdot 3600}{2F} \tag{17}$$

$$P_{H_2O,2} \cdot [F_{H_2}(g) + F_{H_2O,2}(g)] = P \cdot F_{H_2O,2}(g) \tag{18}$$

Energy balance

$$\Delta H(kcalh^{-1}) = q - \left(\frac{E \cdot I \cdot 3600}{4{,}18}\right) \tag{19}$$

$$\Delta H = \Delta H_p + \Delta H_{rxn,25} \tag{20}$$

$$\begin{aligned} \Delta H_p = {} & C_{pm,Cl_2}(T-25)F_{Cl_2} \cdot 71 + C_{pm,H_2} \cdot (T-25)F_{H_2} \cdot 2 + C_{pm,O_2}(T-25)F_{O_2} \cdot \\ & \cdot 32 + (H_{NaOH,T} - H_{NaOH,25})Q_2 d_2 + (H_{H_2O(g),T} - H_{H_2O,25}) \cdot [F_{H_2O,1}(g) \cdot 18 + \\ & + F_{H_2O,2}(g) \cdot 18] \end{aligned} \tag{21}$$

$$\Delta H_{rxn,25} = \Delta H_{rxn1,25} + \Delta H_{rxn2,25} \tag{22}$$

$$\Delta H_{rxn1,25} = XF_{NaCl,1i}[\Delta H_{F,NaOH(aq)} + 1/2\Delta H_{F,Cl_2(g)} + 1/2\Delta H_{F,H_2(g)} - \\ - \Delta H_{F,NaCl(aq)} - \Delta H_{F,H_2O(1)}] \tag{23}$$

$$\Delta H_{rxn2,25} = F_{O_2(g)}[-2\Delta H_{F,H_2O(1)} + \Delta H_{F,O_2(g)} + 2\Delta H_{F,H_2(g)}] \tag{24}$$

Voltage balance

$$E = E_0 + \eta_{ic} - \eta_{ia} - (IR)_{soln,1} - (IR)_{mem} - (IR)_{soln,2} \tag{25}$$

$$E_0 = -2{,}187 + 0{,}0004272(T - 25) + 8{,}314(T + 273)\ln(K)/96500 \tag{26}$$

$$(K) = a_{NaOH}(P_{Cl_2})^{1/2}(P_{H_2})^{1/2}/a_{NaCl} \tag{27}$$

$$\eta_{ia} = 0{,}0277 \log (i_p/0{,}0125) \tag{28}$$

$$\eta_{ic} = 0{,}0656 \ln (i_p/i_{0,H_2}) \tag{29}$$

$$\log (i_{0,H_2}) = (-0{,}0045\, m^2_{NaOH}) + (0{,}203\, m_{NaOH}) - 5{,}92 \tag{30}$$

$$(IR)_{soln,1} = [i_p l_1/K_1] \cdot 1000 \tag{31}$$

$$(IR)_{mem} = [\delta i_p/K_m) \cdot 1000 \tag{32}$$

$$(IR)_{soln,2} = [i_p l_2/K_2] \cdot 1000 \tag{33}$$

There are other equations too, expressing the intermediate terms in these equations above, but because of the scope of this paper, we did not consider necessary to write them down.

We have solved the model in MATLAB software and one set of typical results is given in Appendix 2.

Appendix **2**

Set of typical results obtained from the model of an IEM cell

Bilanțul de masă pentru spațiul anodic

Intrat [kmol/s]		Ieșit [kmol/s]	
Saramura alimentare		Saramura epuizată	
H_2O	6.275239101	H_2O	5.919456437
NaCl	0.662265819	NaCl	0.548155229
HCl	0.000127443	HCl	0.000127379
		Cl^-	0.005655530
		Gaze	
		Cl	0.051399782
		O	0.002147243
		H_2O(vap)	0.009156408
		Transfer prin membrană	
		Na^+	0.114110589
		H_2O	0.342331768
		H^+	0.008588969
Total	6.937632362	Total	7.001129335

Bilanțul de masă pentru spațiul anodic

Intrat [kg/s]		Ieșit [kg/s]	
Saramură alimentare		Saramura epuizată	
H_2O	112.9543038	H_2O	106.5502159
NaCl	38.7425504	NaCl	32.0670809
HCl	0.046517	HCl	0.0046493
		Cl_2	0.4015426
		Cl	3.6493845
		O	0.0687118
		H_2O(vap)	0.1648154
		Transfer prin membrană	
		Na^+	2.6245436
		H_2O	6.1619718
		H^+	0.0085890
Total	151.7015059	Total	151.7015065

Bilanțul de masă pentru spațiul catodic

Intrat [kmol/s]		Ieșit [kmol/s]	
Apa demi alimentare		Soluție NaOH ieșire	
H_2O	0.376716111	H_2O	0.594446626
		NaOH	0.114110589
Transfer prin membrană		Gaze	
Na^+	0.114110589	H	0.061349775
H_2O	0.342331768	H_2O(vap)	0.010490664
H^+	0.008588969		
Total	0.841747438	Total	0.780397655

Bilanțul de masă pentru spațiul catodic

Intrat [kg/s]		Ieșit [kg/s]	
Apa demi alimentare		Soluție NaOH ieșire	
H_2O	6.7808900	H_2O	10.7000393
		NaOH	4.5644236
Transfer prin membrană		Gaze	
Na^+	2.6245436	H	0.1226996
H_2O	6.1619718	H_2O(vap)	0.1888319
H^+	0.0085890		
Total	15.5759944	Total	15.5759943

Bilanțul de tensiune — celula cu MSI

Componenta		[V]	[%]
Tensiunea minimă de electroliză	:	2.1247720	56.3989482
Supratensiunea anodică	:	0.1505104	3.9950783
Supratensiunea catodică	:	1.1824731	31.3870102
Căderea de tensiune pe anolit	:	0.2373252	6.2994489
Căderea de tensiune pe membrană	:	0.0018636	0.0494674
Căderea de tensiune pe catolit	:	0.0704521	1.8700470
Tensiunea totală	:	3.7673965	100.0000000

The multiple runs of the model showed us many difficulties in solving the algebraic equations representing the steady state. We have used a procedure of solving nonlinear systems of equations "fsolve" implemented in MATLAB which is very sensitive at the initial point and the range in which the variables can change. But we have succeeded to obtain good results in the range of real working of the reactor.

The model we have discussed about "fmod" is used in the optimization program afterwards, with the scope of minimizing the expenses with electricity, raw materials and thermal energy.

Using a sensitivity study on the model, we decided that the most important variables in the minimization of the cost function, are: feed temperature (T [°C]), total current on the electrolyser (I [A]) and feed brine flow (F [m^3/s]). We used the polyhedron method for the optimization, subjected to constraints. Due to the intricate structure of the model, the running time is awfully long.

We had runs of 7 hours and more on a PC 486/50 MHz with no proper results.

That's why we had the idea of using a model based on neural networks. In this case, the computation of the model is reduced at a small number of matricial equations. The running time of the optimization program using the neural networks was of 8 seconds. The way we have built the model based on neutral networks is explained in the following section of this paper.

REFERENCES

1. R. R. Chandran, D. T. Chin — Reactor analysis of a chlor-alkali membrane cell, *Electrochemica Acta*, **31**, Nr. 1, pag. 39—50, 1986.

NOMENCLATURE:

$C_{p,j}$ — *specific heat of aqueous solution of species j,* [$kcal\ kg^{-1}{}^{\circ}C^{-1}$]

$C_{pm,j}$.— *mean specific heat of the gases given by subscript j with reference temperature of 25°C* [$kcal\ kg^{-1}{}^{\circ}C^{-1}$]

d_s — *density of the exist solution from catholyte compartment,* [$kmol\ m^{-3}$]

E — *total cell voltage,* [V]

E_0 — *open circuit cell voltage,* [V]

F — *Faraday's constant,* [$96487 \cdot 10^6\ C\ kg\ eq^{-1}$]

$F_{j,1i}$ — *inlet molar flow rate of species j to anolyte compartment,* [$kmol\ s^{-1}$]

$F_{j,2i}$ — *inlet molar flow rate of species j to catholyte compartment,* [$kmol\ s^{-1}$]

$F_{j,1}$ — *exit molar flow rate of species j from anolyte compartment,* [$kmol\ s^{-1}$]

$F_{j,2}$ — *exit molar flow rate of species j from catholyte compartment,* [$kmol\ s^{-1}$]

$F_{j,M}$ — *molar flow rate of species j through the membrane,* [$kmol^{-1}\ s^{-1}$]

$H_{H_2O,T}(g)$ — *enthalpy of saturated water vapour at temperature T°C,* [$kcal\ kg^{-1}$]

$H_{H_2O,T}$ — *enthalpy of water at temperature T°C,* [$kcal\ kg^{-1}$]

$H_{j,T}$ — *enthalpy of the aqueous solution of species j, at temperature of T °C,* [$kcal\ kg^{-1}$]
$\Delta H_{rxn,25}$ — *heat of reaction at 25 °C,* [$kcal\ kmol^{-1}$]
i_{0,H_2} — *exchange current density of H_2 evolution on steel electrode,* [$A\ m^{-2}$]
i_p — *apparent current density based on the apparent area of the membrane A ,* [$A\ m^{-2}$]
I — *total cell current,* [A]
$(IR)_{soln,1}$ — *solution voltage drop between the anode and the membrane,* [V]
$IR)_{mem}$ — *voltage drop across the membrane,* [V]
$(IR)_{soln,2}$ — *solution voltage drop between the cathode and the membrane,* [V]
$(K_1$ — *conductivity of the anolyte solution,* [$ohm^{-1}\ m^{-1}$]
K_M — *conductivity of the membrane,* [$ohm^{-1}\ m^{-1}$]
$K_{2,T}$ — *conductivity of the catholyte NaOH solution at T °C,* [$ohm^{-1}\ m^{-1}$]
l_1 — *distance between the anode and the membrane,* [m]
l_2 — *distance between the cathode and the membrane,* [m]
m_j — *molality of the aqueous solution of species j,* [$kmol\ (1000\ kg\ water)^{-1}$]
P — *total atmospheric pressure,* [atm]
Q_2 — *exit volumetric flow rate from catholyte compartment,* [$m^3\ h^{-1}$]
t_j — *transport number of ion j*
T — *cell temperature,* [°C]
X — *conversion based on the amount of NaCl fed*
Y — *concentration of aqueous solution of NaCl,* [$kmol\ H_2O\ (kmol\ NaCl)^{-1}$]
Z — *concentration of aqueous solution of NaOH,* [$kmol\ H_2O\ (kmol\ NaOH)^{-1}$]
δ — *membrane thickness,* [m]
η — *current efficiency,* [%]
η_a — *anodic overpotential,* [V]
η_c — *cathodic overpotential,* [V]

SUBSCRIPTS

1i — inlet to the anolyte compartment
2i — inlet to the catholyte compartment
1 — exit flow from the anolyte compartment; also represents the anolyte compartment
2 — exit flow rate from the catholyte compartment; also represents the catholyte compartment

STUDIA UNIV. BABEŞ-BOLYAI, CHEMIA, XXXIX, 1 – 1994

USING NEURAL NETWORKS IN MODELING AND OPTIMIZATION OF THE ION EXCHANGE MEMBRANE ELECTROLYSERS

PART II – NEURAL NETWORK MODEL

ŞERBAN AGACHI, IOANA BUNEA, ARPAD IMRE-LUCACI

ABSTRACT. The paper describes the way of using MathWork's Neural Network Toolbox software, with direct application at an industrial chloralkali electrolyser. More alternatives of learning techniques and learning data sets were tried. The best results are reported.

1. **Introduction.** The neural network tests described in this report are concerned primarily with the ability of a neural network to learn the functional relationship between variables. We have seen in the previous part of the present paper, that there are great inconveniences at the optimization, using the intricate model containing mass and energy balance and electrochemical equations. So, we decided that a model based on neural networks, if it does a proper identification of the process, is much better to be used. At the same time, we have to stress on the strengths and weaknesses of neural network identification.

2. **Neural Network.** A neural network consists of a large number of simple units, called neurons. An artificial neuron is defined using the following five elements:

— nature of inputs to the neuron

— input function

— activation function which determines the inner state of the neuron, based on the total value of the inputs

— output function which determines the output of the neuron, based on the total value of the inputs

— nature of the outputs from the neuron.

The following notations are adopted:

h — input function
f — activation function
g — output function
$x_t = h(x_1, x_2, \ldots, x_n)$ — total value of the inputs
$a = f(x_t)$ — activation state of the neuron
$y = g(a)$ — output of the neuron.

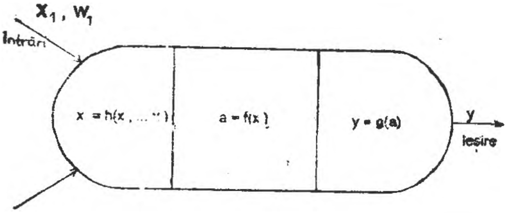

Fig. 1 — The representation of a neuron.

A neuron is represented in figure 1.

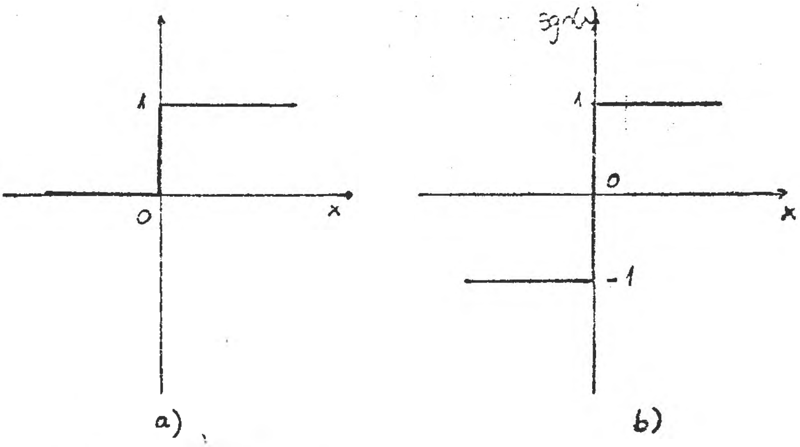

Fig. 2 — Types of activation functions. Step functions.

The inputs to the neuron can be ±1, or 0, 1 or continuous, real numbers respectively.

The input functions, h, can be

— boole type functions

$$linear: h(x_1, \ldots, x_m) = \sum_{i=1}^{n} w_i x_i$$

$$affine: h(x_1, \ldots, x_n) = \sum_{i=1}^{n} w_i x_i - c$$

The last two functions are mostly used. The term "$-c$" can be implemented using a "bias"; that means an additional neuron which transfers the value -1 to the previously considered neuron.

Generally speakink, the activation functions are step functions (Heaviside or signum — figure 2) or other linear saturated functions. But mostly used are the sigmoid functions (figure 3)

$$f(x) = \frac{1}{1 + e^{-x}} \qquad (1)$$

$$f(x) = a\frac{e^{kx} - 1}{e^{kx} + 1} \qquad (2)$$

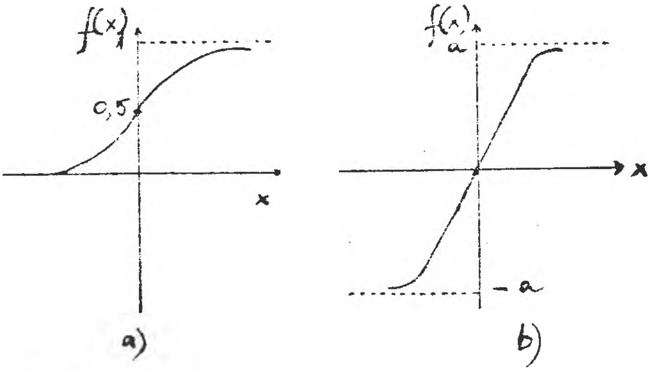

Fig. 3 — Types of activation functions. Sigmoid functions.

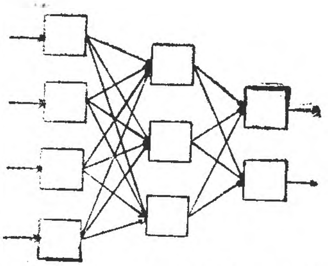

Fig. 4 — Multilayer network

corresponding to figure 3*a* and 3*b* respectively. Usually, the output function, *g*, is the identity function

$$y = g(a) = a \tag{3}$$

These simple processing units called neurons, are arranged in layers as shown in figure 4.

The networks used in this study have three layers. Each neuron in the first layer has only one input, which is the external input to the neural network. Each neuron in the second layer has an input from every neuron in the first layer and, possible, one input with a fixed value of unity. Each neuron in the third layer has an input from every neuron in the second layer, and, like the second layer, one additional input with a fixed value of unity. The number of outputs of the third layer is equal with the number of external outputs of the network.

The purpose for using the neural network is to obtain a mapping from a vector X to a vector Y. The size of the input and output layers are fixed by the number of components of X and Y, respectively. The user specifies the number of neurons in the hidden layer. For a network with a single hidden layer, the number of weighting terms in the network is:

$$N_w = (n_x + 1) \prod_{k=1}^{n_1} (n_{N,k} + 1) n_y \tag{4}$$

where

N_w is the total number of weighting terms

n_x — the dimension of X

n_y — the dimension of Y, and

$n_{N,k}$ — the size of the hidden layer, k

For a given external input X to the neural network, the network returns an external output value $\hat{Y}$:

$$\hat{Y} = f(X, N_w, w_i, 1 = 1, N_i) \tag{5}$$

where Y is the network prediction of $\hat{Y}$, the vector of observed output values associated to the observed inputs X. It is desired that the difference between the predicted and observed values to be as small as possible. Usually, the user specifies the network topology. After that, the network weighting terms w_i, are found as a solution of an optimization problem: minimization of a criterion similar to

$$\min_{\substack{w_k \\ k = 1, \ldots, N}} \sqrt{\sum_{j=1}^{M} \sum_{i=1}^{n_y} \frac{(y_{j,1} - \hat{y}_{j,1})^2}{M}} \tag{6}$$

where

M is the dimension of the set of input vectors X_j and output vectors Y_j and the indexes are:

j — refers to the vector

i — refers to the element in the individual vector.

The finding of the set of weights which minimized the error between Y and $\hat{Y}$ is called the training of the network. The set of input and output vectors that the network is trained on is commonly refered to as the training set.

The solution of this problem has been commonly solved using a gradient algorithm. We have used the training methods implemented in Neural Network Toolbox [1] of MathWorks.

There are more training methods and we shall introduce some of them only:

— one of the first methods tried, was based on Widrow-Hoff model. This introduces the adaptive linear element, ADALINE, making possible the learning of the network based on the associativity between the input and output vectors, by means of a linear approximation of the transfer function. It can handle only one layer network, but this is not such a disadvantage, because in some situations this one layer can be the substitute of several layers. In this case there is one satisfying solution, the linear adaptive element will minimize the sum of squared errors. The network will find a solution as accurate as the function linearity will allow. In our case, due to the nonlinearities existent between the parameters of the studied process, the approximation functions "hardlim" and "purelin" existent in Neural Network Toolbox of Mathworks' do not give good results, generating very large errors.

— another learning method used is that of "backpropagation" as being the most complete and with which we obtained the best results. This algorithm is as a matter of fact the application of the gradient optimization method at the minimization of the scope function $E(W)$. This scope function is defined with relation 8.

$$E(W) = \frac{1}{2} || Y - D ||^2 \tag{8}$$

where Y are the outputs of the network and D are the desired or experimental outputs of the process modeled via neural networks. Thus, the input vector being X, via the algorithm of direct propagation through the networks, this will give the output Y, meanwhile the desired output associated with the input X is D. The output of the network is better when Y tends to D. Function E can be simple or cumulative, summing the deviations of the real responses from the desired (experimental) ones at different sets of data (relation 9)

$$E(W) = \frac{1}{2} \sum_{p=1}^{n_p} ||Y^{(p)} - D^{(p)}||^2 \tag{9}$$

where n_p represents the number of data sets presented to the network for learning.

After introducing one more data sets, the weights w are modified with $\Delta^{(p)}w_{ij}$ computed as the relation 10 shows

$$\Delta w_{ij}^{(p)} = \eta\delta_j^{(p)} + \alpha\Delta w_{ij}^{(p-1)} \tag{10}$$

where η is the so called learning rate and α is a momentum term which hinders too drastic changes of w_{ij} compared with the previous learning step $p-1$. $\delta_{j(p)}$ is the error signal back propagated which represents the difference between the j^{th} neuron activated state at step p and its desired activated state. More details about the backpropagation procedure are given in [2]. The function used in Neural Network Tools is "trainbpx" which has the advantage of using momentum and adaptive learning rate techniques.

The procedure used in the electrolyser neural network modeling was the following: using the analytical model based on the equations written in [3], for different sets of input data, we computed the corresponding values of the objective function. The learning data sets are given in Table 1, together with the results.

At the beginning of our experiments, we tried randomly computed sets of data, but the results were not very satisfying; that meant the calculated scope function via neural network was very different of that computed via analytical model. We decided then that the data have to be very carefully chosen, but we can not advise of any method of choosing them. Additionally we have to say that the proper processing of the data is very important: we had a special case where the difference between the magnitudes of the data is huge; usual values of the input data used were $I = 8.0e6$ [A], $T = 40.0$ [°C], $F = 0,1$ [m^3/s]; this fact makes more difficult the learning process. That's why we tried different types of introducing the data: normalized data, or multiplied with a "smoothing" factor. This last case gave superior results. Anyway, normalized data could not be used in the optimization, because, in this case, one has know apriori the maximum and the minimum of the obiective function and the optimization makes no sense anymore.

Another problem was that of the number of layers in the network. We tried more networks with one, two or three hidden layers and with different numbers of neurons on a layer. The best results were obtained with two hidden layers with five and seven neurons on each layer. The improvements obtained with more layers or with more neurons on a layer were insignificant and additionally shadowed by the huge increase of the learning ti me.

A problem which had to be treated with care was that of the initial weight matrices which were created randomly using "rand" procedure. There were often the cases when a wrongly chosen initial weight matrix ruined the whole learning procedure, the results being very far of the desired ones. That's why we decided to choose, for initialization of the weights, the procedure "nwlog" which gave far better results.

Finally, the last class of problems to be surmounted, was that of proper choosing of the display frequency (disp-freq) and that of the number of learning cycles (epochs). We have found that the "optimum" disp_freq = 100 and max_epoch = 20000. With these data specified, the measure of the precision of the network, the "sums of the squared elements" of the errors (SSE) was of the order of magnitude 1e—6.

The program and the results are given in Appendix and Table 1 respectively.

Appendix

The program representing the neural network modeling

```
% date6
% condiţii de plecare imbunătăţite
% invăţare adaptivă
% incărcat cu T vector linie
% presentation phase;

P=[      7.60e6       36.00        p.1274
         8.00e6       36.00        0.1274
         8.50e6       36.00        0.1274
         9.00e6       36.00        0.1274
         0.50e6       36.00        0.1274
        10.00e6       36.00        0.1274
        10.50e6       36.00        0.1274
        11.00e6       36.00        0.1274
        11.00e6       36.00        0.1274
        11.00e6       40.00        0.1274
        11.00e6       45.00        0.1274
        11.00e6       50.00        0.1274
        11.00e6       55.00        0.1274
        11.00e6       60.00        0.1274
        11.00e6       36.00        0.0750
        11.00e6       36.00        0.1000
        11.00e6       36.00        0.1250
        11.00e6       36.00        0.1500
        11.00e6       36.00        0.1750
        11.00e6       36.00        0.2000];

h=[   7.6e6 40 0.075
     10.0e6 50 0.1274
      9.0e6 55 0.1
     11.0e6 45 0.175
      8.0e6 60 0.2
      8.5e6 53 0.15];

P=[P; h];
P1=P;
save P P
P=[(P(:, 1)-min(P(:, 1)))/(max(P(:, 1))-min(P(:, 1))) ...
     (P(:, 2)-min(P(:, 2)))/(max(P(:, 2))-min(P(:, 2))) ..
     (P(:, 3)-min(P(:, 3)))/(max(P(:, 3))-min(P(:, 3)))]';

T=[      1.9910e5
        2.0129e5
        2.0350e5
        2.0520e5
        2.0670e5
        2.0790e5
        2.0890e5
```

Appendix (continued)

```
              2.0970e5
              2.0970e5
              2.0140e5
              1.9100e5
              1.8060e5
              1.7020e5
              1.5900e5
              2.2900e5
              2.2100e5
              2.1080e5
              1.9980e5
              1.8850e5
              1.7690e5];

T1=[     2.2500e5
         1.7627e5
         1.8135e5
         1.6380e5
         0.5276e5
         1.3800e5];

T=[T; T1]
cave T T
T=[(T(:, 1)-min(T(:, 1)))/(max(T(:, 1)) - min(T(:, 1)))]';
[R, Q]=size(P);
S1=5;
S2=7;
[S3, Q]=size(T);
[W1, B1]=nwlog(S1, R);
[W2, B2]=nwlog(S1, S1);
[W3, B3]=nwlog(S3, S2);
disp_freq=100
max_epoch=15000;
err_goal=0.0001;
lr=1;
momentum=0.95;
lr_inc=1.05;
lr_dec=0.7;
err_ratio=1.04;
TP=[disp¯freq max_epoch err_goal lr lr_inc lr_dec ... momentum err_ratio];
[W1, B1, W2, B2, W3, B3, epochs, TR]=trainbpx(W1, B1, 'logsig', W2, B2, 'logsig', ..
                                    W3, B3, 'logsig', P, T, TP);

A1=logsig(W1*P, B1);
A2=logsig(W2*A1, B2);
A3=logsig(W3*A2, B3);
A=A3;
E=T-A;
SSE=sumsqr(E);
```

Table 1

The learning set and the results of the neural network modeling

Date de invatare a rețelei neuronale			Fob. calculată cu măsurători experimentale	Fob. calculată cu rețeaua neuronală
I [A]-e6	T [°C]	F [m³/s]	—e5	—e5
7.6000	36.0000	0.1274	0.8303	0.8306
8.0000	36.0000	0.1274	0.8428	0.8422
8.5000	36.0000	0.1274	0.8553	0.8550
9.0000	36.0000	0.1274	0.8650	0.8647
9.5000	36.0000	0.1274	0.8735	0.8740
10.0000	36.0000	0.1274	0.8803	0.8789
10.5000	36.0000	0.1274	0.8860	0.8847
11.0000	36.0000	0.1274	0.8905	0.8886
11.0000	36.0000	0.1274	0.8905	0.8886
11.0000	40.0000	0.1274	0.8434	0.8479
11.0000	45.0000	0.1274	0.7844	0.7833
11.0000	50.0000	0.1274	0.7254	0.7208
11.0000	55.0000	0.1274	0.6664	0.6694
11.0000	60.0000	0.1274	0.6028	0.6015
11.0000	36.0000	0.0750	1.0000	0.9927
11.0000	36.0000	0.1000	0.9546	0.9590
11.0000	36.0000	0.1250	0.8967	0.8941
11.0000	36.0000	0.1500	0.8343	0.8362
11.0000	36.0000	0.1750	0.7702	0.7721
11.0000	36.0000	0.2000	0.7044	0.7014
7.6000	40.0000	0.0750	0.9773	0.9787
10.0000	50.0000	0.1274	0.7008	0.7003
9.0000	55.0000	0.1000	0.7296	0.7293
11.0000	45.0000	0.1750	0.6300	0.6313
8.0000	60.0000	0.2000	0.0000	0.0054
8.5000	53.0000	0.1500	0.4837	0.4831

As the main result of the network modeling was the replacement of the intricate analytical model presented in [3] with a very simple matricial model able to compute the results in seconds. The matricial equations are given by the relation 11.

$$\begin{aligned} \mathrm{A1} &= \mathrm{logsig}\ (W1 * P,\ B1) \\ A2 &= \mathrm{logsig}\ (W2 * \mathrm{A1},\ B2) \end{aligned} \tag{11}$$

where P is the input vector,

$W1$, $W2$ are the weight matrices multiplying the outputs of the neurons,
$A1$, $A2$ contain the outputs of the neurons,
$B1$, $B2$ are the bias matrices.

We have chosen the sigmoid activation function "logsig" which gives the best correspondence between the computed data using the network and those computed with the analytical model.

In conclusion, needing a fast computational model to optimize the process of chloralkali electrolysis with Ion Exchange Membrane, we tried a neural network modeling. The results were fairly good, but we have take care that the neural networks are better for interpolation in a given range of data than for extrapolation over the range. Because of that, using the neural networks models in optimization has to be handeled with utmost care. Our results of optimization were good from the point of view of the running time, but not the best from that of the consistency of the optimized results. This is the reason we did not report yet the results of the minimization of the expenses of the chloralkali electrolyser. This is a study to be continued.

REFERENCES

1. H. Demuth, M. Beale, — *Neural Network Toolbox User's Guide*, 1993, The MathWorks Inc., Natick, Massachusetts, USA
2. E. Woinarosky, — *Reţele Neuronale*, curs litografiat, Universitatea Politehnică Bucureşti, 1994, cap. 2.
3. A. Imre-Lucaci, Ioana Bunea, Ş. Agachi, — Using Neural Networks in modeling and Optimization of the Ion Exchange Membrane Electrolysers, Part I, *Studia Universitatis Babeş-Bolyai*, 1–2 1994.

STUDIA UNIV. BABEŞ-BOLYAI, CHEMIA, XXXIX, 1–2, 1994

THE REPRESENTATION OF SOME HYBRID ORBITALS

OSSI HOROVITZ*, LAURA DAMIAN*

ABSTRACT. Hybrid orbitals obtained form s-, p- and d-hydrogenlike atomic orbitals (sp^3d^2 and sp^2d) are represented by plots of the wave function along the orbital axis and in a section through a symmetry plane of the orbital, as well as by contour maps of the electronic density.

Representations of hybrid sp orbitals are rather common in papers and textbooks [1], but *d*-containing hybrid orbitals have rarely been represented and students have quite a vague picture about their spatial distribution. To represent atomic or hybrid orbitals we can use plots of the wave function ψ or of its square ψ^2 (the density probability) along a selected direction in the atom (for instance a symmetry axis), polar graphs, representations of the ψ or ψ^2 values in a planar section through the orbital, isometric surfaces (in space) or isometric contours in a plane (contour maps), boundary surfaces or contours and dot plots, modeling the charge distribution of the electronic cloud. A number of steric models are also in use [2].

In order to build hybrid orbitals, we can use as a basis hydrogenlike orbitals, Slater-type or SCF atomic orbitals [3]. An *octahedral hybrid* orbital sp^3d^2, directed along the z-axis, can be obtained [4] from the s, p_z and d_{z^2} atomic orbitals:

$$\psi_{\mathrm{oct}} = (s + \sqrt{3}p_2 + \sqrt{2}d_{z^2})/\sqrt{6} \qquad (1$$

Orbitals of this kind are involved in bonding in molecules such as SF_6, PF_6^- or $[Fe(CN)_6]^{3-}$.

Tetragonal hybrids sp^2d, as in the square planar molecules XeF_4, $AuCl_1^-$, $[Ni(CN)_4]^{2-}$ or in $PdCl_2$, may involve s, p_x, p_y and $d_{x^2-y^2}$ atomic orbitals. Such an orbital, with the x-axis as symmetry axis, is:

$$\psi_{tc} = (s + \sqrt{2}p_x + d_{x^2-y^2})/2. \qquad (2)$$

With hydrogen orbitals $3s$, $3p$ and $3d$, these hybrids have two nodal surfaces each. For the octahedral orbital, they are solutions of the equation:

$$(1 - 3\sqrt{2}\cos\theta + 3\cos^2\theta)r^2 - 18(1 - \sqrt{2}\cos\theta)r + 27 = 0, \qquad (3)$$

where r means the polar radius (the distance from the nucleus) and θ its angle to the z-axis. For the distance we'll always use atomic units, i.e. the Bohr radius of the first orbit in the hydrogen atom $r_8 = 5 \cdot 29 \cdot 10^{-11}$ m taken as unity. One of the nodes is a parabolalike surface, as those for sp hybrid orbitals; it cuts the z-axis at $z = -4.553\ r_B$ and the x- and y-axes twice, at $16.348\ r_8$ from the nucleus. The other node is a closed surface, cutting the z-axis at

---

* Department of Chemistry, Faculty of Material Science and Engineering, Technical University Cluj-Napoca.

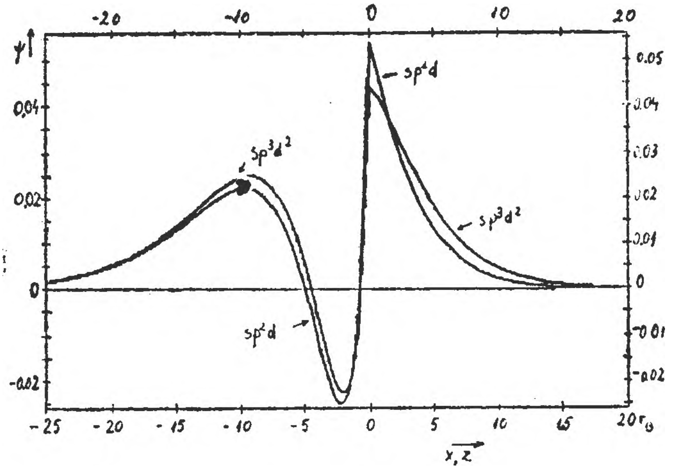

Fig. 1. The wave function for an sp^3d^2 orbital along the z-axis and for an sp^2d orbital along the x-axis.

-0.72 and 34 and the x-and y-axes at ± 1.652. Therefore, the electronic cloud is divided into three lobes, with maxima on the z-axis.

On the plot of the wave function ψ_{oct} along this axis (Fig. 1) we can see these maxima: the largest is at the origin, for the inner (positive) lobe and ψ shows a very sharp decrease for negative z-values. The other positive lobe has the maximum at $z = -9.20$; it is lower than the first one, but this lobe does contain the greater part of the electronic cloud and it's this lobe that overlaps in forming the chemical bonds. The negative lobe is surrounding the closed nodal surface, but it has a significant density in the area near the nucleus, between the two positive lobes only. In order to make visible the outer region of this lobe (at large positive z values), we must use another scale, as in Fig. 1a.

By joining together a set of ψ-plots for parallel directions in a plane (for instance the xz-plane), we get a quasi-three-dimensional plot of the wave function in this plane, a representation of the $\psi(x, 0, z)$-surface, using the third coordinate to draw (in perspective) the calculated values. For the octahedral hybrid such a representation is given in Fig. 2a, using the plots of the wave function along 21 lines, parallel to the symmetry axis, in the xz-plane. We chose the ψ rather than the ψ^2 plots, in order to show the sign of the function as well.

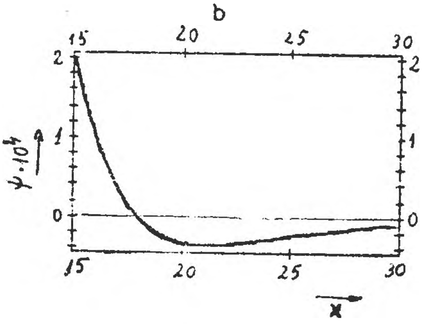

Fig. 1a. The sp^3d^2 wave function along the z-axis (detail).

The wave function in a plane can also be represented by contour lines, for some selected ψ-values together with the nodal lines

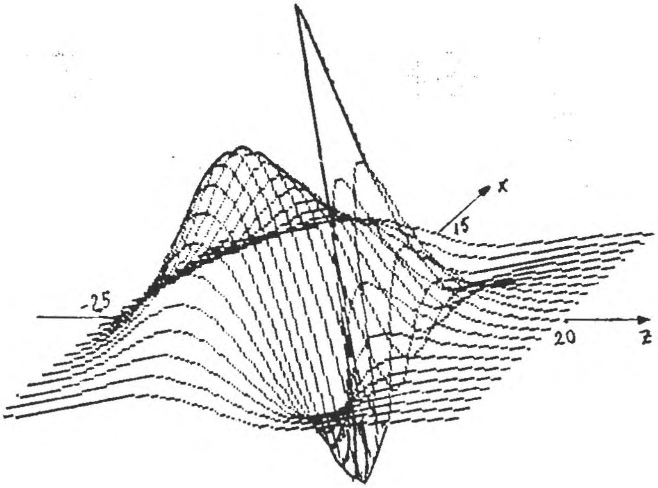

Fig. 2. The wave function of a hybrid orbital in its symmetry plane (all distances are in r_8). (a) sp^3d^2 hybrid in the xz plane

($\psi = 0$), as in Fig. 3. It is evident that for the smallest ψ-values, the shape of the boundary line is approaching a circular one (spherical in space). We can also draw a contour map (perhaps more suggestive) by alternating hatched areas with blanks for different intervals of ψ-values (Fig. 4).

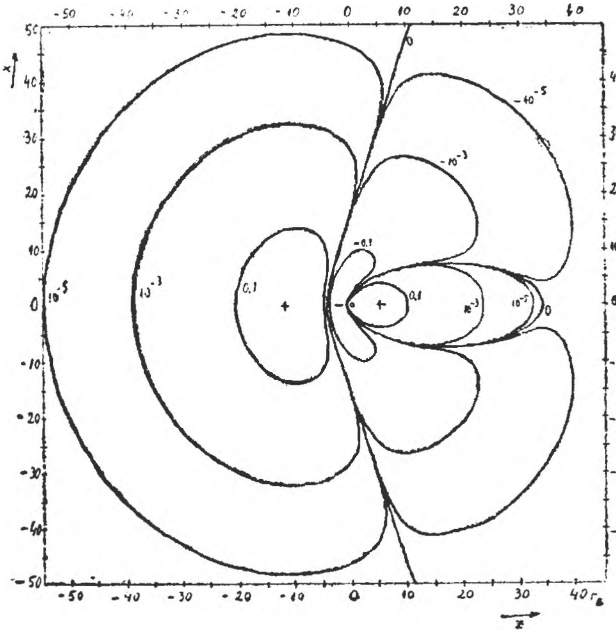

Fig. 3. Contour lines for the sp^3d^2 hybrid in the xz plane, for values ψ/ψ_{max}: ± 0.1; $\pm 10^{-3}$; $\pm 10^{-5}$ and 0; the little circle shows the position of the nucleus.

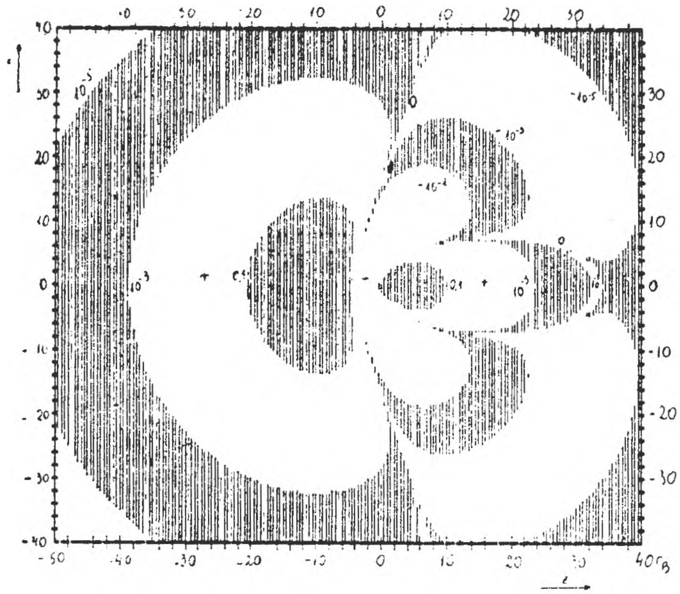

Fig. 4. Contour map for the octahedral hybrid sp^3d^2 in the xz plane; the hatched areas are for values of ψ/ψ_{xm} : > 0.1; 10^{-3} to 10^{-5}; 0 to -10^{-5}; -10^{-3} to -10^{-2}.

The *tetragonal hybrid* sp^2d is very similar to the previous one. Its nodal lines in the xy-plane (the symmetry plane) are given by:

$$(2\sqrt{2} - 2\sqrt{6}\cos\varphi + \sqrt{3}\cos 2\varphi)r^2 - (18\sqrt{2} - 12\sqrt{6}\cos\varphi)r + 27\sqrt{2} = 0 \quad (3)$$

where φ is the polar angle between the projection of the r-vector on the xy-plane and the x-axis. Here the closed nodal surface is less extended along the symmetry axes than in the octahedral hybrid. It cuts the x-axis at -0.81 and $17.93r_B$ the open nodal surface cuts the x-axis at -4.91 and the y-axis at ± 21.61. The large positive lobe has its maximum at $x = -9.56$.

The wave function along the x-axis is given together with that for the octahedral hybrid (along its axis, z) in Fig. 1. One can see that the main maximum and the minimum are more pronounced for the tetragonal hybrid. In fig. 1b, the wave function is scaled up for larger x-values, so that its zero-point could be seen.

There are no important differences between the plot of the sp^2d wave function in its symmetry plane xz (Fig. 2b) and that for the sp^3d^2 hybrid in Fig. 2a. The contour lines for ψ-values of 1/10, 1/100 and 1/1000 of the maximum value and the nodal lines in the xy-plane are drawn in Fig. 5.

We can ask how these pictures would change if we modified the effective charge Z_{ef} in the atomic wave functions. The orbital exponents are rather scale factors, which expand or contract the function, but do not change its overall shape. Thus, with $Z_{ef} > 1$, but the same for all the hybridized orbitals,

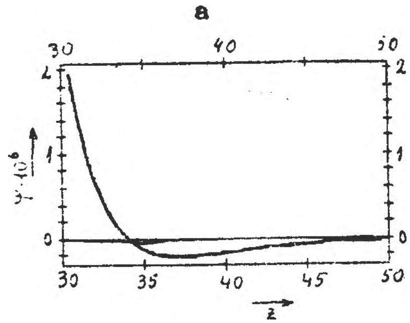

Fig. 1b. The sp^2d wave function along the x-axis (detail).

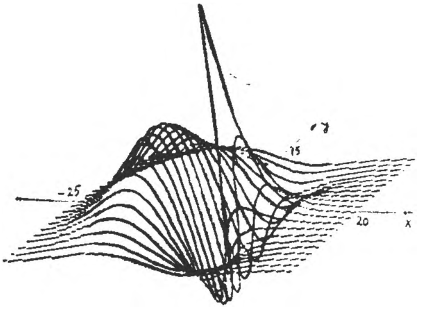

Fig. 2b. sp^2d hybrid in the xz plane.

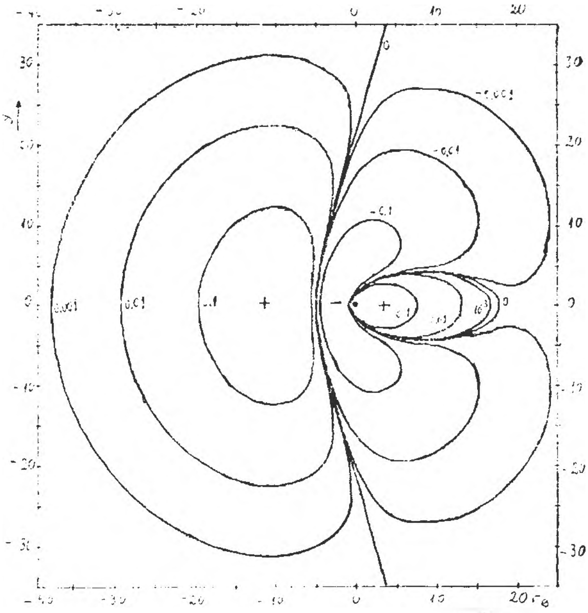

Fig. 5. Contour lines for the tetragonal hybrid sp^2d in the xy plane for values ψ/β_{max}: ±0.1; ±0.01; ±0.001 and 0.

the shape of the hybrid would be the same, but the orbital would be "smaller" or "denser".

On the other hand, sometimes octahedral or tetragonal hybrid orbitals are build from s and p orbitals of the outer shell (ns, np) and d orbitals from the previous shell, $(n-1)d$, for instance $4s$, $4p$ and $3d$. For such hybrid d^2sp^3 and dsp^2 orbitals, the plots of the wave function along their symmetry axes are given in Fig. 6. The plots of the wave function in the symmetry plane of the hybrid are shown in Fig. 7. and some contour lines in the same plane, for the octahedral hybrid, are presented in Fig. 8. We can see that the overall shape of these hybrids with inner shell d orbitals is similar to that of the former orbitals, althought the negative lobe is now surrounding the other positive lobe, not the one centered on the nucleus and the spacial extensions are different.

A quite new situation arises by using different effective nuclear charges for the atomic orbitals within the hybrid; if these differences are large (for instance $Z_{3d} > Z_{4s} > Z_{4p}$), it will not be an effective "mixing" of the atomic orbitals in the hybrid; the more condensed $3d$ orbital will appear nearly "pure"

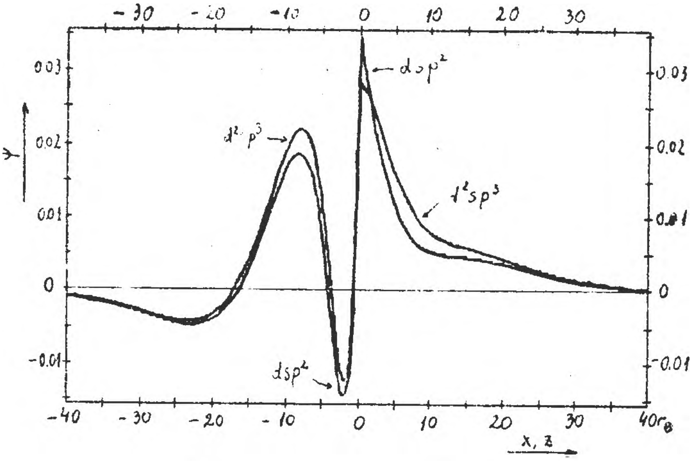

Fig. 6. The wave function for an d^2sp^3 orbital along the z-axis and for an dsp^2 orbital along the x-axis.

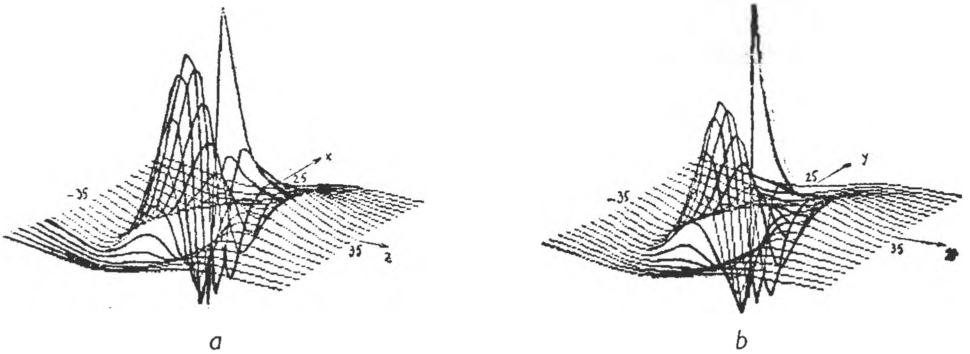

Fig. 7. The wave function in the symmetry plane for the hybrid orbitals: (a) d^2sp^3; (b) dsp^2.

in the central area of the cloud, the more “expanded” $4p$ orbital will prevail in the outer area.

The representation of octahedral hybrids obtained from hydrogenlike orbitals with $Z_{ef} = 10$ [5] are quite similar with the present ones. Calculations for the d^2sp^3 orbitals of iron and sp^2d of sulphur [6] with more refined wave functions gave contour maps of the same kind as ours for iron, but for sulphur the second nodal surface appears to be also open.

It's worth noticing that the use of so-called "polar graphs" for the “angular part" of hybrid wave functions is not justified, since a separation in radial and angular part is not possible here. Accordingly, the representation of such an angular dependence [7] bears little resemblance with the shapes presented here.

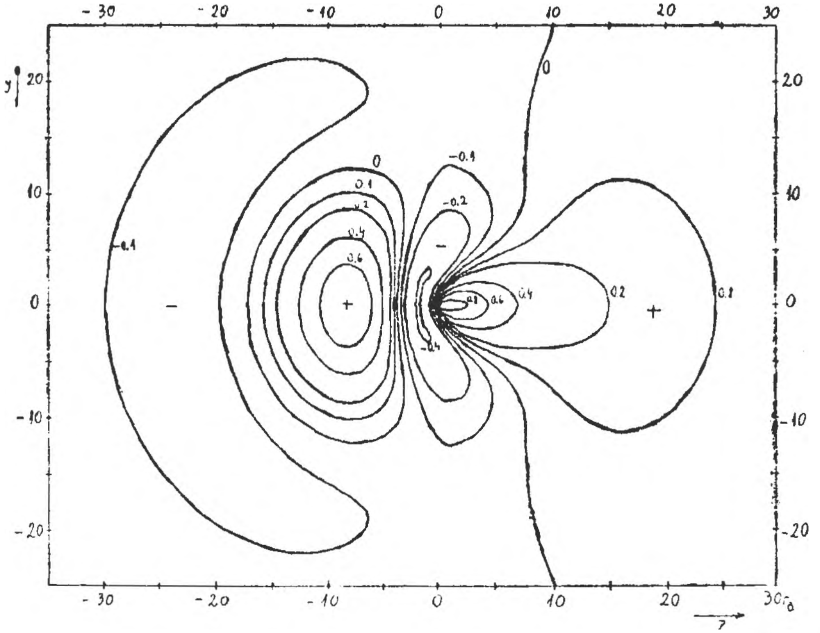

Fig. 8. Contour lines for the d^2sp^3 hybrid in the xz plane for values ψ/ψ_{max}: 0.8; 0.6; 0.4; 0.2; 0.1; 0; −0.1; −0.2; −0.4.

REFERENCES

1. C. A. Coulson, *Valence*, Oxford Univ. Press, 1951, chapter VIII; A. Streitwieser Jr. and R. S. Owens, *Orbital and Electron Density Diagrams*, McMillan Co., New York, 1973; J.W. Moore and W. G. Davies, J. Chem. Educ., **52**, 426 (1976); G. Niac and O Horovitz, Rev. Fiz. Chim., **22**, 433 (1985); L. J. Schwartz, J. Chem. Educ., **67**, 505 (1990); P. J. Pavlik, ibid. **69**, 637 (1992).
2. A. H. Norbury, *Educ. Chem.*, **5**, 31 (1968); A. J. Gordon, *J. Chem. Educ.*, **47**, 30 (1970).
3. R. S. Berry, *J. Chem. Educ.*, **43**, 283 (1966).
4. F. A. Cotton, *Chemical Application of Group Theory*, Interscience Publ., 1964, Chapter 6.
5. J. Cohen and T. Bustard, *J. Chem. Educ.*, **43**, 187 (1966).
6. J. Cohen and J. Del Bene, *J. Chem. Educ.*, **46**, 487 (1969).
7. L. Pauling, *The Nature of the Chemical Bond*, 3-rd Ed., Cornell Univ. Press, Ithaca, New York, 1960, p. 149.

STUDIA UNIV. BABEŞ-BOLYAI, CHEMIA, XXXIX, 1–2, 1994

REPREZENTATIONS OF RELATIVISTIC (DIRAC) ORBITALS

OSSI HOROVITZ*, LAURA DAMIAN*

ABSTRACT. The atomic orbitals obtained from the relativistic equation of Dirac for the hydrogen atom are represented by plots of the density probability along a straight line and in a plane passing through the atom, by contour maps and by boundary surfaces. The differences to the ordinary atomic orbitals (from Schrödinger's equation) are emphasized.

Schrödinger's equation was adapted by Dirac [1] to meet the requirements of the relativistic theory. The wave function of this equation is a column matrix (vector) of four components:

$$\psi = \begin{pmatrix} \psi_1 \\ \psi_2 \\ \psi_3 \\ \psi_4 \end{pmatrix}$$ and the probability density is given by:

$$|\psi|^2 = \psi^* \psi = \psi_1^* \psi_1 + \psi_2^* \psi_2 + \psi_3^* \psi_3 + \psi_4^* \psi_4.$$

These four components are familiarly called the large components spin up (ψ_1) and spin down (ψ_2) and the small ones spin down (ψ_3) and spin up (ψ_4). The ratio of the "small" components to the "large" ones is $\alpha Z \approx Z/137$.

This equation was exactly solved for hydrogen-like atoms [2]. The solutions are described by 4 quantum numbers: n (principal), l (azimuthal), j (of angular moment or inner quantum number) and m (magnetic) The n- and l-values are the same as for the quantum numbers n and l of the Schrödinger equation, and the orbitals are similarly noted s, p, d, f, ... The inner quantum numbers $j = |l \pm 1/2|$ are always positive, while, m has negative and positive values from $-j$ to j. The energy levels of hydrogen, according to the relativistic theory are: $1^2S_{1/2}$, $2^2P_{1/2}$, $2^2S_{1/2}$, $2^2P_{3/2}$ (with $m = \pm 3/2$ and $m = \pm 1/2$), $3^2P_{1/2}$, $3^2S_{1/2}$, $3^2D_{3/2}$($m = \pm 3/2$; $m = \pm 1/2$), $3^2P_{3/2}$ ($m = \pm 3/2$; $m = \pm 1/2$), $3^2D_{5/2}$ ($m = \pm 5/2$; $m = \pm 3/2$ and $m = \pm 1/2$).

The wave function components are the product of a radial part and an angular one; the shapes of the atomic orbitals (AO's) are determined by the j- and m-values), which decide the angular functions [3]. These orbitals, unlike the Schrodinger ones, have no nodes.

Representations of relativistic AO's are quite old: White proposed such pictures as early as in 1931 [4]. It's interesting to note that' White published these pictures of the relativistic orbitals before the ones for Schrödinger orbital [5] which became so popular in various textbooks.

The representation of the probability density against the distance from the nucleus, for the $2s_{1/2}$ Dirac AO points out the absence of radial nodes:

---

* Dept. of Chemistry, Technical University Cluj-Napoca

at $r = 2r_8$[1], where the Schrödinger 2*s* AO has such a node, there is still a small residual probability density [3], as a consequence of the fact that in the wave function, the large and the small component have nodes at different radii. Szabo [6] gave contour diagrams for some relativistic orbitals, which illustrate the absence of nodal surface in the angular distribution too [7].

Here we use various kinds of representation for the Dirac AO's: plots of the density probability $|\psi^2|$ along a selected direction in the atom, representations of $|\psi|^2$ values in a planar section through the orbital, isometric contours in a plane and boundary surfaces in space.

The $1s_{1/2}$ orbital is similar to the Schrödinger 1s wave function and so is the $2s_{1/2}$ orbital to the Schrödinger 2*s* function, except for the small components, which cause the nodal sphere $r = 2r_8$ to be only a "nearby" nodal surface. The $2p_{1/2}$ *orbital* is also spherically symmetrical. From the $|\psi|^2$ plot along a line passing through the nucleus, for instance the *z*-axis (Fig. 1), it's found that the electron density is zero at the nucleus and has a maximum at $r = 2r_8$. The electron density in a plane passing through the origin, for instance the *xz*- or *yz*- plane, is represented in Fig. 2 by the plots of $|\psi|^2$ along 21 equidistant parallel straight lines in this plane, giving together a quasi-threedimensional picture in perspective. The central minimum of zero-electron density is clearly shown here.

For the same plane, the lines of identical electron density (contour lines, isometric contours) are shown in Fig. 3 for values of the electron density representing 0.8; 0.6; 0.4; 0.2 and 0.1 of maximum $|\psi|^2$ value. They are all concen-

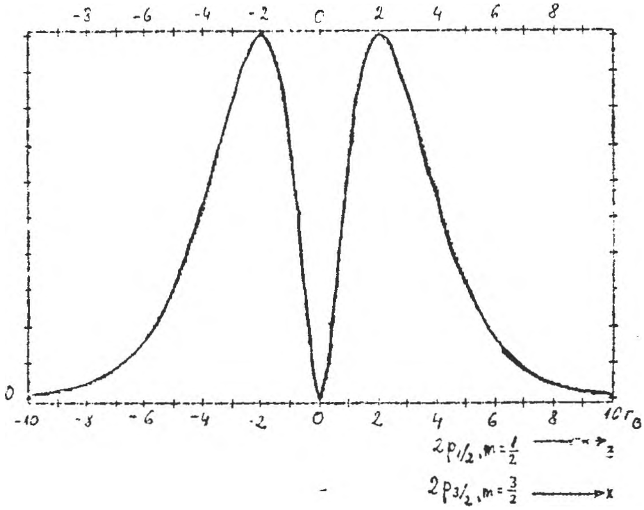

Fig. 1. Plot of the electron density for the $2p_{1/2}$ Dirac orbital, along a line crossing the nucleus, on for a $2p_{3/2}$, $m = 3/2$ orbital, along its symmetry axis.

---

[1] *r_8 is the radius of the first Boht orbit in the hydrogen atom.*

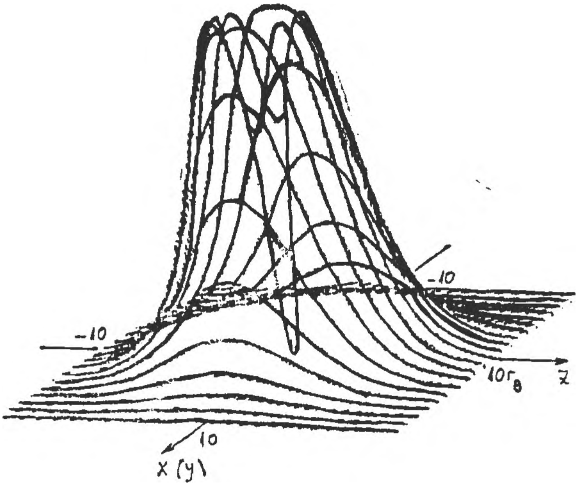

Fig. 2. The electron density in a central section through a $2p_{1/2}$ Dirac orbital.

tric circles of course, due to the overall spherical symmetry of the orbital. This symmetry is clearly shown by the drawing in perspective of a set of isometric contours, for a certain value of the electron density, in several parallel plane sections through the orbital. This gives a pseudo-3D representation of a boundary surface for the orbital (Fig. 4). This surface, given in Fig. 4. for an electron density representing 1/4 of the maximum one, is a sphere. A second sphere for the inner boundary surface at the same $|\psi|^2$ value is too small to be clearly seen in the picture.

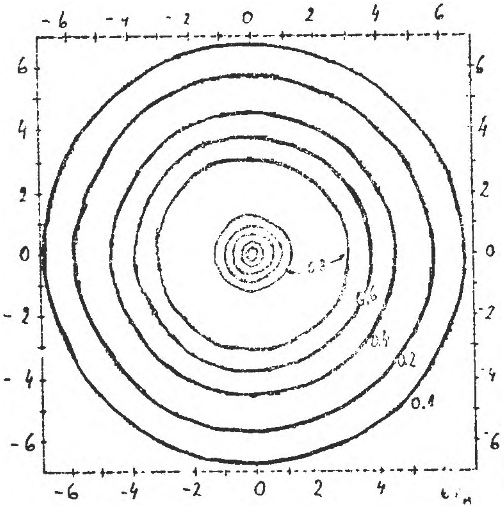

Fig. 3. Contour lines for a $2p_{1/2}$ Dirac orbital in a central section.

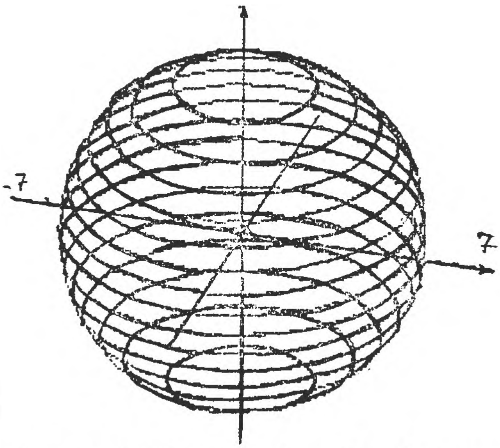

Fig. 4. Boundary lines for a $2p_{1/2}$ Dirac orbital ($|\psi|^2/|\psi|^2_{max} = 0.25$).

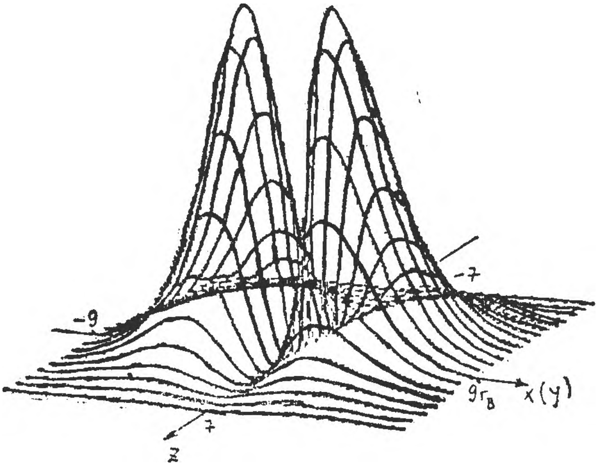

Fig. 5. The electron density in a section through a $2p_{3/2}$ (m = 3/2) orbital.

For the $2p_{3/2}$ *orbital* with $m = \pm 3/2$, the plot of the probability density along an horizontal symmetry axis (let's be the x- or the y-axis) is the same as the one in Fig. 1, for the $2p_{1/2}$ orbital, and so is the plot of the electron density or the contour map in a horizontal plane, containing these axes (xy-plane) identical with the drawings in Fig. 2 and 3. On the other hand, the plot of the electron density in a vertical plane (let's be the xz- or yz-plane) is similar to that of a $2p_x$ or $2p_y$ Schrödinger orbital (Fig. 5). and so are the contour lines in that plane (Fig. 6). But here there is no more a nodal plane. The dashed line in Fig. 6, the z-axis, is here a rotational axis, and the electron

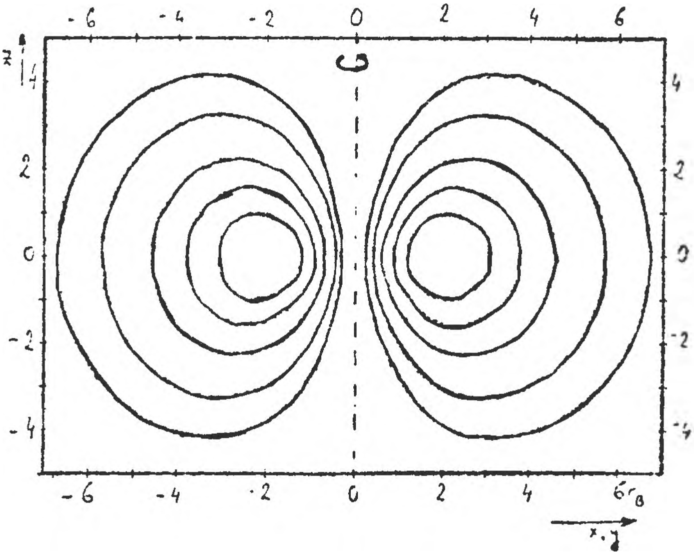

Fig. 6 Contour lines in a section through the x axis of a $2p_{3/2}$ (m = 3/2) orbital.

density is zero along this line only, but not in any plane passing through this axis. The boundary lines in Fig. 7 show that the charge cloud is doughnut shaped; it is analoguos to the imaginary Schrödinger wave functions pair $2p_+$ and $2p_-$ (for $m = \pm 1$). The inner circles in Fig. 7 define the inner boundary surface of the orbital, for the same $|\psi|^2$ value.

The $2p_{3/2}$ *orbital* with $m = \pm 1/2$ has the electron density plot along the z-axis also similar to the one in Fig. 1, but its plot in a plane passing through this axis (xz- or yz-plane) is somewhat different (Fig. 8) and so are the contour lines (Fig. 9a).

An alternative representation of the electron density in this plane is given by a picture of the zones for different probability density ranges (Fig. 9b). Such pictures are much easier to obtain with a PC and a printer than the contour lines. The minimum of the electron density is no more along an axis, but in a point (the origin). The general "shape" of the electron cloud in these figures, as

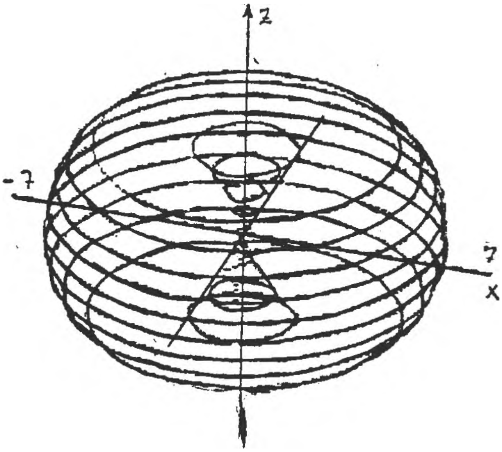

Fig. 7. Boundary lines for a $2p_{3/2}$ ($m = 3/2$) orbital ($|\psi|^2/|\psi|^2_{max} = 0.1$).

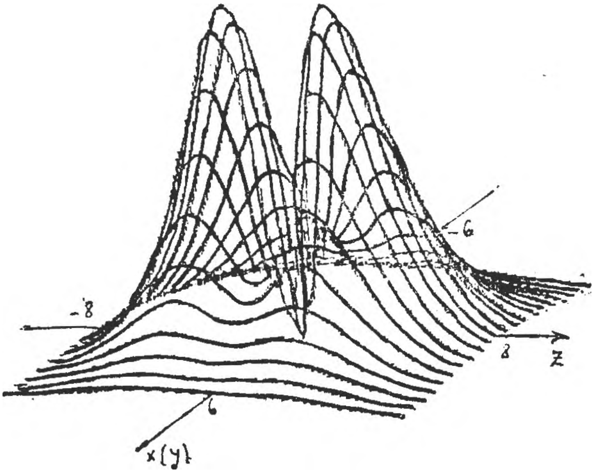

Fig. 8. The electron density in a section through a $2p_{3/2}$ ($m = 1/2$) orbital.

well as in the representation of a boundary surface (Fig. 10) reminds us of the Schrödinger $2p_z$ orbital ($m = 0$), but the absence of the nodal plane is clearly shown by the Fig. 9 and 10.

The *$3p_{3/2}$ orbital* with $m = \pm 1/2$ differs from the previous one by the presence of a pseudo-nodal sphere. Due to the small components of the wave function,

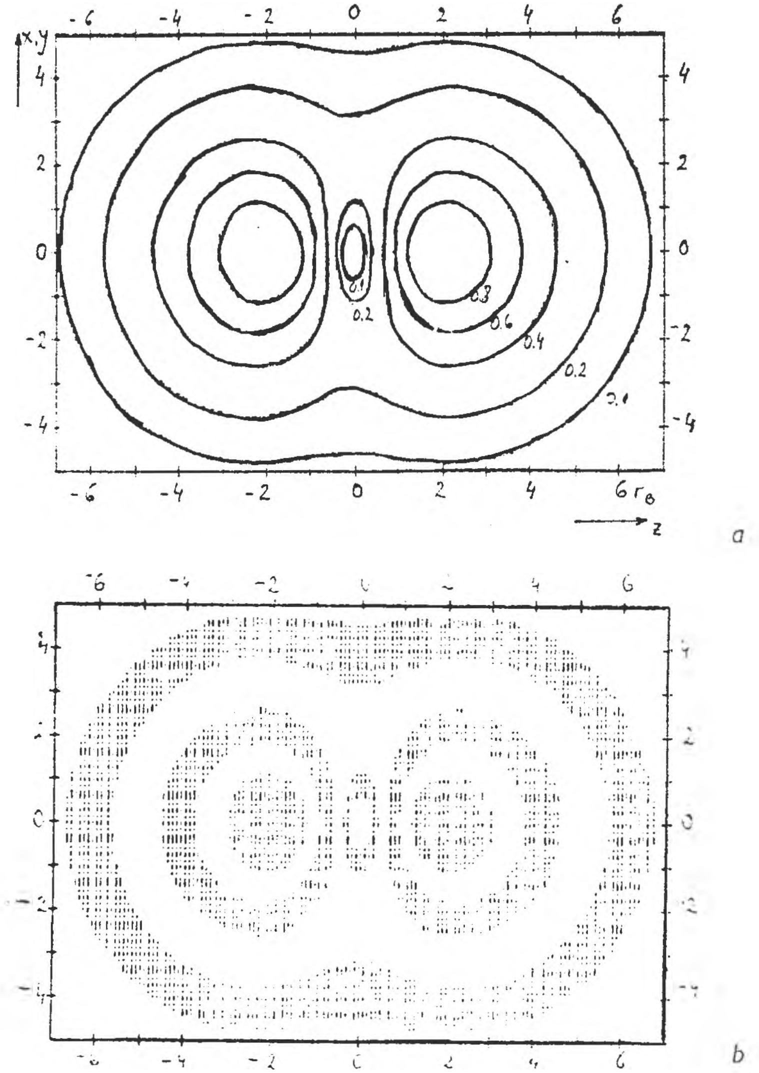

Fig. 9. a. Contour lines in a section through the z axis of a $2p_{3/2}$ ($m = 1/2$) orbital. b. Zones of different electron densities in the same section (are hatched the zones for $|\psi|^2/|\psi|^2_{max}$ = 1 ... 0.8; 0.6 ... 0.4 and 0.2 ... 0.1.

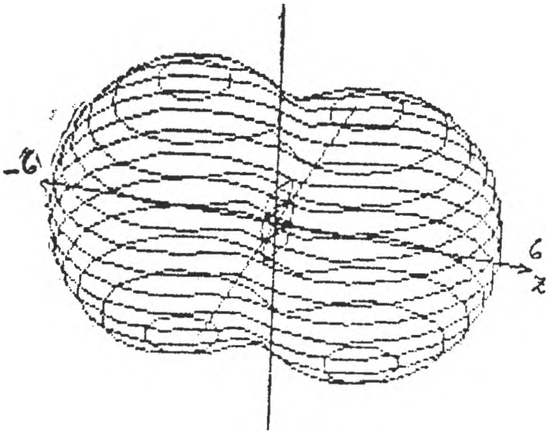

Fig. 10. Boundary lines for a $2p_{3/2}$ (m = 1/2) orbital ($|\psi|^2/|\psi|^2_{max} = 0.2$).

the electron density in the radial function here is not exactly zero, as it appears in the electron density plot along the z-axis (Fig. 11). The peaks for the central pseudo-lobe are much higher than those for the outer one, but the latter is much more extended in space. The plot of the electron density in a plane containing the z-axis (Fig. 12) shows the inner lobe similar to the orbital represented in Fig. 8, surrounded by the much lower outer lobe. In the contour map of Fig. 13, the dashed circle between the two lobes represents the pseudo-node. The inner part of the drawing is much the same as the contour map in Fig. 14. The two pseudo-lobes are clearly seen also in the picture of a boundary surface (for an electron density representing 1/25 of the maximum one).

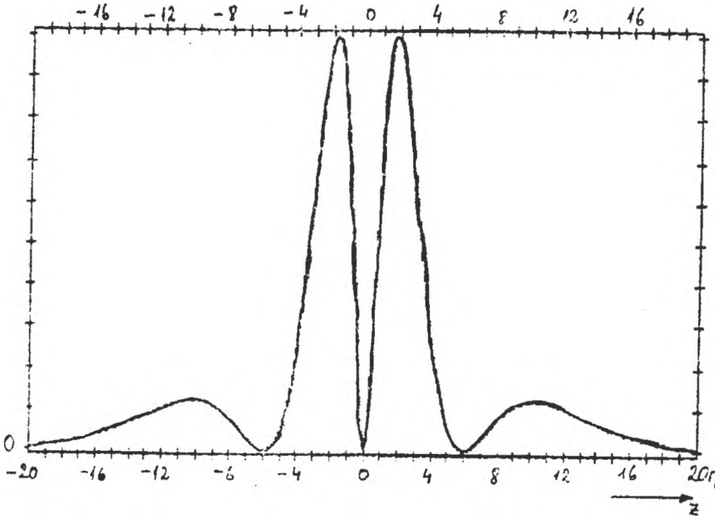

Fig. 11. The electron density along the z-axis of a $3p_{3/2}$(m = 1/2) orbital.

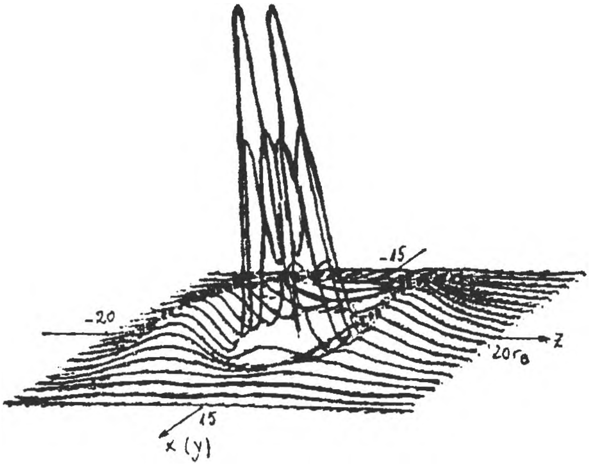

Fig. 12. The electron density in a section through a $3p_{3/2}$ ($m = 1/2$) orbital.

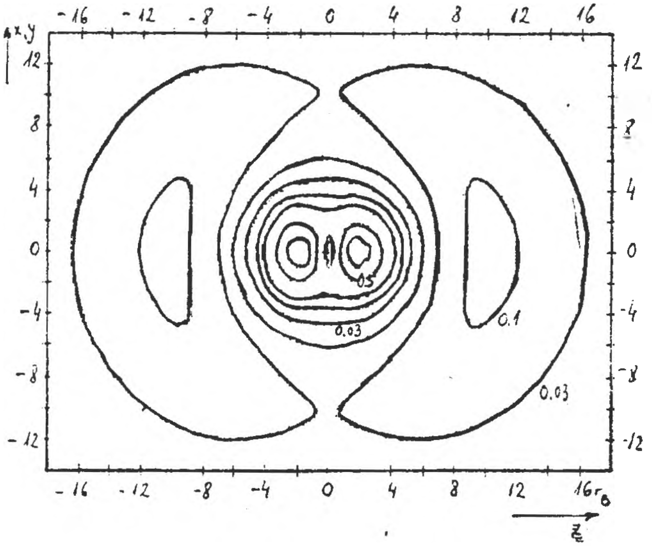

Fig. 13. Contour lines in a section through a $3p_{3/2}$ ($m = 1/2$) orbital.

Two d-type orbitals are also represented here, $3d_{5/2}$, $m = 1/2$ and $3d_{5/2}$, $m = 3/2$. The plot of the electron density in a central section, through the z-axis for the first one (Fig. 15) shows the presence of two high peaks along the z-axis and of two lower ones along the x- (or y-axis). The contour map in Fig. 16 reveals the resemblance to the d_{z^2} — Schrödinger orbital, but also the differences risen from the lack of any nodal surfaces, which leads to joined contour lines for lower

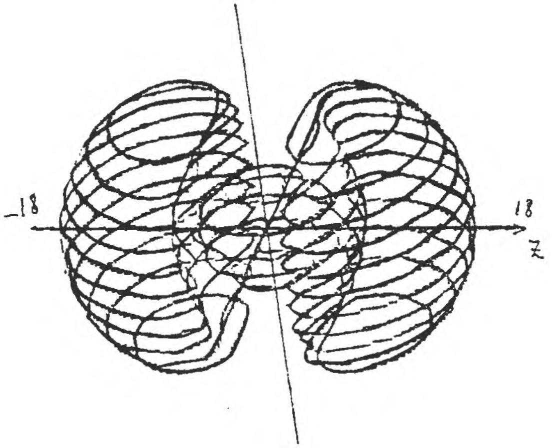

Fig. 14. Boundary lines for a $3p_{3/2}$ ($m = 1/2$) orbital ($|\psi|^2/|\psi|^2_{max} = 0.04$).

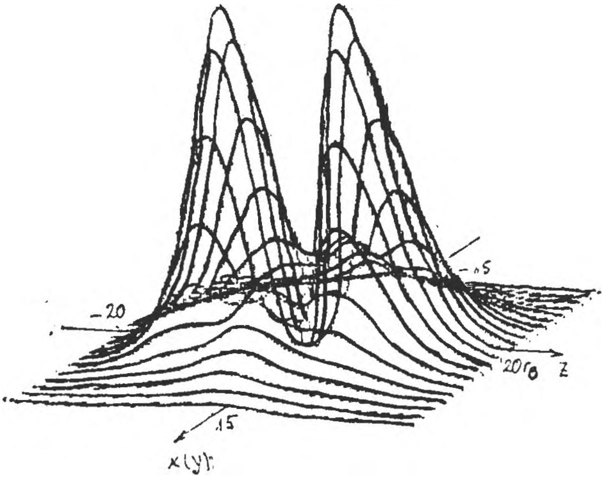

Fig. 15. The electron density in a section through a $3d_{5/2}$ ($m = 1/2$) orbital.

electron densities. The differences are still better seen in the plot of a boundary surface in Fig. 17.

For the $3d_{5/2}$, $m = 3/2$ orbital, in the plot of the electron density in a central section, the *xz-* (or *yz-*) plane (Fig. 18), four maxima are found (the figure is not quite clear, due to the superpositions of many lines) and a minimum along the z-axis. The contour map (Fig. 19) reminds us of the $3d_{xz}$ or $3d_{yz}$ Schrödinger orbitals, but here also the nodal planes are absent. As well as in Fig. 6, the dashed line is not the intersection of such a plane, but a rotational axis for the orbital (the *z*-axis); along it the electron density is zero. The boundary surfaces for an electron density of 1/10 from the maximum one (Fig. 20 a) also show that

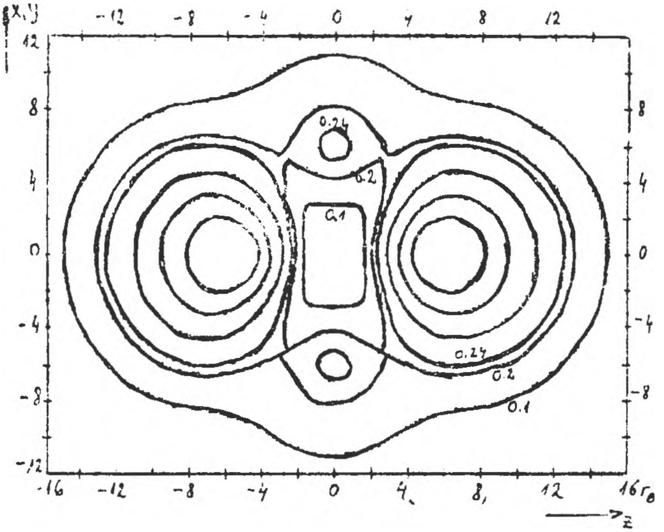

Fig. 16. Contour lines in a section through a $3d_{5/2}$ $(m = 1/2)$ orbital.

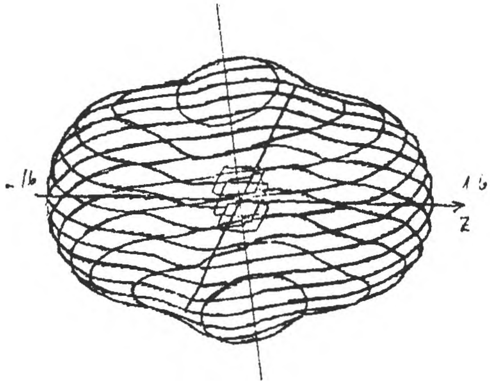

Fig. 17. Boundary lines for a $3d_{5/2}$ $(m = 1/2)$ orbital $(|\psi|^2/|\psi|^2_{max} = 0.1)$.

the four lobes of the Schrödinger $3d_{xz}$ orbital for instance are here joined together, as in the imaginary Schrödinger $3d$ orbitals. In Fig. 20 b, only half of the boundary surface is represented, in order to have a clearer look upon its shape.

The various manners used here to represent the orbitals are complementary, and all of them together give a concrete picture of the electron cloud. Some of these methods are applied here for the first time to the representation of relativistic wave functions. Such images should contribute to a better knowledge of these orbitals, up to present still seldom to be found in the chemistry textbooks.

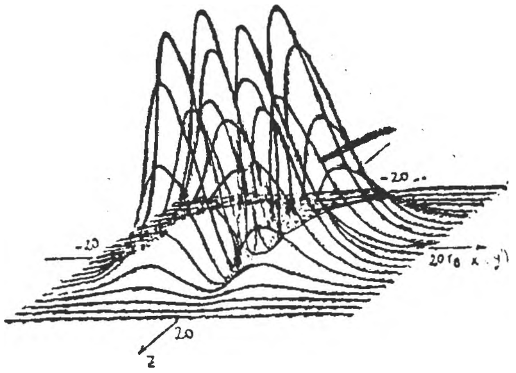

Fig. 18. The electron density in a section through a $3d_{5/2}$ (m = 3/2) orbital.

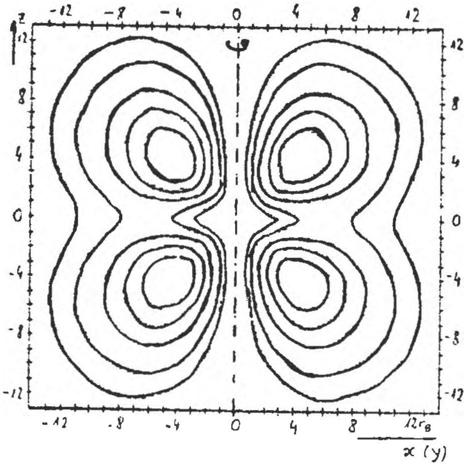

Fig. 19. Contour lines in a section through a $3d_{5/2}$ (m = 3/2) orbital.

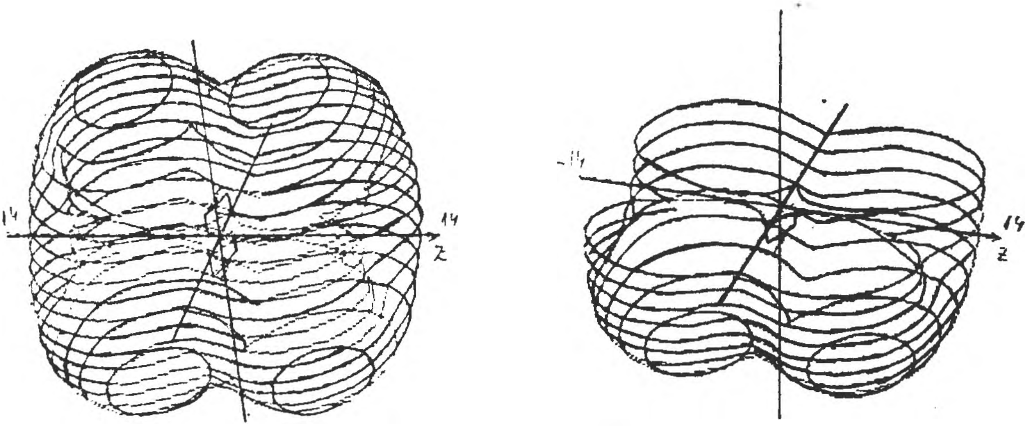

Fig. 20. Boundary lines for a $3d_{5/2}$ (m = 3/2) orbital ($|\psi|^2/|\psi|^2_{max} = 0.1$). b. The lower half of the boundary surface.

REFERENCES

1. P. A. M. Dirac, *Proc. Roy. Soc.* (London), **A117**, 610; **A118**, 351 (1928).
2. C. G. Darwin, *Proc. Roy. Soc.* (London), **A118**, 654 (1928).
3. R. E. Powell, *J. Chem. Educ.*, **45**, 558 (1968).
4. H. E. White, *Phys. Rev.*, **38**, 513 (1931).
5. H. E. White, *Phys. Rev.*, **37**, 1416 (1931); **48**, 948 (1935).
6. A. Szabo, *J. Chem. Educ.*, **46**, 678 (1969).
7. D. R. McKelvey, *J. Chem. Educ.*, **60**, 112 (1983).

STUDIA UNIV. BABEŞ-BOLYAI, CHEMIA, XXXIX, 1–2, 1994

CONTRIBUTIONS TO QUANTITATIVE STRUCTURE-ACTIVITY RELATIONSHIP (QSAR) STUDIES. THE MINIMAL STERIC DIFFERENCE (MTD AND MSD) METHODS AND APPLICATION

S. MUREŞAN*, D. DRAGOŞ,** C. BOLOGA***, D. CIUBOTARIU**

ABSTRACT: Original Timişoara methods for QSAR studies: MTD (Minimal Topological Difference) and MSD (Minimal Steric Difference) are detailed and updated. The multiconformational MTD method is applied on a set of 25 acetic esters vs. the acetylcholinesterase hydrolysis rates, and results are discussed.

1. **Introduction.** Modern approaches to the design of bioactive molecules such as drugs, insecticides, herbicides and fungicides is based on the quantification of bioactivity as a function of molecular structure. The bioactivity A is determined, commonly as log(1/c), c being the molar concentration (or dose) that elicits a constant biological response (e.g. ED_{50}, IC_{50}, etc), and then related to structure. This is generally carried out by means of multiple linear regression analysis using a correlation equation of the type:

$$A_x = a_0 + a_1\tau_x + a_2\tau_x^2 + a_3\sigma_{I,x} + a_4\sigma_{D,x} + a_5 S \qquad (1)$$

where τ is a transport parameter, σ_I and σ_D are the localized (field and/or inductive) and delocalized (resonance) electrical effect parameters, and S is a steric parameter.

Generally, the transport parameter used is the logarithm of the partition coefficient of effector (bioactive substance), determined between water and octanol, log P, or some quantity derived from it. The term in τ^2 was introduced to account for the frequently observed parabolic dependence of data set of effectors on the transport parameter. In general, this behaviour is accounted for by the fact than when an effector molecule crosses a biomembrane, it must first transfer from the aqueous phase to the biomembrane (more lipidic) and must then transfer from the other side of the biomembrane back into an aqueous phase.

Frequently, the electrical effect parameter σ, are combined into a composite substituent constant. The well-known Hammett [1] σ_m and σ_p or Taft [2] σ^* (polar) constants are examples of such composite electrical effect parameters.

There are several distinct methods available for the parametrization of steric effects. The first group of parameters is defined from chemical reactivities (Taft E parameters and their modifications [2]), from van der Waals radii and molecular geometries (Verloop [3]) from a combination of these sources (Charton [4]). The second one are the topological methods such as DARC-PELCO (Dubois and coworkers [5]), the branching equation [4] and molecular connectivity [6].

---

* *Technical Univ. Timişoara, Faculty of Chemistry, P-ţa Victoriei nr.* 2, 1900 *Timişoara, Romania.*
** *Univ. of Medicine and Pharmacy, Dpt. of Biochemistry, P-ţa E. Murgu nr. 2, 1900 Timişoara, Romania*
*** *West University Timişoara*

An alternative to these parameters is the use of the overlapping methods such as minimal stearic difference, MSD and MTD methods.

The purpose of this paper is to present these last methods in some detail. Multiconformational MTD method was introduced to derive QSAR for a series of molecules with high conformational flexibility, where more than one conformation per molecule may exist, within the mean thermal energy, kI-limit (i.e. 2.5 kJ/mole or 0.6 kcal/mole above the lowest energy conformation) [8—11]. In this note we intend to give a systematic description of the multiconformational MTD-method in order to asses, for flexible molecules, the conformations which must be considered for the QSAR.

The application selected for this note is $N = 25$ acetic acid esters, with acetylcholinesterase hydrolysis rates (an application of MTD-multiconformational approach) [12]. The molecules are of moderate complexity; each has only a few low energy conformations to be considered [8]. We will use also the cross-validation procedure (with two subseries, each containing 50% of the molecules) in order to asses the real predictive capacity of our results.

2. **The MDS and MTD Methods.** Minimal steric difference [7, 13], MSD, depends both on the shape of the effector molecule and of the biological receptor. The basic idea of the minimal steric difference concept is that the affinity of effectors for a receptor is a linearly decreasing function of the sum of nonoverlapping volumes of effector molecule and receptor cavity. In order to have this concept at work, one must have a guess for the shape of the receptor cavity and a simple method to evaluate the nonoverlapping volumes which is, in fact, the MDS. Thus, if A_i is the biological activity of molecule M_i, for correlational equations it should depend on MSD_i as:

$$\hat{A}_i = a - \beta\, MSD_i \tag{2}$$

A first guess for the receptor cavity shape will be the natural effector of the molecule of highest activity known. This molecule with the shape (approximately) complementary to the receptor cavity is called "standard" and denoted by S. One seeks the maximal superposition of the molecule M_i upon S. The number of nonsuperposable (nonhydrogen) atoms from both M_i and S gives MSD_i. Hydrogen atoms are neglected in order to simplify the problem, since their van der Waals (vdW) volumes and covalent radii are rather low. As heavy atoms have larger vdW volumes one can attribute a weight 1 to First Row (second period) atoms (C, N, O), 1.5 to Second Row (third period) atoms (S, Cl) and 2 to higher period atoms (Br, I).

In the superposition procedure, differences between bond lengths and bond angles are neglected. However, one must avoid to superimpose pairs of atoms bonded in one molecule on nonbonded pairs of atoms in the second one, as vdW contact distances are much larger (3—4 Å) than covalent bonds (1.2—2 Å). If the molecule M has several low energy conformations it will enter to the receptor with the conformation which fits best the cavity: one must consider for M_i as MSD_i the conformation which gives maximal superposition on S, i.e., one must select the minimal stearic difference. Sometimes certain atoms within M_i will have to be superimposed on a certain group of atoms from S: for example, in enzymatic reactions, the atoms of bonds to be cleared in M_i and in S must be superimposed one upon another, respecting also the corresponding orientation of bonds. Groups suspected to give strong interactions with the receptor, for example electrically charged groups, should also be suitably superimposed within the M_i on S.

In conclusion, the MSD (Minimal Stearic Difference) method offer a very simple way to express by a single number the molecular shape dissimilarity between the effector molecules and S, which is considered as a complementary shape of the receptor cavity. For details about this method and its applications one may consult the ref. [14].

The Minimal Topological Difference (abbreviated as MTD) denotes a "hypermolecule optimization" procedure based on the MSD method. MTD is the MSD parameter calculated against a "hypermolecule" as standard. The MTD method consists in the following aspects:

(i) One obtains the hypermolecule, $\hat{H}$, by approximate atom per atom superposition of the all molecules of the data set, seeking maximal overlap (as in MSD; see above). Occasionally, the rule is supplemented with other criteria, such as: the reactive groups, or the hydrogen-bonding groups, the pharmacophores, etc., of each molecule should be superimposed.

(ii) $\hat{H}$ is used as topological framework for describing the stereochemistry of each molecule i (involved in the construction of $\hat{H}$) by the vector $X_i = \{x_{ij}\}$, $j = 1,m$ (vertices of $\hat{H}$), $i = 1,n$ (molecules of studied series). The entry x_{ij} is taken to be 1 if the vertex j of $\hat{H}$ is occupied by a nonhydrogen atom of the molecule i, and $x_{ij} = 0$ if it is not occupied.

(iii) Selection of a start receptor map, $S^0(\varepsilon_j)$, derived from $\hat{H}$ and describing three categories of vertices: receptor cavity (beneficial) vertices with $\varepsilon_j = -1$; the wall (detrimental) vertices with $\varepsilon_j = +1$; and the exterior (i.e. the irrelevant space of the receptor) vertices with $\varepsilon_j = 0$.

The steric misfit of molecule i is measured by MTD_i, the minimal steric (or topologic) difference defined as:

$$\mathrm{MTD}_i = S + \sum_{j=1}^{m} \varepsilon_j x_{ij}; \qquad i = 1,n) \tag{3}$$

where s is the total number of cavty vertices in the $\hat{H}$. The MTD_i value signifies the number of relevant, nonsuperposable atoms of the molecule i and hypermolecule $\hat{H}$, i.e. the number of unoccupied receptor cavity vertices plus the number of occupied wall vertices.

The calculated biological activity $\hat{A}_i$ is given by:

$$\hat{A}_i = a_0 + a_1 P_{i1} + a_2 P_{i2} + \ldots - b\mathrm{MTD}_i \tag{4}$$

where a_0, a_1, a_2, ..., b are regressional coefficients and P_k, $k = 1,M$ stand for various parameters designing other effects (e.g. electrical, hydrophobic, etc.) if necessary.

(iv) Optimization of the receptor map: in the optimization procedure, one starts from the initial set S^0 of ε_j assignments, i.e. $S^0 = \{\varepsilon_j^0\}$ (j = 1,m), and changes them, one by one, aiming at minimizing the sum Y of squares of differences between experimental activities, A_i, and corresponding calculated activities $\hat{A}_i$ (from eq. 2):

$$Y = \sum_{i=1}^{n} (A_i - \hat{A}_i)^2 = \text{minimum} \qquad (5)$$

The receptor map is considered to be optimized, $S^* = \{\varepsilon_j^*\}$ (j = 1,m), if other singular ε_j changes do not further reduce Y from (5). This optimized receptor map, S, is a model of the receptor site, the main result of the MTD method.

The treatment of effectors with several low energy conformations is based on the assumption that each molecule will adopt a single conformation which fits the best the hypermolecule H (allowing the maximal superposition) and this rigid effector structure is maintained during the optimization process. This restriction is eliminated by means of multiconformational approach, described below.

3. The multiconformational MTD Method. The minimal steric difference MTD, is a measure of steric misfit between the molecules of a series of bioactive substances and the combining site of the biological receptor, represented by the hypermolecule $\hat{H}$, which can be considered as a topological network [7]. As described above, this hypermolecule $\hat{H}$ is constructed by atom per atom superposition of the whole set of molecules, and the obtained vertices, denoted by $j = 1, 2, \ldots$, m, represent the approximate positions of the atoms of the molecules, combined with receptor site. The molecules M_i, $i = 1, 2, \ldots$, n, can be described by a vectorial, topographic descripsor $X = \{x_{j,k}\}$, which contains, for each conformation k of the molecule M_i, a number of m structural descriptors x_{ijk} ($i = 1$,n; $j = 1$,m; $k = C_1, C_n$) corresponding to the m vertices of the $\hat{H}$, with $x_{ijk} = 1$ if vertex j of $\hat{H}$ is occupied by molecule M_i in conformation k, and $x_{ijk} = 0$ if this vertex is not occupied.

If a molecule M_i has several low energy conformations, C_i, it will adopt the one which fits the best to the receptor, i.e. that conformation with the lowest MTD value. For a given receptor, i.e. a given distribution of vertices to receptor cavity, $\varepsilon_j = 1$, or exterior vertices (steric irrelevant zone) the steric misfit of molecule M_i in conformation k, as measured by MTD_i from relation (3), is now:

$$\text{MTD}_{ik} = S + \sum_{j=1}^{m} \varepsilon_j x_{ij} \qquad (6)$$

where s represents the total number of cavity vertices. During the optimization procedure we consider that MTD_i is the minimum over k of the MTD_{ik} ($k = C_i$) values. These MTD_i values are used in the expression of experimental activities of the type (4). The vertex distribution ε_j ($j = 1$,m) is modified such as minimize the sum of quadratic difference between calculated and experimental biological activities ($\hat{A}_i$ and A_i, respectively) — see relation (5) — using as optimization parameter the correlation coefficient of equation (4). The optimized receptor map $S^* = \{\varepsilon_j^*\}$, $(j = 1,m)$ corresponds to the maximal correlation coefficient, $r = r_{max}$, namely to the best fit of experimental activities A_i by regressional equation (2). (Details about the multiconformation MTD method and its optimization procedure are also given in refs. [8—11]).

4. **Applications.** We report here a QSAR study by means of minimal steric difference method: a multiconformation MTD approach of acetic acid esters with acetylcholinesterase activity.

Structure-Acetylcholinesterase Hydrolysis Rates Relations for Acetic Acid Esters

In this section we present the application of multiconformational MTD method in a QSAR for acetylcholinesterase catalyzed hydrolysis rates of a series of 25 acetic acid esters [12].

Conformations were selected for the QSAR study according to their energies calculated by the COSMIC modelling program [16]. Information from an X-ray crystallographic study, together with results of conformational energy calculations was used in constructing the hypermolecule $\hat{H}$ (figure) for the 25 acetic acid ester molecules.

For the MTD — QSAR, only the σ^* — Taft constant has been considered as a second structural parameter. The start map S° was chosen with vertices $j = 4—8$ occupied by $R = -CH_2-CH_2-N^+(CH_3)_3$ in acetylcholine, the natural substrate as cavity vertices, and $j = 1$ as wall vertex:

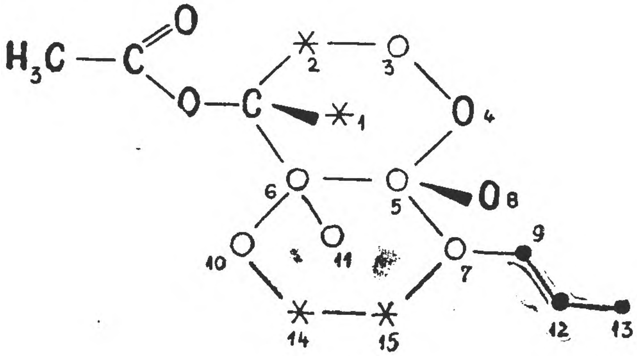

Fig. 1

Hypermolecule $\hat{H}$, vertex (j) numeration and optimized receptor map, S^*, for the 25 acetic acid esters. Vertices occupied in all molecules are not numerated.

Cavity vertices, $\varepsilon_j = -1$ marked by circles; wall vertices $\varepsilon_j = +1$ by asterisks; exterior vertices $\varepsilon_j = 0$ by dots.

$$S^0 = \begin{cases} j(\varepsilon = -1) : 4-8 \\ j(\varepsilon = +1) : 1 \\ j(\varepsilon = 0) : 2,3,9-15 \end{cases}$$

if MTD values with respect to S° are considered, as well as σ^* — Taft values, a rather good explanation of the decreasing A rate order is obtained, with $r = 0.888$.

With the optimization procedure of multiconformational MTD, the following optimized map, S*, and correlational equation are obtained:

$$S^* = \begin{cases} j(\varepsilon = -1) : 3-8,\ 10,\ 11 \\ j(\varepsilon = +1) : 1,\ 2,\ 14,\ 15 \\ j(\varepsilon = 0) : 9,\ 12,\ 13 \end{cases}$$

$$\hat{A}_1 = (8.434 \pm 0{,}433) + (1.683 \pm 0.459)\sigma^* - (0.753 \pm 0.071)\mathrm{MTD}^* \qquad (8)$$

$$(n = 25;\ s = 0.488;\ F(2{,}22) = 72.01;\ r^2 = 0.867;\ r^2_{CV} = 0.661)$$

Introduction of π and E_s into the correlation yields to following correlational equation:

$$\hat{A}_2 = (7.194 \pm 0.905) + (1.902 \pm 0.524\sigma^* + (0.263 \pm 0.199)\Pi + (0.814 \pm 0.325)E -$$
$$- (0.552 \pm 0.113)\mathrm{MTD}^*$$

$$(n = 15;\ s = 0.447;\ F(4{,}20) = 44.6;\ r^2 = 0.899)$$

but the coefficient of Π (0.263) must be rejected because of the low Fisher test value ($F(1{,}20) = 1.75$). If one introduces only the E_s values into the correlation (beside σ and MTD*), the coefficient of this parameter is also rejected from the obtained equation (Fisher test $F(1{,}21) = 4.37$). Thus equation (8) can be considered the last correlation obtained.

The correlation results of this multiconformational MTD study, $r = 0.931$ for a correlation equation with σ^* — Taft and MTD as structural parameters and $r^2_{CV} = 0.661$ for cross-validation (with explained variance of 0.885 and good statistical test results), as compared to a classical Hansch QSAR with σ^*, Π and E_s as structural parameters, with $r = 0.882$ and $r^2_{CV} = 0.577$ (explained variance 0.747), indicate the success and significant predicative power of the multiconformational MTD-method.

This QSAR study brings a significant contribution to the study of this enzymatic reaction. The positive effect of σ^* — Taft, of electron withdrawing esteric R-groups is in agreement with the general nature of this hydrolytic reaction. Our results indicate the binding of the trimethylamonium cation of acetylcholine to an aromatic cavity of the enzyme binding site, in agreement with X-ray analysis and model studies. The enzyme cavity which accommodates acetylcholine is rather similar in shape to acetylcholine, but somewhat larger as indicated by the receptor map (see figure).

5. **Conclusion.** The MSD and MTD methods for quantitative structure-activity study of receptor-effector interactions are valuable tools to look inside of these biological processes. QSAR studies with the aid of the MSD and MTD techniques, described above, are able to yield supplementary details to those given by *X*-ray studies.

REFERENCES

1. L. P. Hammett, *J. Am. Chem. Soc.*, **59**, 96, (1937)
2. R. W. Taft, "The Separation of Polar, Steric and Resonance Effects in Reactivity", *Steric Effects in Organic Chemistry*, (Newman, M. S., ed.), Wiley, New York, 1956, p. 556.
3. A. Verloop, W. Hoogenstraaten and J. Tipker, *Drug Design*, **7**, 165 (1976)
4. M. Charton, *J. Org. Chem.*, **43**, 3995 (1978).
5. J. E. Dubois, D. Laurent, A. Aranda, *J. Chim. Phys.*, **70**, 1616, (1973)
6. L. B. Kier and L. H. Hall, *Molecular Connectivity in Chemistry and Drug Research*, Academic Press, New York, 1976.
7. Z. Simon, A. Chiriac, S. Holban, D. Ciubotariu and I. G. Mihalaş, *Minimum Steric Difference. The MTD-Method for QSAR Studies*, Res. Studies Press, Letchworth, 1984.
8. D. Ciubotariu, E. Deretey, T. I. Oprea, T. Sulea, Z. Simon, L. Kurunczi and A. Chiriac, *Quant. Struct. Act. Relat.*, 12, 367, (1993).
9. D. Ciubotariu, *Structure-Rreactivity Relations in the Class of Carbonic Acid Derivatives*, Ph. D. Thesis, Polytechnical Institute of Bucarest, 1987, p. 143.
10. A. Motsenigos, D. Ciubotariu, A. Chiriac and Z. Simon, *Rev. Roumaine Chim.*, **34**, 2101, (1989).
11. I. Niculescu-Duvăz, D. Ciubotariu, Z. Simon and N. Voiculetz, in *Modeling of Cancer Genesis and Prevention*, (N. Voiculetz, A. T. Balaban, I. Niculescu-Duvăz and Z. Simon, eds.) CRC Press, Bora Raton, Flo., 1991, p. 157.
12. J. Järv, T. Kesvatera and A. Aaviksaar, *Eur. J. Biochem.*, **67**, 315, (1976)
13. Z. Simon and Z. Szabadai, *Studia Biophys*, (Berlin), **39**, 123, (1973)
14. A. T. Balaban, A. Chiriac, I. Mator and Z. Simon, "Steric fit in QSAR", *Lecture Notes in Chemistry*, vol. 15, Springer, Berlin, 1980.
15. A. Chiriac, D. Ciubotariu, Z. Sabadai, R. Vilceanu and Z. Simon, *Rev. Roum. Chim.*, **12**, 143, (1975).
16. J. G. Vinter, A. Davis and M. R. Saunders, *J. Comput.-Aided Mol. Ses.*, **1**, 31 (1987).
17. J. L. Sussman, H. Marel, C. F. Oefuer, A. Goldman, L. Toker and J. Silman, *Science*, **253**, 872 (1991).
18. D. A. Dougherty and D. A. Stauffer, *Science*, **250**, 1558, (1990).

STUDIA UNIV. BABEŞ-BOLYAI, CHEMIA, XXXIX, 1-2, 1994

HIGH PERFORMANCE LIQUID CHROMATOGRAPHY IN CAROTENOID RESEARCH

H. PFANDER*, C. SOCACIU**, G. NEAMŢU**

ABSTRACT: Today HPLC is an indispensable analytical method in carotenoid research. The principles of HPLC separation, the methodology and its application for the separation of carotenoid pigments is reviewed. Different systems for the separation of carotenes, hydroxycarotenoids (lutein/zeaxanthin, violaxanthin/neoxanthin), E/Z and optical izomers are discussed. Aplications of carotenoid separations by HPLC with relevance in medicine, cell biology and genetics are also presented.

Introduction. Almost every research in chemistry, including biochemistry, medical chemistry, food and agricultural chemistry or many other research fields, depends on a proper elucidation of structure of a chemical compound. The structure elucidation is performed mainly by spectroscopic methods, especially high resolution NMR spectroscopy and of course other methods such as MS, IR, UV/Vis, CD, etc. But before the spectroscopical methods can be applied, it is necessary in most cases to obtain the compound in pure state, although in some cases information can be obtained from mixtures. Therefore the first task is separation and for this purpose HPLC is one of the most powerful methods.

The correct meaning of HPLC is High Performance Liquid Chromatography and the term of "high pressure" should not be used. Looking back to the history of separations, of course the term "chromatography" is connected with the name of Micheal Tswett, the russian botanist who invented chromatography in his famous paper which appeared in 1960 in "Berichte der Deutchen Botanischer Gesellschaft". He reported the separation of chlorophyll *a* and *b*, carotenes and xanthophylls. Tswett tested more than a hundered different inorganic and organic materials for their suitability as stationary phase e.g. powered sucrose and precipitated calcium carbonate [1]. Afterwards liquid-liquid or partition chromatography, GC, TLC and paper chromatography were developed. In 1963 Giddings published a paper entitled "LC with Operating Conditions Analogous to those of GC". After that time a breathtaking development took place and today HPLC has become a wonderful but at the same time dangerous tool for analysis. The "power" of HPLC is illustrated by the number of theoretical plates, which is a measure for the efficiency of the separation.

Different definitions for HPLC can be found in textbooks and publications [2, 3]. Using a pragmatic criterion it can be said that HPLC is a liquid chromatographic method using stationary phases with very small particles, not larger than 10 μm. This normally leads to a pressure of >20 bar (300 psi)

---

* *Institute of Organic Chemistry, University of Berne, 3012 Berne, Switzerland*
** *Dept. Chemistry and Plant Biochemistry, University of Agricultural Sciences, 3400 Cluj-Napoca, Romania*

for the separation. These two restrictions necessitate the utilisation of an HPLC apparatus. A schematic diagram of an HPLC unit including the pump, the column and the detector is shown in Figure 1.

The apparatus includes usually only one pump, so that only isocratic separations can be carried out. An isocratic separation means that the mobile phase is not varied during the separation. For the separation of mixtures with a relatively wide range of polarities the composition of the mobile phase can or be changed during the separation and this is termed a gradient elution. The composition of the eluent can be changed either stepwise or continuously. This technique is very important and allows the separation also of complex mixtures. Gradient elutions require two pumps, a mixing chamber and also an electronic control, which makes, of course, the apparatus more expensive. If such a device is not available, the reservoir of the mobile phase can be changed during the separation: this results in a stepwise gradient. Although the more sophisticated gradient elution system has many advantages, the isocratic system can be carried out, efficiently: the approach is to fractionate the mixture of compounds in a first separation and in a second step to separate these fractions in a different system. Although more timeconsuming, the results are comparable.

The column is the most important part, the "heart" of the HPLC apparatus. The column is responsible for the separation, so must be treated with utmost care. It is recommended that a column which gives a good separation in a demanding problem is reserved for this specific problem, in order to avoid the decline in quality of the column. For each column, it is recommended to keep a record of the specific data (including test chromatograms). In this, every user should also record each experiment carried out with the column.

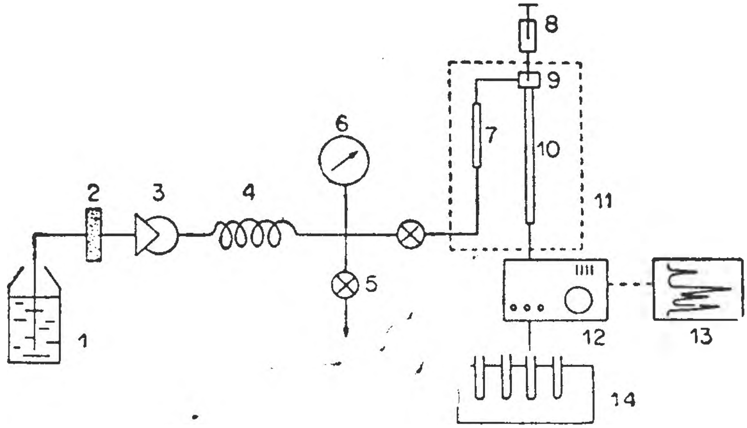

Fig. 1. Schematic diagram of HPLC unit. 1 = solvent reservoir; 2 = sintered frit; 3 = highpressure pump; 4 = pulse damper; 5 = drain valve; 6 = manometer; 7 = precolumn (optional);8 = injection valve; 10 = column; 11 = termostat; 12 = detector; 13 = recorder (may include integrator and printer); 14 = fraction collector (optional)

An important aspect to consider is whether to buy a packed column or to pack the column in the laboratory (so called "homemade" columns). Packed columns, bought from one of the many distributors are much more expensive. On the other hand, one has to consider that additional equipment is needed and a lot of experience to pack a column with good separation qualities. However, it must be pointed out that the properties and the quality of industrially produced columns from different manufacturers are not identical and may vary significantly.

In a recent review it was shown that for HPLC, the socalled bonded phase, which are used on reversed—phase conditions is the prefered separation systems. The bonded phases are obtained by the modification of the reactive groups on the surface of the stationary phase. For example, for silicagel the reactive groups are the OH-groups, the silanol groups. The octadecylsilane (ODS) derivative where $R = C$ is the most widely used system. The desired stationary phase is obtained by the reaction of the silicagel with a chlorosilane derivative. The stationary phase becomes non-polar, especially with ODS and the mobile phase has to be polar. This is called reversed phase chromatography (RPC). This system is very powerful and has many advantages also for the separation of carotenoids. The other system which is often used is the normal phase liquid chromatography, where the stationary phase is polar and the mobile phase non-polar. This is the "classical" system of Tswett. As stationary phase mostly silicagel, sometimes alumina and rarely $MgCO_3$, $Ca(OH)_2$, etc. are used. The physical phenomenon controlling a separation in normal phase chromatography is adsorbtion, whereas in reversed phase chromatography is partition. In both cases, it is important that the particles have a defined diameter of 3—10 μm and furthermore that they have a narrow particle size distribution.

The detection in the case of carotenoids is not really a problem. Due to conjugated polyene system and their bright colour, the UV/Vis detector with a flow cell is the detector of choice. The detection is quite simple if one is working qualitatively. For quantitative determinations, problems may arise because of the small differences between the absorbtion spectra of each carotenoid. A milestone for the development of HPLC performances was the development of the photodiode array detector (PDA). To measure a spectra with the UV/Vis spectrophotometer, the wavelenght is changed slowly, either by prism or monochromator and the data are aquired in series. In the PDA, after the polychromatic radiation has passed through the sample, it is dispersed by a fixed grating and then falls onto an array of photodiodes. Each diode measures a narrow band of wavelenghts of the spectrum thus the PDA has parallel, simultaneous data acquisition. Although computer-assisted PDA's are more expensive than conventional UV/Vis detectors, they have a number of advantages. The spectrum of each peak in the chromatogram can be stored and subsequently compared with standard spectra. The chromatogram, the UV/Vis spectra and the map-like contour plot can be obtained simultaneously. The device is very suitable for the detection of impurities. The chromatogram looks clean, but on the contour diagram one can easily detect an impurity and this is confirmed by the UV/Vis spectrum, where it is obvious that at the position *a* of the peak an impurity is present.

Separation of carotenoids. The beautiful coloured carotenoids consist of a polyene chain and different end groups. The combination of these end groups results in many different compounds and up to now, more than 600 different carotenoids have been isolated from natural sources [4]. Carotenoids are ubiquitous, occurring in almost every living organism, plants as well as animals and also in human beings. The carotenoids are brilliantly coloured — from yellow and orange to red and they please our eyes. Carotenoids are unstable to heat, light, air, oxygen, acids and sometimes bases. Therefore, a lot of experience and a lot of experimental skill is necessary for carotenoid research and also their separation is highly demanding.

The first separation of carotenoids by HPLC was published in 1971 by Ivan Stewart [5]. He separated carotenes, i.e. hydrocarbons on magnesium oxide and oxygenated carotenoids, the xanthophylls, on zinc carbonate. The retention times were rather long but the results were remarkable.

From then on the field developed to such a point that today one can say that every carotenoid separation problem can be solved by HPLC! What follows is a discussion about some results, taken from literature [3, 6, 7, 8] and from our laboratories.

1. A standard problem, which is also relevant in medicine, is the separation of α- and β-carotene. These two compounds only differ in the position of one double bond and therefore the separation is quite difficult. The results of a recent publication [9] is shown in Figure 2. The separation was carried out on Ca(OH)$_2$ and the retention time of about 20 minutes is noteworthy.

2. Another very common problem is the separation of the xanthophylls, the oxygenated carotenoids, which are widely distributed in plants. The first problem is the separation of lutein and zeaxanthin. These two carotenoids also differ as α- and β-carotene in the position of one double bond. The other problem is the separation of violaxanthin and neoxanthin which have very similar polarities. A interesting separation system on reversed phase C$_{18}$ by a stepwise gradient, from a mixture containing carotenoids (neoxanthin, violaxanthin, zeaxanthin, lutein, β-carotene) and chlorophylls [10] is shown in Figure 3.

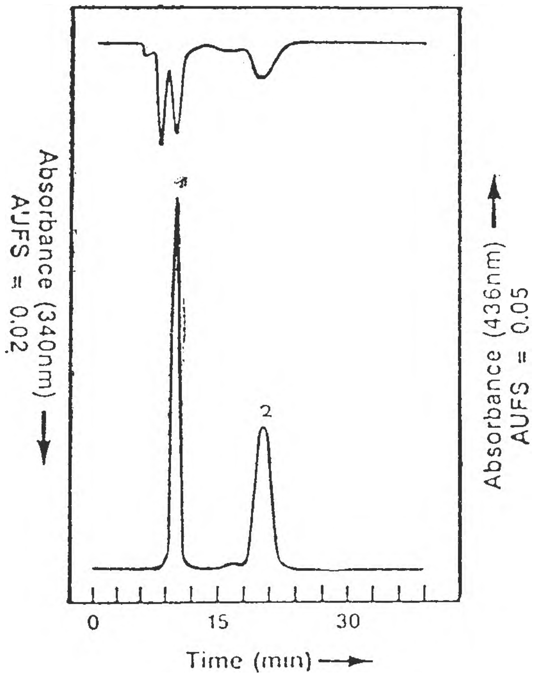

Fig. 2. Separation of (all-E)-α-carotene (1) and (all-E)-β-carotene (2) on Ca(OH)$_2$ (Chandler and Schwartz, 1987).

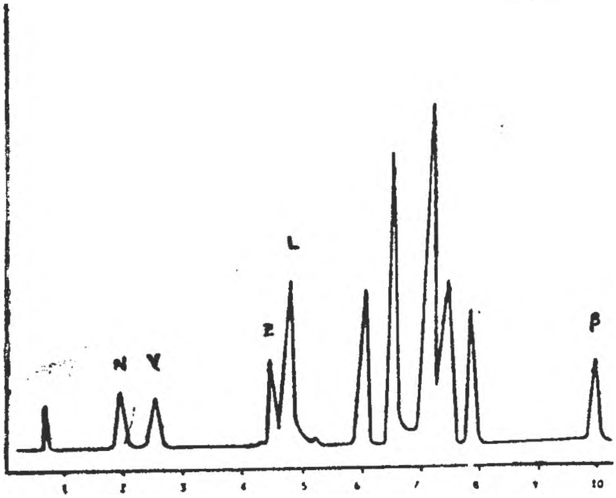

Fig. 3. Reversed-phase separation of a mixture of neoxanthin (N), violaxanthin (V), zeaxanthin (Z), lutein (L), chlorophylls a and b, pheophytins a and b, β-carotene (β) (Bailey and Chen, 1988)

3. A problem which is even more demanding in the separation of stereoisomers. It is obvious from the constitution of carotenoids that the double bonds of the polyene chain may have either the *cis-* or the *trans-* configuration. According to the nomenclature rules approved by IUPAC the E/Z — nomenclature should be used nowadays. Therefore E is equivalent to trans and Z is equivalent to cis. E/Z — isomerization gives rise to many stereoisomers of carotenoids (for β-carotenes 528 isomers are possible). In fact the carotenoids very easily undergo isomerization as long as they are in solution. The double bonds of the polyene chain are not equivalent, one can distinguish between hindered and unhindered double bonds and the number of stable possible isomers decrease. Nevertheless the problem of E/Z isomerization exists and this makes the handling of carotenoids even more difficult. The separation of these E/Z isomers is very demanding, as they have similar chromatographic properties and furthermore one has to be careful that no izomerization takes place during the separation. This problem has been at least partly solved, as is shown in the Figures 4 and 5. The first example is the separation of the E/Z isomers of β-carotene on a column packed with alumina [11]. The second one is the separation of the C_{50}-carotenoid stereoisomers (all-E)-, (5Z)-, (9Z)-(13Z)- and (15Z)-bacterioruberin, carried out under reversed phase conditions with an ODS column [12].

4. An even more demanding problem is the separation of optical isomers. Two approaches are possible for the separations of optical isomers:

— the enantiomers can be converted to diastereoisomers by reaction with an optically active pure compound. Diastereoisomers have different properties and can be separated on a achiral column. A racemic mixture of astaxanthin was reacted with camphanic acid chloride to give the corresponding camphanates and afterwards separated under normal phase conditions [13] (Fig. 6). A chiral column for resolving optical isomers of astaxanthin was also reported [14].

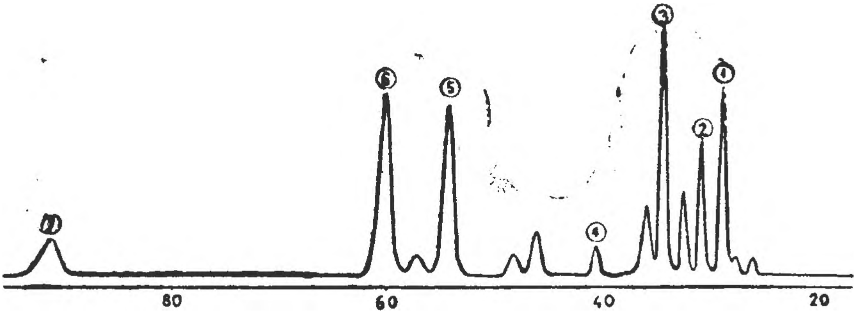

Fig. 4. HPLC separation of a mixture of 7 (E/Z)-isomers of β-carotene (Vecchi et al., 1981)

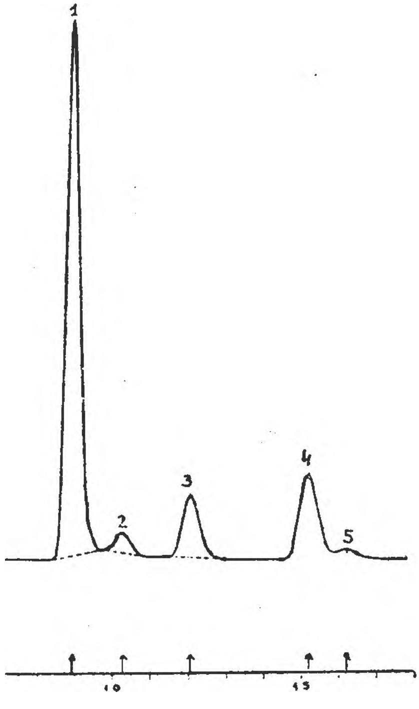

Fig. 5. Separation of (all-E)-, (5Z)-, (9Z)-, (13Z)- and (15Z)- bacterioruberin (Riesen and Pfander, 1990)

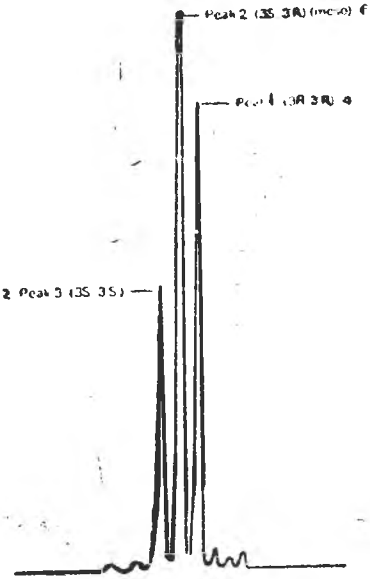

Fig. 6. Separation of (all-E)-astaxanthin stereoisomers after derivatization with camphanic acid (Vecchi and Muller, 1979)

— the use of columns with optically active stationary phase. In this case also a diastereomeric relationship is established but no covalent bond is formed. Figure 7 shows the separation of the isomers of the zeaxanthin dibenzoates [15].

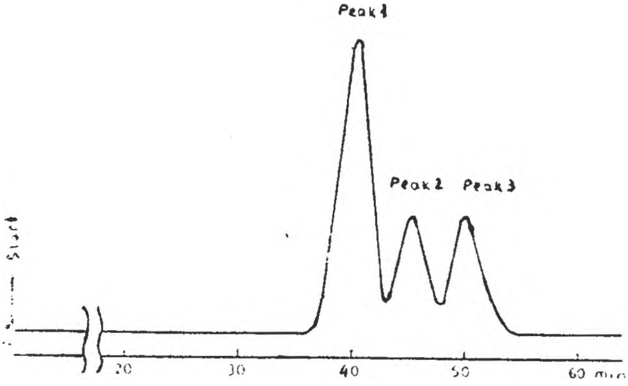

Fig. 7. Separation of zeaxanthin stereoisomers on chiral phase (peak 1 = 3R, 3′S [= meso]; peak 2 = 3R, 3′R; peak 3 = 3S, 3′S) (Maoka et, al., 1986)

These selected examples have shown that difficult separation problems in carotenoid research can be solved with HPLC.

Scope and limitations. HPLC is the most powerful of all the chromato graphic techniques. It can often easily achieve separations and analyses that would be difficult or impossible using other forms of chromatography. On the other hand, many things can go wrong with such separations; there are probably more pitfalls in HPLC than in any other form of chromatography. To avoid these mistakes it is not enough to read textbooks or to listen to lectures. Only by doing a great deal of experimental work and making many mistakes you can achieve the necessary practical skill. The more sophisticated a method is, the more mistakes can occur.

Two points are also critical for the analyse of HPLC performances: the retention time and the identification.

A chromatographic separation is theoretically reproducible, if the parameters of the separation are constant. But in practice the HPLC separations and also retention times are not strictly reproducible. According to our experience the t_R — values differ from column to column and furthermore one can observe that even during a working day the t_R value is not constant.

And therefore proper identification is essential. Is not allowed to postulate the structure of a carotenoid based only on the t -value and an electronic spectrum. The minimal criteria for the identification of a carotenoid are the Vis spectrum, co-chromatography with a standard and the mass-spectrum.

Summary and Outlook. The development of HPLC has opened new dimensions in analytical chemistry and also in the field of carotenoid research. One condition for HPLC separations is that one should be very critical in the interpretation of results: the high sensitivity of HPLC makes this method extremely dangerous. Separation is only one step for structure elucidation, which should involve indispensable spectroscopical methods as MS, NMR, CD, etc.

Nevertheless, carotenoid research has continued to develop over the decades, just alone the increasing number of publications in the field is a clear indication of this. The medical applications, especially cancer prevention, has increased the interest in carotenoid. It can be envisaged that this trend will continue in the future.

REFERENCES

1. Molnar, P., J. Szabolcs and L. Radics, *Phytochem.*, **25,** 195 (1986).
2. Meyer V., *Practical High-Performance Liquid Chromatography* (2nd ed.), J. Wiley & Sons, New York (1994).
3. *Carotenoids*, vol. la (G. Britton, S. Liaaen-Jensen and H. Pfander, eds.) Birkhauser, Basel (1993).
4. H. Pfander, (ed), *Key to Carotenoids*, Birkhauser, Basel (1987).
5. I. Stewart, and T. A. Wheaton, J. *Chrom.*, **55,** 325 (1971).
6. H. Pfander, R. Riesen and U. Niggli, *Pure Appl. Chem.*, **66,** 947 (1994)
7. F. Khachik, G. Beecher, M. B. Goli, W. R. Lusby and C. E. Daiten *Meth. Enzym.*, **213,** 205 (1992).
8. N. E. Craft, *Meth. Enzym.*, **213,** 185 (1992).
9. L. A. Chandler, and S. J. Schwartz, *J. Food Sci.*, **52,** 669 (1987).
10. C. A. Bailey and B. H. Chen, *J. Chrom.*, **455,** 396 (1988).
11. M. Vecchi, G. Englert, R Maurer and V. Meduna, *Helv. Chim. Acta.*, **64,** 2746 (1981).
12. R. Riesen and H. Pfander, Proc. 9th Int. Symp. Carotenoids, Kyoto, Japan, **1990**.
13. M. Vecchi and R. K. Muller, *J. HRC & CC*, **2,** 195 (1979).
14. T. Matsuno, T. Maoka, M. Katsuyama, M. Ookubo, K. Katagiri and H. Jimura, *Nippon Suidan Gakkaishi*, **50,** 1589 (1984).
15. T. Maoka, A. Arai, M. Shimizu and T. Matsuno, *Comp. Biochem. Physiol.*, **83**B, 121 (1986).

STUDIA UNIV. BABEŞ-BOLYAI, CHEMIA, XXXIX, 1–2, 1994

SYNTHESIS AND STEREOCHEMISTRY OF SOME BICYCLIC ACETALS OBTAINED FROM 1,2-CYCLOHEXANEDIOL

I. GROSU*, I. HOPÂRTEAN*, G. PLÉ**, G. MUNTEANU*, S. MAGER*

ABSTRACT. — New compounds having a 2,4-dioxabicyclo[4.3.0]nonane skeleton were obtained by the acealisation reaction of o-, m- and p-nitrobenzaldehydes with the cis and trans diastereomers of 1,2-cyclohexanediol. The stereochemical investigations by means of Dreiding models and the ^{1}H-NMR spectra of the compounds show rigid structures.

In order to continue our investigations in the field of the stereochemistry of cyclic acetals obtained from 1,3-[1] and 1,4-[2] cyclohexanediols and cyclohexanepolyols [3], the acetalisation reaction of o-, m- and p-nitrobenzaldehydes with the cis and trans diastereomers of 1,2-cyclohexanediol (Scheme 1) was

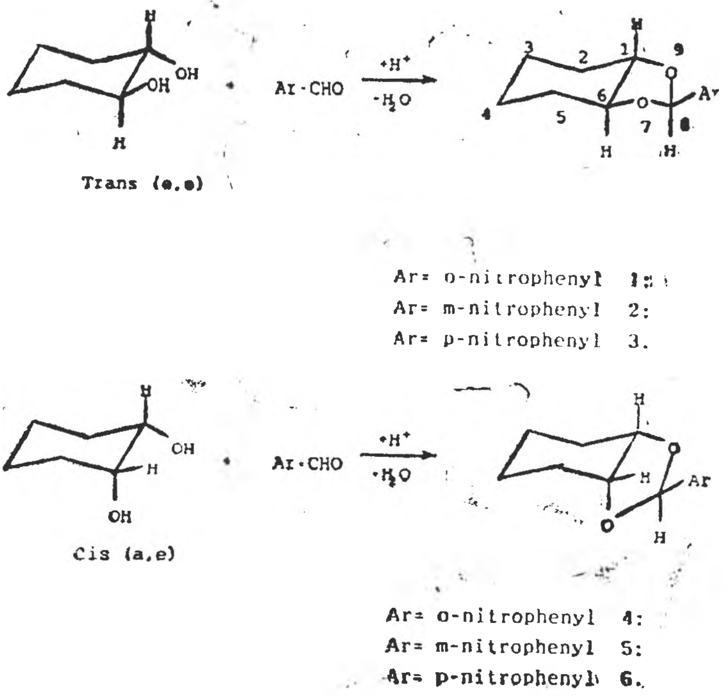

Ar= o-nitrophenyl 1;
Ar= m-nitrophenyl 2;
Ar= p-nitrophenyl 3.

Ar= o-nitrophenyl 4;
Ar= m-nitrophenyl 5;
Ar= p-nitrophenyl 6.

Scheme 1

---

* „Babeş-Bolyai" University, Organic Chemistry Department, 11 Arany Janoş Str., 3400 Cluj-Napoca, Romania.
** Université de Rouen et IRCOF, Laboratoire associe au CNRS DO-464. Faculte des Sciences de Rouen, 76821 Mont Saint-Aignan, Cedex, France

carried out under usual conditions (acid catalyst and azeotropic distillation for removing the resulted water).

The stereochemistry of compounds 1—6 was investigated using Dreiding models and high field (360 MHz) ^{1}H-NMR spectra. The Dreiding models inspection reveals the rigid structure of both cyclohexanic and 1,3-dioxolanic rings. The nitrophenyl group located at C^3 adopts an equatorial orientation, the conformational free energie of the aryl group in the acetalic part of the 1,3-dioxolanic ring being enough high to induce anancomericity [4]. The rigid structure of compounds 1—6 was confirmed by their complex ^{1}H-NMR spectra when distinct signals for the equatorial and axial protons of the six membered rings are recorded (Figure 1 and Figure 2).

The spectra of the acetals obtained from the cis or trans 1,2-cyclohexanediol (Figure 1 and 2) present some peculiar aspects.

If the diol used is the trans isomer, in the bicyclic compound the 1,3-dioxolanic ring is linked to the cyclohexanic one by equatorial — equatorial bonds and the protons located at the carbon atom of the bridge (positions 1 and 5) have an axial — axial orientation. This disposal of the hydrogen atoms can be also confirmed analyzing the values of the coupling constants of one of these protons with the other one and with the equatorial and axial protons of the neighbouring positions (6 and 9). Thus, in the case of compound 3, for the protons located at C^1 and C^5, characteristic values [5—7] for the axial — axial coupling constants are measured ($J = 8.8$ Hz, $J = 11.5$ Hz). An other value ($J = 3.9$ Hz), characteristic for the coupling between vicinal axial and equatorial protons [7—9], was also indentified. In the synthesis of compounds 4—6, obtained from the cis isomer of 1,2-cyclohexane-

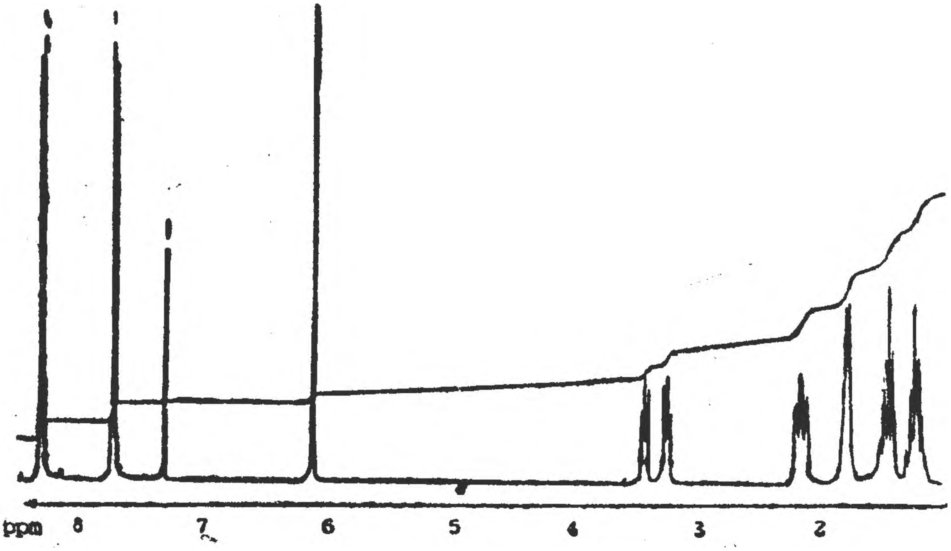

F i g. 1. ^{1}H-NMR spectrum of compound 3.

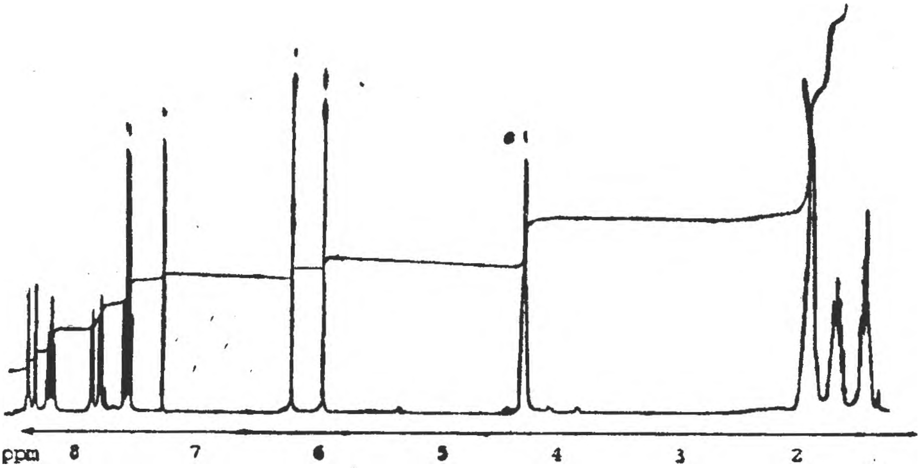

Fig. 2. ^{1}H-NMR spectrum of compound 5.

diol, the 1,3-dioxolanic ring is linked to the cyclohexanic one by an equatorial-axial bond system. The protons located at the carbon atoms of the bridge (positions 1 and 5) have an axial-equatorial orientation. The spectrum of compound 5 shows a splitting of the signals corresponding to the protons located to C^1 and C^5 due to small coupling constants, which are characteristic for a coupling between axial and equatorial protons and between equatorial and equatorial ones. As a consequence of these small values of the coupling constants, the peaks of the signals are overlapped and give a complex unresolvable multiplet (4.15—4.25 ppm).

A remarkable feature is the recording in the spectra of compounds 2 and 5 (obtained using *m*-nitrobenzaldehyde) of two singlets with the same intensity for the proton located at C^3 (2 : $\delta_1 = 5.75$, $\delta_2 = 6.02$ ppm ; 5 : $\delta_1 = 5.91$, $\delta_2 = 6.17$ ppm), while in the case of the other compounds (obtained from o- and p-benzaldehyde) for this kind of proton only one peak is recorded (1 : $\delta = 6.47$, 3 : $\delta = 6.07$, 4 : $\delta = 6.73$, 6 : $\delta = 5.90$ ppm). A reasonable explanation can be done if it is taken into account the possibility of the m-nitrophenyl group to exist in two rigid bisectional rotamers (in one of them the NO_2 group and the C^3 proton have a "cis" orientation and in the other one they have a "trans" orientation). In the case of p-nitrophenyl group only one bisectional rotamer is possible and in the case of the o-nitrophenyl group one of the possible rotamers (the rotamer with the NO_2 and the proton located at C^3 proton have a "cis" orientation) is very instable and its population can be neglected. Thus, in the last two cases only one singlet for the C^3 proton is recorded.

~~In~~ the ^{1}H-NMR spectra of compounds 1—6 the characteristic signals for the cyclohexanic ring and for the 1,3-dioxolanic one are recorded, the structure of the compounds being confirmed in this way, too.

EXPERIMENTAL

Compounds 1–6 general procedure: A mixture of 2 g (0.017 mol) 1,2-cyclohexanediol (cis or trans), 3 g (0.02 mol) nitrobenzaldehyde (ortho, meta or para) and 0.1 g p-toluenesulphonic acid (as catalyst), was refluxed in 150 ml benzene, under stirring, until no more water was collected in the Dean-Stark trap (reaction time 10–12 h). After cooling, the catalyst was neutralized with 0.1 g sodium acetate. The benzenic solution was separated from the solid residue and then washed twice with 75 ml of water. The benzenic solution was evaporated to dryness and the residue was boiled with ligroine and after that with ethanol for removing the unreacted nitrobenzaldehyde. The new residue was solved in chloroform purified with charcoal and precipitated with ligroine.
M.p.s. are uncorrected.

High resolution ^{1}H-NMR spectra were recorded at room temperature, in C_6D_6 solution, in 5-mm tubes, on a Bruker AM 360 Fourier transform NMR spectrometer equipped with an Aspect 3000 computer and with a dual $^{13}C-^1H$ probe head operating at 360 MHz for protons and 90 MHz for carbon atoms. No TMS was added, rather, shifts were referenced to the solvent line (C_6D_6). All coupling constants and chemical shifts are given with a precision of 0.1 Hz and 0.01 ppm. The usual spectra were run with an 80 Mhz TESLA BS 487 C NMR spectrometer in $CDCl_3$ solution using TMS as standard.

Trans-3-(o-nitrophenyl)-2,4-dioxabicyclo[4.3.0]nonane 1. Solid, mp. = 144–145°C. Found: C, 62.40; H, 6.30; N, 5.85. $C_{13}H_{15}NO_4$ requires C, 62.68; H, 6.05; N, 5.60. ^{1}H-NMR($CDCl_3$, 80 MHz) $\delta = 0.75-2.35$ (8H, m, C^{6-9}), 2.85–3.75 (2H, m, $C^{1,5}$), 6.47 (1H, s, C^3), 7.10–8.25 ppm (4H, m, 3-$C_6H_4NO_2$).

Trans-3-(m-nitrophenyl)-2,4-dioxabicyclo[4.3.0]nonane 2. Solid, m.p. = 45–46°C. Found: C, 62.32; H, 6.23; N, 5.79. $C_{12}H_{15}NO_4$ requires: C, 62.68; H, 6.05; N, 5.60. ^{1}H-NMR($CDCl_3$, 80 MHz) $\delta = 0.87-2.00$ (8H, m, C^{6-9}), 3.75–4.12 (2H, m, $C^{1,5}$), 5.75 and 6.02 (1H, s, and s, C^3), 7.00–8.25 ppm (4H, m, 3-$C_6H_4NO_2$).

Trans-3-(p-nitrophenyl)-2,4-dioxabicyclo[4.3.0]nonane 3. Solid, m.p. = 114–5°C. Found: C, 62.51; H, 6.13; N, 5.69. $C_{13}H_{15}NO_4$ requires: C, 62.68; H, 6.05; N, 5.60. ^{1}H-NMR(C_6D_6, 360 MHz) $\delta = 1.20-2.30$ (8H, m, C^{6-9}), 3.26 (1H, ddd, J = 11.5, 8.8, 3.9 Hz, C^1), 3.44 (1H, ddd, J = 11.5 8.8, 3.9 Hz, C_9), 6.07 (1H, s, C^3), 7.64 (2H, d, J = 8.8 Hz, 3-$C_6H_4NO_2$), 8.21 ppm (2H, d, J = 8.8 Hz, 3-$C_6H_4NO_2$).

Cis-3-(o-nitrophenyl)-2,4-dioxabicyclo[4.3.0]nonane 4. Solid, m.p. = 104–105°C Found: C, 62.71; H, 6.37; N, 5.87. $C_{13}H_{15}NO_4$ requires: C, 62.68; H, 6.05; N, 5.60. ^{1}H-NMR(C_6D_6, 360 MHz) $\delta = 0.75-1.90$ (8H, m, C^{6-9}), 4.04–4.09 (2H, m, $C^{1,5}$), 6.73 (1H, s, C^3), 7.44 (1H, dt, J = 8.5, 1.0 Hz, 3-$C_6H_4NO_2$), 7.57 (1H, dt, J = 8.5, 1.0 Hz, 3-$C_6H_4NO_2$), 7.76 (1H, dd, J = 8.5, 1.0 Hz, 3-, $C_6H_4NO_2$), 7.86 ppm (1H, dd, J = 8.5, 1.0 Hz, 3-$C_6H_4NO_2$).

Cis-3-(m-nitrophenyl)-2,4-dioxabicyclo[4.3.0]nonane 5. Liquid, b.p. = 196–198 C (15–17 mm. col. Hg). Found: C, 62.29; H, 6.51; N, 5.89. $C_{13}H_{15}NO_4$ requires: C, 62.68; H, 6.05; N, 5.60. ^{1}H-NMR (C_6D_6, 360 MHz) $\delta = 1.20-1.90$ (8H, m, C^{6-9}), 4.15–4.25 (2H, m, $C^{1,5}$), 5.91 and 6.17 (1H, s, and s, C^3), 7.50–7.58 (1H, m, 3-$C_6H_4NO_2$), 7.75–7.85 (1H, m, 3-$C_6H_4NO_2$), 8.15–8.23 (1H, m, 3-$C_6H_4NO_2$), 8.32–8.38 ppm (1H, m, 3-$C_6H_4NO_2$).

Cis-3-(-p-nitrophenyl)-2,4-dioxabicyclo[4.3.0]nonane. 6. Solid. m.p. = 82–3°C. Found: C, 62.43; H, 6.33; N, 5.76. $C_{13}H_{15}NO_4$ requires: C, 62.68; H, 6.05; N, 5.60. ^{1}H-NMR (C_6D_6, 360 MHz) $\delta = 1.25-1.85$ (8H, m, C^{6-9}), 4.18–4.24 (2H, m, $C^{1,5}$), 5.90 (1H, s, C^3), 7.66 (2H, d, J = 8.6 Hz, 3-$C_6H_4NO_2$), 8.21 ppm (2H, d, J = 8.6 Hz, 3-$C_6H_4NO_2$).

REFERENCES

1. S. Mager, I. Hopârtean and M. Horn, *Stud. Univ. Babeş-Bolyai. Chem.*, **26**, (1), 34 (1981).
2. S. Mager, I. Hopârtean and Viorica Cristian, *Stud. Univ. Babeş-Bolyai. Chem.*, (2, **23**), 28 (1978).

3. M. Ionescu and S. Mager, *Stud. Univ. Babeş-Bolyai, Chem.*, **9**, 13 (1964).
4. F. G. Riddell, *The conformational analysis of heterocyclic compounds*, Academic Press., New-York, p. 56 (1980) and references mentioned
5. E. Bernaert and M. Anteunis, *Bull. Soc. Chim. Belges*, **79**, 25 (1970).
6. K. Pihlaja and P. Ayras, *Acta Chem. Scand.*, **25**, 204 (1970).
7. M. Anteunis, D. Tavernier and F. Borremans, *Heterocycles*, **4**, 300 (1974).
8. H. R. Buys and E. L. Eliel, *Tetrahedron Letters*, **26**, 2779 (1970).
9. E. W. Garbisch and M. G. Griffith, *J. Am. Chem. Soc.*, **90**, 6543 (1968).

STUDIA UNIV. BABEŞ-BOLYAI, CHEMIA, XXXIX, 1–2, 1994

ALKYLATION OF PHENOTHIAZINES USING LIQUID-SOLID PHASE TRANSFER CATALYSIS WITHOUT SOLVENT

MIRCEA VLASSA*, MIRCEA CENAN**, CERASELLA AFLOROAEI**

ABSTRACT. — The influence of Aliquat 336 (tricaprylmethylammonium chloride "capryl" is a mixture of alkyl groups averaging aproximatively $C_{10}H_{21}$) and PEG-400 (polyethylene glycol, average molecular weight ca. 400) catalysis on reaction yields alkylated phenothiazines using liquid-solid phase transfer catalysis are presented.

Introduction. The preparation of N-alkylphenothiazines derivatives by phase transfer catalysis (PTC) without solvent was achieved using solid state catalysis such as tetrabutylammonium bromide [1] or trioctylammonium chloride [2]. Due to the fact that liquid state catalysis are able to provide a better homogeneity of the reaction system and so to improve the reaction yield, we tryed to carry out N-alkylation of phenothiazines in presence of such catalysts, namely Aliquat 336 and PEG-400:

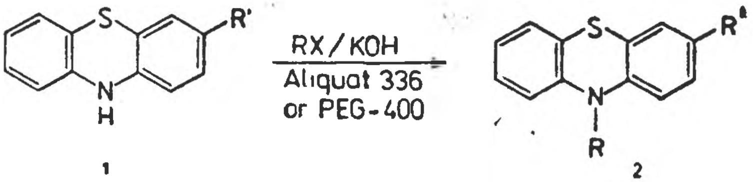

1 2

Material and methods. For makeing a comparison between the influence of solid or liquid state catalysts, on reaction yields unsubstituted and chlorosubstituted phenothiazines were alkyalted according to procedure of Vlassa et al. [1] or by method of Galons et al [2].

Results and discussion. The results of our experiments are shown in Table 1.

Our experiments proved that liquid state catalysts are comparable or better than solid state catalysts. Also, PEG-400, a catalyst which was not used before in PTC without solvent, is comparable with Aliquat 336.

These facts show that for this type of catalysis liquid catalyst are most recommanded.

Experimental. Melting points were not corrected. A Tabor apparatus was used for shaking the reaction mixture. TLC analyses were run on plates covered with silica gel eluted with C_6H_6—EtOH (10 : 1), visualizing agent iodine (unreacted phenothiazines have a green colour and the alkylated product a brown one).

---

* *Department of Organic Chemistry, Faculty of Chemistry Babeş-Bolyai University, 3400 Cluj-Napoca, Romania*
** *Institute of Chemistry, 3400 Cluj-Napoca, Romania*

Table 1

N-Alkylation of phenothiazines using Aliquat 336 or PEG-400 as catalyst.

Compound	R'/R	Yield %			mp. or b.p. (lit. m.p. or b.p.) °C
		Aliquat-336	PEG-400	Literature	
2a	H/CH_3	80	85	70/1/	99 – 100 (99 – 100/5/)
2b	H/C_2H_5	85	85	68/1/	104 – 105 (102,5 – 103/4/)
2c	$H/CH_2{=}CH-CH_3$	90	85	70/1/	228 – 230/13 mm (226 – 230/13 mm /5/)
2d	$Cl/(CH_2)_3N(CH_3)_2$	85	85	85/2/	170 – 172 (170/2/)
2e	$H/(CH_2)_3N(CH_3)_2$	85	80	78/2/	200 – 202 (200 /2/)
2f	$Cl/(CH_2)_2N(i\text{-}Pr)_2$	85	85	79/2/	195 – 197 (187 /2/)

Compounds 2d – 2f were separated as chlorohydrates

General procedure. Phenothiazine (0.1 mol) finely ground KOH (1.22 g, 0.2 mol) and catalyst (0.01 mol) were well mixed. After that alkylating agent (0.2 mol) was added and the resulting mixture was shaken at room temperature for one hour, then left for 12 days at the same temperature. After that the reaction mixture was chromatographed with toluene on an alumina column, the organic solvent was removed *in vacuo* and the residue purified by recrystallization from ethanol-(charcoal was added), for compounds 2a, 2b, 2d – 2f, or by distillation, for compounds 2e and 2f. Compounds 2d – 2f were separated as chlorohydrates in usual way.

REFERENCES

1. M. Vlassa and M. Cenan, *Rev. Roumaine Chim.*, **33**, 192, (1980).
2. H. Galon, M. Micque, C. Combet-Farnoux, T. Bensoid and C. Bram, *Chem. and Pharm. Bull.*, **33**, 5108, (1985).
3. A. Burger and A. Ch. Schmoltz, *J. Org. Chem.*, **19**, 1841, (1954).
4. H. Gilman, R. D. Nelson and J. F. Champaigne jr., *J. Amer. Chem. Soc.*, **74**, 4205 (1952).
5. H. Gilman and D. A. Shirley, *J. Amer. Chem. Soc.*, **60**, 888 (1944).

STUDIA UNIV. BABEŞ-BOLYAI, CHEMIA, XXXIX, 1-2, 1994

ON THE DIOXIMINE COMPLEXES OF TRANSITION METALS.

XCVI. Spectrophotometric study on the deprotonation of some $[Co(DH)_2XY]^n$ type complexes

JÁNOS ZSAKÓ*, CSABA VÁRHELYI**, FERENC MAKKAY*, KINGA KOVÁCS-LUDESCHER*

ABSTRACT. — A number of 10 dimethylglyoximine complexes of cobalt of the type $[Co(DH)_2L_2)X$ (L = aromatic amines: aniline, alkyl-anilines, amino-phenols or H_2O) and $[Co(DH)_2Y_2]H$ ($Y = Br^-$, NCS^-, NO_3^-) were obtained. The deprotonation reaction of these complexes was studied by means of spectrophotometric measurements. As observed, the bridging H atoms of the $Co(DH)_2$ moiety present weak acidic properties corresponding to a pK_a value of about 9.3. The co-ordinated H_2O molecules behave as a little stronger acids with $pK_a \approx 6.4$.

Introduction. The acidic reaction of the aqueous solutions of the transition metal salts can be attributed, partially, to the deprotonation of the hydrated cation (e.g. $[Cr(H_2O)_6]^{3+}$, $[Cr(H_2O)_5(OH)]^{2+}$). The equilibrium constant of this type of reactions is of about $0.5\ldots1-2 \times 10^{-4}$ [1]. Proton release processes can be also observed in the solutions of the cobalt(III)- and platinum (II, IV)-amines [2—5)]. The formation of amido-platin(IV) derivatives was proved by Grinberg et al. [6] on preparative and spectrophotometric way, e.g.:

$$[Pt(NH_3)_5Cl]^{3+} + OH^- \rightarrow (Pt(NH_3)_4(NH_2)Cl]^{2+} + H_2O$$

The corresponding amido-complexes of Co(III) are unknown in the solid state. Their formation in solution was demonstrated by heavy water exchange process [7]:

$$[Co(NH_3)_6]^{3+} \rightarrow [Co(NH_3)_5NH_2]^{2+} + H^+$$

$$[Co(NH_3)_5NH_2]^{2+} + HDO \rightarrow [Co(NH_3)_5(NH_2D)]^{3+} + OH^-$$

It was observed, that in the case of the $[Co(NH_3)_x(H_2O)_y]^{3+}$ derivatives the acidic character of the complexes increases parallel with the number of the coordinated water molecules [8]. Analogous deprotonation processes were also mentioned in the case of some dimethylglyoximino cobalt(III) complexes. Chugaev et al. [9,10] found that the action of NaOH upon the $[Co(DH)_2(pyridine)_2]Cl$ do not lead to the formation of a strong monoacidic complex base. The reaction product is a sparingly soluble anhydrobase:

$$[Co(DH)_2(Py)_2]Cl + OH^- \rightarrow [Co(DH)_2(Py)_2]OH \rightarrow [Co(D_2H)(Py)_2] + H_2O$$

The electric conductivity measurements prove also the nonelectrolytic character of this substance.

---

* *Faculty of Chemistry, Babeş-Bolyai University, Cluj-Napoca, Romania*

** *Dept. of Nat. Sciences and Mathematics, Transylvanian Museum Association, Cluj-Napoca, Romania. (Sponsored by he Soros Foundation)*

Some anhydrobases $[Co(D_2H)(Py)_2]$ were obtained by Ablov [11] and Nakatsuka et al. [12] (Am = NH_3, naphtylamine).

It was observed the recombination of the starting binary salt by solvation in diluted acides.

The situation is more complicated in the case of mixed bis-dimethylglyoximato-aqua-complexes. Here the deprotonation can take place in two ways, e.g.:

$$[Co(DH)_2(H_2O)_2]^+ \rightarrow [Co(DH)_2(H_2O)(OH)] + H^+ \qquad (I)$$

or

$$[Co(DH)_2(H_2O)_2]^+ \rightarrow [Co(D_2H)(H_2O)_2] + H^+ \qquad (II)$$

The spectrophotometric measurements in acidic and basic media plead for the reaction (I). Analogous phenomenon can be observed also in the case of trans-$[Co(en)_2(H_2O)_2]^+$ [13]. Birk et al. [14] presume that the deprotonation in alkaline media is a general process for all complexes of the type $[Co(DH)_2XY]^n$. By total reversible precesses the alkaline solutions of the complexes of this type regain their original spectral characteristics after acidulation (e.g. $[Co(DH)_2(NO_2)_2]^-$, $[Co(DH)_2Py]Br$, etc.).

These authors determined from spectrophotometric data the kinetic parameters of the mentioned reversible reactions. It was observed, that the positiv charge of complexes, e.g. $[Co(DH)_2(NH_3)_2]^+$ increases the rate of the proton release as compared to that of the negative charged anions (e.g. $[Co(DH)_2(NO_2)_2]^-$).

In this paper the deprotonation equilibrium of some $[Co(DH)_2(amine)_2]X$ and $M[Co(DH)_2Y_2](M = H, Na, K)$ type complexes was studied spectrophotometrically in a wide pH-range.

Results and discussions. The complexes were obtained by the classical air oxidation of the components (CoX_2, DH_2, amine) in dil. alcoholic solutions. The amine components were aromatic amines and amino-phenols. From the anions halides (Cl^-, Br^-), acetate and pseudohalides (CN^-, NCS^-, $NCSe^-$) were used for the synthesis. In the latter case only the $[Co(DH)_2(CN)_2]^-$ was used for the equilibrium measurements because insoluble $[Co(DH)_2(H_2O)(NCS)]$ and $[Co(DH)_2(H_2O)(NCSe)]$ are formed at higher pH values.

The spectral measurements were made in aqueous (dil. methanolic) solutions in the presence of Britton-Robinson buffer solutions.

In the case of the $[Co(DH)_2(amine)_2]^+$ derivatives the following successive equilibria can be supposed:

$$\underset{a}{[Co(DH_2)_2(amine_2]^{3+}} \underset{H^+}{\rightleftarrows} \underset{b}{[Co(DH_2)(DH)(amine)_2]^{2+}} \underset{H^+}{\rightleftharpoons} \underset{c}{[Co(DH)_2(amine)_2]^+} \underset{H^+}{\rightleftharpoons}$$

$$\underset{H^+}{\rightleftarrows} \underset{d}{[Co(D)(DH)(amine)_2]} \underset{H^+}{\rightleftarrows} \underset{e}{[Co(D)_2(amine)_2]^-}$$

In strong acidic media the partial or total destruction of Co-Dioximin ring system occurs, especially at higher temperatures. In strong basic solutions analogous phenomenon can be presumed with simultaneous exchange of the amine ligands. In our experimental conditions the protolytic equilibria between the b, c and d forms can be taken into account. The proton release from these chelates is a reversible process, as shown by the spectral changes as function of the pH value of the solutions. By total reversible processes the UV spectra show two isobestic points at 245—250 and 263 nm, in agreement with the existence of two complex forms with significant absorption properties in the above mentioned spectral range. By acidulation of the alkaline solutions the spectra regain their original forms.

Ablov et al. [15, 16] observed in some cases modifications in the spectral data after reacidulation, probably due to an irreversible aquation process:

$$[Co(D)(DH)(amine)_2] + H_2O \rightleftarrows [Co(D)(DH)(amine)(H_2O)] + amine$$

One can presume that the proton release from the hydrogen bridge takes place according to the reaction:

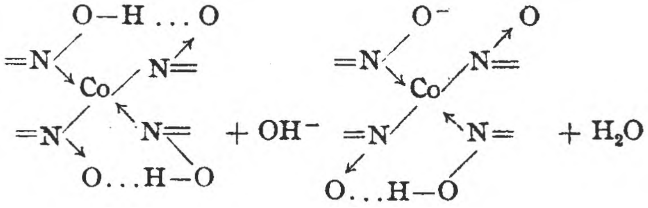

[17]

Eigen et al. [18] found that the value of the rate constant of the proton transfer reactions between —N—H and —O—H donors and OH^- is situated aproximatelly at $10^9 - 10^{11}\ M^{-1} \cdot s^{-1}$. This process takes place much slower when the donor group is protected by intramolecular hydrogen bridge

$$\begin{aligned}(\text{e.g. } & O{-}H..N + OH^- - k = 4 \cdot 10^{-5} - 4.10^{-6}\ M^{-1} \cdot s^{-1}\\ & O{-}H..O + OH^- - k = 7 \cdot 10^{-7} - 7 \cdot 10^{-8}\ M^{-1} \cdot s^{-1}).\end{aligned}$$

Steric factors and electrical charge of the atomic group influence also the rate constants values of the above reaction.

The spectra recorded at different pH values showed a pH dependence at certain wave lengths, corresponding to absorption bands either of the protonated AH form, or of the deprotonated A form. As an exemple, the electronic spectra of the $[Co(DH)_2(m\text{-aminophenol})_2]Br$ at various pH values were represented in Fig. 1.

In some cases the extinction values (E) obtained in the pH range of the pH dependence of the spectrum allowed us to derive the acidity constant of the protonated form. For this purpose, at the corresponding wave length the extinction in strong acidic media (E_a) and in strong basic media (E_b) was determined. By using our spectral data, the acidity constant K_a could be obtained by means of the following formula:

$$pK_a = pH_b + \lg\frac{E - E_b}{E_a - E},$$

where E stands for the extinction at pH value of the buffer solution (pH_b).

The mean value of pK_a derived from several pH_b — E pairs, recorded at the wave lenghts indicated, are presented in Table 1.

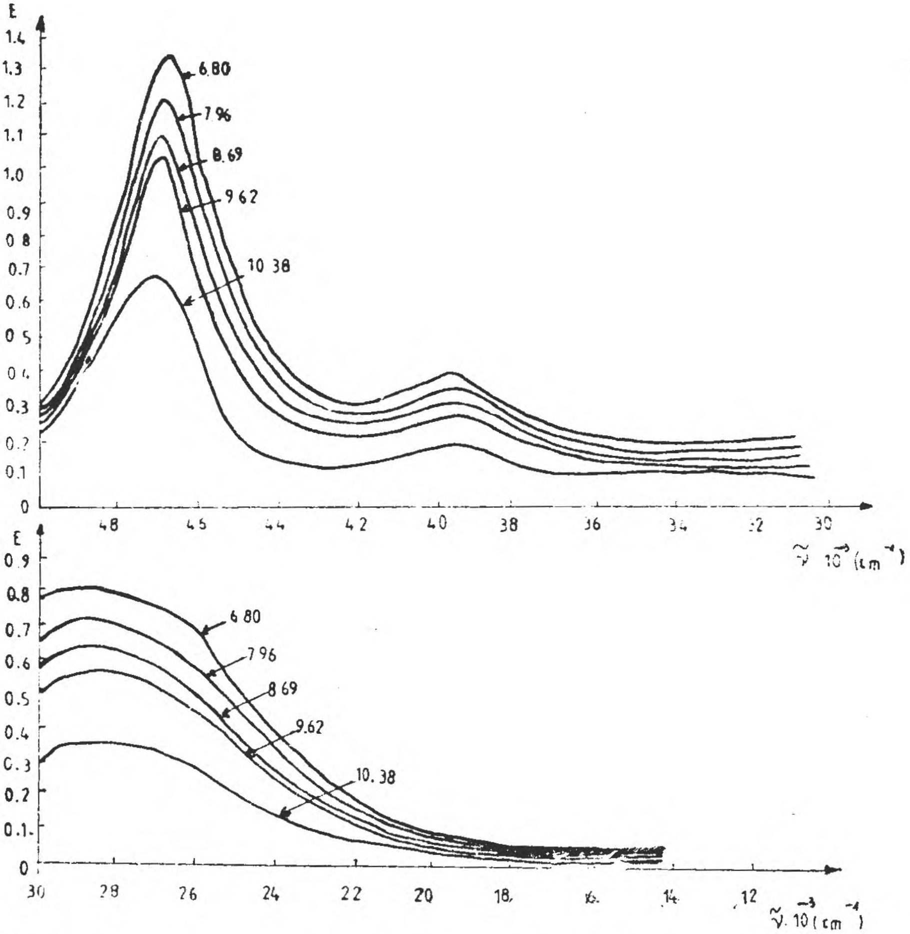

Fig. 1. Electronic spectra of the [Co(DH)$_2$(m-aminophenol)$_2$]Br at various pH values

Table **1**

Acidity constants from spectrophotometric data

Complex	Wave lengths	pK$_a$
[Co(DH)$_2$(o-tol)$_2$]Br	371	9.33
[Co(DH)$_2$(o-anis)$_2$]Br	209, 250, 407	9.42
[Co(DH)$_2$(m-aminophenol)$_2$]Br	214, 253, 358	9.25
[Co(DH)$_2$(H$_2$O)$_2$]NO$_3$	263	6.37

Obviously, in the case of the first 3 complexes the deprotonation reaction consists of the release of the proton establishing one of the hydrogen bridges. With the last complex, the leaving proton belongs to one of the co-ordinated water molecules.

Experimental. The synthesis of the $[Co(DH)_2(amine)_2]X$ ($X = Cl, Br$) type complexes is described in our earlier paper [19, 20].

The spectrophotometric measurements were carried out with a "SPECORD" (Germany) recording spectrophotometer (Carl Zeiss Jena). Dilutions: visible region: $1-2 \times 10^{-3}$ M complex + + 5 ml Britton-Robinson solution in 50 ml volum (UV region: $10^{-4}-10^{-5}$ M complex/l).

REFERENCES

1. J. N. Brönsted, D. Volquartz, *Z. physik. Chem.*, **134**, 97 (1928).
2. L. A. Chugaev, *Z. anorg. allg. Chem.*, **137**, 1, 401 (1924).
3. L. A. Chugaev, *Compt. rend.*, **160**, 840 (1915); **161**, 699 (1915).
4. A. Grinberg, . Faerman, *Z. anorg. allg. Chem.*, **193**, 193 (1930).
5. A. Grinberg, *Z. anorg. allg. Chem.*, **138**, 333 (1924).
6. A. Grinberg, H. J. Hildenhersel, *Izv. Akad. Nauk SSSR.*, **5**, 479 (1948).
7. Anderson, Briscoe, Spoor, *J. Chem. Soc.*, **1943**, 361.
8. J. N. Brönsted, J. King, *Z. physik. Chem.*, **130**, 699 (1927).
9. L. A. Chugaev, *Ber. dtsch. chem. Ges.*, **39**, 2692 (1906).
10. L. A. Chugaev, A. Postnikov, *Zhur. Russ. Khim. Obsch.*, **42**, 1466 (1910).
11. A. V. Ablov, *Zhur. neorg. Khim.*, **3**, 1118 (1958).
12. Y. Nakatsuka, H. Iinuma, *Bull Chem. Soc. Japan*, **11**, 48 (1936).
13. C. J. Hawkins, A. M. Sargeson, G. H. Searle, *Austr. J. Chem.*, **17**, 598 (1964).
14. J. P. Birk, P. Boon Chock, J. Halpern, *J. Amer. Chem. Soc.*, **90**, 6959 (1968).
15. A. V. Ablov, M. P. Filippov, *Zhur. neorg. Khim.*, **5**, 2717 (1960); **7**, 1021 (1962).
16. A. V. Ablov, B. A. Bovikhim, N. M. Samush, *Zhur. neorg. Khim.*, **11**, 1832 (1966).
17. J. Jamano, J. Masuda, K. Shinra, *Inorg. Nucl. Chem. Lett.*, **4**, 581 (1968).
18. M. Eigen, W. Kruse, G. Maass, L. D. Maeyer, *Progr. Reaction Kinetics*, **2**, 285 (1964).
19. R. Ripan, Cs. Várhelyi, B. Böhm, *Stud. Univ. Babeş-Bolyai*, Ser. Chem., **8** (1), 113 (1963).
20. R. Ripan, Cs. Várhelyi, J. Urmosi, Acad. RPR. *Studii şi Cercet. Chim.*, Fil. Cluj. **14** (2), 215 (1963).

STUDIA UNIV. BABEŞ-BOLYAI, CHEMIA, XXXIX, 1–2, 1994

THE POLYOXOMETALIC KRYPTATE $Na_{27}[NaAs_4W_{40}O_{140}]$ AS COORDINATIVE LIGAND FOR Th(IV)

AUGUSTIN CURTICĂPEAN*, ALEXANDRU BOTAR*, MARIANA RUSU**

ABSTRACT. The polyoxometalic kryptate $Na_{27}[NaAs_4W_{40}O_{140}]$, because of its special coordinative capacity, could coordinate, after chemical reactions, the Th(IV) cation, resulting a complex with the formula $Na_{19}[NaAs_4W_{40}O_{140}Th_2]$. After it was synthezised, this complex was analyzed from different points of view, to make the characterization of the compound. So, by conductometry was determined the ratio ligand/cation, and the crystalized compound was studied by IR and UV-VIS spectroscopy, and of course, by thermogravimetry. The relation between the data obtained through all these analysis has showed that the formula of the obtained complex is $Na_{19}[NaAs_4W_{40}O_{140}Th_2]\cdot 59H_2O$, and structuraly speaking, the thorium is coordinated by two secundary active sites of the ligand.

Introduction. The polyoxometalates are a class of inorganic complexes, with special properties and characteristics, being different from the most part of the inorganic compounds. The distinguishing elements of this class of compounds are: [1]

— the particular polycondensed structure, with multiple properties of combination between different oxoions.

— the synthesis take place in aqueous solution, the condensation ratio being very large, corresponding to the work conditions (pH, concentrations, temperature)

— the solubility of these compounds is big, not like the one of the oxides or mixed oxides.

A special group from this class of compounds, are the kryptates, which have moleculare weights and volumes very big, and special coordinative capacities for the transitional cations.

One of these polyoxometalates, is $Na_{27}[NaAs_4W_{40}O_{140}]$, which present the following structural characteristics:

a) is formed by polycondensation of four subunits AsW_9 linked together by four WO_6 octahedra [2, 3].

b) each subunit has three triplets W_3O_{13} of WO_6 octahedra, condensed around the arsenic tetrahedron [4, 5].

c) because of the condensation, results five active sites, one of them is kryptand, in the core of the molecule and it coordinates one alcaline cation (Na^+, K^+, etc.) and the other four are secondary, placed neer to the central one (fig. 1 and fig. 2).

d) has coordinative capacity in the secondary active sites, for different transitional cations [6, 7].

---

* *Institute of Chemistry Cluj-Napoca*

** *„Babeş-Bolyai" University, Faculty of Chemistry Cluj-Napoca*

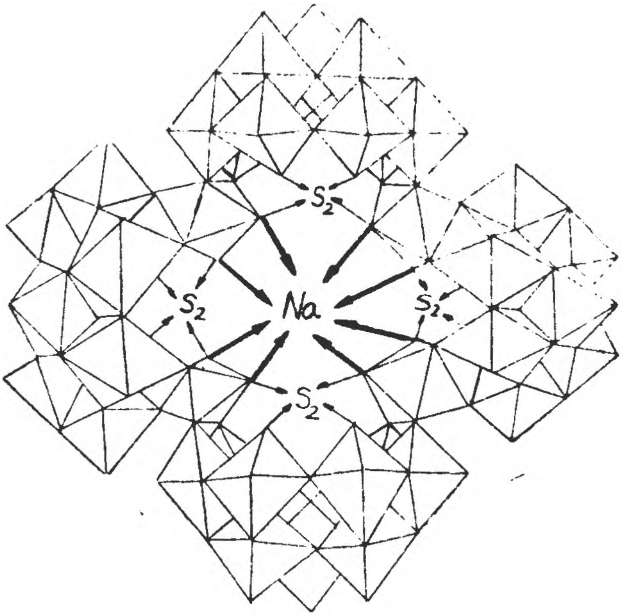

Fig. 1 — The polyhedric model of the polyoxometalic ligand $Na_{27}[NaAs_4W_{40}O_{140}]$

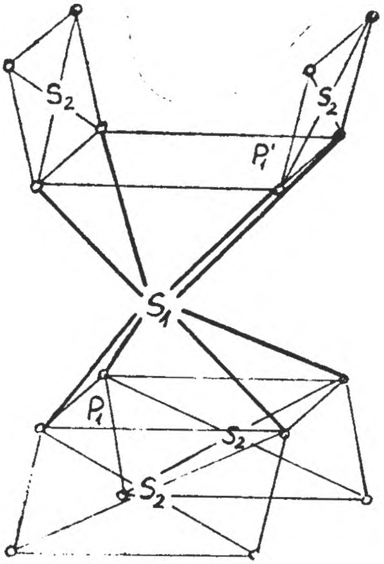

Fig. 2 — The view in space of the active sites of the ligand

As could be seen from fig. 2, the secondary active sites are simetricaly placed two by two to the kryptand site, and they are not in the same plane, fact which make be possible the octacoordination of the Th(IV) cation.

Experimental.

— The synthesis of the thorium complex was made by adding the stoichiometric necessary soluble thorium compound, that means 0,552 g $Th(NO_3)_4 \cdot 4H_2O$. The thorium nitrate is solved in 5 ml distiled water, the pH on the solution is 1, so it must be correlated in the synthesis. Then, a weight of 11,4 g of $Na_{27}[Na\ As_4W_{40}O_{140}] \cdot 46H_2O$ is solved in 100 ml distiled hot water (70—80°C), and the pH is established at 5. In the hot ligand solution is added very showly and carefuly the thorium nitrate solution, mentaining constant the temperature and a corresponding stiring. It could be observed that the reactio it occurs very slowly, and biger adding of thorium nitrate could give the hidrolization of the thorium.

$$Na_{27}[NaAs_4W_{40}O_{140}] + 2Th(NO_3)_4 - Na_{19}[NaAs_4W_{40}O_{140}Th_2] + 8NaNO_3$$

Finaly, the complex crystalize from the solution in white crystals.

— The ratio of combination was determined by conductometry, by titration of 10^{-3} M solution of ligand with a $2 \cdot 10^{-3}$ M solution of thorium nitrate. The conductibility data were determined with an Radelkis conductivity meter in 25 ml cuve having platinum electrodes.

— The thermogravimetrical analysis was made between 20—650°C, whitout maintaining in isotherme conditions, for a sample of 200 mg.

— With the UV-VIS and IR spectra were distinguished more aspects concerning the new compound. So, it could be observed that the structure of the polytungstic edifice remain the same after thorium coordination, but there are small movings of the absorbtion bands. The UV-VIS spectra were recorded on aqueous solutions havind 10^{-4} M concentrations, with an SPECORD UV-VIS spectrophotometer having automatic recording, and the IR spectrum was recorded with an Carl Zeiss Jena spectrophotometer on KBr plates.

Results and discussions. The chemical reaction was written after the determination of combination ratio by conductometry. This titration was made using 10^{-3} M solution of ligand and $2 \cdot 10^{-3}$ M solution of thorium nitrate. The data obtained are listed in table 1, and the values were reprezented grafically (fig. 3) for the conductivity as a function of volume adding ($1/R = f_{(v)}$). It could be observed that the cross point of the two lines with different angles is corresponding for the ratio ligand/cation = 1/2.

Table 1

The values of conductometry measurements

V(ml)	1/R(mS)	V(ml)	1/R(mS)	V(ml)	1/R(mS)
0	12,0	4,0	25,2	8,0	31,8
0,5	14,3	4,5	26,1	8,5	32,5
1,0	16,2	5,0	27,1	9,0	33,0
1,5	17,8	5,5	28,1	9,5	33,3
2,0	20,0	6,0	29,0	10,0	33,9
2,5	21,5	6,5	29,6	10,5	34,3
3,0	22,9	7,0	30,4	11,0	34,8
3,5	24,1	7,5	31,0	11,5	35,2

The thermogravimetrical analysis made on 200 mg of compound, is presented in fig. 4, and the curves are:
— curve 1 — TG; — curve 2 — DTG; — curve 3 — DTA; — curve 4 — T.

On the first curve which is representing the lost in weight, could be seen that the decreasing of the compound weight is 9%, this phenomenon being observed between 50 and 450°C. This lost is representing the crystalization water-59 molecules. The water losing in just one step is the results of the thorium coordination in the secondary active sites.

On the DTG curve it could be seen two important phenomenon, at 130°C an endo, coresponding to the water losing and at 490°C an exothermic phenomenon corresponding to the breaking of polytungstic edifice and new bonds formation.

By UV absorbtion spectra recordings of the 10^{-4} M aqueous solutions of the ligand and complex, if could be observed that the maximum values recorded are almost the same in ligand and complex. The small moving being determined by the thorium coordination (fig. 5.). So, the maximum for W = O, from

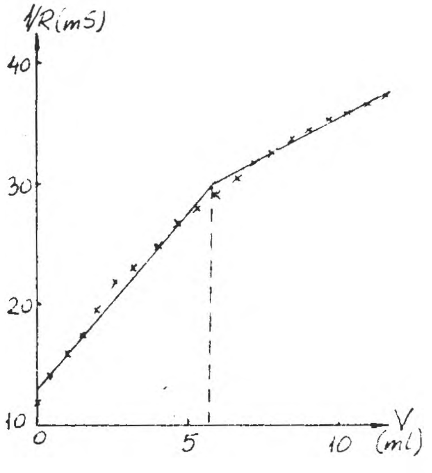

Fig. 3 — The conductometric titration of the ligand with $Th(NO_3)_4$

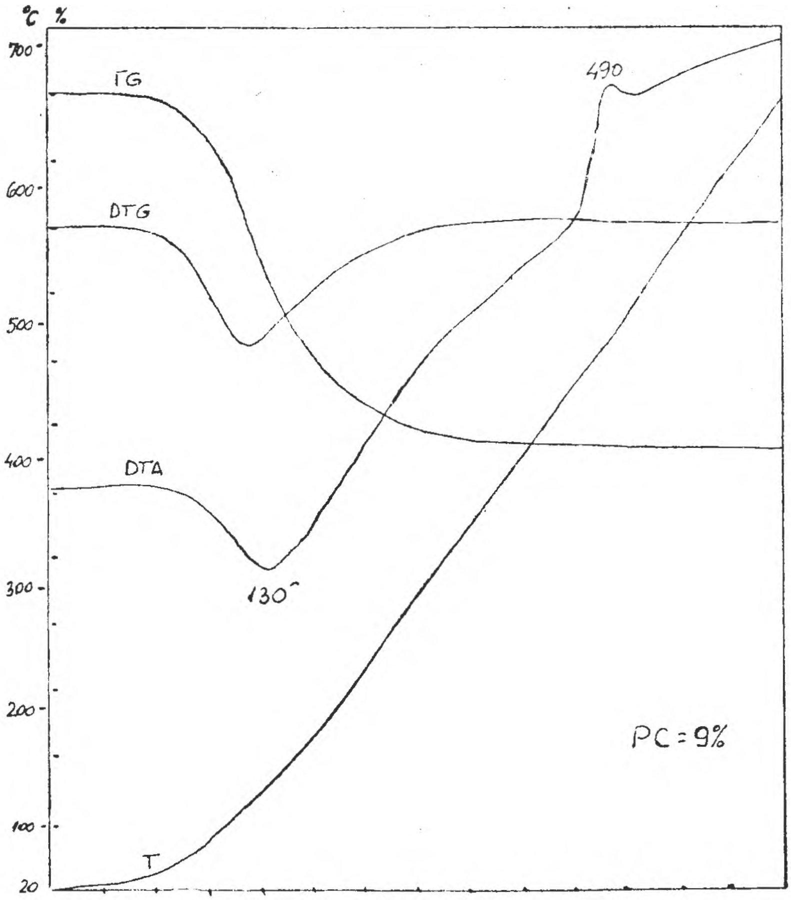

Fig. 4 — The thermic analysis of the complex $Na_{19}[NaAs_4W_{40}O_{140}Th_2] \cdot 59H_2O$

215 nm (46512 cm^{-1}) of the ligand if moves at 212 nm (47170 cm^{-1}) for the thorium complex. This effect is explained by the bonding of terminal W = O bonds to coordinate the Th(IV) cation. In the same time, the broad band for the electronic tranzitions triatomic bonds W—O—W from 240 to 260 nm (41667 and 38462 cm^{-1}) it is found between 250 and 280 nm (40000 and 35715 cm^{-1}).

In the visible spectra of radiation, neither the ligand or the complex present absorption maximum.

But, in IR field, the recorded spectrum (fig. 6) confirms that the structure of the polytungstic edifice is the same in ligand and complex, the absorption bands corresponding to the types of bonds from ligand, the small movings being determined by the thorium coordination.

The values of the absorption maximum of the vibrational spectra and the corresponding bonds are listed in table 2.

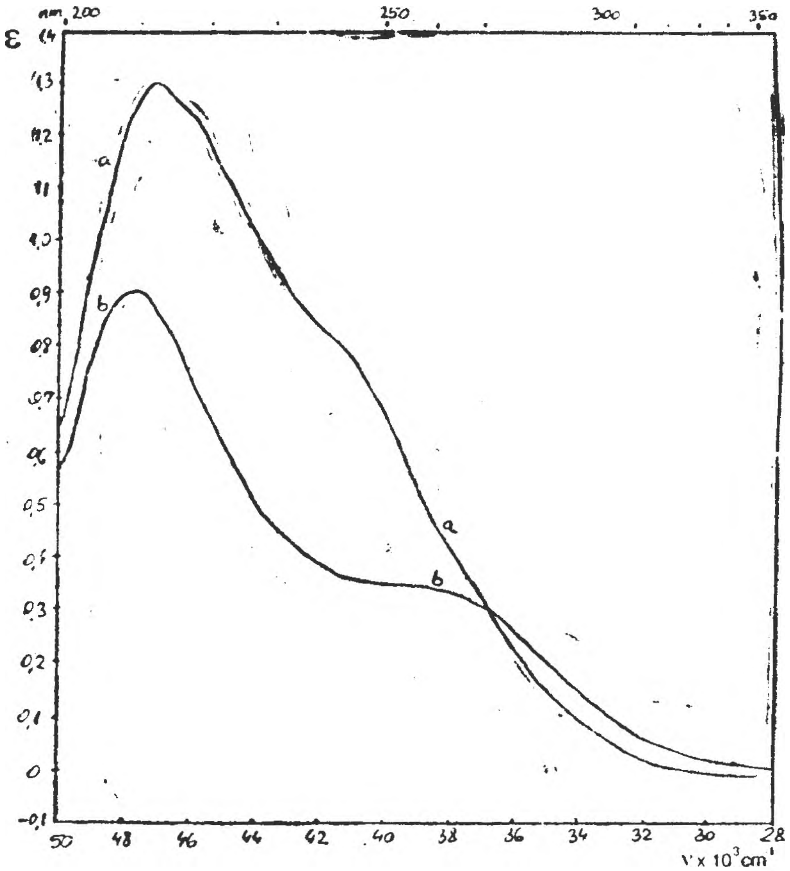

Fig. 5 — The UV spectra for — a — ligand $Na_{28}[NaAs_4W_{40}O_{140}]$ ($c = 10^{-4}$M) — b — complex $Na_{19}[NaAs_4W_{40}O_{140}Th_2]$

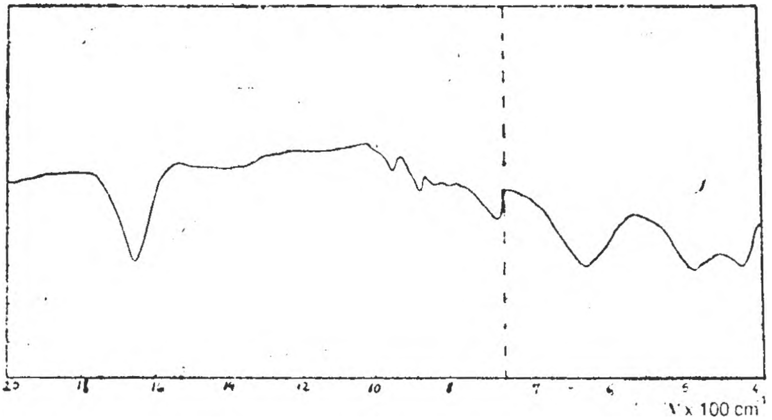

Fig. 6 — The IR spectrum of the complex $Na_{19}[NaAs_4W_{40}O_{140}Th_2]$

Table 2

The maximum values of the IR spectra of the ligand and the complex with Th, and the corresponding bonds

$Na_{27}[NaAs_4W_{40}O_{140}]$	$Na_{19}[NaAs_4W_{40}O_{140}Th_2]$	Atrib.
510 (m, b)	480 (m, b)	$\delta As-O$
625 (m, b)	660 (m, b)	$\delta W-O_a-W$
720 (s, b)	720 (m, b)	$\nu_{as} As-O$
810 (s, sp)	840 (m, b)	$\nu_{as} W-O_b-W$
890 (s, b)	895 (s, b)	$\nu_{as} W-O_c-W$
960 (s, sp)	965 (s, b)	$\nu_{as} W=O_d$
1650 (vs, sp)	1660 (vs, sp)	$\delta H-O-H$

The analysis which were done, offer important data for the interpretation, and there are few relevant aspect concerning the coordination way of the thorium cation by the kryptate ligand.

It could be seen that the ligand structure is the same after the thorium coordination, except the small movings determined by octacoordination of thorium. So, one Th(IV) cation is coordinated by eight oxygen atoms from two different secondary active sites (fig. 7).

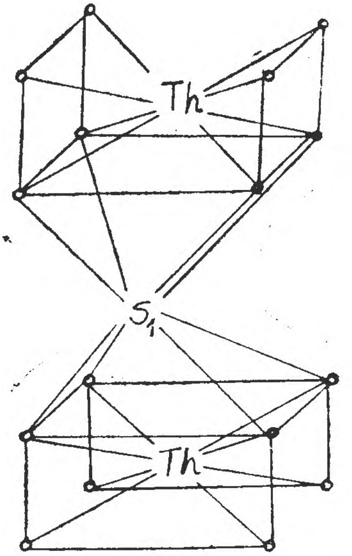

Fig. 7 – The octacoordination of the thorium cation by the polyoxometalic ligand.

Conclusions: 1) It was obtained by direct synthesis the polyoxometalic complex $Na_{19}[NaAs_4W_{40}O_{140}Th_2]$.

2) The conductometry showed that the combination ratio is ligand/cation = 1/2, that conffirm our proposed formula.

3) The spectrophotometric study for UV and IR fields, conffirm the complex formation whitout modifyind the structure of the polytungstic edifice of the ligand.

4) By octacoordination of the thorium cation, this one is bonded by two different secondary active sites (S_2) determining the small movings of the terminal oxygen atoms.

REFERENCES

1. M. T. Pope, *"Heteropoly and Isopoly Oxometalates"*, Springer-Verlag, Berlin, Haidelberg, New-York, Tokyo, 1983.
2. Y. Jeannin, J. Martin-Frére, *J. Inorg. Chem.*, 1979, **18**, 3010–15.
3. Y. Jeannin, J. Martin-Frére, *J. Am. Chem. Soc.*, 1981, **103**, 1664–69.

4. K. Womiya, M. Miwa, *Polyhedron*, 1985, **4**, 89–97.
5. K. Womiya, M. Miwa, *Polyhedron*, 1985, **4**, 1407–15.
6. M. Leyrie, G. Hérvé, A. Tézé, Y. Jeannin, *Inorg. Chem.*, 1979, **19**, 1746–9.
7. M. Leyrie, G. Hérvé, *Nouv. J. Chim.*, 1978, **2**(3), 233–38.
8. G. M. Varga, E. Papaconstantinou, M. T. Pope, *Inorg. Chem.*, 1970, **9**, 662–8.
9. V. I. Spitsyn, E. A. Torchenova, I. P. Kazanskii, P. Baidala, *Zhur. Neorg. Khim.*, 1974, **1**, 1–9.

STUDIA UNIV. BABEŞ-BOLYAI, CHEMIA, XXXIX, 1–2, 1994

NEW POLYOXOMETALATES CONTAINING Sb(III) AND U(IV)

ENIKŐ TOMA*, AUGUSTIN CURTICĂPEAN*, ALEXANDRU BOTAR*,
MARIANA RUSU**

ABSTRACT. The compound $Na_{18}[NaSb_9W_{21}O_{86}]$ which falls under the large category of polyoxometalates shows outstanding properties, among which the coordinative capacity is the most striking. Thus, owing to its molecular structure, it presents several coordinative sites to which different cations of the transition metals can be coordinated.

After being synthesized, the complex with uranium $Na_6[NaSb_9W_{21}O_{86}U_3]$ crystallized as brownish crystals and afterwards it was subjected to a set of chemical analyses (photocolorimetry, IR, UV–VIS spectra and thermogravimetric analysis) in order to be characterized.

As a result of the analyses performed, the combination ratio cation/ligand= = 3 and the octahedral coordination of the cation U(IV) have been demonstrated.

Introduction. The class of polyoxometalates has been enriched with new types of compounds which have aroused a great interest due to their structural peculiarities and to their applicability in various fields, especially in biology where their activity is of almost importance. Thus, polyoxometalates containing Sb as heteroatom in their molecule, exhibit peculiar physico-chemical properties on account of the pair of significantly active free electrons belonging to the heteroelement.

It is common knowledge that the obtaining of polyoxotungstates is strictly dependent on a few factors which exert a considerable influence [1]:

a) the pH of the synthesis medium represents a factor which greatly influences the condensation ratios of the oxoions;

b) the temperature of the reaction medium;

c) as the syntheses are carried out in solutions the nature of the solvents is a very important factor;

d) the concentrations of the reagents.

Particulary, polyoxotungstates containing Sb are found in a fairly wide range of polycondensation ratios, which proves their numerous possibilities of combination. Out of the polyoxotungstates with Sb, the compound $Na_{18}[NaSb_9W_{21}O_{86}]$ draws special attention because it manifests some supplementary features, besides the properties characteristic of this class, namely, a remarkable coordinative capacity (it is capable to coordinate 6 metallic to one ligand molecule) and also an uncommon biological activity due to its peculiar structure [2–6].

Studies have been undertaken on the structure of this vast inorganic compound and as a results it has been found that it consists of three subunits SbW_7O_{24} formed by the condensation of seven octahedra WO_6 around the tetrahedron of

---

* *Institute of Chemistry Cluj-Napoca*
** *Babeş-Bolyai University, Faculty of Chemistry Cluj-Napoca*

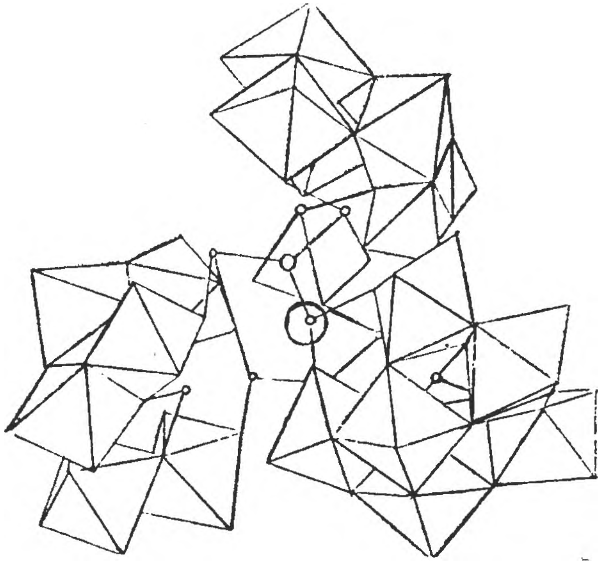

Fig. 1. The polyhedral structural pattern of the ligand polyoxotungstate.

Sb heteroatom, these subunits are bound by two Sb_3O_7 group, the overall symetry of the molecule begin D_{3h} (fig. 1 and fig. 2).

From Fig. 1 can observe that the molecule is a trigonal assembly with the sodium cation occupying the central site. The subunits of SbW_7 are derived from a saturated molecule with β-Keggin structure by removal of five octahedra of WO_6 (a triplet W_3O_{13} and one octahedron from two different triplets). Each SbW_7 subunit is bound to both groups of Sb_3O_7 by two bridging oxygen bonds.

Owing to this polycondensation in the molecule, seven active sites make their occurence, one of them being central and occupied by an alkaline cation (Na^+, K^+, etc) whereas the other six are disposed by twos towards the three SbW_7 subunits. These secondary active sites have identical properties thus permitting the coordination of six metallic ions. When the volume and the electric charge of the cations have increased values, the coordinative capacity is reduced to 3.

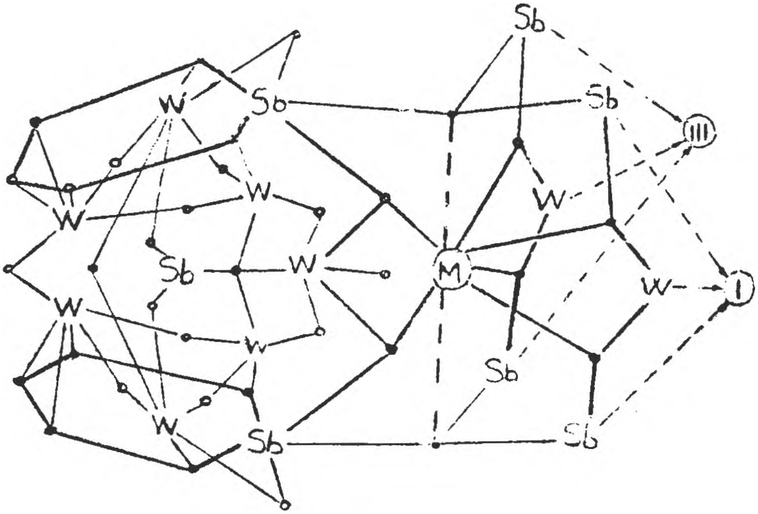

Fig. 2. The schematic reprezentation of a Sb_3W_7 subunit.

This statement is supported by the coordination of U(IV) cations which results in the formation of the complex polyoxotungstate with the formula $Na_6[NaSb_9W_{21}O_{86}U_3]$.

Experimental Part: — The synthesis of the complex with Uranium was carried out by adding a corresponding amount of $U(SO_4)_2$ to 7,1 g ligand polyoxotungstate $Na_{18}[NaSb_9W_{21}O_{86}]$. The solution of uranium sulphate is added to the ligand solution (100 ml distilled water in which 7,1 ligand is dissolved) cautiously, on heat (70—80°C) with slight stirring in order to maintain the pH of the solution at 7,5. The reaction is completed rather slowly that is why the reagents are added dropwise.

$$Na_{18}[NaSb_9W_{21}O_{86}] + 3U(SO_4)_2 \rightarrow Na_6[NaSb_9W_{21}O_{86}U_3] + 6Na_2SO_4$$

After the solution charges its colour to dark-brown, it is cooled until it crystallizes as the uranium complex with brown colour.

— The combination ratio was determined by means of the photocolorimetric titration; it was established that three cations of U(IV) are necesary to one molecule of ligand polyoxotungstate.

— The thermogram of the complex was recorded in the range 20—650°C without maintenance in isothermal conditions, for a sample of 900 mg.

— UV—VIS and IR spectra put into evidence the absorption maxima characteristic of the metal-oxygen bands within this category of compounds, thus proving that the structure of the polyoxotungstic edifice remains unchanged, undergraded by the coordination of U(IV) cations. UV—VIS spectra were registered by s SPECORD UV—VIS spectrophotometer on solutions of concentrations $5 \cdot 10^{-5}$M (in the UV domain) and $5 \cdot 10^{-3}$ M (in visibil) respectively whereas IR spectra were registered by a Carl-Zeiss-Jena spectrophotometer on KBr pellets.

Results and discussion. The study of the formation of the complex polyoxometalates with U(IV) has been performed by photocolorimetric titration thus measuring the extinction of the absorption maximum at 211 nm (47393 cm^{-1}) — specific to the complex.

Measurement of the extinctions have been made for several samples containing 10 ml ligand solution with the titer $T_1 = 7{,}32 \cdot 10^{-4}$ by adding variable amounts of $U(SO_4)_2$ solution with the titer $T = 1{,}97 \cdot 10^{-4}$.

According to the reaction stoichiometry, the ratio cation/ligand = 3/1, hence the theoretical value of the equivalence point can be calculated. Afterwards, the theoretical volume, of 3,675 was determined. Table 1 renders the values of the extinctions measured for increased values of the added uranium solution.

Table 1

Values of the extinctions measured for increased values of the added uranium solution

ml. U^{4+}add/10 ml Sb_9W_{21}	$\varepsilon \cdot 10^5$
0	0,840
1,0	0,955
2,0	1,110
2,5	1,185
3,0	1,220
3,5	1,300
4,0	1,390
4,5	1,395
5,0	1,390
6,0	1,380
7,0	1,380
8,0	1,385

By plotting the extinctions of the previously measured solutions on the volume of the added uranium sulphate solution, two semistraight lines are obtained which cross in the equivalence point equal to 3,85 ml. (fig. 3).

UV and VIS Spectra of $Na_6[NaSb_9W_{21}O_{86}U_3)]$

UV electronic absorption spectra have been registered on aqueous solutions having the value $c = 5 \cdot 10^{-5}$ M in the ligand or complex.

It is worth noticing that the UV spectrum of the complex $Na_6[NaSb_9W_{21}O_{86}U_3]$ is quite similar to the spectrum of the ligand Sb_9W_{21}, but the UV spectrum of the complex presents a maximum slightly less intense ($\varepsilon = 1{,}085$) than that of the ligand ($\varepsilon = 1{,}18$) and displaced towards higher energies (lower $\lambda = 211$), versus the ligand ($\lambda = 213$ nm).

The blurring and shift of the maximum, in the complex with uranium, towards higher energies can be explained by the formation of U—O bond with the oxygen from the terminal W = O groups in the ligand and also by the strengthening of the other W = O bonds which take no part in the formation of U—O bond.

The absorption spectrum in visible, registered on aqueous solutions having the value $c = 5.10^{-3}$ in the complex, exhibits absorption spectra characteristic of the configuration f^2 or octahedrally coordinated U(IV). By analysing the spectrum it is obvious that the band L from 15128 cm^{-1} is well resolved as compared to the bands O and R from 17762 and 20243 cm^{-1} respectivelly, which are weaker.

By comparing the M ions with electronic structure f with those with electronic structure d, it is evident that even the spin forbidden transitions are easily resolved, here in this case band O.

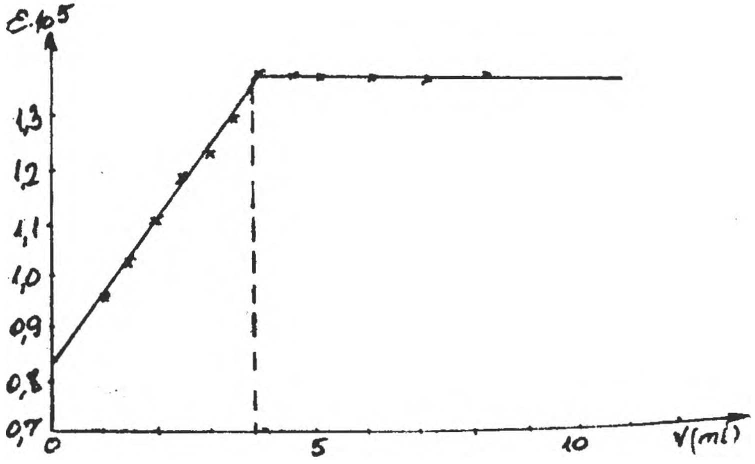

Fig. 3. The plot of the dependence of the solution extinction as a result of the photocolorimetric titration.

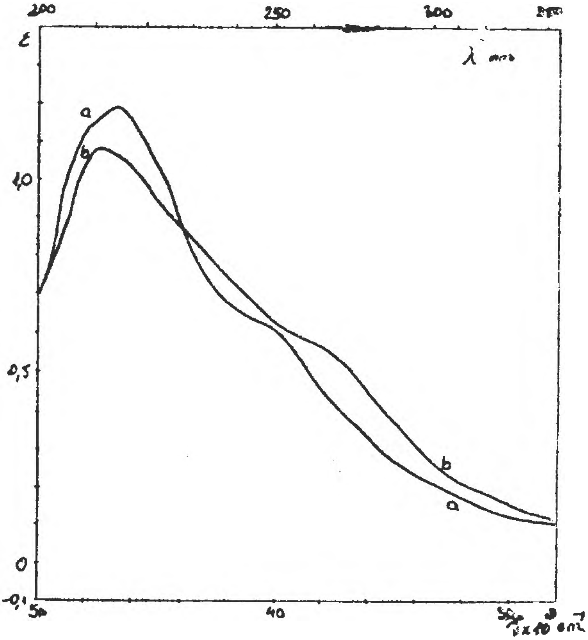

F i g. 4. UV Spectra of a) the ligand b) the complex with U(IV).

The bands L, O and R are generated by the inner transitions taking place among the orbitals f of uranium, in the case of the present spectrum the bands U and W remain unresolved because of the charge transfer from U(IV) to W(VI).

The IR vibrational absorption spectrum confirms the maintenance of the polyoxotungstic edifice as a result of the coordination of U cations, the absorbtion maxima being only slightly shifted because of the uranium influence.

Table 3 renders the recording of IR spectrum the values of the absorption maxima as well as their assignments.

The thermogravimetric analysis has been completed for a sample of 900 mg, the thermogram being rendered in Fig. 4. On the curve of weight loss (TG, one can observe that the decrease in the mass of the complex is 7,5%, the phenomenon taking place within a temperature range of 100—400°C. This weight loss corresponds to the elimination of 32 molecules of crystallization water. The process of dehydration develops in one stage only owing to the coordination of U(IV) cation in the secondary active sites of the ligand.

On the thermodifferential curve (DTA) two phenomena become apparent, more precisely, at 130°C a caloric absorption process (endothermal, corresponding to the dehidration stage is developed, whereas at 440°C a caloric release process (exothermal) takes place which represents the effect of the degradation of polytungstic edifice and the formation of new bands (fig. 7).

The data provided by the analyses confirm the coordination of three U(IV) cations to one molecule of polyoxometallic ligand with no further significant mo-

Table 2

The Electronic transitions of the $Na_6[NaSb_9W_{21}O_{86}U_3]$ compound spectra

Band	$\tilde{\nu}$ in cm⁻¹	λ in nm	Electron transitions
L	15128	661	${}^3H_4 \rightarrow {}^3P_0$
O	17762	563	${}^3H_4 \rightarrow {}^1D_4({}^1G_4)$
R	20243	494	${}^3H_4 \rightarrow {}^3P_1$

Table 3

Infrared absorptions of $Na_6[NaSb_9W_{21}O_{86}U_3]$

assignt	$\tilde{\nu}(cm^{-1})$
$\delta H-O-H$	1630
$\nu_{as}U-O$	1160
$\nu_{as}W=O$	940
$\nu_{as}W-O_{(c)}-W$	830
$\nu_{as}W-O_{(b)}-W$	760
$\nu_{as}Sb-O$	580
	540

dification in the structural pattern of the polytungstic edifice; the way in which uranium is coordinated has been put into evidence by VIS spectra which demonstrated that U(IV) is octahedrally coordinated.

Conclusions. 1) A new polyoxotungstate has been synthesized by coordinating U(IV) cations to the ligand $Na_{18}[NaSb_9W_{21}O_{86}]$.

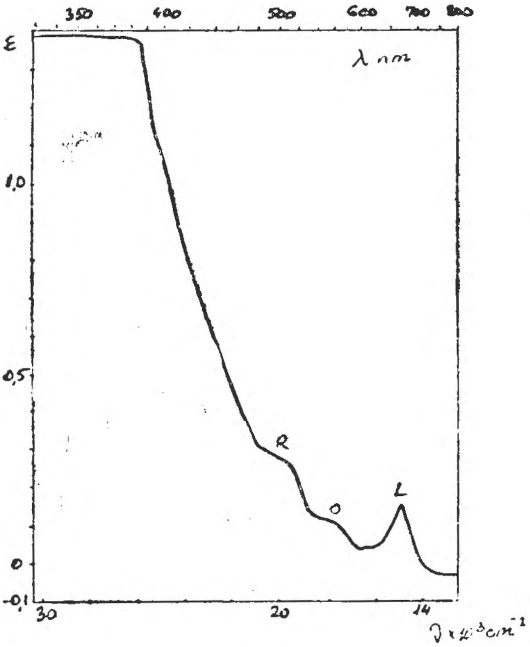

Fig. 5. VIS Spectrum of the complex with U(IV).

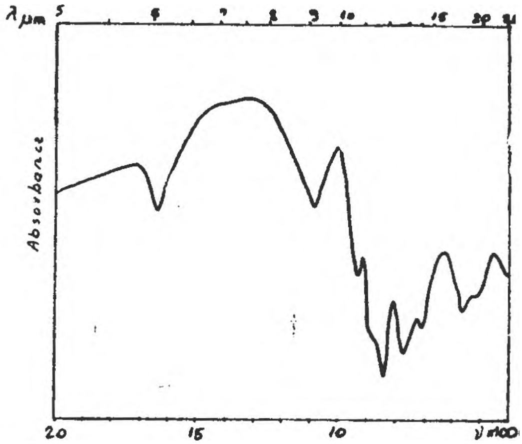

Fig. 6. IR Spectrum of the complex polyo tungstate.

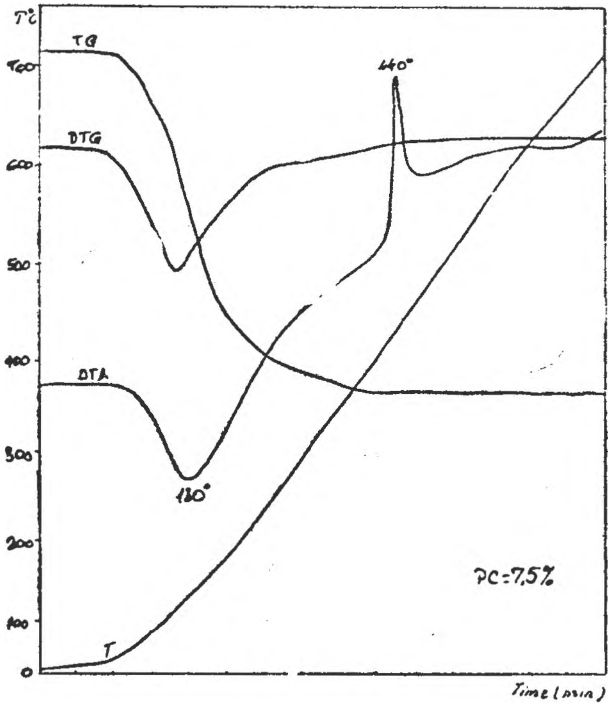

Fig. 7. The thermogram of the complex polyoxotungstate curves.

2) The photocolorimetric titration demonstrates the coordination of three U(IV) cations to one ligand molecule, thus confirming the postulated formula $Na_6[NaSb_9W_{21}O_{86}U_3]$.

3) The recordings of UV—VIS and IR spectra reveal the formation of the complex polyoxotungstate the maintenance of the polycondensed structure of the polyoxotungstate as well as the octahedral coordination of uranium.

4) The thermal analysis points out that the complex polyoxotungstate crystallizes as a crystallohydrate with 32 molecules of crystallization water.

REFERENCES

1. M. T. Pope, *Heteropoly and Isopoly Oxometalates*, Springer-Verlag, Berlin, Heidelberg, New, York, Tokyo, 1983.
2. R. G. Finke, B. Rapko, T. J. R. Weakley, *Inorg. Chem.*, 1989, **28** (**8**), 1573—9.
3. P. W. Carr, E. H. Smith, S. R. Betso, R. H. Callicoti, *Termochim. Acta* 1976, **15**, 105—10.
4. G. H. Werner, C. Jasmin, J. C. Chermann, *J. Gen. Virology*, 1976, **31**, 59—66
5. O. Glemser, K. H. Tyfko, *Z. Naturforsch* 1969, **24b**, 648—52.
6. F. Bussereau, *Ann. Inst. Pasteur Virol.*, 1986, 1374—391.

STUDIA UNIV. BABEŞ-BOLYAI, CHEMIA, XXXIX, 1-2, 1994

A STUDY ON THE FORMATION OF ANTIMONY AND BISMUTH POLYOXOMETALATES WITH U(IV)

M. RUSU*, E. TOMA**, A. BOTAR**

ABSTRACT. The chemical reactions between the uranium ions and polyoxometallic anions $SbW_{11}O_{38}H^{6-}$ and $BiW_{11}O_{38}H^{6-}$ respectively, have been studied by the method of electrophoresis with the aim at establishing the optimum stability and pH range of complex formation and calculating the stability constants of the formed polyoxometallic complexes. By applying the molar ratio method to photocolorimetry, the combination ratio of polyoxometallic ligands and U(IV) ions has been found to have the value of 2:1 for this ratio.

Introduction. Previously, we reported that U(IV) ion can give polyoxometalates of UL_2 type, where L is $PW_{11}O_{39}^{7-}$, $SiW_{11}O_{39}^{8-}$, $BW_{11}O_{39}^{8-}$, $P_2W_{17}O_{61}^{10-}$ and $As_2W_{17}O_{61}^{10-}$ [1].

The present paper reports our results concerning the formation in solution of U(IV) polyoxometalates with ligands of the type $SbW_{11}O_{38}H^{6-}$ and $BiW_{11}O_{38}H^{6-}$ respectively, by the method of paper electophoresis which permits the identification of the formed polyoxometalates in very limiting pH ranges, thus enabling them to separate in the electric field due to the different electrophoretic mobilities of the existing ionic species [2].

One of the largely used method in establishing the stoichiometry of the formation reactions of the complex combinations is the method of the molar ratio variation applied to the photocolorimetric study [3, 4, 5]. This method. has been also applied to the systems U(IV) — $SbW_{11}O_{38}H^{6-}$ and U(IV) — — $BiW_{11}O_{38}H^{6-}$ in order to establish the value of the combination ratio between U(IV) ion and polyoxometallic ligands with Sb and Bi.

Experimental Part.

1. *Electrophoretic Study.* The experiments were carried out in media of polyoxometalates of type $Na_6[SbW_{11}O_{38}H] \cdot 18H_2O$ and $Na_6[BiW_{11}O_{38}H] \cdot 14H_2O$ prepared according to [6] 9f 10^{-2} M concentrations in the ligand, at pH values ranging from 2 to 8,5. The pH was adjusted with HCl and NaOH solutions and their values were measured on a OK — 102 Radelkis pH-meter. The ionic strength was maintained at constant value by a corresponding addition of $NaClO_4$ 10^{-1} M.

Use was made of an ordinary electrophoresis apparatus, at usual voltage, cooled with water. The $U(SO_4)_2$ solution, of 10^{-2} M concentration was deposited with a micropipette in the center of Karl-Schneider Schull chromatographic paper imbibed in the ligand solutions with different pH. Experiments were performed at a difference in voltage of 360 V, at a temperature of 15 ± 2°C, for 3600 s. The formed polyoxometalates were identified by their brownish coloration, the U(IV) ion was identified by developing with a $K_4[Fe(CN)_6]$, and the uncomplexing ligand by reduction with UV radiations.

Besides the solutions containing the metallic cation, a glucose drop was added, electrically neutral, towards which the shifts of the ionic species after electromigration were adjusted. The Rf values of the formed polyoxometalates were determined by the ascending paper chromatography, relating the shift of the formed chemical species to the front of the saturated NaCl eluent.

---

* *Faculty of Chemistry, Univ. „Babeş-Bolyai" Cluj-Napoca*

** *Institute of Chemistry, Cluj-Napoca*

2. *Photocolorimetric Study.* The following polyoxometallic ligands $Na_8[SbW_{11}O_{38}H] \cdot 18H_2O$ and $Na_6[BiW_{11}O_{38}H] \cdot 14H_2O$ were used to preparing aqueous solutions of 10^{-2} M concentrations in the ligand. To these solutions different volumes of $U(SO_4)_2$ 10^{-2} M obtained from $UO_2(CH_3COO)_2$ in solutions strongly acidulated with H_2SO_4 and reduced with amalgamated zinc [7] were added to obtain different mole ratios.

The pH of the solutions was adjusted to the value of 4,5 with NaOH 10^{-1} M and HCl 10^{-1} M respectively, in order to be within the optimum pH range of the formation of U(IV) polyoxometalates.

The extinctions of the sets of solutions with different mole ratios (ion U(IV)-polyoxometallic ligand) were measured on a φEK–KM spectrophotometer, by using a green filter and a vat of 1 cm.

Results and discussion. The formation of U(IV) polyoxometalates in the studied systems takes place according to some chemical reactions, which are likely to appear, and can be rendered by the equations:

1. $2Na_6[SbW_{11}O_{38}H] + U(SO_4)_2 = Na_8[U(SbW_{11}O_{38}H)_2] + 2Na_2SO_4$

2. $2Na_6[BiW_{11}O_{38}H] + U(SO_4)_2 = Na_8[U(BiW_{11}O_{38}H)_2] + 2Na_2SO_4$

The displacement in centimetres of the formed polyoxometalates was followed experimentally, thus allowing the calculation of the electrophoretic mobilities (μ), the determination of Rf values and the calculation of the real μ_d mobilities of the formed species by means of the Kunkel-Tiselius relation [8]:

$$\mu_d = d\,\frac{1}{V.t.Rf}\left(\frac{l'}{l}\right)^2$$

where: μ_d = the sum of the experimentally determined electrophoretic mobilities;
d = the migration of the ionic species in cm;
V = difference of potential;
t = time of electromigration;
l = the length of the chromatographic paper (38,5 cm);
$\frac{l'}{l}$ = 1,69, the porosity factor of the chromatographic paper;
Rf = Rf values, 0,99 for $Na_8[U(SbW_{11}O_{38}H)_2]$ and 0,98 for $Na_8[U(BiW_{11}O_{38}H)_2]$.

The migration of the ionic species and the sum of the electrophoretic mobilities depending on pH are shown in Tables 1 and 2.

On the basis of the values given in Table 1. and Table 2. the variation of the sum of the electrophoretic mobilities depending on pH is plotted.

In case the formation equations of the complex polyoxometalates (relationship 1 and 2) are put down under the general form of an equilibrium equation:

$$U + 2L \rightleftarrows UL_2$$

the sum of the electrophoretic mobilities of the species present in the system, in our case, is rendered through the relation:

$$\mu = \frac{\mu_U^{4+} \cdot [U^{4+}] + \mu_{UL_2}[UL_2]}{[U^{4+}] + [UL_2]}$$

Table 1

The migration and the sum of the electrophoretic mobilities in the system U(IV) — $SbW_{11}O_{36}H^{6-}$

pH	d(cm)	$\mu_d \cdot 10^{-6}$ cm^{2}V^{-1}S^{-1}
2,0	−0,86	−0,590
2,5	−0,78	−0,540
3,0	−0,60	−0,410
3,5	+0,06	−0,040
4,0	+0,86	+0,684
4,5	+1,78	+1,220
5,0	+2,36	+1,616
5,5	+2,70	+1,848
6,0	+2,90	+2,010
6,5	+2,08	+2,104
7,0	+2,32	+2,180
7,5	+2,49	+2,290
8,0	+2,41	+2,230

Table 2

The migration of the ionic species and the sum of the electrophoretic mobilities in the system U(IV) — $BiW_{11}O_{38}H^{5-}$

pH	d(cm)	$\mu_d \cdot 10^{-6}$ cm^{2}V^{-1}S^{-1}
2,0	−0,84	−0,670
2,5	−0,56	−0,440
3,0	−0,36	−0,280
3,5	+0,10	+0,082
4,0	+1,24	+0,990
4,5	+2,04	+1,620
5,0	+2,32	+1,850
5,5	+2,46	+1,960
6,0	+2,56	+2,045
6,5	+2,57	+2,050
7,0	+2,60	+2,080
7,5	+2,56	+2,040
8,0	+2,48	+1,960

MOTE: The values d and μ_d are noted with + or — depending on the direction of the ionic species towards the cathode or the anode.

where: μ = the sum of the electrophoretic mobilities;
$\mu_{U^{4+}}$, μ_{UL_2} = the electrophoretic mobilities of the ions in the species U^{4+} and UL_2;
$[U^{4+}]$, $[UL_2]$ = the mole concentrations of the ionic species U^{4+} and UL_2;

Since $\mu = \mu_{U^{4+}}$ for minimum μ, when the formation of the polyoxometalate UL_2 and $UL_2 = 0$ has not proceeded yet and $\mu = \mu_{UL_2}$ for maximum μ, when U^{4+} is totally lost and $U^{4+} = 0$, by extrapolating to the ordonate the minimum and maximum values of the sum of the electrophoretic mobilities, the values of the electrophoretic mobilities of the ionic species in the system can be obtained (see Table 3).

The formation domain of U(IV) polyoxometalates is correlated with their stability domain. Taking into account that the range within which a minimum of 90% of the U(IV) cation undergoes complexing in the polyoxometalates $[U(SbW_{11}O_{38}H)_2]^{-8}$ and $[U(BiW_{11}O_{38}H)_2]^{8-}$ respectively, the sum of the electrophoretic mobilities will be $\mu_{90\%} = 0{,}1\mu_U^{4+} + 0{,}9\mu_{UL_2}$.

The optimum formation range of the compounds was determined from the electrophoretic curves and corresponds to the pH range within which the sum of the electrophoretic mobilities is:

$$\mu_{formation} \geqslant 90\%$$

$\mu_{90\%}$ values and the optimum pH formation ranges of the formed polyoxometalates are given in Table 4.

In order to study the equilibrium and stability constants of the chemical reaction of formation, that is, of the formed polyoxometalates, the relationship belonging to R. Cousden, A. H. Gordon and A. P. Martin is applied to the systems under study [9].

$$\lg \frac{\mu_{gl} - \mu_U^{4+}}{\mu_{UL_2} - \mu_{gl}} = \lg K + \lg C$$

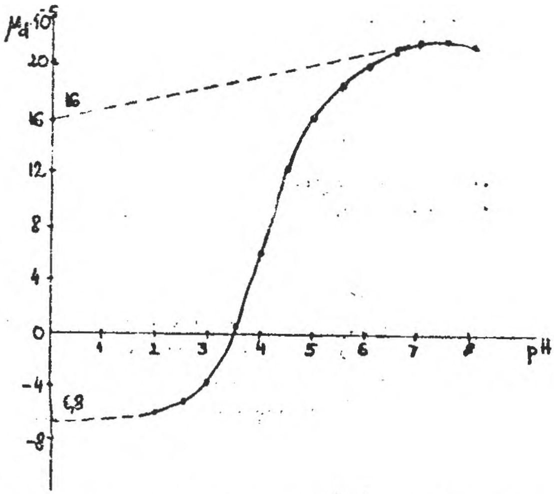

Fig. 2. The graphical representation of the sum of the electrophoretic mobilities μ_d depending on pH for the system $U^{4+} - BiW_{11}O_{38}H^{-6}$

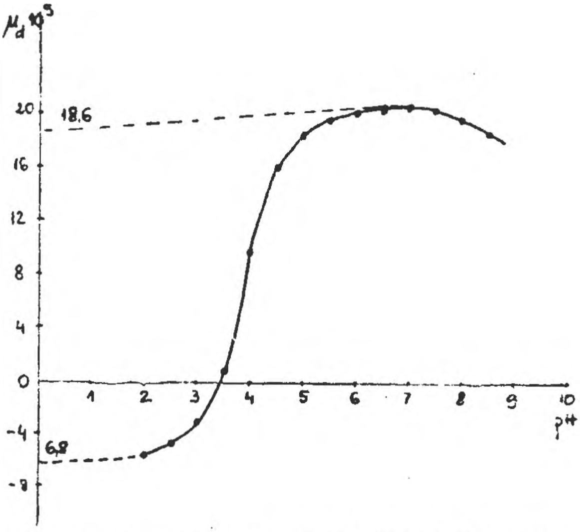

Fig. 1. The graphical representation of the sum of the electrophoretic mobilities μ_d depending on pH for the system $U^{4+} - SbW_{11}O_{38}H^{6-}$

Between the equilibrium constant K and the stability constant β there exists the relation:

$$\lg \beta = \lg K + \lg C$$

Table 3

The electrophoretic mobilities of the ionic species existing in the systems U^{4+} — $SbW_{11}O_{38}H^{6-}$ and U^{4+} — $BiW_{11}O_{38}H^{6-}$

Compound	$\mu_{UL_2} \cdot 10^{-5}$ ($cm^2 \cdot V^{-1}S^{-1}$)	$\mu_{gl} \cdot 10^{-6}$	$\mu_{U}^{4+} \cdot 10^{-5}$
Na $[U(SbW_{11}O_{38}H)_2]$	16,00	0,2965	−0,68
Na $[U(BiW_{11}O_{38}H)_2]$	18,60	0,4285	−0,62

Table 4

$\mu_{90\%}$ values and the optimum pH formation ranges of the polyoxometalates $Na_8[U(SbW_{11}O_{38}H)_2]$ and $Na_8[U(BiW_{11}O_{38}H)_2]$

Compound	$\mu_{90\%}$	the optimum pH formation range
$[U(SbW_{11}O_{38}H)_2]$	4,80	4,5—7,5
$[U(BiW_{11}O_{38}H)_2]$	4,70	4,5—7,0

where: C = the mole concentration of the polyoxometallic ligands;
$u_{UL_2, U^{4+}}$ = the mobilities of the ionic species existing in the system;
u_{gl} = glucose mobility;
K = the equilibrium constant
β = the stability constant

The data for the equilibrium and stability constants are to be found in Table 5.

Table 5

The equilibrium and stability constants for $Na_8[U(SbW_{11}O_{38}H)_2]$ and $Na_8[U(BiW_{11}O_{38}H)_2]$.

Compound	K	β
$Na_8[U(SbW_{11}O_{38}H)_2]$	$10^{1.655}$	$10^{3.655}$
$Na_8[U(BiW_{11}O_{38}H)_2]$	$10^{1.602}$	$10^{3.602}$

Provided that to the colourless diluted aqueous solutions of $10^{-2}M$ in the ligand polyoxometalates $Na_6[SbW_{11}OH_{88}]$ and $Na_6[BiW_{11}OH_{38}]$ are added dropwise solutions containing U(IV) cation, we have a good evidence for the immediate occurence of a brownish coloration, weaker in the first case and stronger in the case of the bismuth compound, owing to the formation of the uranium complex polyoxometalates, according to the chemical reactions (1) and (2). This fact allows the study in solution of the formation of uranium, antimony and bismuth polyoxometalates by the molar ratio method applied to photocolorimetry.

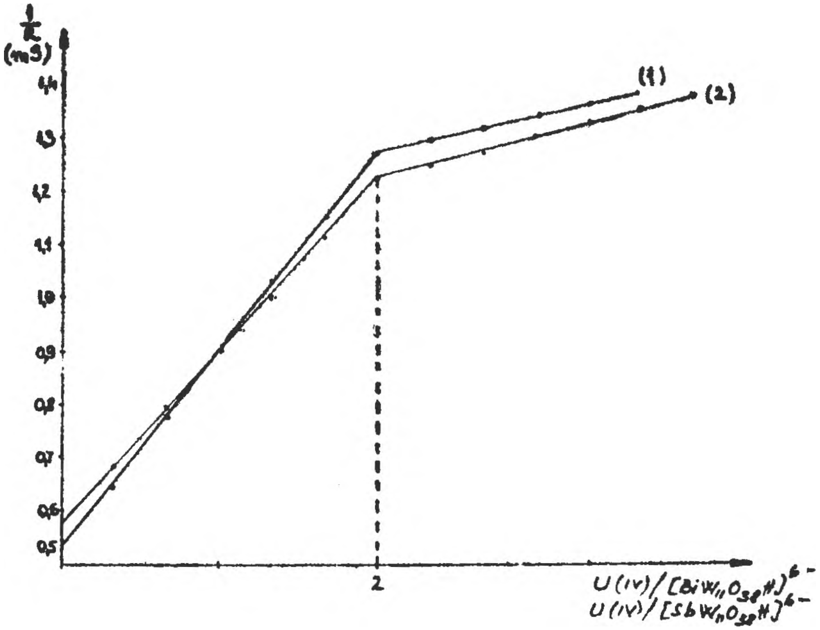

Fig. 3. The graphical representation of the variation of the extinction of the systems containing different molar ratios of the components:
1) $U^{4+} - SbW_{11}O_{38}H^{6-}$ 2) $U^{4+} - BiW_{11}O_{38}H^{6-}$

By plotting the variation of the extinction of the solutions obtained by mixing-up the reagents U^{4+}—$SbW_{11}O_{38}H^{6-}$ and U^{4+}—$BiW_{11}O_{38}H^{6-}$ respectively, depending on their molar ratio, the following curves, presented in Figure **3**, are obtained.

The photocolorimetric curves are made-up of two semi-straight lines which intersect in a point corresponding to a molar ratio polyoxometallic ligand: uranium = 2.

The extinction of the solutions increases to the equivalence point proportionally to the increase in the concentration of the reaction product and then it increases much lower.

The linear increase of the extinction with the increase of the combination molar ratio up to the equivalence point suggests the development of some chemical reactions of U(IV) ion addition to two ligand ions, resulting in the formation of UL_2 type complexes, whereas the unsignificant increase of the extinction after the equivalence point and the blurring of the samples, which need to be filtered before measuring the extinction, demonstrate the replacement of the sodium ions outside the coordination sphere of the polyoxometallic complexes with U(IV) ions as well as the formation of some brownish precipitates.

Conclusions. As a result of the electrophoretic study on the systems U^{4+}—$SbW_{11}O_{28}H^{6-}$ and U^{4+}—$BiW_{11}O_{38}H^{6-}$ respectively, by paper electrophoresis, there is clear-cut evidence of the formation, in every case, of a single pure complex polyoxometallic species.

The formation pH ranges of these compounds are to be found between 4,5—7,5 for $Na_8[U(SbW_{11}O_{38}H)_2]$ and 4,5—7,0 for $Na_8[U(BiW_{11}O_{38}H)_2]$. The approximate values of the electrophoretically determined stability constants are of $10^{3.6}$ order, which points out the formation of some stable complex polyoxometalates.

By the photocolorimetric study and the method of the variation of molar ratios, the formation, in both cases, of the compounds with the molar ratio metallic cation : polyoxometallic ligand = 1 : 2 has been established.

REFERENCES

1. M. Rusu, A. Botar and Gh. Marcu, *Rev. Roumaine Chim.*, **19**, 827 (1974).
2. G. Hervé, *Am. Chim.* (France), **6**, 219 (1971).
3. C. Tourné, G. Tourné, S. A. Malik and T. J. R. Weakley, *J. Inorg. Nucl. Chem.*, **32**, 3875 (1970).
4. R. D. Peacock and T. J. R. Weakley, *J. Chem. Soc. A*. 1836 (1971).
5. A. Botar and R. Ripan, **15**, 1577 (1970).
6. M. P. Souchay, M. Leroy, G. Hervé, C. R. Acad. Sc. Paris, **271**, 1337, (1970).
7. J. H. Kennedy, *Analyt. Chem.*, **32**, 150 (1960).
8. H. G. Kunkel and A. Tiselius, *J. Gen. Phisol*, **35**, 89 (1951).
9. R. Cousden, A. H. Gordon and A. P. Martin, *J. Biochim.*, **40**, 33 (1946).

STUDIA UNIV. BABEŞ-BOLYAI, CHEMIA, XXXIX 1-2, 1994

DETERMINATION OF DIFFUSION COEFFICIENTS OF SOME METALLIC CATION IN ION-EXCHANGE MEMBRANES

LIVIU ONICIU*, ADRIAN NICOARĂ*, CRISTINA CORĂBIAN*

ABSTRACT. Electrodialysis processes have been applied in an increasing number of industrial applications including chemical processing and treatment of industrial waste waters. The main parameter that describes the membrane ionic transport is the diffusion coefficient. The diffusion coefficients of Fe^{3+} and Fe^{2+} in 0.5 M H_2SO_4 and in a strong acid ion-exchange membrane, at 18 °C using cyclic voltammetry and hydrodynamic voltammetry have been determined using a membrane coated platinum electrode.

Introduction. The use of ion-exchange membranes is growing rapidly in the field of separations due especially to the development of the Nafion and other fluoropolymer membranes that have extremely good performance. Their use in electrodialysis processes have been applied to the production of the salt from sea water, desalination, chemical processing and treatment of industrial waste waters and others processes. Ion-exchange membranes differ from ion-exchange resins, in that ions selectively permeate exchange membranes by migrating from one side to the other side of the membrane under the influence of an applied electric field, rather then being absorbed as by resins [1, 2]. Due to the nature of this separation process, for estimate the electrodialysis performance is essentially to find the parameters of ionic transport. As it is shown in Nernst-Planck equation (1), the diffusion coefficient decides both diffusions (first) and migrating (second) terms of ionic flux transport.

$$N_j = -D_j \nabla C_j - D_j C_j \frac{z_j \mathcal{F}}{RT} \nabla \Phi + C_j V \tag{1}$$

If the convective velocity, V, of solution in membrane is extremely slow, it can be easily neglected the third, convective ionic membrane flux transport term. So, the main parameter that describe the membrane ionic transport is the diffusion coefficient of a particular ion in specified ion-exchange membrane. The aim of this paper is to find out the diffusion coefficient of Fe^{3+} and Fe^{2+} both in a sulphuric acid solution and in a strong acid cationic exchange membrane, produced by CCMMM Bucharest, immersed in sulphuric acid solution.

Theory. *Linear sweep cyclic voltammetry.* Linear sweep cyclic voltammetry consists of cycling the potential of an electrode, which is immersed in an unstirred solution, and measuring the resulting current. The applied potential to working electrode is a linear scan with a triangular waveform.

---

* *Babeş-Bolyai University, Faculty of Chemistry and Chemical Engineering, 11 Arany Janos, 3400 Cluj-Napoca*

The important parameters of a cyclic voltammogram are the magnitudes of anodic peak current, I_{pa}, cathodic peak current, I_{pc}, the anodic peak potential, E_{pa}, and the cathodic peak potential, E_{pc}.

A redox couple in which both species rapidty exchange electrons with the working electrode is termed as an electrochemically reversible couple. Other sufficient reversibility condition is that the electron's exchange rate is much greater than ion transport through solution.

The number of electrons transferred in the electrode reaction, z, for a reversible redox couple can be determined from the separation between the peak potentials:

$$\Delta E_p = E_{pa} - E_{pc} \cong \frac{0.059}{z} \; [V] \tag{2}$$

Thus, a one-electron process, such as examined electrochemical system, exhibits a ΔE_p of 0.059 V regardless scanning rate. Slow electron transfer at the electrode surface, for a less reversible system (quasireversible or even irreversible for very slow electron transfer), causes the peak separation to increase.

The peak current for a reversible system is described by the Randles-Sevcik equation for the forward sweep of the first cycle [3]:

$$I_p = 0.269 \cdot 10^5 \cdot z^{3/2} \cdot A \cdot D_0^{1/2} \cdot C_0^* \cdot \nu^{1/2} \tag{3}$$

where I_p is the peak current (A), z is electron stoichiometry, A is electrode area (cm^2), D is diffusion coefficient (cm^2/s), C is the concentration (mol/cm^3) and ν is the scan rate (V/s).

Values of I_{pa} and I_{pc} should be identical, or anyhow closer. Their ratio should not regard the scan rate excepting if there are chemical reactions coupled to the electrode process [4].

Hydrodynamic voltammetry. Hydrodynamic voltammetry is a method involving convective mass transport of reactants and products, and measurement of limiting current on i-E curves. The advantage of hydrodynamic methods is that a steady state is attained quicker and measurements can be made with high accuracy with less sophisticated device. In addition, due to the steady state regime, double-layer charging does not enter the measurement. The potential scan rate must be slow enough to ensure the steady state regime.

The important parameters of a hydrodynamic voltammogram are the limiting current density, i_{lim} and half-wave potential $E^{1/2}$.

The current density in the convective-diffusion control condition, at steady state, is:

$$i = z \cdot \mathcal{F} \cdot D_0^{2/3} \cdot \left(\frac{\partial C_0}{\partial x}\right)\Bigg|_{x=0} \tag{4}$$

where, under the limiting current conditions we obtain Levich equation after integration,

$$i_{lim} = 620 \cdot z \cdot \mathcal{F} \cdot D_0^{2/3} \cdot \nu^{-1/6} \cdot C_0^* \cdot \omega^{1/2} \tag{5}$$

where ν (cm^2/s) is the solution viscosity, ω (rad/s) is the angular velocity and C_0^* is the bulk concentration.

For membrane coated electrode, both ionic transports in membrane and solution must be taken in consideration [5]. In figure 1 the concentration profile is shown for the reactant (Fe^{2+}); C^*_{Fe2+} is the bulk concentration, C^m_{Fe2+} is the membrane-solution interface concentration and C^S_{Fe2+} is the platinum-solution interface concentration.

For ionic transport in solution, the current is given for pure diffusive control by:

$$i = \mathcal{F}\frac{D_{Fe^{2+}}}{\delta_S(\omega)}(C^*_{Fe^{2+}} - C^m_{Fe^{2+}}) \qquad (6)$$

where D_{Fe2+} is the diffusion coefficient in solution and $\delta_S(\omega)$ is the solution diffusion layer thickness given by:

$$\delta_S(\omega) = 1.61 \cdot D^{1/3}_{Fe^{2+}} \cdot \nu^{1/6} \cdot \omega^{-1/2} \qquad (7)$$

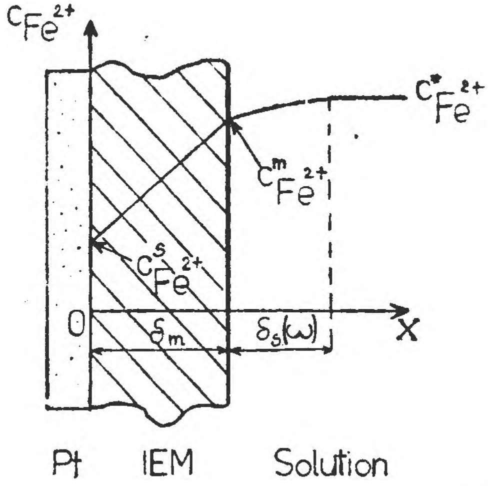

Fig. 1. The concentration profiles in membrane.

Also, for the ionic transport in membrane, the current density is given for pure diffusive control by:

$$i = \mathcal{F}\frac{D_{Fe^{2+},m}}{\delta_m}(C^m_{Fe^{2+}} - C^S_{Fe^{2+}}) \qquad (8)$$

where $D_{Fe2+,m}$ is the diffusion coefficient in membrane and δ_m is the membrane thickness.

The limiting current density expression of the membrane coated electrode is obtained if $C^S_{Fe2+} = 0$, and using last tree equations we obtained:

$$\frac{1}{i_{\lim}} = \frac{\delta_m}{\mathcal{F}D_{Fe^{2+},m}C^*_{Fe^{2+}}} + \frac{\nu^{1/6}}{0.62\mathcal{F}D_{Fe^{2+},s}C^*_{Fe^{2+}}}\omega^{-1/2} \qquad (9)$$

from where both in membrane and in solution diffusion coefficients can be calculated from $i^{-1}_{\lim}$ vs $\cdot\ \omega^{-1/2}$ plot.

Experimental. A conventional three-electrode cell equipped with a platinum counter electrode and a saturated calomel reference electrode was used. The working electrode was a platinum rotating electrode embedded in a Teflon holder and coated, or no, with an ion-exchange membrane layer In all cases the temperature was 18°C. The electrolyte solution was 0.005 M $FeSO_4$ and 0.5 M H_2SO_4 or only 0,5 M H_2SO_4 aqueous solution. The sulphuric acid had been used to assure the pure diffusion regime, both in solution and membrane, and to prevent the anodic oxygen evolution. Due to the chosen potential range, deoxygenation was not required because of the limited cathodic polarization that prevent the oxygen reduction.

The platinum electrode was mechanical polished with fine sand paper and rinsed in distilled water. The coated platinum electrode was obtained attaching a dry 0.1 mm membrane to the platinum electrode using a concentrate solution of same ion-exchange resins in N-methyl pyrolidone. Before any experiment, the membrane coated electrode was immersed overnight in the electrolyte solution. Special attention was taken for prevent the gas formation at this electrode, which can eventually obstruct the electrode. This technique gave reproducible results.

The used ion-exchange membranes, supplied by CCMMM Bucharest, were made from a strong acid cation-exchange, sulphonate poly-sulphone resin.

The measurements were made using a LP7e Laboratorni Pristroje Praha polarograph, a PS3 Forschungsinstitut potentiostat, in a classical tree electrode electrical draft, a manufactured rotating disk electrode and a XY recorder.

Results and discussion. The results of cyclical voltammetry using platinum electrode after subtracting the values obtained using the base electrolyte, are given in table 1.

Table 1

Values of peak current on platinum electrode

v [V/min]	I_{pa} [μA]	I_{pc} [μA]
0.1	2.14	1.765
0.2	3.025	2.515
0.4	4.082	3.36
0.75	5.51	4.62
1.2	6.46	5.62
1.5	7.1	6.09

Table 2 contains the results of cyclic voltammetry using membrane coated platinum electrode after subtracting the values obtained using the base electrolyte.

Table 2

Values of peak current on membrane coated platinum electrode.

v [V/min]	I_{pa} [μA]	I_{pc} [μA]
0.1	0.82	0.62
0.2	1.14	0.89
0.4	1.62	1.25
0.75	2.06	1.66
1.2	2.39	2.06

In figure 2 and 3 is shown the *I* vs. sqr(v) plot of platinum electrode and membrane coated platinum electrode. The validity of Randles-Sevcik equation is proved only at low scan rate, and is better for the membrane coated electrode due to a slower ion transport in ion-exchange membrane.

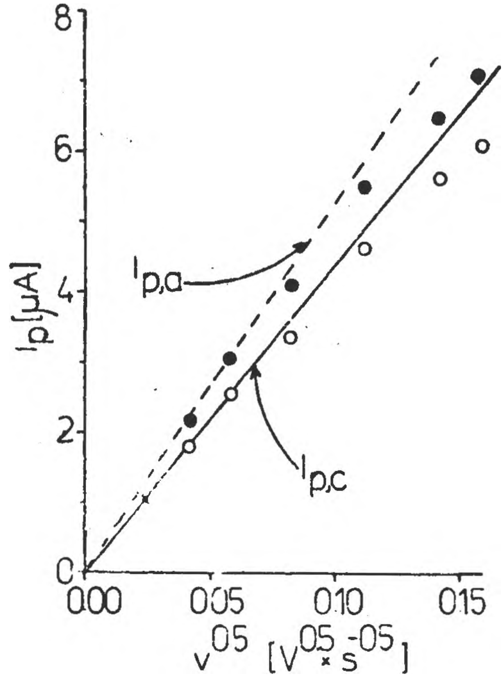

Fig. 2. Peak current magnitude vs. square root of scan rate obtained in cyclic voltammetry, using platinum electrode.

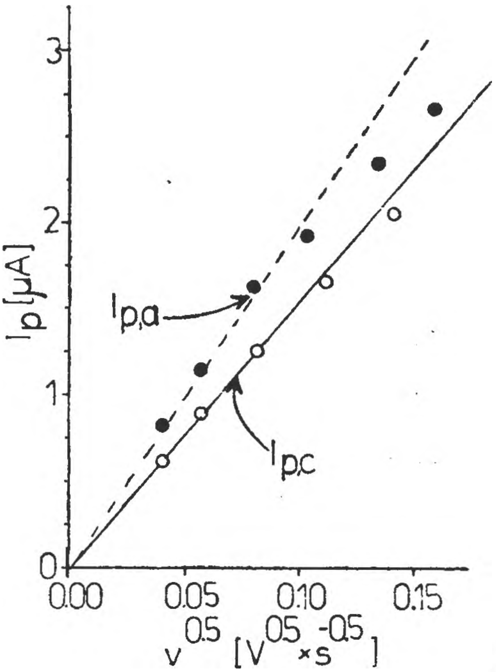

Fig. 3. Peak current magnitude vs. square root of scan rate obtained in cyclic voltammetry, using membrane coated platinum electrode.

The diffusion coefficients were calculated from the slope of the function I_p vs. sqr(v) using first three points, and their values are presented in table 5.

The experiments using rotating disk electrodes were carried out only in the anodic direction for avoiding the influence of reduction of oxygen.

Table 3

The dependence of limited current density on the rotating platinum electrode angular velocity

ω [s^{-1}]	i_{lim} [mA/cm²]
34.6	1.119
45.6	1.197
50.3	1.283
56.5	1.387
64.4	1.460
69.1	1.541
75.4	1.606

Table 4

The dependence of limited current density on the rotating membrane coated platinum electrode angular velocity

ω [s^{-1}]	i_{lim} [nA/cm²]
36.13	33
48.69	33.2
62.83	33.5
78.54	33.3
95.82	33.5
111.52	33.6
191.63	33.6

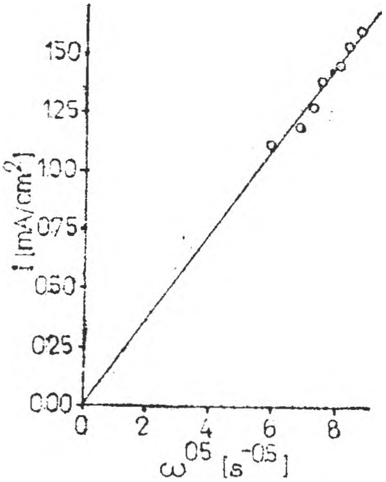

Fig. 4. Limited current density vs. square root angular velocity in hydrodynamic voltammetry, using platinum electrode.

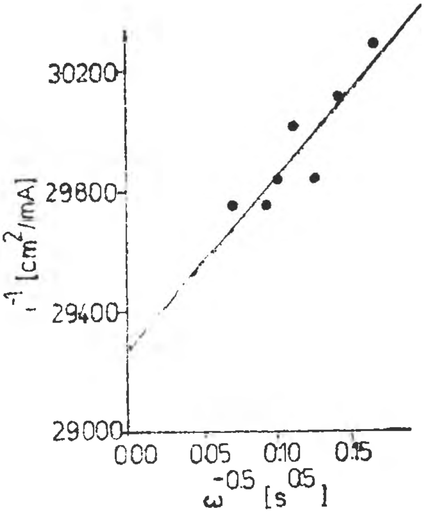

Fig. 5. Limited current density vs square root angular velocity in hydrodynamic voltammetry, using membrane coated platinum electrode.

The results of the rotating disk electrodes are presented in tables 3 and 4, and in figures 5 and 6 are the limited current vs. square root angular velocity, from were the diffusion coefficients have been calculated (table 5).

Table 5

Determined diffusion coefficients.

Investigation method	D_{Fe2+}*10⁶[cm²/s]		D_{Fe3+}*10⁶[cm²/s]	
	solution	membrane	solution	membrane
Cyclic voltammetry	4.89	0.706	3.51	0.438
Hydrodynamic voltammetry – Pt electrode	5.12	—	—	—
Hydrodynamic voltammetry – coated Pt electrode	4.35	0.728	—	—

Conclusions. The obtained diffusion coefficients in solution are close to the literature values. Excepting the value of solution diffusion coefficient determinated using membrane coated electrode, all the values had good accuracy. This could be explained by the poor ionic diffusion transport in ion-exchange membrane in a relative tick membrane, in which the ionic transport in solution even at low angular velocity is much faster than in membrane.

Also, the possible chemical coupled steps were not observed.

REFERENCES

1. V. Baltazar, G. B. Harris, C. W. White, *Hydromettalurgy*, **31**, 463 (1992).
2. P. Meares, *Membrane Separation Processes*, Elsevier, Amsterdam, 1976.
3. A. J. Bard, L. R. Faulkner, *Electrochemical Methods: Fundamentals and Applications*, Willey, New York, 1980.
4. R. S. Nicholson, *Anal. Chem.*, **37**, 1351 (1965).
5. E. H. Cwirko, R. G. Carbonell, *J. Membr. Sci.*, **67**, 211 (1992).

STUDIA UNIV. BABEŞ-BOLYAI, CHEMIA, XXXIX, 1–2, 1994

CONCENTRATION OF LEVELLING AGENTS AND LEVELLING EFFICIENCY IN LEAD ELECTROREFINING IN FLUOROSILICATE ELECTROLYTES

L. ONICIU, LIANA MUREŞAN, V. A. TOPAN, D. GHERŢOIU, LIDIA SZANTÓ

ABSTRACT. In order to appreciate cantitatively the quality of the lead cathodes obtained by electrorefining of impure lead in solutions containing hexafluorosilicic acid, lead hexafluorosilicate and different additives, a criterium based on the apparent density of the electrodes, is proposed. The existence of a maximum of apparent density — additives concentrations curves suggests that a certain ratio between the concentrations of the two tested additives (sodium lignin sulphonate and horse — chestnut extract) is necessary to ensure an optimum levelling of the cathodes.

1. **Introduction.** High purity lead (>99,99%) is produced almost exclusively by Betts process by electrorefining of impure lead (~98%) in a solution containing 60—100 gl^{-1} hexafluorosilicic acid and 30—270 gl^{-1} of lead and as fluorosilicate [1, 2].

To avoid dendritic growth of the cathodic deposit, various organic compounds acting as levelling agents are added to the electrolyte [3]. In the classical Betts process, the levelling agents are Ca or Na ligning sulphonate [LS] and animal glue [4].

In previous works, it was shown that an extract of horse chestnut (HCE) has a beneficial effect on the quality of the lead deposits, replacing successfully the animal glue [5, 6]. With the simultaneous presence of LS and HCE, the dendritic growth is totally suppressed, and the resulting smooth layers present characteristic morphologies [7].

It has also been shown that these two levelling agents increase the cathodic polarization and this inhibiting effect is particularly sensitive to electrolyte stirring [7]. Thus, the coverage with LS of the cathode decreases with the stirring rate, while the coverage with HCE increases with the stirring rate, mainly in the range of low cathodic overpotentials.

A reaction model of lead electrodeposition in the presence of LS alone and of LS-HCE mixtures was proposed [8, 9]. The synergism of the two organic compounds seems to result from their specific action during the different steps of the electrocrystallisation and from their opposite dependence on the electrolyte stirring. LS inhibits moderately the charge transfer reaction and blocks the quantity of active sites on the metal surface, while HCE inhibits strongly the charge transfer reaction and allows a moderate and controlled increase of the number of active sites due to a vanishing inhibition with increasing current.

The aim of the present work is to study the influence of LS and HCE concentration on the quality of the lead cathodic deposit and to correlate the result with the reaction model proposed previously [8, 9].

2. **Experimental.** The electrolyte used in all experiments was a solution of 80 gl^{-1} H_2SiF_6 and 80 gl^{-1} Pb^{2+} as $PbSiF_6$, prepared from pure chemicals dissolved in distilled water.

The experiments were carried out in a 4 l cell containing a sheet of pure lead as cathode and two anodes of impure lead, in a mechanical stirred electrolyte, and at a current density of 180 A m^{-2} (fig. 1).

Various concentration of LS at a constant concentration of HCE and various concentrations of HCE at constant concentrations of LS were used to obtain pure lead cathodes by electrolysis.

A set of polarisation curves in the absence and in the presence of different amounts of additives was drawn with a rotating disk working electrode made of titanium (S = 1,13 cm^2), a lead counter electrode and a saturated calomel reference electrode protected by a KNO_3 salt bridge. The electrode rotation speed was electronically maintained at 1200 rpm.

3. **Results and discussion.** A comparison between the different cathodes obtained in the electrorefining cell reveals that in the absence of any additive, the lead deposit is the worse, consisting of large nonuniform, crystals and being dendritic.

In the presence of LS alone as in the presence of HCE alone, the deposit becomes levelled but rough, displaying a structure built up of rounded polygonal aggregates, with bumpy edges.

Simultaneous use of LS and HCE leads to an improvement of the deposit quality, resulting in smaller crystals denoting a higher nucleation rate and a compact microstructure of the deposit. The aspect of the electrodes is influenced by the LS and HCE concentrations; the best was the electrodes obtained with 3 gl^{-1} LS and 2–3 gl^{-1} HCE (fig. 3).

In order to appreciate cantitatively the quality of the cathodes, a criterium based on the apparent density, ρ_{ap}, of the electrode was proposed. The apparent density may be calculated with the relation:

$$\rho_{ap} = \frac{m_{Pb}}{V_P - V_I} \qquad (1)$$

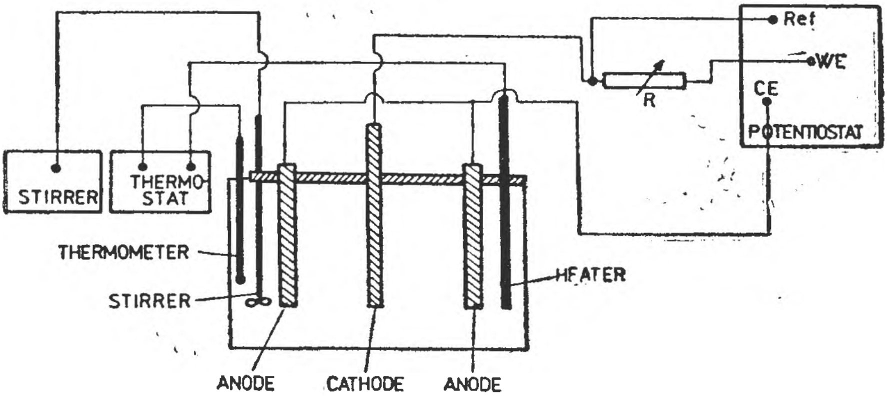

Fig. 1. Experimental device for lead electrorefining.

Fig. 2. Electrode obtained without additives (Pb^{2+} 80 gl^{-1}, H_2SiF_6 80 gl^{-1}, i = = 180 A·m^{-2}, t = 20°C, mechanical stirring).

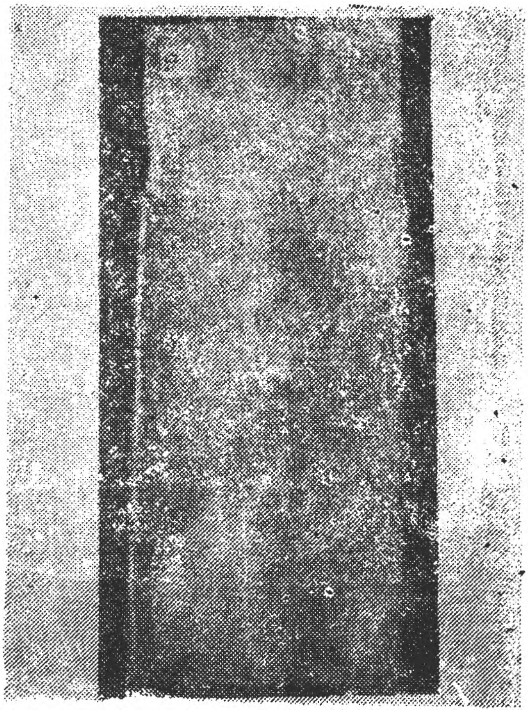

Fig. 3. Electrode with 3 gl^{-1} LS and 2 gl^{-1} HCE (mechanical stirring, t° = 20°C, i = 180 A · m^{-2})

where m_{Pb} is the deposited lead mass, V_p the volume of the parallelepiped in which the electrode may be inscripted and V_i the volume of the initial lead cathode.

Despite levelling is a characteristic of a microprofile and ρ_{ap} is a characteristic of a macroprofile, this criterium was used successfully for appreciate the quality of the cathodes. The grater the levelling of the deposit, the greater is the apparent density; the upper limit is 11.4 g·cm^{-3}, the absolute density of pure lead.

Representing ρ_{ap} for a set of electrodes obtained at a constant concentration of HCE (2 gl^{-1}) and various concentration of LS, a curve with a maximum was obtained (fig. 4).

The maximum corresponds to a concentration of LS of 3 gl^{-1}. Maintaining a constant concentration of LS (3 gl^{-1}), at various HCE concentrations ρ_{ap} varies as shown in fig. 5.

The concentrations of HCE which ensure the best levelling of the deposit in the working conditions, were 2 gl^{-1} at 20°C (fig. 4.) and 3 gl^{-1} at 40°C (fig. 5.). The deplacement of maximum towards large concentrations at higher temperature is due to the inverse proportionality of adsorption of HCE at the interface with the temperature. The vertical deplacement of the maxi-

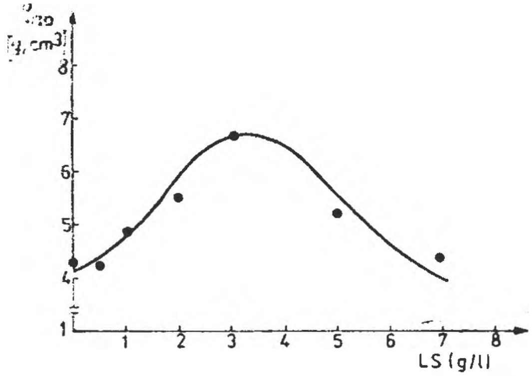

Fig. 4. Influence of LS concentration on ρ_{ap} (conc. HCE = 2 gl^{-1}).

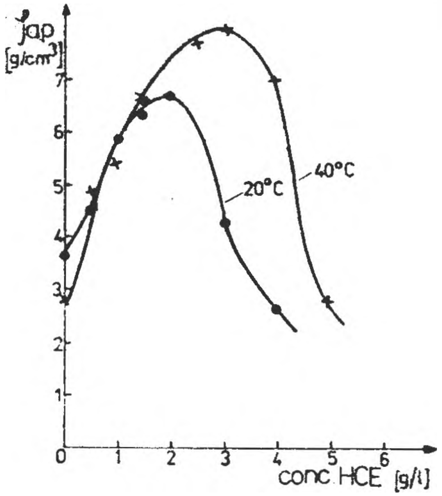

Fig. 5. Influence of HCE concentration on ρ_{ap} (conc. LS = 3 gl^{-1}).

mum was attributed to the improvement of levelling by modifying the balance between the different types of overpotentials occurring in the steps of the electrocrystalization process.

The existence of a maximum of the levelling corresponding to a certain concentration of organic additives is mentioned also in some other electrodeposition process, like nickel electrodeposition from Watts-type electrolytes [10].

The maximum of ρ_{ap} — additive concentration curves suggests that a certain ratio between the concentrations of the two additives is necessary to ensure an optimum levelling. This ratio can result from a competitive adsorption at the interface of the two organic compounds. The relative position of the polarization curves obtained in the presence of each of the two additives used separately, as compared with the curve obtained in the presence of optimum LS + HCE mixtures, supports this idea (fig. 6).

The position of the curve corresponding to the LS + HCE mixtures between the curves corresponding to the individual additives suggests the existence of an

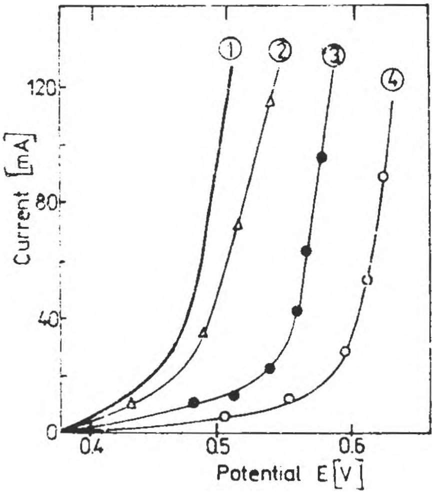

Fig. 6. Polarization curves (with ohmic drop correction). (1) without additives; (2) with 3 gl^{-1} LS; (3) with 3 gl^{-1} LS and 3 gl^{-1} HCE; (4) with 3 gl^{-1} HCE (1200 rpm).

interference (may be a competitive adsorption) of the two levelling agents.

The kinetic results obtained previously by impedance spectroscopy [8, 9], demonstrate that the two levelling agents act specifically during the different stages of the electrocrystallization process and their behaviour is differently influenced by the electrolyte stirring. We can conclude that the maximum of ρ_{ap} — concentration of additives (optimum levelling) corresponds to that concentration ratio which is able to ensure a moderate activation overpotential and a moderate nucleation overpotential at the interface. The synergism of the two additives can thus be explained by their complementarity.

REFERENCES

1. A. G. Betts, *Ger. Pat.*, **198**, 288 (1902/08).
2. J. A. Gonzales-Dominques, E. Peters, D. B. Dreisinger, *J. Appl. Electrochem.*, **21**, (1991), 189—202.
3. *GmelinsHandbuch der Anorganischen Chemie*, Verlag Chemie GbmH, Weinheim, Bergstrasse 1972, Teil B 2, 360.
4. A. G. Betts, *Lead Refining by Electrolysis*, Wiley & Sons, N.Y. (1908), **15**.
5. L. Oniciu, L. Mureşan, V. A. Topan, D. Gherţoiu, *Brevet. Rom.*, **104**, 946 (1991).
6. L. Ghergari, L. Oniciu, L. Mureşan, A. Pântea, V. A. Topan, D. Gherţoiu, *J. Electroanal. Chem.*, **313**, (1991), 303—11.
7. L. Mureşan, L. Oniciu, G. Maurin, *Electrochim. Acta*, **37**, (12), (1992), 2249—54.
8. L. Mureşan, L. Oniciu, R. Wiart, *J. Appl. Electrochem.*, **23** (1993) 66—71.
9. L. Mureşan, L. Oniciu, R. Wiart, *J. Appl. Electrochem* **24** (1994), 332—36.
10. S. A. Watson, J. Edwards, *Trans. Inst. Met. Finish*, **34** (1957), 167.

TSUDIA UNIV. BABEŞ-BOLYAI, CHEMIA, XXXIX, 1- 2, 1994

BEHAVIOUR OF THE Zn-ELECTRODE IN Ni-Zn BATTERIES

I. ONICIU*, VIOLETA VOINA**, ELEONORA MARIA RUS*, DELIA CONSTANTIN**,
CRISTINA BARTEŞ**

ABSTRACT. The unequal redistribution of the zinc, the undersirable morphologies modification during recharge and the corrosion of the zinc electrode are discussed in the present paper.

1. **Introduction.** Zinc is the most commonly used baterry electrode because of its low equilibrium potential, reversibility, compatibility with aqueous electrolytes, the relative low equivalent weight, high specific energy and volumetric energy density, abundance, low cost, low toxicity and case of handling.

Two important characteristics of zinc, its high solubility in alkaline electrolytes and its rapid electrochemical kinetics are linked to the formation of the unwanted Zn electrode morphologics (dendrites, filamentary growths, nodules) and to the redistribution of Zn active material during recharge.

The Zn/NiOOH battery is recognized for its high specific energy of 80 Wh/kg, its excelent peak specific power (260 W/kg), its good low-temperature performance (until −40°C) and moderate self-discharge rate (< 0,8%/day).

The uses for Ni-Zn batteries include power sources for communication equipment, electric vehicles, portable electric-powered equipment and energy sotrage [1−3].

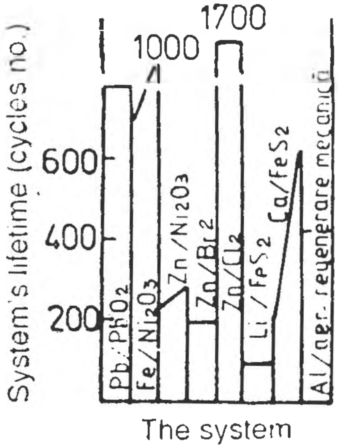

Fig. 1. The lifetimes of some secondary systems.

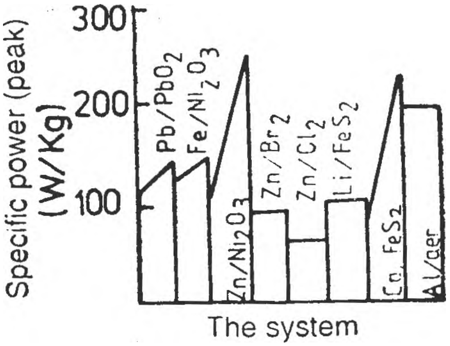

Fig. 2. The specific power of some secondary systems.

---

* *Babeş-Bolyai University, Dept. of Physical chemistry, 3400 Cluj-Napoca*
** *Babeş-Bolyai University, Laboratory of Electrochemistry, 3400 Cluj-Napoca, Romania*

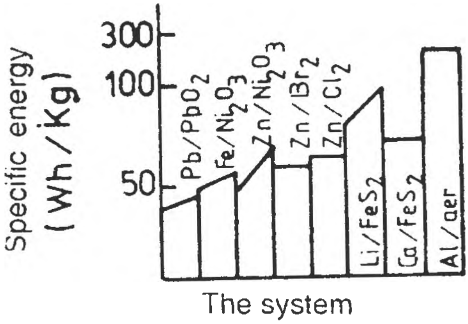

Fig. 3. The specific energy of some secondary systems.

The Ni-Zn battery has recieved serious consideration especially for applications in electric drive.

The plots of the life-times, specific power and specific energy of the secondary systems are presented in the fig. 1—3.

2. The functionality of the Ni-Zn batteries The functionality of the Ni-Zn batteries could be explained by following reactions [5—6]:

— in a minimum amount of electrolyte, to the positive electrode:

$$2NiOOH + 2H_2O + 2e^- \xrightleftharpoons[\text{recharge}]{\text{discharge}} 2Ni(OH)_2 + 2OH^- \qquad (1)$$

— to the negative electrode:

$$Zn + 2OH^- \xrightleftharpoons[\text{recharge}]{\text{discharge}} ZnO + H_2O + 2e^- \qquad (2)$$

The cell recharge reaction is:

$$2NiOOH + Zn + H_2O \xrightleftharpoons[\text{recharge}]{\text{discarge}} 2Ni(OH)_2 + ZnO \qquad (3)$$

— in an excess amount of electrolyte, to the positive electrode:

$$2NiOOH + 2H_2O + 2e^- \xrightleftharpoons[\text{recharge}]{\text{discharge}} 2Ni(OH)_2 + 2OH^- \qquad (4)$$

— to the negative electrode:

$$Zn + 2KOH + 2OH^- \xrightleftharpoons[\text{recharge}]{\text{discharge}} ZnK_2(OH)_4 + 2e^- \qquad (5)$$

The cell reaction is:

$$Zn + 2NiOOH + 2KOH + 2H_2O \xrightleftharpoons[\text{recharge}]{\text{discharge}} ZnK_2(OH)_4 + 2Ni(OH)_2 \qquad (6)$$

The active electromotive reaction of the Ni-Zn battery is spontaneous and the temperature coefficient of EMF, in isobar conditions, is negative:

$$\left(\frac{dE}{dT}\right)_p = \frac{S}{zF} < 0, \text{ where } \Delta S < 0 \qquad (7)$$

it means that a part of the entalpy is transformed in heat, warming up the battery.

The reversible cell voltage is about 1,65 V, where the theoretical specific energy is 386 Wh/kg.

3. The behaviour of zinc anode

3.1. *Model for zinc dissolution.* The reaction mechanism of the deposition and dissolution of zinc in alkaline solutions are still a subject for discussion. A controversy exists about the mechanisms of reaction which have been derived from the values of reaction orders, Tafel slopes, and from exchange current densities deduced from measurements [6—13].

Dirkse and Hampson [7—8] proposed the following mechanism of dissolution (oxidation) reaction of zinc:

$$Zn + OH^- \rightleftarrows ZnOH^- \tag{8}$$

$$ZnOH^- \rightleftarrows ZnOH + e^- \tag{9}$$

$$ZnOH + OH^- \rightleftarrows Zn(OH)_2 + e^- \tag{10}$$

$$Zn(OH)_2 + 2OH^- \rightleftarrows Zn(OH)_4^{2-} \tag{11}$$

where (9) is the rate-determining step.

Later, Dirkse [9] pointed out that the zinc electrode behaviour is sensitive to the ionic strength in the electrolyte and he confirmed the mechanism proposed previously.

A second mechanism was proposed by Bockris at al. [10]:

$$Zn + OH^- \rightleftarrows ZnOH + e^- \tag{12}$$

$$ZnOH + OH^- \rightleftarrows Zn(OH)_2^- \tag{13}$$

$$Zn(OH)_2^- + OH^- \rightleftarrows Zn(OH)_3^- + e^- \tag{14}$$

$$Zn(OH)_3^- + OH^- \rightleftarrows Zn(OH)_4^{2-} \tag{15}$$

where reaction (14) is the rate-determining step, in both anodic and cathodic directions.

More recent measurements of galvanostatic transients carried out at constant ionic strenght [11] have been reported to be consistent with the suggested mechanism of Bockris et al.

Moreover it was shown that the ionic strength has no influence on the kinetics of the zinc electrode [8].

The pseudo-equilibrium method was also used to interpret the potentiodynamic curves of Chang and Prentice [11] whose results could be explained by the following sequence for zinc dissolution:

$$Zn + OH^- \rightleftarrows ZnOH + e^- \tag{16}$$

$$ZnOH + 2OH^- \rightleftarrows Zn(OH)_3^- + e^- \tag{17}$$

$$Zn(OH)_3^- + OH^- \rightleftarrows Zn(OH)_4^{2-} \tag{18}$$

where the rate-determining step is reaction (17).

This model can be regarded as a simplified version of the Bockris model since reaction (17) involves reaction (13) and (14).

Impedance spectroscopy measurements have been shown that all these mechanisms involve a multistep discharge and generally several adsorbed intermediates [12—16].

Recently, Cachet and colab. proposed a new mechanism of zinc electrode discharge, which involves two succesive charge-transfer reactions [17]:

$$Zn \rightleftarrows Zn^+ + e^- \quad (19)$$

$$Zn^+ \rightleftarrows Zn^{2+} + e^- \quad (20)$$

where Zn^{2+} denotes the zincate species $Zn(OH)_4^{2-}$ and the monovalent intermediate Zn^+ is probably hydroxylated such as the compounds ZnOH or $Zn(OH)_4^{2-}$ involved in the reaction models proposed by Dirkse, Bockris and Prentice [5—11]. Any possible chemical step associated with a change in the hydroxylation degree of intermediates is supposed to be fast in comparison with the electrochemical steps (19) and (20).

In addition, it is considered that reactions (19) and (20) take place through a porous layer of thickness L (fig. 4), which is supposed to be made of cylindrical pores through a conductive material, probably a mixture of zinc oxide and zinc metal of composition Zn_xO_y $(x > y)$. The renewal of the conductive material during the active dissolution of zinc electrode can be ensured by a precipitation process from the superconcentrated zincate ions.

$$Zn(OH)_4^{2-} \rightleftarrows ZnO + H_2O + 2OH^- \quad (21)$$

and/or by a disproportionation process from the intermediate ZnOH:

$$2ZnOH \rightleftarrows Zn + ZnO + H_2O \quad (22)$$

Therefore, the electron conductivity of this material is sufficient to allow reactions (19) and (20) and to take place both at the pore base and along the pore wall. Most of the zincate species formed inside the pore diffuses away towards through the Nernst layer towards the bulk of the electrolyte.

3.2. *Model for zinc deposition devoted to the connection between the mechanism of zinc deposition and the deposit morphology.* In a recent work [18], it was mentioned that, at low cathodic polarizations, granular compact deposits are formed.

Cachet and his coworkers [19] have proposed a model for zinc deposition with two succesive charge-transfer steps:

$$Zn^{2+} + e^- \rightleftarrows Zn^+ \quad (23)$$

$$Zn^+ \rightleftarrows e^- + Zn \quad (24)$$

where Zn^{2+} denotes the discharging zincate species $Zn(OH)_{4-}^{2}$ and the intermediate Zn^+ is probably ZnOH or $Zn(OH)_2^-$.

It is considered that the reactions (23) and (24) take place through Zn_xO_y, a layer of mixed conductivity and composition (fig. 5). On the conductive fraction θ of the electrode, reaction (23) is assumed to occur at the

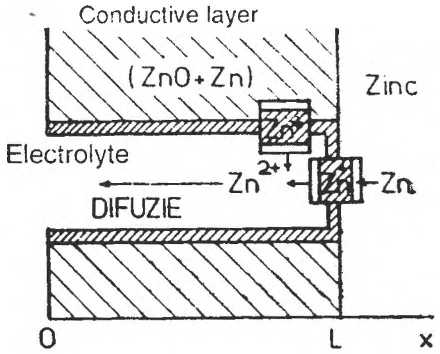

Fig. 4. Model for zinc dissolution.

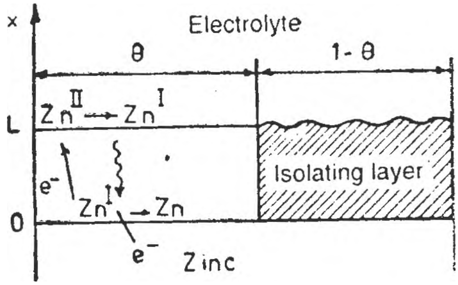

Fig. 5. Model for zinc deposition.

distance L from the metal layer interface ($x = L$), whereas reaction (24) leading to the metal atom will take place at $x = 0$.

Although there is no experimental data about the layer conductivity, it can be supposed that inhomogeneities in the composition, the thickness or the structure of the surface layer induce inhomogeneities in the layer conductivity.

It may be concluded that the discharge of zincate ions in alkaline electrolytes takes place in the two succesive charge-transfer reactions, probably coupled to relative fast chemical steps. It is also shown that the electrode steady state is controlled by the presence of an interfacial layer whose geometrical properties and conductivity depend on the electrode polarization.

3.3. *The formation of dendrites.* A difficult problem in the function of the zinc electrode at recharge consist in the formation of the dendrites, which can be the origine of a short circuit in the battery.

Mashtev and Zlatilova [20] have studied the kinetics of the cristalites appearance, which preceds the dendrites and they also found that the precursors gowth up lineary in time, inside the diffusion layer. The rate of the precursors growht, v_p, can be represented at each moment by the ratio y/tr where the medium height y of the precursors, measured at the time $\mathscr{T}_1$, is equal to the thickness of the diffusion layer δ. Based on this equality and on the constancy of v_p, the determination ot the rate of the precursors growth in function by the overpotential η and the thickness δ of the diffusion layer is possible:

$$\frac{1}{v_p} = z\mathscr{F}/\mathrm{v}i_0\exp(-\eta\cdot\mathscr{F}/RT + r\delta/y\cdot v\cdot DC_0)\quad(\mathrm{s/cm})\tag{25}$$

where: r is the radius of curvature in time of precursors growth
v — the molar volume of zincate
D — the diffusion coefficient of the zincate
C_0 — the bulk solution concentration of zincate
i_0 — the exchange current density

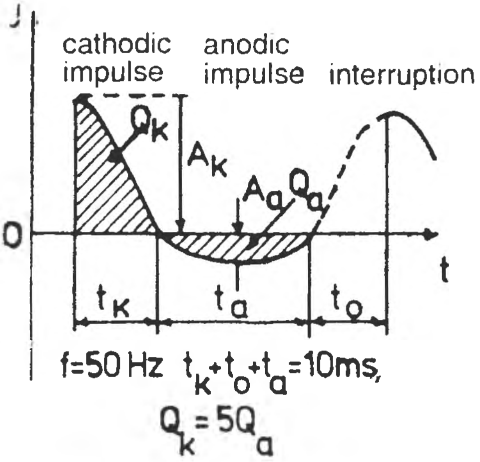

Fig. 6. The recharge of zinc electrode in impulses.

The time of the dendrites apparence $\mathfrak{T}$ generated by equation (21) is given by:

$$\mathfrak{T} = \delta/v_d + r\delta/v\mathrm{DC}_0 \qquad (26)$$

which lead to the rate of the dendrites growth, v_d:

$$\frac{1}{v_d} = z\mathfrak{F}/vi_0\exp(-\eta\mathfrak{F}/\mathrm{RT}) \qquad (27)$$

It comes out that the effect on the zincate concentration on the time of dendrites appereance corresponding to the equation (26).

The time of dendrites appearance can be increased and therefore the phenomenon belated, by introduction of some metalic ions in the zincate solution which decreases the current density of the dendrite deposition. Similar effects have the galium, strontium, calcium hydroxide or salts additives. The formation of the dendrites can be inhibited by an alloy of the zinc electrode with other metals, In or Tl [21].

It has been observed [22] that the zinc deposition during the charge can be realized by use of a cathodic impulse, followed by another anodic impulse and an interruption, as shown in fig. 6. The cycle is repeated. The cathodic impulse separates the zinc, the anodic impulse aplits the nonadherent dendritic forms and during the charge the mass transport is ensured.

3.4. *Active-material redistribution of zinc anodes*. Another problem of the zinc electrode is active-material redistribution on surface of electrode.

As concerning this process, investigations of Raman and NMR spectra, video microscopy [23], etc., have identified several mechanisms by which zinc active-material redistribution might take place in a quiescent secondary cell:

1) Electroosmotic forces caninduce the flow of electrolyte, which results in convective transport of soluble zinc-bearing species [24];

2) Non-uniform current density distribution leads to concentration gradients which result in the diffusion of soluble zinc-bearing species [25];

3) Preferential nucleation of zinc, rather than onto the electrode current-collector, and cathodic H_2 evolution at the electrode edges can result in non-uniform zinc deposition during charge [26];

4) Autocatalytic dissolution of zinc via $Zn(OH)_4^{2-}$ ions leads to an accelerated zinc dissolution near the electrode edges, where the $Zn(OH)_4^{2-}$ concentration tends to be higher [27];

5) Isolated zinc fragments can migrate across the electrode under the influence of potential gradients [28].

Models 1) and 2) suggest that the rate of zinc-material redistribution is strongly dependent upon the solubility of zinc-bearing species in the electrolyte. Model 3) would predict the zinc redistribution rate is strongly affected by the choice of current-collector material. The change of shape could be a combination of these effects [29].

3.5. *The corrosion of zinc electrodes.* The zinc deposited during the charge of the battery has the tendency to corrode in alkaline solution of electrolyte. The process is based on the equation of Tafel:

$$\eta = a + b \cdot \lg i \tag{28}$$

where a and b are constants. The relationship is valid provided the charge transfer is the rate determining step.

The corrosion potential ε_{cor} and the corrosion current i_{cor} can be derived from graphical plots of η against ln i.

Overpotential η is related to the corrosion current i_{cor} by [30]:

$$\eta = \frac{RT}{\alpha ZF} \ln \frac{i}{i_{cor}} \tag{29}$$

where α, Z, F, R, T have their usual significance (fig. 7).

Stern and Geary established a relationship between the corrosion potential and corrosion current:

$$\frac{d\varepsilon}{di} = \frac{b_a \cdot b_c}{2{,}3 i_{cor} (b_a + b_c)} \tag{30}$$

assuming that ε is remoted from the reversible potentials.

The zinc corrosion is linked by the hydrogen ions discharge reaction (hdr):

$$Zn + 2H_2O \rightarrow Zn(OH)_2 + 2H^+ + 2e^- \tag{31}$$

The zinc electrode corrosion is accelerated by the presence in the active mass of some metalic ions impurities like Ni^{+2}, Fe^{2+}, Pt^{2+}, Pd^{2+} because of the lower hdr overpotential on these metals.

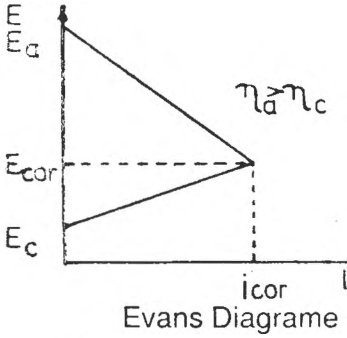

Fig. 7. The Edeleanu-Evans diagram.

The amalgamated zinc has an increased hdr overpotential and therefore it is used for anticorrosive protection of zinc electrodes. The Pb, In, $TlNO_3$, $SnCl_2$, ZnO additives have the same role [31—33].

More recently, were studied the additives in the electrolyte solution (inorganic and organic complexes) for the inhibition of zinc electrode corrosion. Fig. 7 and 8 shown the corrosion percent of the zinc electrode in standard electrolyte in comparison with solutions containing inorganic (metals) and organic additives, respectively inhibitors of the corrosion inhibition. The anticorrosive pro-

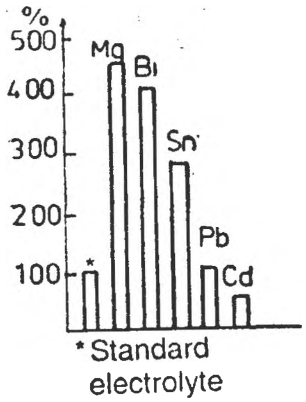

Fig. 8. The corrosion of zinc electrode in standard electrolyte and in electrolyte containing metalic additives.

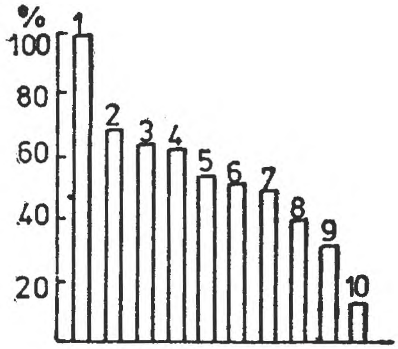

Fig. 9. Corrosion of zinc in presence of some organic inhibitors in eletrolyte: 1 — electrolyte containin: additives: 2 — quanidine-HCl; 3 — hydrochinon; 4 — nitrobenzoicacid; 5 — glycine; 6 — nitrotoluene; 7 — dinitrobenzene; 8 — nitrophenol; 9 — nitroaniline; 10 — α-diphenylglyoxime.

tecting effect of some organic substances is shown in fig. 9 and the accelerator role of some metals in electrolyte.

4. Types of Ni-Zn batteries. Four basic cell designs have been developed:
— vented static-electrolyte cells;
— sealed static-electrolyte cells;
— vibrating-electrode cells;
— flowing-electrolyte cells.

4.1. *Vented static-electrolyte cells.* Cells of this type are designed to be capacity-limited by the NiOOH positive electrode, which is typically a porous sintered structure. The porous Zn electrode is usually prepared by applying a polymer-bondedpaste of ZnO to a screen or mesh current collector. The Zn/Ni mass ratio has a significant effect on cell lifetime, as does the Zn/electrolyte mass ratio [34, 35]. The electrolyte is usually an aqueous solutio containing 25—30% KOH and 1% LiOH, saturated with ZnO. The height of the electrolyte meniscus can have a significant effect on the rate and extent of Zn material redistribution.

Microporous separator materials serve to retard Zn dendrite growth. To prevent the shortcircuit of a battery due to the dendrites formation, the nickel electrode is coated with a fine nickel mesh, which contains a catalysts with a lower overpotential for hdr. Therefore the dendrites disappear by the corrosion reaction on the mesh.

4.2. *Sealed static-electrolyte cells.* The development of a sealed Zn/NiOOH cell is necesary for battery applications that require low maintenance and safe operations. Cell design requires the efficient transfer of O_2 from NiOOH electrode to the Zn electrode. Also, a H_2 recombination device may be necessary for long lived cells. Such devices have been incorporated as auxiliary electrodes which have also been used to dissolve residual Zn deposits, react with excess O_2, and serve intermittently as extra-positive electrodes.

The hydrogen evolution on zinc electrode can be suppressed by zinc amalgamation, impurities elimination with a low overpotential for hydrogen discharge reaction, or by incorporation of ZnO in the NiOOH electrode.

Cells of this type, having capacities of 1,2—10 Ah were developed by YUHASA [36].

4.3. *Vibrating-electrode cells.* By vibration of zinc electrode is prevented the dendritic deposits during the charge. A cam arrangement was used to vibrate a planar Zn electrode, typically at a frequency of 20 Hz and an amplitude of 1,5—2,5 mm [37]. Agitation of the electrolyte resulted in homogenization of zincate-ion concentrations, which effectively eliminated the Zn active material redistribution problem. Lifetimes greater than 1000 cycles were obtained; however, the specific energy was typically less than 50 Wh/kg because of the heavy mechanical parts and the excess volume of electrolyte that were required.

Alternatives of this constructive solution include Zn/NiOOH cells with rotating shutter separators, moving sheet and rotating electrodes.

4.4. *Flowing-electrolyte cells.* Cells using flowing electrolyte have been developed by SORAPEC and RENAULT [38]. An original concept was the use of Zn-coated polymer beads, which were circulated through the negative-electrode compartment by flowing electrolyte. Single-cell lifetimes greater than 1000 cycles were obtained.

Future prospects. Significant increases in the lifetime of Zn/NiOOH cells have poised this technology for entry into commercial portable power applications; however, longer lifetimes are needed before a viable electric which battery can be built.

Recent investigations of the pulse-power characteristics of NiOOH electrodes [39] confer that the Zn/NiOOH cell is suitable for high-power applications as well.

Secondary alkaline Zn cell research and development has made great strides during the past fifteen years. There is strong interest in cells of this type, and we can expect similar advances during the years ahead.

REFERENCES

1. Frank R. McLarnon, Elton J. Cairns, *J. Electrochem. Soc.*, **138,** 2, (1991).
2. R. F. Savinell and H. S. Burney, *J. Electrochem. Soc.*, **137,** 485 c, (1990).
3. S. U. Falk and A. J. Salkind, *Alkaline Storage Batteries*, John Wiley and Sons, Inc. New York, (1969).
4. L. Oniciu, Eleonora Maria Rus, *Electrochemical Power Sources*, Ed. Dacia, Cluj-Napoca, (1987).
5. J. Hendrikx, W. Visscher, E. Barendrecht, *J. of Appl. Electrochem.*, **16,** 1, 175, (1986).
6. Guy Bronoel, *L'actualité chimique*, **5—6,** 117, (1990).

7. N. A. Hampson, G. A. Herdman and R. Taylor, *J. Electroanal. Chem.*, **25**, 9, (1970).
8. T. P. Dirkse and N. A. Hampson, *Electrochim Acta*, **17**, 135, 1113, (1972).
9. T. P. Dirkse, *J. Electrochem. Soc.*, **127**, 1452, (1980).
10. J. O'M. Bockris, Z. Nagy and A. Damjanovic, *J. Electrochem. Soc.*, **119**, 285, (1972).
11. Y. C. Chang and G. Prentice, *J. Electrochem. Soc.*, **132**, 375, (1985); **131**, 1465, (1984).
12. I. Epelboin, M. Ksouri and R. Wiart, *J. Electrochem. Soc.*, **122**,, 1206, (1975).
13. C. Cachet, U. Ströder and R. Wiart, *Electrochim. Acta*, **27**, 903, (1982).
14. J. Hendriks, W Visscher and E. Barendrecht, *Electrochim. Acta*, **29**, 81, (1984); **30**, 999, (1985).
15. C. Cachet, Z. Chami and R. Wiart, *Electrochim. Acta*, **32**, 465, (1987).
16. C. Cachet, B. Saïdani and R. Wiart, *Electrochim. Acta*, **33**, 405, (1988).
17. C. Cachet, B. Saïdani, R. Wiart, *J. Electrochem. Soc.*, **139**, 3, (1992).
18. A. Hugot-Le Goff, S. Joiret, B. Saïdani and R. Wiart, *J. Electroanal. Chem.*, **263**, 127, (1989).
19. C. Cachet, Z. Chami and R. Wiart, *Electrochim. Acta*, **32**, 469, (1987).
20. R. V. Mashtev and P. Zlatilova, 28 Meeting of ISE, Varna, sept. 18—25, 96, (1977).
21. L. Oniciu, Eleonora Maria Rus, Violeta Voina, Delia Constantin, *Modern Science and Energy*, Cluj-Napoca, **X**, 94, (1991).
22. J. P. Diard, B. Le Geve, 28 Meeting of ISE, Varna, sept. 18—25, 95, (1977).
23. R. E. F. Einerhand, W. Visscher, J. J. M. de Geey, E. Barendrecht, *J. Electrochem. Soc.*, **138**, 1, (1991).
24. K. W. Choi, D. N. Bennien, J. Newmans, *J. Electrochem. Soc.*, **123**, 130, (1976).
25. J. Mc Breen, *J. Electrochem. Soc.*, **119**, 1620, (1972).
26. S. Januszkiawicz, H. Vaidyanathan, M. Dadin, T. Lee, *Argonne National Laboratory Report*, ANJ/OEPM — 80 — 13, (1981).
27. M. C. H. Mc Hubre, Lawrence Berkeley Laboratory, Report LBL—16141, (1983).
28. S. Szpak, C. J. Gabriel, T. Katan, *J. Electrochem. Soc.*, **127**, 1063, (1988).
29. R. Jain, T. C. Adler, F. R. Mc Larnon, E. J. Cairns, *J. of Appl. Electrochem.*, **22**, 11, (1992).
30. T. Keily, T. J. Sinclair, *J. of Power Sources*, **6**, 47, (1981).
31. L. Z. Vorkapič, D. M. Drazič, A. R. Despič, *J. Electrochem. Soc.*, **121**, 1385, (1974).
32. M. Cenek, O. Kouril, NASA Tech. Transl. F — 14, 693, (1973).
33. C. J. Booker, G. Manahar, Note City London, Polytechn., iun. (1977).
34. S. Furukawa, K. Inouue, M. Nogami, Jpn Pat., 63, 76, 270, (1988).
35. Toshiba Battery Co. Ltd., Jpn. Pat., 58, 189, 966, (1983).
36. Y. Ishikura, Y. Fujiwara, T. Ueda, Sanyo Electric Co. Ltd., Jpn. Pat., 63, 131, 479, (1988).
37. O. von Krusentierna, *US Pat.*, 4, 015, 052, (1977).
38. G. Bronoel, R. Rouget, N. Tassin, A. Millet, *The Electrochem. Soc. Extended Abstr.*, Hollywood, Florida, 15—20 oct., 89—2, (1989).
39. D. A. Corrigan, *J. Power Sources*, **21**, 33, (1987).

STUDIA UNIV. BABEȘ-BOLYAI, CHEMIA, XXXIX, 1–2, 1994

CONDUCTIVITY OF SOME LITHIUM SALTS IN ORGANIC SOLVENT

L. ONICIU*, CS. BOLLA*, G. ȚĂRĂLUNGĂ**, L. D. BOBOȘ*, E. DEMETER*, E. CSALTO

ABSTRACT. In this paper are studied the specific conductivity and viscosity of some aprotic electrolytic solutions used in the lithium batteries. The properties of some $LiClO_4$ and $LiBF_4$ solutions in mixture of organic solvents (CP with DME or THF, respectively) are investigated.

1. **Introduction.** Since 3 decenies ago it was begun the research of the lithium batteries with nonaqueous electrolytic solutions [1]. These cells have a high energy density, but their power density, because of highly internal resistance, is lower [2].

One of the main battery problem is the optimization of the electrolytic solutions in view to obtain better specific characteristics as high electrochemical stability towards to the electrodes, high specific conductivity and low viscosity. These desiderata are not obtained when it use only one aprotic solvent [3–5].

The aprotic solvents used in lithium battery and their physical properties are shown in Table 1.

Table 1

Physical constants of some aprotic solvents used in lithium cells

Solvent	mp (°C)	bp (°C)	D	η (CP)	D/η	d(g/cm³)
Acetonitrile (AN)	−45.7	91.6	36	0.35	103	0.78
γ-Butirolactone (BL)	−42	206	39.1	1.75	22.3	1.13
Ethylene carbonate (EC)	36.4	249	89.6	1.85	49.6	1.32
Propylene carbonate (PC)	−39	242	66.1	2.5	25.4	1.2
1,2-Dimethoxyethane (DME)	−58	83	7.2	0.45	16.0	0.86
N,N-Dimethylformamide (DMFA)	−61	153	36.71	0.8	46.2	0.94
Tetrahydrofuran (THF)	−65	65	7.39	1.09	6.8	0.89
1,3-Dioxolane (DOL)	−95	78	7.13	—	—	1.06

mp : melting point ; b.p. : boiling point ; D : dielectric constant ; η : viscosity and d : density

On the basis of above data, it can be observed that propylene carbonate (PC) and ethylene carbonate (EC) have a high dielectric constant, but they have a very high viscosity. On the other hand, dimethoxyethane (DME) and tetrahydrofurane (THF) have a low dielectric constant and lower viscosity. Therefore is recommanded using a mixture of two types of solvents.

In this work are investigated the conductivity and the viscosity of some $LiClO_4$ and $LiBF_4$ solution in mixtures of PC with DME/THF.

---

* *Babes-Bolyai University, Dept. of Physical Chemistry, 3400 Cluj-Napoca, Romania*

** *Babeș-Bolyai University, Laboratory of [illegible], 3400 Cluj-Napoca, Romania*

2. **Preparation of electrolytic solutions.** Because traces of water and alcohol in the electrolytic solution degrade considerably the lithium electrode, an advanced purification of the solvent is necessary. This was achieved with PC by distillation in vacuum, using a Vigreaux column and with DME by distillation at normal pressure. The peroxide impurities from THF were eliminated with alkaline hidroxyde. The distillated solvent purity was controlled by gas chromatography.

Lithium salts were prepared from $LiOH \cdot H_2O$ and $HClO_4$, respectively HBF_4 solutions. From the prepared solutions, the salts, as trihydrates, were crystallized. The crystallohydrates were purified by repeated crystallization (about three times) from the deionizated water. The dehydratation of the salts was performed into a vacuum drier, where was achieved a vacuum of 0.02 atm. The increase of the temperature was marked gradually taking care of the salt does not melt in the crystallizing water of the salt. After the elimination of the main amount of water, an advanced dehydratation of the salts was performed through the maintenance of $LiClO_4$ fertnight in the vacuum drier, at 105°C, respectively $LiBF_4$ at about 65°C.

After the overall removal of the water, $LiBF_4$ was recrystallized from DME to eliminate LiF which is present always in $LiBF_4$ as impurity. Through the recrystallization were obtained $LiBF_4$ and DME; the later was eliminated through same trateament as the water.

The electrolytic solutions ($LiClO_4$, $LiBF_4$ respectively in DME + PC and $LiBF_4$ in DME + THF) were prepared in a dry box, having the concentrations between $4 \cdot 10^{-3} - 9 \cdot 10^{-1}$ mol/l.

3. **Determination of the electrolytic solution conductivities and viscosities.** The conductivity of the solutions was measured with a Radelkis conductometer OK 102/1, using one conductometer cell with three contacts having $C = 0{,}6653\ cm^{-1}$. The experimental measurements were performed in dry box and the results are showed in Table 2.

From the above experimental data we were plotted specific conductivity as function of the electrolyte concentration and the percentage composition of the solvent mixture (Fig. 1, 2, 3).

On the basis of these results one can observe that in the all cases the conductivity variation presents a maximum, which is more pronounced when the solution concentration of the electrolyte is greater. The maximum value is situated between $8 \cdot 10^{-3} - 12 \cdot 10^{-3}\ \Omega^{-1} \cdot cm^{-1}$, and it can be observed in $LiClO_4$ solutions in PC — DME mixture. Also, it can be see that specific conductivity of the electrolytic solution obtained with solvent mixtures is about two-three times higher than the solutions obtained with a single solvent.

The viscosity of the solutions was determined with a Ubbelohde viscosimeter with the suspended level from the measurement of the flowing times. Each measurement was repeated five times; the values of relative viscosity are in the Table 3.

From these data it can be see that the viscosity increases monotonously with the concentration of the electrolyte, respectively with the PC content. It has been found that these increases have a exponential aspect.

Table 2

The conductivities of some electrolytic solutions

Solvents mixtures	λ[10^3 Ω^{-1}cm^{-1}]				
PC — DME	Concentration of $LiClO_4$				
% %	$4 \cdot 10^{-3}$M	$2 \cdot 10^{-2}$ M	$1 \cdot 10^{-1}$ M	$5 \cdot 10^{-1}$ M	
100—0	0.094	0.366	1.490	4.258	
73.56—26.44	—	0.649	2.578	7.185	
58.18—41.82	0.225	0.852	3.393	9.713	
41.03—58.97	0.243	0.911	3.526	10.512	
29.10—70.90	0.279	1.031	3.659	10.149	
17.12—82.88	0.186	0.798	2.794	8.982	
0—100	0.008	0.030	0.366	4.926	
PC—DME	concentration of $LiBF_4$				
% %	$4 \cdot 10^{-3}$ M	$2 \cdot 10^{-2}$ M	$1 \cdot 10^{-2}$ M	$4 \cdot 10^{-2}$ M	$9 \cdot 10^{-2}$ M
100—0	0.066	0.306	1.397	3.526	3.998
73.56—26.44	0.213	0.599	2.195	5.522	7.450
58.18—41.82	0.333	0.699	2.661	6.121	8.190
41.03—58.97	0.353	0.852	2.861	5.988	8.316
29.10—70.90	0.346	0.812	2.595	5.256	8.117
17.12—82.88	0.246	0.632	1.996	4.125	6.985
0—100	0.006	0.018	0.164	0.918	3.326
PC—THF	concentration of $LiBF_4$				
% %		$2 \cdot 10^{-3}$ M	$1 \cdot 10^{-3}$ M	$4 \cdot 10^{-3}$ M	$9 \cdot 10^{-3}$ M
100—0		0.306	1.397	3.526	3.990
73.56—26.44		1.363	2.328	5.189	6.250
58.18—41.82		1.729	2.494	5.322	6.780
41.03—58.97		1.663	2.528	5.189	6.850
29.10—70.90		1.463	2.328	4.657	6.650
17.12—82.88		1.064	1.796	4.124	5.380
0—100		0.025	0.199	0.864	2.690

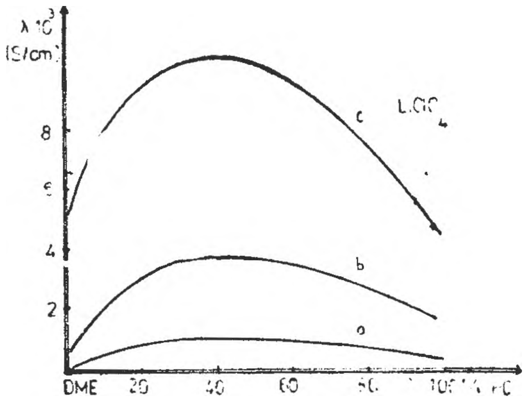

Fig. 1. Specific conductivity of $LiClO_4$ solution in PC + DME mixture (concentration of $LiClO_4$ is: (a) — $2 \cdot 10^{-2}$ M; (b) — $1 \cdot 10^{-1}$ M and (c) — $5 \cdot 10^{-1}$ M)

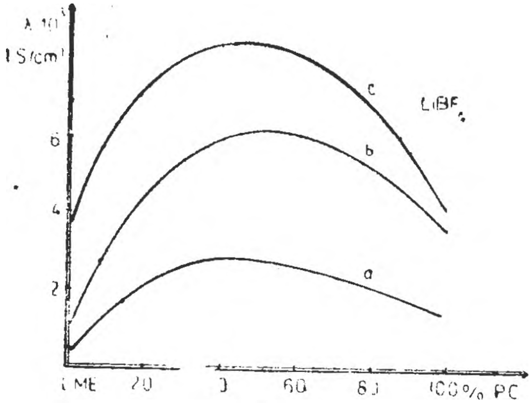

Fig. 2. Specific conductivity of LiBF$_4$ solution in PC + DME mixture (concentration of LiBF$_4$ is: (a) — $1 \cdot 10^{-1}$ M; (b) — $4 \cdot 10^{-1}$ M and (c) — $9 \cdot 10^{-1}$ M)

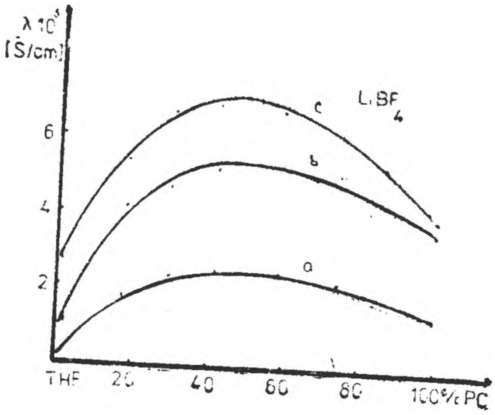

Fig. 3. Specific conductivity of LiBF$_4$ solution in PC + THF mixture (concentration of LiBF$_4$ is: (a) — $1 \cdot 10^{-1}$ M; (b) — $4 \cdot 10^{-1}$ M and (c) — $9 \cdot 10^{-1}$ M)

Table 3

The relative viscosities of some electrolitye solutions

Solvents mixtures	η_r				
PC — DME % %	Concentration of LiClO$_4$				
	$4 \cdot 10^{-3}$ M	$2 \cdot 10^{-2}$ M	$1 \cdot 10^{-1}$ M	$5 \cdot 10^{-1}$ M	
100—0	7.129	7.031	7.204	9.489	
73.56—26.44	—	3.509	3.945	5.191	
58.18—41.82	2.476	2.536	2.701	3.880	
41.03—58.97	1.861	1.915	2.025	2.873	
29.10—70.90	1.523	1.546	1.668	2.326	
17.12—82.88	1.279	1.274	1.357	1.924	
0—100	1.001	1.010	1.080	1.513	
PC—DME % %	concentration of LiBF$_4$				
	$4 \cdot 10^{-3}$ M	$2 \cdot 10^{-2}$ M	$1 \cdot 10^{-1}$ M	$4 \cdot 10^{-1}$ M	$9 \cdot 10^{-1}$ M
100—0	6.018	6.037	6.329	8.361	12.114
73.56—26.44	3.384	3.919	4.113	4.987	7.296
58.18—41.82	2.421	3.103	3.168	3.532	4.795
41.03—58.97	1.915	2.234	2.462	2.577	3.758
29.10—70.90	1.404	1.797	1.965	2.134	3.032
17.12—82.88	1.299	1.429	1.564	1.753	2.127
0—100	1.001	1.001	—	1.192	1.635
PC—THF % %	concentration of LiBF$_4$				
		$2 \cdot 10^{-2}$ M	$1 \cdot 10^{-1}$ M	$4 \cdot 10^{-1}$ M	$9 \cdot 10^{-1}$ M
100—0		6.037	6.328	8.359	12.117
73.56—26.44		3.032	3.258	3.893	6.641
58.18—41.82		2.460	2.527	3.132	5.378
41.03—58.97		1.814	2.009	2.473	4.276
29.10—70.90		1.544	1.760	2.181	3.510
17.12—82.88		1.285	1.436	1.825	2.732
0—100		1.043	1.130	1.319	1.911

Conclusions. It can be observed the advantages concerning specific conductivities and viscosities of the electrolytic solutions obtained with mixtures of organic solvents in comparison with them obtained in a single solvent.

REFERENCES

1. F. Bonino, M. Lazzari, L. Peralde Biceli, B. Rivolta, B. Di Pietro, B. Scrosati and M. A. Voso, *Lithium organic electrolyte batteries*, Roma (1981).
2. L. Oniciu, *Conversia electrochimică a energiei*, Ed. Şt. şi Enciclopedică, Bucureşti (1977).
3. Z. Barthel, H. J. Gores and G. Schmeer, *Ber. Bunsenges Phys. Chem.*, **83**, 911 (1978).
4. Z. Barthel, R. Gerber and H. J. Gores, *Ber. Bunsenges Phys. Chem.*, **88**, 616 (1984).
5. P. V. S. Prabhu, G. Prem-Kumar, P. N. N. Namboodina and R. Gongadharun, *J. of Appl. Electrochem.*, **23**, 156 (1993).

STUDIA UNIV. BABEŞ-BOLYAI, CHEMIA, XXXIX, 1–2, 1994

THE REACTION BETWEEN CHROMATE AND THIOLS. V. THE OXIDATION OF MERCAPTOSUCCINIC ACID

IOAN BALDEA

ABSTRACT. The oxidation of mercaptosuccinic acid proceeds via a relative rapid pre-equilibrium in which a thioester is formed

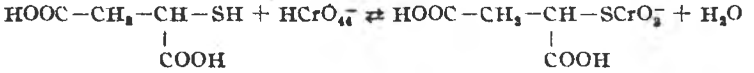

$$\mathrm{HOOC-CH_2-\underset{\displaystyle COOH}{\underset{|}{CH}}-SH + HCrO_4^- \rightleftarrows HOOC-CH_2-\underset{\displaystyle COOH}{\underset{|}{CH}}-SCrO_3^- + H_2O} \qquad K_f$$

An equilibrium constant of $K_f = (1.48 \pm 0.07) \times 10^3\ \mathrm{dm^3mol^{-1}}$ has been determined at 25.0°C and ionic strength of 0.5. The visible and u.v. absorption spectrum of intermediate has been recorded.

Kinetic measurements have been made to obtain the rate of thioester intermediate formation, as well as the rate of the redox process, whem disulfide has been formed, using a two-step model, each process being of the first-order under a large excess of mercaptosuccinic acid. The following rate laws have been found:

$$\mathrm{rate}_f = \{k_f^0 + k_f^H[H^+]\}[RSH][HCrO_4^-]$$

for the thioester formation, with $k_f^0 = 44.1 \pm 0.3\ \mathrm{dm^3mol^{-1}s^{-1}}$ and $k_f^H = (1.92 \pm 0.01) \times 10^2\ \mathrm{dm^6mol^{-2}s^{-1}}$ at 25°C and $\mu = 0.5$, and

$$\mathrm{rate_{ox}} = \{k + k^H[H^+]\}[RSH]\,]RSCrO_3^-]$$

for the electron-transfer process, with $k = 23 \cdot 8 \pm 0.3\ \mathrm{dm^3mol^{-1}s^{-1}}$ and $k^H = (2.03 \pm 0.13) \times 10^2\ \mathrm{dm^6mol^{-2}s^{-1}}$.

Both the substitution of OH^- in $HOCrO_3^-$ and subsequent oxidation processes are discussed.

Introduction. A considerable amount of work has been done on the chromic acid oxidation of various inorganic and organic compounds. The oxidation of cysteine and related thiols by Cr(VI) in acidic solution have been studied by McAuley and co-workes [1], Baldea and Niac [2, 3] and Kwong and Pennington [4] in neutral media. Growth and decay of a chromate-substrate complex 1 : 1 as a transient intermediate of various inorganic and organic compounds have been already estabilished [1—11]. Both the equilibrium spectrophotometric data and the kinetics support these mechanistic steps. When a Chromiun(VI)-Sulfur bonding is formed, the intermediate condensed compound presents spectra with important red shift maxima as compared to the similar oxygen-bridged compounds [2, 7.12]. On the other hand, the equilibrium constants for such sulfur-bridged intermediates are 2—3 orders of magnitude higher as compared to the corresponding oxygen-bridged compounds [5, 6, 10]. The stoichiometry of 3 : 1 thiol : Cr(VI) has been found under a substantial excess of thiol [1—5, 10]. The intermediate undergoes redox decomposition alone or by a reaction with another thiol molecule to give disulfide.

The formation of the condensed compound is quite rapid as compared to its subsequent electron-transfer process in the case of cysteine [1, 2, 4], ethanethiol [5], thiosulfate [10], but the ratio of growth/decay of intermediate is not so high in the case of mercaptoacetic acid oxidation [3].

To get more information about the role of the substrate nature on the relative rate of intermediate buildup and decay through electron-transfer process, mercaptosuccinic acid has been chosen as thiol substrate to be oxidized by Cr(VI), taking into account the possibility of its chelation to intermediate Cr(V), Cr(IV) as well as to the final reduction product Cr(III). Some other reactions as oxidation of oxalic acid [13] and lactic acid [14] were interpreted as sequence of bi- and mono-equivalent steps with a dominant role of Cr(V).

Experimental. Chemicals were of reagent grade purity as obtained from commercial sources and used without further purification. Stock solutions of reactants were prepared using doubly distilled water, appropriately diluted, and their acidity adjusted as required when they were employed for experiments. Standardization was performed by usual means as described previously [2, 3]. Mercaptosuccinic (thiomalic) acid solution was freshly prepared before each set of measurements after passing de-aerated methane through twice distilled water. Absorption spectra of the intermediate condensed compound was recorded by means of a Specord-UV VIS spectrophotometer for small ranges of wavelength, with freshly mixed solutions. Each range was covered two or three times. Low concentrations were chosed to avoid the subsequent redox reaction as much as possible. Kinetic measurements were performed by using a Zeiss VSU-1 spectrophotometer able to monitor the dissapearance of Cr(VI)-thiomalic complex at 410 nm in a simple stopped-flow device, manually operated, builded by us and adjusted to the spectrophotometer. The stopped-flow device was equiped with a thermostated jacket as well as with a trigger to mark the start of the reaction on the recordings. A Zeiss G—1 B—1 universal recorder was connected to the spectrophotometer. It used an 1 cm · s^{-1} speed for the recording paper.
The reaction went to completion within 20—50 seconds, and corrections for the monitored transmitted light intensity versus time were necessary to account for the delay of the recorder as compared to the reaction progress.

The formation constants of Cr(VI)-mercaptosuccinic acid was determined spectrophotometrically at 410 nm using a concentration range where the redox process was quite slow.

Results and discussion.

1. *The stoichiometry* of the process was estabilished by spectrophotometric titration of Cr(VI) with thiomalic acid after each mixture was allowed to react for at least 5—6 half periods [15]. Ratios close to 3:1 mercaptosuccinic acid: Cr(VI) were obtained, showing that the main oxidation product is disulfide $S_2(CH(COOH)-CH_2-COOH)_2$. It has been previously found that thiols were oxidized to disulfide even by strong oxidizing agents as Co(III) and Ce(IV) [16].

2. *The formation of thioester.* A change of solution colour from yellow to orange took place rapidly when chromate solution was injected into thiomalic acid solution. The spectra of 3×10^{-4} mol · dm^{-3} $HCrO_4$ solution and its mixtures with mercaptosuccinic acid in the ratios Cr(VI):$C_4H_6O_4S$ of 3:1 and 1:4.3 respectively were recorded progressively for small ranges of wavelength with freshly mixed solutions. They are presented in fig. 1. The acidity was 1.0×10^{-2} mol · dm^{-3} $HClO_4$ for all three cases. Two isosbestic points, located at 321 and 392 nm were observed, indicating that only two absorbing species were present in the mixture. The red shift of the peaks is apparent, and a sulfur-chromium bonding seems to be involved. The following equilibrium has been considered to

take place prior the oxidizing process, the condensed compound being a thioester:

$$\mathrm{RSH} + \mathrm{HCrO_4^-} \rightleftharpoons \mathrm{RSCrO_3^-} + \mathrm{H_2O} \qquad k_f,\ k_b\ K_f \tag{1}$$

RSH is the abbreviation for HOOC—CH$_2$—CH(COOH)SH. The HCrO$_4^-$ ion is practically the only form of Cr(VI) present in the solution to react with thiol, under the range of concentration and acidity employed [17]. To evaluate the equilibrium constant K_f for chromate-mercaptosuccinic acid complex, a procedure described previously was used [2]. Table 1 contains the absorbance measurements under conditions where redox reaction was quite slow. Each value at equilibrium is a mean of 4—6 individual measurements, which do not differ to more than 3%. The absorbance is given by the two coloured species. For an 1 cm path length cell, it is:

$$A = \varepsilon_0\{[\mathrm{HCrO_4^-}]_0 - [\mathrm{RSCrO_3^-}]\} + \varepsilon_1[\mathrm{RSCrO_3^-}] \tag{2}$$

where ε_0 and ε_1 stand for the molar absorptivities for HCrO$_4^-$ and RSCrO$_3^-$ species respectively. Equation (2) can be related to K_f and an expression is developed for calculating both ε_1 and K_f values:

$$\varepsilon_{obsd} = \varepsilon_1 - \frac{1}{K_f}\,\frac{\varepsilon_{obsd} - \varepsilon_0}{[\mathrm{RSH}]_f} \tag{3}$$

where $\varepsilon_{obsd} = A/[\mathrm{Cr(VI)}]_0$ is the mean absorption coefficient for the mixture and $[\mathrm{RSH}]_f$ stands for free mercaptosuccinic acid concentration. An iterative

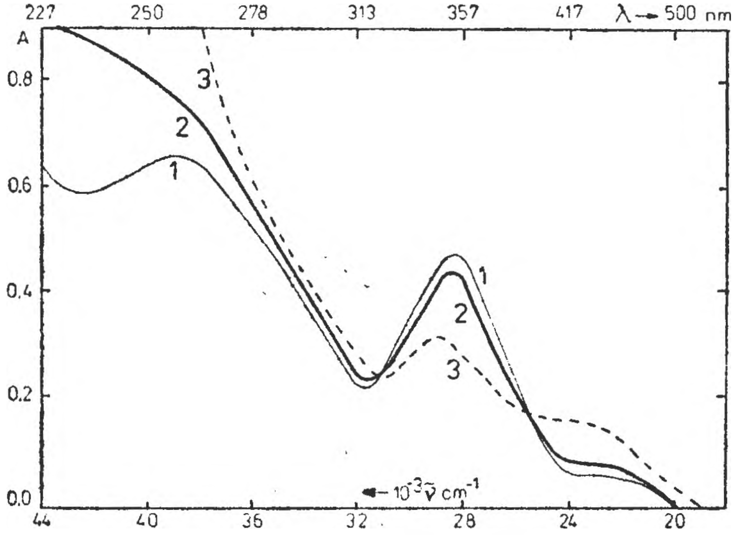

Fig. 1. Absorption spectra of 3.0 × 10^{-4} mol dm^{-3} HCrO$_4^-$(1) and its mixtures with 1.0 × 10^{-4} mol dm^{-3} (2) and 1.33 × 10^{-3} mol dm^{-3} (3) mercaptosuccinic acid.

procedure, using an objective least-squares method gave ε_1 as the intercept and K_f^{-1} as the slope of the line described by equation (3). Figure 2 shows a good fit of the data after four iterations, where convergence has been attained. K_f determined in each iteration was used to calculate $[RSH]_f$ for the next iteration. First approximation started by considering $[RSH]_f = [RSH]_0$. The results are: $K_f = (1.48 \pm 0.07) \times 10^3$ dm³mol⁻¹ at 25°C and $\mu = 0.5$, and $\varepsilon_1 = 740 \pm 11$ dm³mol⁻¹cm⁻¹ at 410 nm.

Table 1

Absorbance measurements at equilibrium and calculated values for eq. (3). T = 298 ± 0.2K, $[H^+] = 0.005$ $\mu = 0.5$ $[Cr(VI)] = 5 \times 10^{-4}$ $\lambda = 410$ nm

10^3 [RSH]	A	ε	$\frac{\varepsilon_{obsd} - \varepsilon_0}{[RSH]_0} \times 10^{-5}$	$\frac{\varepsilon_{obsd} - \varepsilon_0}{[RSH]_f} \times 10^{-5}$
5.0	0.337	673	0.932	1.021
2.5	0.303	606	1.596	1.876
2.0	0.293	586	1.895	2.303
1.5	0.276	553	2.307	2.940
1.0	0.241	481	2.740	3.683
0.5	0.192	384	3.540	5.284
0.4	0.178	356	3.725	5.704
			first iteration	fourth iteration

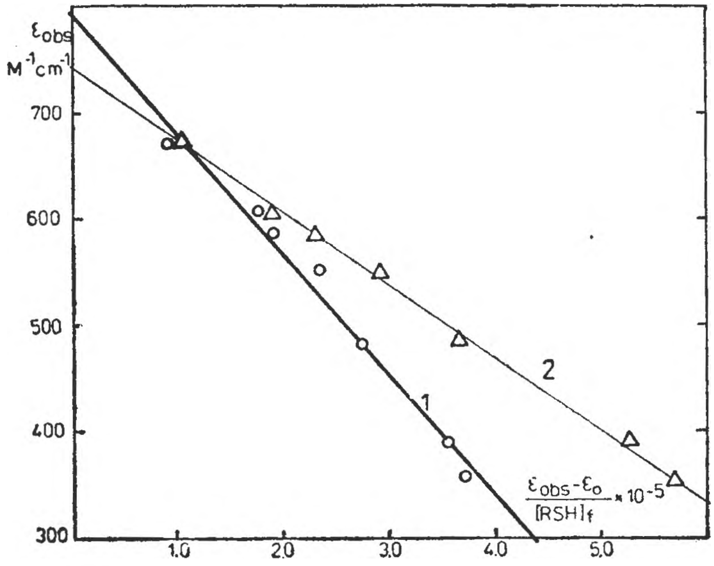

Fig. 2. Linear dependence given by eq. (3). 1 — First iteration with $[RSH]_f = [RSH]_0$; 2 — Fourth interation when convergence has been achieved

3. *Kinetic measurements.* Because the buildup of thioester and its subsequent redox process take place with rates having the same order of magnitude under the excess concentration of mercaptosuccinic acid (5.43×10^{-3} to 1.6×10^{-2} mol · dm^{-3} as compared to 4×10^{-4} mol · dm^{-3} for Cr(VI)), the two processes have been treated as a series of first-order steps. Figure 3 presents a recorded curve showing percent of transmitted light intensity versus time together with the corrected one, taking into account the response period of the recorder ($\tau = 0.5$ s)

$$J_{corr} = J + \tau \frac{dJ}{dt} \qquad (4)$$

All recorded curves were corrected and transposed into absorbance as a function of time. An analysis of figure 3 reveals that the formation of thioester is a little faster than its decay in the oxidation process. By comparison to the mercaptoacetic acid [3] and cysteine [1, 2] oxidation mechanism, in the present case of thiomalic acid oxidation, the process should follow the same sequence of steps. At acidity held constant the following consecutive reactions to be measured have been considered:

$$RSH + HCrO_4^- \rightleftharpoons RSCrO_3^- + H_2O \qquad k_f,\ k_b\ K_f$$

$$RSCrO_3^- + RSH \rightarrow R_2S_2 + Cr(IV) \qquad (5)$$

with (5) as the rate- determining step. R_2S_2 stands for disulfide. Cr(IV) undergoes further rapid processes by direct oxidation of mercaptosuccinic acid to

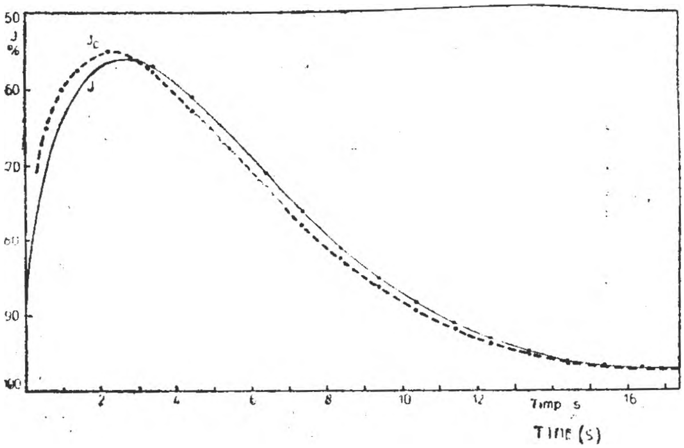

Fig. 3. Transmitted light intensity in percentage versus time and corrected curve. $[HCrO_4^-] = 4.0 \times 10^{-4}$, $[RSH] = 8.2 \times 10^{-3}$ $[H^+] = 2.02 \times 10^{-2}$ at 25.0°C and $\mu = 0.5$.

form Cr(III) and a thiyl free radical, or by forming Cr(V) species in an one-equivalent reaction with Cr(VI) [1—4].

$$\mathrm{Cr(IV)} + \mathrm{RSH} \rightarrow \mathrm{Cr(III)} + \mathrm{RS^{\circ}} \tag{6}$$

$$\mathrm{Cr(IV)} + \mathrm{Cr(VI)} \rightarrow 2\,\mathrm{Cr(V)} \tag{7}$$

Chromium (V) behaves like chromate, condensing and oxidizing mercaptosuccinic acid.

$$\mathrm{Cr(V)} + 2\,\mathrm{RSH} \rightarrow \mathrm{Cr(III)} + \mathrm{R_2S_2} \tag{8}$$

$$2\,\mathrm{RS^{\circ}} \rightarrow \mathrm{R_2S_2} \tag{9}$$

Kinetic measurements have been carried out under the conditions of a large excess of organic substrate to ensure first-order conditions. Under such circumstance the system becomes much simple:

$$\mathrm{HCrO_4^-} \xrightarrow[k_1']{+\mathrm{RSH}} \mathrm{RSCrO_3^-} \xrightarrow[k_2']{+\mathrm{RSH}} \text{Products} \tag{10}$$

with

$$k_1' = k_f[\mathrm{RSH}] + k_b = k_f\{[\mathrm{RSH}] + K_f^{-1}\}$$

$$k_2' = k_2[\mathrm{RSH}] \tag{11}$$

Following the absorbance at 410 nm where $\mathrm{HCrO_4^-}$, $\mathrm{RSCrO_3^-}$ and the final product Cr(III) having some excess mercaptosuccinic acid trapped as ligand, are the absorbing species

$$A = \varepsilon_0[\mathrm{HCrO_4^-}] + \varepsilon_1[\mathrm{RSCrO_3^-}] + \varepsilon_2[\mathrm{Cr(III)}] \tag{12}$$

with $\varepsilon_1 > \varepsilon_0 > \varepsilon_2$. Using the integrated rate law for a first-order series, the following relation is ontained [18]:

$$A - \varepsilon_2[\mathrm{Cr(VI)}]_0 = \left\{\varepsilon_0 + (\varepsilon_1 - \varepsilon_2)\frac{k_1'}{k_2' - k_1'}\right\}[\mathrm{Cr(VI)}]_0 \exp(-k_1't) + $$
$$+ (\varepsilon_1 - \varepsilon_2)\frac{k_1'}{k_2' - k_1'}[\mathrm{Cr(VI)}]_0 \exp(-k_2't) \tag{13}$$

Making the notation

$$\gamma_1 = \left\{\varepsilon_0 + (\varepsilon_1 - \varepsilon_2)\frac{k_1'}{k_2' - k_1'}\right\}[\mathrm{Cr(VI)}]_0$$

$$\gamma_2 = (\varepsilon_1 - \varepsilon_2)\frac{k_1'}{k_2' - k_1'}[\mathrm{Cr(VI)}]_0 \tag{14}$$

$$A_\infty = \varepsilon_2[\mathrm{Cr(VI)}]_0$$

equation (13) becomes

$$A - A_\infty = \gamma_1 \exp(-k_1't) + \gamma_2 \exp(-k_2't) \tag{15}$$

It seems reasonably to consider the electron-transfer process as rate-determining step. Therefore $k_1' > k_2'$ and towards the end of the reaction, the first step has been completely accomplished. The term $\exp(-k_1't)$ becomes very small compared to $\exp(-k_2't)$. Under this circumstance, neglecting first term in equation (15), the semilogarithmic representation of eq. (15) gives a straight line

$$\ln (A - A_\infty) = \ln \gamma_2 - k_2't \tag{16}$$

Both the pre-exponential term γ_2 and the rate coefficient for the slower process k_2' are obtainable from the intercept and the slope of the line. By means of these values, the differences $\gamma_2 \exp(-k_2't) - (A - A_\infty)$ can be computed and a new linear equation may be derived:

$$\ln\{\gamma_2 \exp(-k_2't) - (A - A_\infty)\} = \ln \gamma_1 - k_1't \tag{17}$$

from which the pre-exponential term and the rate coefficient for the faster process can be obtained. Plots of eqs. (16) and (17) are presented in figure 4. The points fit well with eq. (16) towards the end of the whole process, and eq. (17) at the begining of it. The correlation coefficients determined by using a least-square method were between 0.9940 and 0.9995. Table 2 collects the values of k_1' and k_2' for various mercaptosuccinic acid excess concentrations at 25°C, $\mu = 0.5$ and $[H^+] = 1.05 \times 10^{-2}$. The contribution of mercaptosuccinic acid to the total acidity is quite small (pK_a of 3.30, 4.92 and 10.64 [19]). Plots of both first-order rate coefficients k_1' and k_2' versus mercaptosuccinic acid concentration gave straight lines. The equations of the lines (least-square calculated) are:

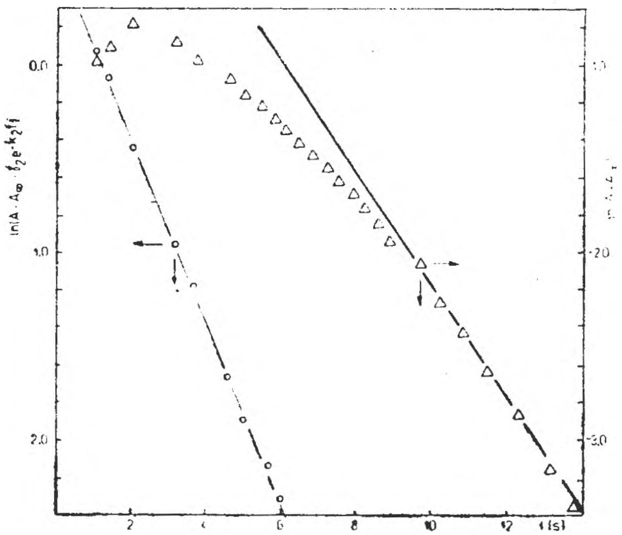

F i g. 4. Linear plots of eqs (16) and (17) for $[HCrO_4^-] = 4.0 \times 10^{-4}$, $[RSH] = 1.07 \times 10^{-2}$, $[H^+] = 1.05 \times 10^{-2}$.

$$k_1' = (2.8 \pm 1.1) \times 10^{-3} + (47.1 \pm 1.4)\,[RSH] \tag{18}$$

(correlation coefficient $r = 0.9975$) and

$$k_2' = (-7.4 \pm 0.8) \times 10^{[illegible]} + (28.4 \pm 1.2)\,[RSH] \tag{19}$$

(correlation coefficient $r = 0.9940$).

At acidity held constant one can identify $k_f = 47.1$ dm^{3}mol^{-1}s^{-1} and $k_b = 2.8 \times 10^{-3}$ s^{-1}. The ratio of these rate coefficients gives $K_f = k_f/k_b = (1.7 \pm 0.7) \times 10^3$ dm^{3}mol^{-1}. The equilibrium constant K_f kinetically determined is of the same order of magnitude as the value determined spectro-

Table 2

Kinetic data for various mercaptosuccinic acid concentrations. $[Cr(VI)] = 4 \times 10^{-4}$, $[H^+] = 1.05 \times 10^{-2}$, $\mu = 0.5$, T = 298 K

$10^2[RSH]$	$k_1'(s^{-1})$	r	$k_2'(s^{-1})$	r	k_f dm^3mol^{-1}	k_2 s^{-1}
0.546	0.280	0.9981	0.157	0.9942	47.911	28.75
	0.302	0.9986	0.152	0.9972		27.84
	0.296	0.9990	0.148	0.9981		27.11
	0.298	0.9988	0.153	0.9978		28.02
0.820	0.408	0.9983	0.214	0.9978	46.42	26.46
	0.416	0.9985	0.210	0.9989		25.61
	0.410	0.9977	0.212	0.9991		25.80
	0.414	0.9975	0.210	0.9978		25.61
1.07	0.525	0.9981	0.293	0.9987	45.10	27.38
	0.502	0.9995	0.291	0.9992		27.20
	0.512	0.9983	0.308	0.9972		28.79
1.25	0.621	0.9949	0.357	0.9978	46.74	28.56
	0.610	0.9988	0.366	0.9971		29.28
	0.616	0.9972	0.370	0.9995		29.60
1.60	0.795	0.9940	0.435	0.9982	47.36	27.19
	0.786	0.9942	0.446	0.9942		27.88
	0.782	0.9952	0.450	0.9945		28.13
	0.798	0.9983	0.431	0.9975		26.94
				Mean :	46.7 ± 1.5	27.6

photometrically from the appropriate measurements above mentioned. Its error is quite large but it overlaps the range $(1.48 \pm 0.07) \times 10^3\ dm^3mol^{-1}$. On the other hand, values of k_f may be calculated from the first-order k_1' divided by $\{[RSH] + K_f^{-1}\}$. These values also apear in Table 2 for all conditions employed. A mean of $46.7 \pm 1.5\ dm^3mol^{-1}s^{-1}$ has been obtained.

Concerning the linear equation (19), at first view one can consider the intercept as being zero. But the error in the intercept is not large enough to compensate for the negative value, and a negative rate coefficient has no rational interpretation. An alternative view-point is that proposed by McAuley and McCann [1] in the case of cysteine oxidation, and Baldea and Niac [10] in the case of thiosulfate oxidation. The rate law is of the form

$$-\frac{d[Cr(VI)]}{dt} = \frac{k_2K_f[RSH]^2}{1 + K_f[RSH]}[Cr(VI)] \tag{20}$$

Similar rate laws result from the accepted mechanisms of Cr(VI) oxidation of various inorganic and organic substrates. Because of the fact that excess of thiol was used, the term $K_f[RSH]$ in the denominator is 23.7 at the largest excess employed and 1 could be neglected, but only 8.1 at the smallest thiol concentration excess, where neglecting 1 brings about some error. The dependence of k_2' on [RSH] is hyperbolic, and it can explain the negative intercept in eq. (19). However, neglecting 1 in eq. (20), than a second-order, first-order in each the thiol and the thioester concentration, could be calculated as $k_2 =$

$= k_2'/[RSH]$. It is worth mentioning here that kinetic measurements followed the buildup and decay of the intermediate thioester. Second-order rate constants calculated in this way are given in the last column of Table 2. The mean value is 27.6 $dm^3mol^{-1}s^{-1}$ (stantdard deviation $\sigma_n = 1.2$).

The effect of hydrogen ion concentration on the rate the condensed compound formation and its decomposition has been investigated in the range of the acidity between 5.8×10^{-3} and 4.01×10^{-2} $mol \cdot dm^{-3}$. Data are presented in table 3. Both processes are dependent on $[H^+]$ as shown in figure 5, where a linear dependence was obtained. Therefore, the formation of 1 : 1 complex between Cr(VI) and mercaptosuccinic acid may be described by the rate law :

Table 3

The effect of hydrogen ion concentration on the rate coefficients at 25°C, $\mu = 0.5$ and $[RSH] = 8.2 \times 10^{-2}$

$10^2[H^+]$	$k_1'(s^{-1})$	r	k_f $dm^3,mol^{-1}s^{-1}$	$k_2'(s^{-1})$	r	k_2 $dm^3mol^{-1}s^{-1}$
0.578	0.398	0.9985	45.07	0.200	0.9981	24.39
	0.402	0.9987		0.206	0.9990	25.12
	0.404	0.9990		0.208	0.9980	25.37
1.041	0.408	0.9987	46.31	0.214	0.9978	26.10
	0.416	0.9985		0.210	0.9985	25.61
	0.410	0.9991		0.212	0.9991	25.85
	0.414	0.9977		0.210	0.9978	25.61
	0.410	0.9975		0.214	0.9988	26.10
2.021	0.426	0.9981	48.00	0.229	0.9940	27.93
	0.423	0.9984		0.228	0.9992	27.80
	0.426	0.9985		0.230	0.9990	28.05
	0.428	0.9979		0.230	0.9989	28.05
3.014	0.442	0.9987	49.8	0.245	0.9991	29.87
	0.446	0.9968		0.242	0.9982	29.51
	0.439	0.9991		0.246	0.9977	30.10
4.01	0.460	0.9964	51.83	0.262	0.9972	31.95
	0.458	0.9988		0.264	0.9982	32.20
	0.463	0.9991		0.260	0.9990	31.71
	0.459	0.9982		0.261	0.9986	31.83

$$rate_f = d[RSCrO_3^-] / dt = \{k_f^0 + k_f^H[H^+]\}[RSH][HCrO_4^-] \qquad (21)$$

with $k_f^0 = 44.1 \pm 0.3$ $dm^3mol^{-1}s^{-1}$ and $k_f^H = (1.92 \pm 0.01) \times 10^2$ $dm^6\ mol^{-2}s^{-1}$ It means that the substitution of OH group in $HOCrO_3^-$ takes place with undissociated mercaptosuccinic acid at the thiol function, and on the other hand, with H_2OCrO_3, formed in a rapid pre-equilibrium

$$\begin{aligned} &RSH + HOCrO_3^- \rightarrow RSCrO_3^- + H_2O \qquad k_f^0 \\ &HOCrO_3^- + H^+ \rightleftharpoons H_2OCrO_3 \qquad\qquad (22) \\ &RSH + H_2OCrO_3 \rightarrow RSCrO_3^- + H_3O^+ \qquad k_f^H \end{aligned}$$

The subsequent redox process obeys the following rate law:

$$\text{rate}_{ox} = -d[\text{Cr(VI)}]/dt = \{k + k^H[H^+]\}[\text{RSH}][\text{RSCrO}_3^-] \quad (23)$$

with $k = 23 \cdot 8 \pm 0.3$ dm^{3}mol^{-1}s^{-1} and $k^H = (2.03 \pm 0.13) \times 10^2$ dm^{6}mol^{-2}s^{-1} at 25°C and $\mu = 0.5$. Similar rate laws were found in the Cr(VI) oxidation of l-cysteine [2] and thioglycolic acid [3] under the conditions of a large excess of substrates and acidic media. The equation (23) illustrates that there are two paths, one without and one with a hydrogen ion involvement in the decomposition of the complex, when it colides with another thiol molecule to yield Cr(IV) and disulfide (bi-equivalent processes)

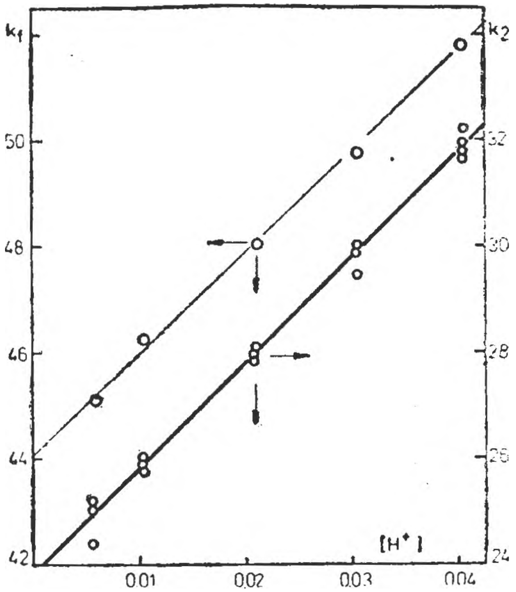

Fig. 5. The effect of hydrogen ion concentration on the second-order rate coefficients k_f and k_2 at growth and decay of complex.

$$\text{RSCrO}_3^- + \text{RSH} \rightarrow \text{Cr(IV)} + R_2S_2 \qquad k$$

$$\text{RSCrO}_3^- + \text{RSH} + H^+ \rightarrow \text{Cr(IV)} + R_2S_2 \qquad k^H \qquad (24')$$

Two alternative ways, kinetically indistinguishable, are those in which Cr(V) and disulfide radical are formed (one-equivalent processes)

$$\text{RSCrO}_3^- + \text{RSH} \rightarrow \text{Cr(V)} + \text{RS}\,{:}.\text{SR} \qquad (24'')$$

$$\text{RSCrO}_3^- + \text{RSH} + H^+ \rightarrow \text{Cr(V)} + \text{RS}\,{:}.\,\text{SR}$$

Disulfide radical, having a sulfur-sulfur three-electron bond with the third electron in an antibonding orbital, has been identified [20]. It is far more stable than thiyl radical RS°. Its formation requires a second thiol molecule. Further Cr(V) can oxidize another two substrate molecules as shown above.

Table 4 compares kinetic data concerning complex formation and redox decay for several thioderivatives oxidized by chromate in acidic media. When ethanethiol was oxidized, the route without hydrogen ion involvement has not been identified, but a monomolecular decomposition of thioester took place [5] similar to the oxidation of cysteine at neutral pH [4]. In all the cases presented, extensive formation of complexes having S—Cr link have been found, with small equilibrium discrimination of the Cr(VI) centre towards these thiols (one order of magnitude on K_f). On the contrary, there is an important kinetic discrimination in both the complex formation and its subsequent redox decomposition (three and respective four orders of magnitude in k_f^H and k^H).

Table 4

Comparation of the kinetic data on the formation of substrate-chromate complex and redox decomposition at 25°C for various thiocompounds.

Substrate	k_f^0	k_f^H	K_f	k	k^H	Ref.
$HS_2O_3^-$	—	3.7×10^5	1.2×10^4	1.79×10^2	1.85×10^4	10,11
C_2H_5SH	—	2.3×10^4	1.15×10^1	—	15	5
l-Cysteine	2.1	1.4×10^2	1.48×10^3	7.7	0.7	2
			1.03×10^3	12		1
$CH_2(SH)COOH$	66.3	2.47×10^3	1.1×10^3	11	4.33×10^2	3
Thiomalic acid	44.1	1.92×10^2	1.48×10^3	23.8	2.03×10^2	This work

the nature of the thiol, concernung redox behaviour, steric effects due to the groups in the vicinity of -SH, brings about large difference between the rates. Comparing cysteine, which has a small $-NH_3^+$ group in α — position, with mercaptoacetic acid and mercaptosuccinic acid, having bulky group — COOH in α — position the order in k_f^H and k^H is: mercaptoacetic acid > mercaptosuccinic acid > cysteine, showing that only steric effects cannot explain this behaviour. If the ratio k_f/k_2 (calculated at a given hydrogen ion concentration and taking into account zero-order and first-order terms in H^+) is compared, it is affected by the nature of thiol in the order cysteine > mercaptoacetic acid > mercaptosuccinic acid. Considering the question of one- versus two-electron transfer for the rate determining step, further experimental evidence as EPR measurements, some induced reaction with Fe(II), Mn(II) [21] are requested. Kwong and Pennington favoured the two-electron transfer way on the basis of stoichiometry, EPR studies and using Mn(II) in the case of cysteine oxidation in neutral media [4], However, this do not unequivocally preclude the participation of Cr(V), which can form some complex with the excess thiol, especially when chelation is probable, prior its reduction to Cr(III).

REFERENCES

1. J. P. McCann, A. McAuley, *J. Chem. Soc. Dalton Trans.*, **1975**, 783; A. McAuley M. A. Olatunji, *Can. J. Chem.*, **55**, 3328, 3335 (1977).
2. I. Baldea, G. Niac, *Studia Univ. Babeş-Bolyai, Chem.*, **31**(2), 41 (1986).
3. I. Baldea, *Studia Univ. Babeş-Bolyai, Chem.*, **32**(2), 42 (1987).
4. D. W. J. Kwong, D. E. Pennington, *Inorg. Chem.*, **23**, 2528 (1984).
5. G. Niac, S. Schön, I. Baldea, *Studia Univ. Babeş-Bolyai, Chem.*, **31**(2), 31 (1986).
6. P. H. Connett, K. E. Wetterhahn, *J. Amer. Chem. Soc.*, **108**, 1842 (1986); *idem.* **107**, 4282 (1985).
7. G. P. Haight, D. C. Richardson, N. H. Coburn, *Inorg. Chem.*, **3**, 1777 (1964); J. Y. Tong, R. J. Johnson, *Inorg. Chem.*, **5**, 1902 (1966).
8. K. K. SenGupta, J. K. Chaklandar, *J. Chem. Soc. Dalton Trans.*, **1974**, 222.
9. F. H. Westheimer, *Chem. Rev.*, **45**, 419 (1949); P. M. Nave, W. S. Trahanovsky, *J. Amer. Chem. Soc.*, **92**, 1120 (1970); J. Roček, A. E. Radkowsky, *J. Amer. Chem. Soc.*, **90**, 2986 (1968).

10. I. Baldea, G. Niac, *Inorg. Chem.*, **7**, 1112 (1968); *idem* **9**, 110 (1970).
11. C. T. Lin, K. J. Beattie, *J. Amer. Chem. Soc.*, **94**, 3011 (1972).
12. U. Kläning, M. C. R. Symons, *J. Chem. Soc.*, **1961**, 3204.
13. V. Srinivasan, J. Roček, *J. Amer. Chem. Soc.*, **96**, 127 (1974).
14. G. P. Haight, G. M. Jurish, M. T. Keslo, P. J. Merrill, *Inorg. Chem.*, **24**, 2740 (1985).
15. Y. Hojo, Y. Sugiura, H. Tanaka, *J. Inorg. Nucl. Chem.*, **39**, **1859** (1977).
16. J. Hill, N. M. Malik, A. McAuley, *J. Chem. Soc.*, **1970 A**, 643; J. Hill, A. McAuley, *idem*, **1968 A**, 156; A. McAuley, *Coord. Chem. Rev.*, **5**, 245 (1970).
17. G. Schwarzenbach, J. Meier, *J. Inorg. Nucl. Chem.*, **8**, 302 (1958); J. Y. Tong, E. L. King, *J. Amer. Chem. Soc.*, **75**, 6180 (1953).
18. A. Haim, N. Sutin, *J. Amer. Chem. Soc.*, **88**, 5343 (1960).
19. R. G. Cheney, Q. Fernando, H. Freiser, *J. Amer. Chem. Soc.*, **63**, 2055 (1959).
20. Z. M. Hoffman, E. Hayon, *J. Amer. Chem. Soc.*, **94**, 7950 (1972); K. D. Asmus, D. Bahnemann, C. H. Fisher, D. Weltwisch, *J. Amer. Chem. Soc.*, **101**, 5322 (1979); K. D. Asmus, *Acc. Ahem. Res.*, **12**, 436 (1979); M. Bonifacic, J. Weiss, S. A. Chaudhri, K. D. Asmus, *J. Phys .Chem.*, **89**, 3910 (1985).
21. W. Watanabe, F. H. Westheimer, *J. Chem. Phys.*, **17**, 61 (1949).

STUDIA UNIV. BABEŞ-BOLYAI, CHEMIA, XXXIX, 1-2, 1994

STUDIUM DER REDUKTION UND DER QUANTITATIVEN BESTIMMUNGSMÖGLICHKEITEN DES In^{+} IN WÄSSRIGEN CHLORIDLÖSUNGEN DURCH KLASSISCHE UND WECHSELSTROMPOLAROGRAPHIE

ION GH. TĂNASE*, IULIA DAVID*, ION IONECI*

ABSTRACT: — The reduction study of the In^{3+}-ion on the dropping mercury electrode. It was studied the reduction of the 'In^{3+}-ion' on the dropping mercury electrode by direct and alternating current polarography. The process is reversible, diffusion-controlled and implies the transfer of 3 electrons, when HCl (0.1—5M) was used as supporting electrolyte. Using alternating current polarography with sensitive phase, In^{3+} can be determined in the concentration range $1 \cdot 10^{-3}$ — $1 \cdot 10^{-6}$ M with a detection limit of $5 \cdot 10^{-7}$ M.

Obwohl Indium ein in Quecksilber leicht lösliches Metall ist, Amalgame bildend und demzufolge zu erwarten ist, daß das In^{3+}-Ion sich in einer Reihe von Grundelektrolyten, auf Quecksilberelektroden reduziert und daß man deutlich ausgebildete $i = f(\varepsilon)$-Kurven erhält, gibt es in der Fachliteratur verhältnismäßig wenige Anweisungen hinsichtlich der Bestimmung der Mikromengen des Indiums durch polarographische und voltammetrische Methoden. Trotzdem, die Kinetik der Oxidation und der Reduktion auf Quecksilberelektroden, der verschiedenen chemischen Arten in denen Indium auftreten kann, bildeten das Thema mehrerer Arbeiten die in der Fachliteratur erschienen sind [1—5]. Infolge dieser Studien kam man zu der Schlußfolgerung, daß in nicht komplexierenden, wässrigen Medien das Polarogramm für die Reduktion des In^{3+} durch einen Wert des Halbstufenpotentials von $\varepsilon_{1/2} = -0{,}550$ V vs. GKE, charakterisiert ist. Das Halbstufenpotential entsprechend der Reduktion des komplexen Ions, in wässrigen Medien mit komplexierender Aktion, welche Halogenidionen [6], 2,2-Dipyridil [7], Zitrat [8], Glyoxalat [9], Thiouree, Cistein und Thiosemicarbazid [10] enthalten in proteinhaltigen Milieu, verschiebt sich gegen negativere Werte, so daß man $\varepsilon_{1/2} = -0{,}600 \div -0{,}620$ V vs. GKE oder sogar noch kathodische Werte erhält.

Bezüglich der Reduktionskinetik des In^{3+}-Ions auf Quecksilberelektroden Markovac und Lowrecek [4] erläuterten die Neigung der Tafel-Gerade, durch die Anwendung der charakteristischen Gleichungen für die anodische und katodische Reaktion und zeigten, daß diese als Kriterium für die Festlegung des Reaktionsmechanismuses benutzt werden kann.

Hinsichtlich der Bestimmung der kinetischen Parameter des nichtkatalytischen Elektroreduktionsprozesses des In^{3+} im wässrigen Milieu, auf Quecksilberkathode, beziehungsweise der standard Geschwindigkeitskonstante (k_s) und des charakteristischen scheinbaren Koeffizienten (α_k), diese wurde von Turyan und Strizkov [12] angepackt, welche die Prozesse die parallel mit der kataly-

---

* *Lehrsuhl fur Analytische Chemie, Fakultat fur Chemie, Universitat Bukarest*

tischen und nichtkatalytischen Entladung des In(III) verlaufen, in Betracht nahmen, Prozesse die die kinetische Analyse viel komplizieren.

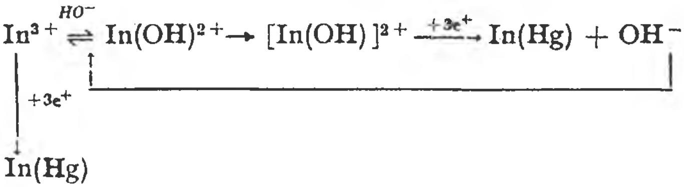

$$In^{3+} \overset{HO^-}{\rightleftharpoons} In(OH)^{2+} \rightarrow [In(OH)]^{2+} \xrightarrow{+3e^+} In(Hg) + OH^-$$

$$In^{3+} \xrightarrow{+3e^+} In(Hg)$$

In der oben aufgeführten katalytischen Reaktion, ist die langsame Etappe der Entwässerung $[In(OH)]^{2+}$ eine Oberflächenreaktion. Auf diese Weise war die Untersuchung der nichtkatalytischen Entladung des In^{3+} mit Hilfe der Gleichstromopolarographie möglich. Auf polarographischer Weise kann man eine deutliche Differenzierung des katalytischen Prozesses sowohl vom nichtkatalytischen Prozess als auch von der Entladung der Wasserstoffionen erreichen. Durch die Festsetzung der kinetischen Parameter der nichtkatalytischen Entladung des In^{3+}, im 1 $mol \cdot L^{-1}$ $NaClO_4 + HClO_4$ Milieu, kann man feststellen, daß sich ihre Werte mit der Veränderung des pH's der Lösung nicht ändern und der Wert der standard Konstante ist $k_s = 1 \cdot 10^{-8}$ $cm \cdot s^{-1}$.

Die Erforschung des Reduktionsmechanismus des In^{3+} auf der Quecksilber-Tropfelektrode, durch die Benutzung der Gleichstrompolarographie als auch der Oszillopolarographie, um die erhaltenen Resultate zu vergleichen, stellt ein einzigartiges Interesse dar [13], weil auf dieser Weise, sowohl die Untersuchung der Reversibilität der Prozesse die auf der Elektrode stattfinden als auch die Berechnung des Diffusionskoeffizienten möglich sind, wenn man als Grundelektrolyt eine 1 $mol \cdot L^{-1}$ HCl Lösung verwendet ($D = 2{,}95 \cdot 10^{-6}$ $cm^2 \cdot s^{-1}$).

In der Literatur gibt es widersprüchliche Resultate bezüglich des Einflusses der verschiedenen Grundelektrolyten. Somit hat man herausgefunden, daß der Reduktionsprozeß des In^{3+} in Cl^- und NO_3^- haltigen Medium ein irreversibeler Prozeß [14, 15] ist, wahrend man festgestellt hat, daß er im Thiocianat- und im nichtkomplexierenden Medium reversibel und in einigen Leitelektrolyten quasireversibel verläuft [16]. Folglich, Kapoor und Jian [17] untersuchten den Einfluß des pH's und der Temperatur auf die polarographische Reduktion des In^{3+}, indem sie $NaClO_4$ als Leitelektrolyt verwendeten. Sie zogen die Schlußfolgerung, daß der pH eine wichtige Rolle spielt, so daß bei $pH \geq 3$ die Reduktion reversibel und bei $pH < 3$ irreversibel ist. Die Irreversibilität der drei-Elektronen-Reduktion des In^{3+} im wassrigen Milieu ist durch die Anwesenheit und durch die Konzentration einiger Anionen und Kationen betont [18].

Durch die Erforschung der Reduktion des In^{3+} im nichtkomplexierenden Medium, indem man als Leitelektrolyt $NaClO_4$, $LiNO_3$, KNO_3, $RbNO_3$, $Ca\ NO_3$ mit Zugabe von $HClO_4$ oder HNO_3 verwendet, bei $pH \leq 3$, versuchte man die verschiedenen katalytischen Prozesse die erscheinen und ihre widernatürliche Abhängigkeit von der Natur des Kations, dessen Salz man als Leitelektrolyt verwendet, zu erklären [19].

Die Bestimmung der niedrigen Konzentrationen des In^{3+} aus verschiedenen Medien wurde durch polarographische und voltammetrische Techniken angepackt. Demzufolge ermöglichen die polarographischen Techniken im Wechselstrom und die Techniken der Stripping-Voltammetrie die Bestimmung des In^{3+} im Konzentrationsbereich $1 \cdot 10^{-5} - 1 \cdot 10^{-6}$ mol · L^{-1} [20–22]

Experimenteller Teil. Für die Verwirklichung der polarographischen Messungen im Gleichstrom und im Wechselstrom, wurde ein polarographisches Komplex mit drei Elektroden PRG3-Tacussel und eine RMO6 Tacussel Zelle, die mit einer thermostatierenden Hülle versehen ist, benützt. Die Kapillare die für die Herstellung der Quecksilber-Tropfelektrode verwendet wurde, hatte folgende Kennzeichen: $m = 1{,}073$ mg · s^{-1}; $\tau = 4{,}185$ s welche mit 0,1 mol · L^{-1} KCl bei $-0{,}500$ V vs. GKE, bei einer Höhe der Quecksilbersäule von $h = 50$ cm, bestimmt wurden. Als Gegenelektrode wurde eine spiralförmige Platin-Elektrode Pt 121 Tacussel verwendet.

Alle Messungen wurden in streng kontrollierten Temperaturbedingungen bei 25 ± 0,1°C ausgeführt und die Potentiale wurden gegen eine gesättigte Kalomell-Elektrode (GKE) bestimmt

Die verwendeten Substanzen waren von hoher Reinigkeit. Für die Zubereitung der Lösungen und für die Ausspülung des Glasgeschirrs wurde dreifach distilliertes Wasser benützt.

Aus allen Lösungen die polarographiert wurden, entfernte man den Sauerstoff durch Durchleiten, für 10 Minuten, von gereinigten Argon.

Ergebnisse und Diskussionen. In der vorliegenden Arbeit wird die Reduktion des In^{3+}-Ions auf der Quecksilber-Tropfelektrode behandelt. In diesem Sinne wurde die klassische und die Wechselstrompolarographie, im Chlorid-Medium als Leitelektrolyt, auf einem breiten Konzentrationsbereich benützt. Somit verfolgt man die Art in der die Grundparameter der Methode die quantitative Bestimmung des Indiums, hinsichtlich der Erhöhung der Empfindlichkeit und der Selektivität der polarographischen und voltammetrischen Bestimmungen beeinflussen, indem man auch den Mechanismus des Elektrodenprozesses der Reduktion des In^{3+}-Ions auf der Quecksilber-Tropfelektrode berücksichtigt. Die Ausarbeitung einer Dosierungsmethode des In^{3+}, ins Besondere bei niedrigen Konzentrationen, auf elektrochemischer Weise, welche die Nachweisgrenze unter $1 \cdot 10^{-5}$ mol · L^{-1} senken soll, benötigt vor allem ein vertieftes Studium der Reduktionskinetik dieses Ions.

Indium besitzt eine große Löslichkeit in Quecksilber ($> 30\%$), demzufolge eine große Tendenz Amalgame zu bilden, welche einen großen Vorteil für die Benützung der Quecksilber-Tropfelektrodee für die Bestimmung des In^{3+} bei niedrigen Konzentrationen darstellt. Die in der Literatur vorhandenen Daten deuten für die Geschwindigkeitskonstante der Reduktionsreaktion des In^{3+} Werte die größer sind als 0,1 cm · s^{-1}, welche einen reversiblen Prozeß im Fall der Gleichstrompolarographie anzeigen.

Für die Festsetzung der optimalen Bedingungen für die Bestimmung des In^{3+} durch Wechselstrompolarographie mit sensibler Phase wurde zu erst ein Studium über die Reduktion des In^{3+}-Ions in HCl-Lösungen von verschiedenen Konzentrationen als Leitelektrolyt, ausgeführt, indem man parallel gleichstrompolarographische und wechselstrompolarographische Messungen durchführte. Die Resultate der Messungen die man mit den zwei Techniken erhiehlt sind in der Tabelle 1 niedergelegt. Dieses Studium erlaubte die Bestimmung der Halbstufenpotentiale, beziehungsweise der Peakpotentiale, der Weite bei der Halbhöhe der wechselstrompolarographischen Kurven $b_{1/2}$, der Neigungen der Geraden der logaritmischen Analyse sowohl für die Gleichstrompolarogramme als auch für die Wechselstrompolarogramme.

In allen getesteten HCl-Lösungen sind die Kurven symmetrisch und gut ausgebildet, sowohl in der klassischen als auch in der Wechselstrompolarographie (Abbildung 1).

Wenn man für die Schätzung des Reversibilitätgrades und der getauschten Elektronenzahl im Reduktionsprozeß des In^{3+} auf der Quecksilber-Tropfelektrode, die Werte der Weite der Kurven in der Wechselstrompolarographie in Betracht nimmt, dann kann man bemerken, daß diese sehr nahe dem Wert 90/z mV sind, anzeigend die Transferierung von z = 3 Elektronen an der Oberfläche des Quecksilbertropfens, gemäß der Gleichung:

$$In^{3+} + 3e^- \rightleftharpoons In(Hg)$$

Für die Bestimmung der Halbstufenpotentiale $\varepsilon_{1/2}$, der Peakpotentiale ε_p und der Ladungstransferkoeffizienten hat man die logaritmische Analyse durchgeführt für die Reduktion des In^{3+} — Ions im wässrigen Medium erhaltenen Gleichstrom und Wechselstrompolarogrammen, wenn man als Leitelektrolyt HCl von verschiedenen Konzentrationen benutzte.

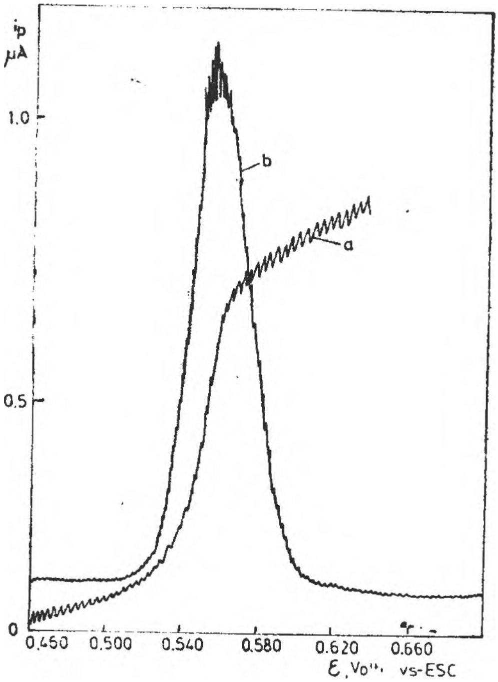

Abb. 1. Polarogramme im Gleichstrom (1) und im Wechselstrom (2) entsprechend der Reduktion einer $5 \cdot 10^{-4}$ mol. L^{-1} In^{3+} — Lösung in 2 mol · L^{-1} HCl · $\nu = 50$ Hz; $\Delta E = 5$ mV; $\varphi = 0^\circ$.

Die graphischen Darstellungen der Abhängigkeiten $\log\left(\frac{i_d - i}{i}\right) = f(\varepsilon)$ für die Wechselstrompolarogramme, beziehungsweise $\log\left[\left(\frac{i_p}{i}\right)^{1/2} \pm \left(\frac{i_p - i}{i}\right)^{1/2}\right] = f(\varepsilon)$ sind linear und die Steilheiten dieser Geraden nähern sich den theoretischen Werten 0,05916/3 V, beziehungsweise 0,120/3 V, was eine reversible Reduktionsreaktion des In^{3+} — Ions auf der Oberfläche der Tropfelektrode anzeigt und die Reduktionsreaktion impliziert den Tausch von 3 Elektronen.

Wenn man die Veränderung des Grenzstromes der bei der Reduktion des In^{3+} erhaltenen Gleichstrompolarogramme als Funktion der Höhe der Quecksilbersäule verfolgt, erhält man eine lineare Abhängigkeit $i_d = f(h^{1/2})$ und auch eine Gerade $\log i_d = f(h^{1/2})$ mit der Neigung 0,51, was ebenfalls einen reversiblen Elektrodenprozeß, dessen Strom diffusionsbedingt ist, indiziert.

In wässrigen Lösungen die als Leitelektrolyt HCl bei verschiedenen Konzentrationen enthalten bleiben das Halbstufenpotential $\varepsilon_{1/2}$ bzw. das Peakpotential ε_p im Bereich $-0{,}535 \div -0{,}563$ V vs. GKE, was beweist, daß in Lösungen die HCl bei diesen Konzentrationen enthalten, Indium nicht als $InCl_6^{-}$ vorhanden ist.

Aus den Vorgezeigten geht hervor, daß in HCl-Medium bei Konzentrationen die sich im Bereich 0,1 — 5M befinden, die Reduktion des In^{3+} — Ion auf der Oberfläche der Quecksilber-Tropfelektrode die Transferierung von $3e^-$ impliziert, ein Prozeß der reversibel, in diffusionskontrollierten Bedingungen verläuft.

Die Resultate die man infolge dieses Studiums, der für die Reduktionsreaktion des In^{3+}-Ions an der Quecksilber-Tropfelektrode durchgeführt wurde, erhielt, können überzeugen, daß die Verwendung des HCl als Leitelektrolyt passend ist um dieser Reaktion einen hohen Reversibilitätsgrad, verstärkte Ströme, symmetrische und gut definierte Wechselstrompolarogramme zu sichern

Nachdem man dieses Reduktionsstudium des In^{3+}-Ions durchgeführt hat, untersuchte man den Einfluß der verschiedenen Parameter der Methode die quantitative Bestimmung des Indiums durch Wechselstrompolarographie bedingen, um die Selektivität und die Empfindlichkeit der Methode zu erhöhen. Um eine hohe Empfindlichkeit, kombiniert mit einer guten Genauigkeit und Selektivität zu erhalten ist es notwendig, daß die charakteristischen Parameter dieser Technik (Amplitude ΔE, und Frequenz ν der übereinandergelegten Wechselspannung, die empfindliche Detektionsphase φ) optimisiert werden. In diesem Sinne wurde zu erst auf den Einfluß der Amplitude ΔE und der Frequenz ν auf die Erhöhung der Empfindlichkeit aktioniert. Somit ist in Abbildung 2 die Veränderungweise der Intensität des maximalen Peakstroms, für die Reduktion des In^{3+}-Ions in HCl-Lösungen von verschiedenen Konzentrationen mit der Amplitude der ubergelegten Wechselspannung dargestellt, wo man eine lineare Abhängigkeit feststellen kann.

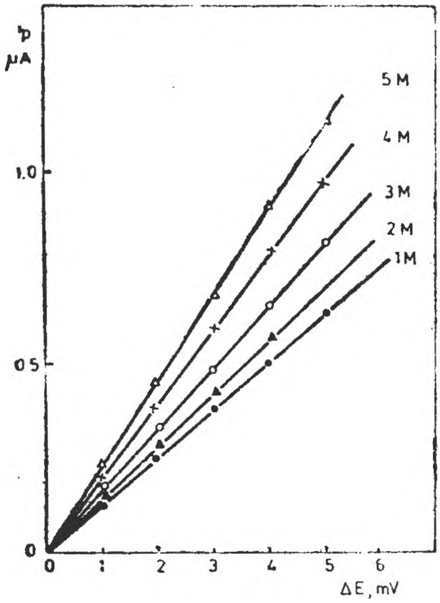

Abb. 2. Veränderung des maximalen Peakstromes i_p, für die Reduktion einer $5 \cdot 10^{-5}$ mol·L^{-1} In^{3+} -Lösung, als Funktion der Amplitude der übergelegten Wechselspannung ΔE, bei verschiedenen Konzentrationen des Leitelektrolytes.

Die Rolle des Phasenwinkels in der Wechselstrompolarographie mit empfindlicher Phase ist sehr wichtig bei der Messung der faradayschen Komponente des Wechselstroms und bei der Beseitigung des kapazitiven Teils.

In Abbildung 3 sind die Wechselstrompolarogramme entsprechend des In^{3+}-Elektrodenprozesses die man bei verschiedenen Werten des Detektionsphasenwinkels φ, in 2M—HCl—Lösung, erhielt, dargestellt.

Der Einfluß der Detektionsphase φ ist deutlich, in erster Reihe in der Form, der

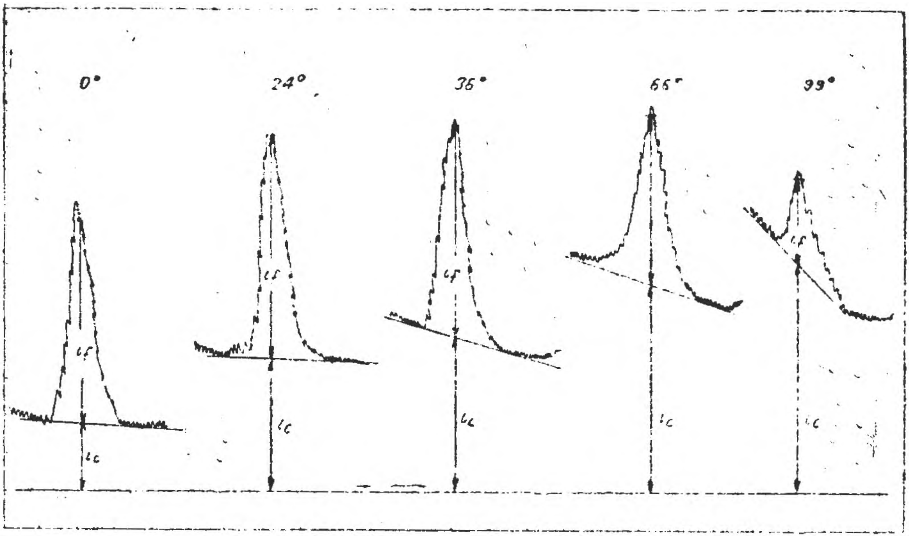

Abb. 3. Der Einfluß des Detektionsphasenwinkels auf die faradayischen (i_f) und kapazitiven (i_c) Strömen bei der Reduktion des In^{3+}-Ions, bei einer Konzentration von $5 \cdot 10^{-5}$ mol $\cdot$ L^{-1}, in 1 mol $\cdot$ L^{-1} HCl $\cdot$ $\Delta E = 5$ mV; $\nu = 50$ Hz; $t = 25$°C.

guten Definierung und der Symmetrie der Wechselstrompolarogramme aber auch in der guten Ausbildung der Polarogramme im Gleichstrom.

Man kann bemerken daß die faradayische Komponente einen maximalen Wert erreicht und das Polarogramm symmetrisch ist für die Werte des Detektionsphasenwinkels um 0°.

Nachdem man die Aktionsweise der Grundparameter der Methode kannte, untersuchte man die Abhängigkeit des maximalen Peakstromes von der Konzentration des Depolarisators (In^{3+}). Weil aber die Konzentration nicht der einzige Parameter ist von dem der maximale Peakstrom abhängt, für die Aufstellung der Eichkurve für die quantitative Bestimmung des In^{3+} durch sinusoidale Wechselstrompolarographie, war es nötig die Aktionsweise der Parameter der Methode für jeden untersuchten Konzentrationsbereich in Betracht zu nehmen, so daß die lineare Abhängigkeit des maximalen Peakstromes von der Konzentration erhalten bleibt. Da die Reduktion des In^{3+} in stark sauren Lösungen reversibel verläuft, für die Aufstellung der Kalibriergeraden wurde eine 1M—HCl—Lösung gewählt. In Abbildungen 4 und 5 sind die Eichkurven für die quantitative Bestimmung des In^{3+}, für die Konzentrationsbereiche $1 \cdot 10^{-4} - 1 \cdot 10^{-5}$ mol. $\cdot$ L^{-1} (Abb. 4) und $1 \cdot 10^{-5} - 1 \cdot 10^{-5}$ mol. $\cdot$ L^{-1} (Abb. 5) vorgezeigt. In Abbildung 6 sind die Polarogramme im sinusoidalen Wechselstrom für $1 \cdot 10^{-6}$ mol.L^{-1} In^{3+} in 0,1 mol.L^{-1} HCl bei verschiedenen Amplituden der übergelegten Wechselspannung ΔE, dargestellt.

Die Nachweisgrenze der quantitativen Bestimmung des In^{3+} durch diese Technik wurde bei $5 \cdot 10^{-7}$ mol $\cdot$ L^{-1} festgelegt.

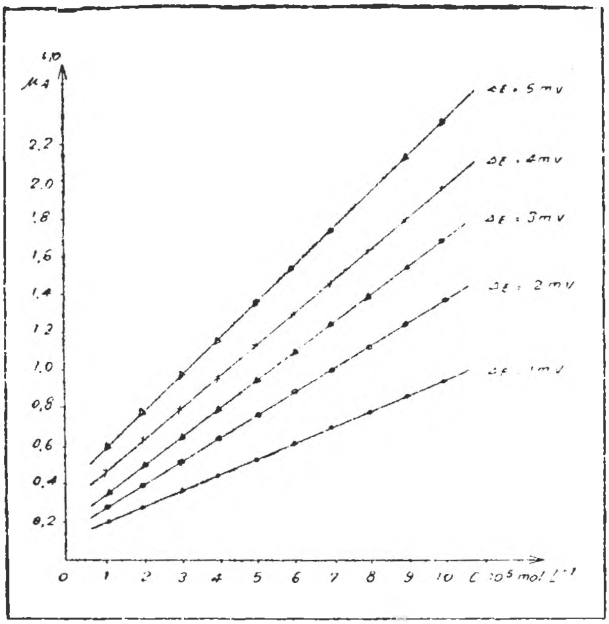

Abb. 4. Eichkurven für die Bestimmung des In^{3+} durch Wechselstrompolarographie mit empfindlicher Phase, im Konzentrationsbereich $1 \cdot 10^{-4} - 1 \cdot 10^{-5}$ mol · $L^{-1} In^{3+}$ in 1 mol · L^{-1} HCl, bei verschiedenen Amplituden der übergelegten Wechselspannung. $\nu = 50$ Hz; $\varphi = 0°$; $t = 25°C$.

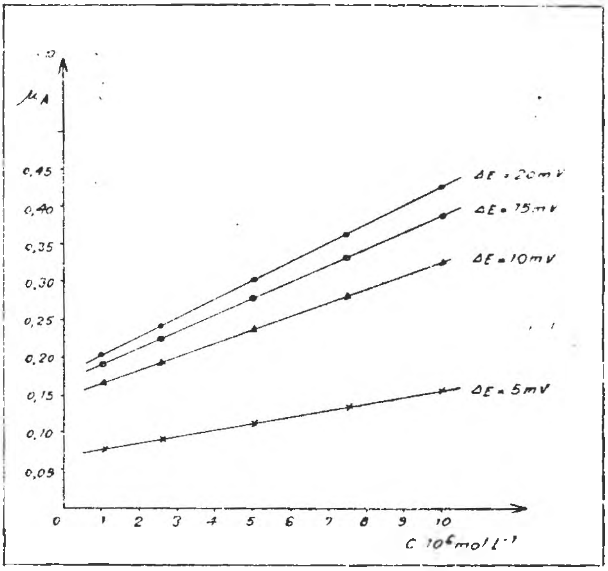

Abb. 5. Eichkurven für die quantitative Bestimmung des In^{3+} durch Wechselstrompolarographie mit empfindlicher Phase, im Konzentrationsbereich $1 \cdot 10^{-4} - 1 \cdot 10^{-5}$ mol · $L^{-1} In^{3+}$ im 1 mol · L^{-1} HCl, bei verschiedenen Amplituden der übergelegten Wechselspannung. $\nu = 50$ Hz; $\varphi = 0°$; $t = 25°C$.

Als Schlußfolgerung kann man behaupten:

— obwohl Indium in Quecksilber leicht löslich ist und zu erwarten wäre, daß die Reduktion des In^{3+} auf der Quecksilber-Tropfelektrode, in einer Vielfaltigkeit von wässrigen Medien die verschiedene Leitelektrolyten enthalten, reversibel und diffusionskontrolliert verläuft, experimentell wurde aber festgestellt daß dieses nur in stark sauren Medien stattfindet. Aus diesem Grund wurde als Leitelektrolyt HCl von verschiedenen Konzentrationen gewählt.

— das Studium des Einflusses der HCl-Konzentration auf die Reduktion des In^{3+}-Ions beweiste daß die Reduktion diffusioneskontrolliert, reversibel und gemäß der Gleichung

$$In^{3+} + 3e^- = In(Hg)$$

verläuft, bei HCl-Konzentrationen zwischen 0,5 M und 5M.

— das Studium des Einflusses der charakteristischen operationalen Parameter der sinusoidalen Wechselstrompolarographie mit sensibler Phase erlaubte die Feststellung der wirksamen Bestimmungsbedingungen des In^{3+} durch diese Technik im Konzentrationsbereich $1 \cdot 10^{-3} - 5 \cdot 10^{-5}$ mol · L^{-1}

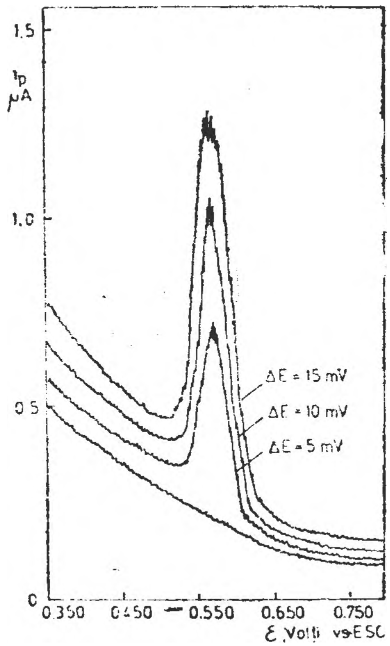

A b b. 6. Wechselstrompolarogramme für $1 \cdot 10^{-6}$ mol·L^{-1} In^{3+} in 1·mol·L^{-1} HCl, bei verschiedenen Werten der Amplitude der übergelegten Wechselspannung. $\nu = 50$Hz; $\varphi = 0°$; $t = 25°$C.

Tabelle 1.

Charakteristiken der für die Reduktion einer 5.10^{-5} mol. L In^{3+} inx.mol.L HCl-Lösung, auf der Quecksilber-Tropfelektrode, erhaltenen Gleichstrom-bzw = Wechselstrompolarogramme. ($t = 25°C$: $\Delta E = 5$ mV; $v = 50$ Hz; $\varphi = 0°$)

Nr. crt.	Leitelektrolyt	Gleichstrompolarographie			Wechselstrompolarographie		
		$\varepsilon_{1/2}$ mV vs. GKE	Neigung, mV	αn	ε_p, mV vs. GKE	Neigung mV	$b_{1/2}$ mV
1	0,1 M HCl	−0,565	17	0,87	−0,557	30	42
2	0,5 M HCl	−0,560	17	0,85	−0,561	31	42
3	1,0 M HCl	−0,563	17	0,84	−0,564	31	43
4	1,5 M HCl	−0,561	18	0,85	−0,563	32	43
5	2,0 M HCl	−0,563	17	0,84	−0,565	31	42
6	2,5 M HCl	−0,550	16	0,84	−0,553	32	43
7	3,0 M HCl	−0,535	16	0,83	−0,538	32	44
8	3,5 M HCl	−0,542	17	0,85	−0,545	31	45
9	4,0 M HCl	−0,548	17	0,84	−0,550	32	44
10	4,5 M HCl	−0,555	18	0,85	−0,557	31	43
11	5,0 M HCl	−0,563	17	0,85	−0,565	32	44

LITERATUR

1. B. Breyer, F. Gutman, S. Hacobran, *Australian J. Sci. Res.*, **A3,** 567 (1950)
2. D. J. Feret, G. W. C. Milner, *Analyst*, **80,** 132 (1955).
3. G. C. Barker, *Anal. Chim. Acta*, **18,** 118 (1958).
4. B. Lovrecek, *J. Phys. Chem.*, **63,** 4785 (1959).
5. B. N. Popov, J. V. Ivshim, *Croatica Chem. Acta*, **60**(**2**). 315, 1987.
6. N. K. Strizhav, *Chem. Abstr.*, **107**(**4**). 1987, 30170a.
7. A. I. Molodov, S. N. Markoslyan, *Electrokhimya*, **10**(**8**). 911 (1974).
8. A. I. Molodov, *Electrokhimya*, **1,** 158, (1965).
9. K. K. Choudhary, D. S. Join, J. N. Gaur, *Indian J. Chem.*, **14A,** 596 (1976).
10. Li Nangiang, Zhang Jiankang, *Chem. Abstr.*, **104**(**18**), 1986, 157944x.
11. S. N. Prabhy, S. S. Kelhar, *J. Electrochem. Soc.*, **29.** 3 (1980).
12. Ya. T. Turyan, N. K. Strizhav, *Electrokhimya*, **24.** 4, (1985).
13. L. S. Kopanskaya, *Electrokhimya*, **3,** 7 (1968).
14. G. W. Dem, K. W. Murray, *J. Electrochem. Soc.*, **113,** 217, (1966).
15. J. N. Gaur, D. S. Join, *Electrochim. Acta*, **11.** 1661, (1966); **12,** 413, (1967).
16. J. N. Gaur, D. S. Join, *J. Chem. Soc.*, 593, (1968).
17. R. C. Kapoor, S. L. Join, *J. Indian Chem. Soc.*, **59,** 203, (1982).
18. Indu Balla, Kailash Chandrs, Mukhtar Sirgh, *Indian J. Chem.*, **22A,** 596 (1983).
19. N. F. Zehkarchuk, T. P. Simova, V. I. Belyi, *Chem. Abstr.*, **102**(**22**), **1984,** 20343W.
20. I. A. Tikhonova, Ya I. Turgen, N. K. Strhav, *Zh, Obshch. Khim.*, **53, 12** (1983).
21. J. P. Auger, H. Barkat, F. Elenga, *Analysis*, **16**(**8**), 1988.
22. Xiangyan Ruan, *Talanta*, **31, 11** (1988).

STUDIA UNIV. BABEŞ-BOLYAI, CHEMIA, XXXIX, 1–2, 1994

SURFACE MOBILITY OF SURFACTANT SOLUTIONS
XVI. INVOLVEMENT OF THE FLUIDS VISCOSITIES IN THE MARANGONI FLOW — SOME ASPECTS

EMIL CHIFU*, EUGENIA GAVRILĂ*, MARIUS SĂLĂJAN*, CĂLIN GHEORGHIU**

ABSTRACT. The influence of viscosity upon the Marangoni flow (induced by surface tension differences) in competition with the gravity flow, through a thin liquid layer of triangular section has been experimentally investigated in the present work. The obtained data are compared with those resulted from numerical analysis by the finite element method. Both approaches indicate the same direction for the influence of viscosity upon the flow.

Introduction. Studies on the behavior of liquids in microgravity conditions arise great interest because of their potential applicability in space technology [2–6].

In earlier works on the mobility of thin liquid layers under the action of surface tension gradients the parametres influencing this phenomenon have been revealed. Mention may be made of some of them: the magnitude of the motive force (the surface tension gradient induced by unequal concentrations of surfactants or by temperature differences), the intensity of the gravity field [7, 8], the presence of a magnetic field [9].

The theoretic description of the flow has been based on the semi-infinite pellicle model [10] as well as on the model of a pellicle having a definite section [11].

The velocity equation, corresponding to the first model, that of a thin liquid layer situated upon a solid inclined plane, is of the following form:

$$v_x = \frac{1}{\mu L}\left[(\sigma - \sigma_0) + \Gamma hg + \rho gh\delta\right]z - \frac{\rho gh}{2\mu L}z^2 \qquad (1)$$

and the total rate of flow through the section of area $1 \times \delta$ will be given by the relationship:

$$Q = \int_0^\delta v_x dz = \frac{(\sigma - \sigma_0)}{2\mu L}\delta^2 + \frac{1}{2\mu L}\Gamma gh\delta^2 + \frac{1}{3\mu L}\rho gh\delta^3 \qquad (2)$$

where $(\sigma - \sigma_0)$ is the surface tension difference acting on the liquid/gas surface; μ is the viscosity of the liquid; Γ — the surface density; ρ — the bulk density of the liquid; g — the gravity acceleration; L — the length of the canal; h — the level difference between the liquids in the two reservoirs; δ — the thickness of the pellicle (see Fig. 1 a).

---

* *Chemical and Chemical Engineering Faculty, „Babeş-Bolyai" University, 3400 Cluj-Napoca, Romania*

** *Institute of Mathematics PO Box 68, 3400 Cluj-Napoca*

We underline that both the bulk viscosity (μ) and the surface viscosity (μ_s) intervene in the equations of the above mentioned models. In the case of the semi-infinite pellicle model, it has been indicated that the term containing μ_s disappears for reasons of problem symmetry [10]. The calculuses based on the model of a definite section pellicle (Fig. 1 b), situated in an adequate "surface" canal, have demonstrated that surface viscosity, having very small values in the studied case [12], does not modify the flow velocity [13, 14].

The object of the present work is to investigate the manner in which the bulk viscosity of the moving liquid influences the velocities and the rates of flow.

Experimental. The experimental measurements of the rates of flow have been performed with a device and in a manner minutely described in a previous paper [7]. Schematically, the device is presented in Fig. 1 a: a canal, of the length L, unites two reservoirs, each of them being filled with liquid. The two liquids are situated at different levels and have the surface tensions σ_0 and σ ($\sigma < \sigma_0$), respectively.

The transverse section of the used canal is an isosceles triangle with its base on the liquid/gas interface. The sizes — Fig. 1 b — are: base (width), $a = 3.87 \times 10^{-2}$ cm; height (thickness) $\delta = 4.8 \times 10^{-2}$ cm.

A variable gravity field can be simulated by changing the level difference h between the reservoirs. Indeed, in Eqs. (1) and (2), the terms specific to the gravity field contain the product $g \times h$, the change of which is possible by varying only one of the two magnitudes (g or h).

The flow has been investigated on the systems characterized in Table 1.

The liquid densities were determined with a pycnometer; the viscosities measured with the Ubbelhode viscosimeter and the surface tensions evaluated by means of the Du Noüy and Wilhelmy methods.

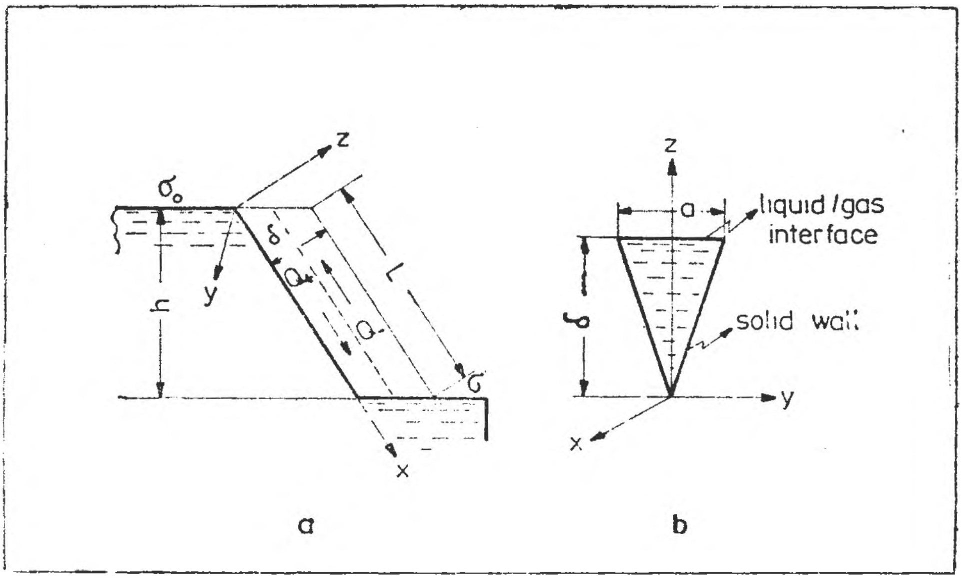

Fig. 1. Scheme of the experimental device and transverse section of the canal.

Table 1

Physical properties for the systems of liquids at temperature 20°C.

System	Descending liquid				Ascending liquid				$\Delta\sigma$ (mN/m)
	Composition	σ_0 (mN/m)	μ_0 (P)	ρ_0 (g/cm^3)	Composition	σ m(N/m)	μ (P)	ρ (g/cm^3)	
1	H_2O	73.0	0.010	0.998	48% E, 48% H_2O, 4% B (% v)	40.4	0.600	1.067	32.6
2	25% G, 75% H_2O	70.5	0.021	1.060	24% G, 72.43% H_2O, 3.47% B (% w)	35.5	0.024	1.050	35.0
3*	H_2O	73.0	0.010	0.998	96% H_2O 4% B (% v)	40.3	0.010	0.993	32.7

---

* System previously studied [7]. E = ethylene glicol, G = glycerine, B = buthyl alcohol.

The experiment was run in two variants:

— with the liquids in the two reservoirs having different viscosities (as in system No 1, Table 1);

— with liquids having identic viscosities (as systems No 2 and 3, Table 1).

By making use of adequate pairs of liquids, in our experiments the upward rates of flow (mainly of surface nature), Q_-; and the downward rates of flow (mainly of gravity nature,) Q_+, have been determined.

Results and discussion. The rates of flow, Q_- and Q_+, for the system No 1 (Table 1), are represented as functions of the hydrostatic level difference h, in Fig. 2. The existence of the two kinds of flow is evidenced: an upward flow, and a downward one. So, at small level differences, the interface draws the liquid towards the negative direction of the Ox axis (upward flow). For a certain range of the level differences there are two streams of liquid: an upward one, due mainly to the surface forces; and a downward one, determined by the gravity forces, then an "antiparallel" flow. Finally, for large level differences, the transport of the liquid takes place downward, with the positive direction of the Ox axis.

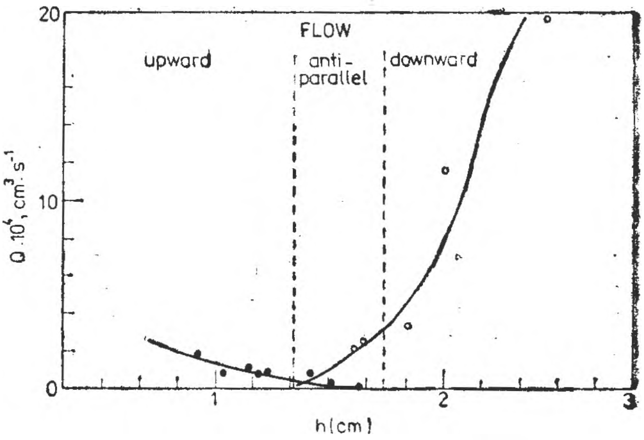

Fig. 2. The dependence $Q_- = f(h)$, $\mu_1 = 0.06$ P (∘); $Q_+ - f(h)$, $\mu_{01} = 0.01$ P (∘) — system 1.

The change of the fluids viscosity afects the range of existence of the "antiparallel" flow, as it is illustrated by the data in Table 2. Witht he increase of viscosity for one of the fluids the interval in wich the two types of flow coexist becomes smaller. The

Table 2

Ranges of "antiparallel" flow

Viscosity of the fluid μ(P)		Antiparallel flow range $h_{Q_+=0} \div h_{Q_-=0}$ (cm)		$h_{Q_+=Q_-}$ (cm)
descending	ascending			
0.01	0.01	1.32	3.96	1.50
0.01	0.06	1.24	1.70	1.30
0.02	0.02	1.02	1.90	1.13

same action is evident also for the level difference at which the two rates of flow are equal, $h_{Q_+=Q_-}$ (the intersection point of the two curves), corresponding to an approximately constant value of the surface tension difference (see $\Delta\sigma$ in Table 1).

The way the viscosity of liquids affects the magnitude of the upward (surface) rate of flow can be seen in Fig. 3. It is to be noticed that, for a given level difference, the rate of flow Q_- diminishes with increasing the viscosity of the fluid drawn into the upward flow, according to all expectations. On the other hand, within the detection limits one finds that the level difference to be established for vanishing the upward flow becomes smaller as the viscosity increases (see the superior limit of the antiparallel flow range — Table 2, or $h_{Q=0}$ in Fig. 3).

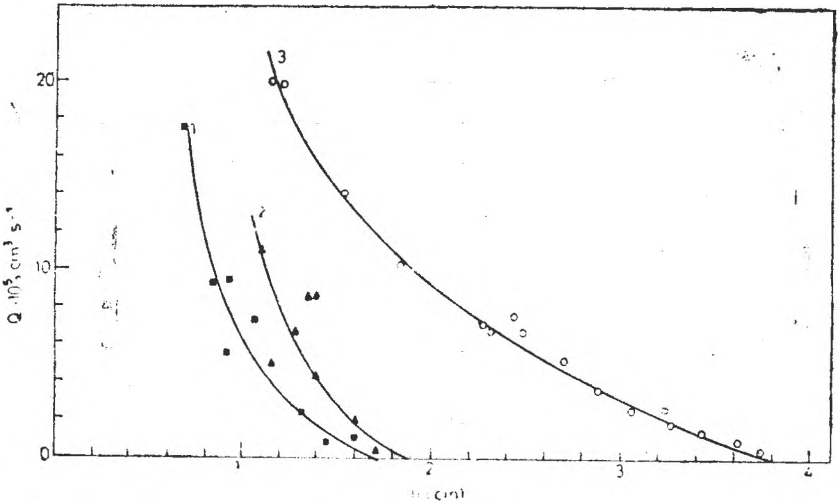

Fig. 3. The dependence $Q_- = f(h)$; $\mu_1 = 0.06$ P (■); $\mu_2 = 0.02$ P (▲); $\mu_3 = 0.01$ P (○); $\Delta\sigma = 33.5$ mN/m. μ_i = viscosity of the liquid in the upward flow for the system i (Table 1).

Table 3

Dependence of the experimental upward rate of flow on viscosity.

$\left(\overline{\frac{Q_1}{Q_2}}\right)$	$\frac{\Delta\sigma_1}{\Delta\sigma_2}\cdot\frac{\mu_2}{\mu_1}$	$\left(\overline{\frac{Q_2}{Q_3}}\right)$	$\frac{\Delta\sigma_2}{\Delta\sigma_3}\cdot\frac{\mu_3}{\mu_2}$	$\left(\overline{\frac{Q_1}{Q_3}}\right)$	$\frac{\Delta\sigma_1}{\Delta\sigma_3}\cdot\frac{\mu_3}{\mu_1}$
2.43	2.24	2.33	2.67	5.71	6.00

Obs. The values $(\overline{Q_i/Q_j})$ represent the average of individual ratios for level differences h in the interval 1.1 ÷ 1.3 cm.

Analysis of Eq. (2) indicates for the rate of flow a dependence of the type $Q \sim \frac{\Delta\sigma}{\mu}$. This is experimentally verified in the case of the upward rate of flow, namely by the data obtained for level differences h ranging from 1.1 to 1.3 cm and given in Table 3. We mention that in this range the downward rate of flow is small (see Fig. 4). Values of the upward rate of flow corresponding to smaller level differences (h < 1 cm) have not been considered because in this range the experimental measurements are affected by large errors. For the interval taken into account the agreement can be thought to be satisfactory.

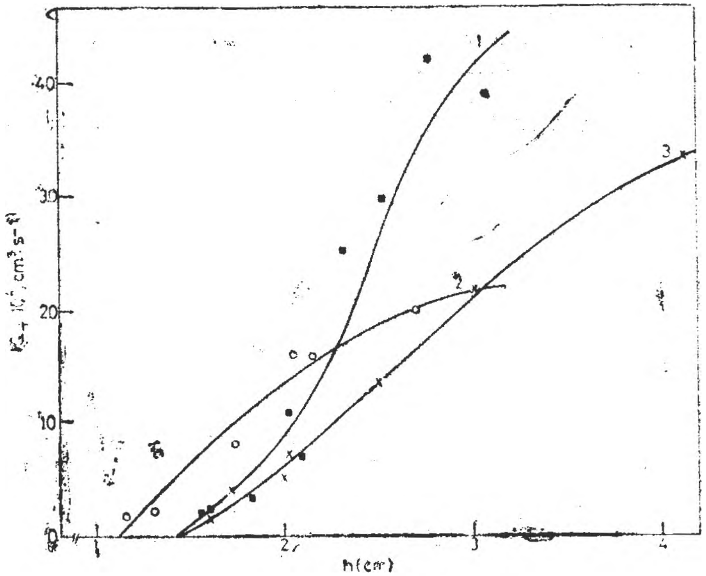

F i g. 4. The dependence $Q_+ = f(h)$; $\mu_{01} = 0.01$ P (■); $\mu_{02} = 0.02$ P (○); $\mu_{03} = 0.01$ P (×). μ_{0i} = viscosity of the liquid in the downward flow for the system i (Table 1).

We specify that the dependence $Q_{\pm} = f(\mu)$ is, in fact, complicated. The rates of flow Q_- and Q_+ are not purely of surface, respectively of gravity nature, since a layer of flowing liquid always draws other layers from the immediate neighbourhood.

The variation of the downward rate of flow with viscosity, presented in Fig. 4, offers data leading to the following findings:

— at large level differences $h > 3$ cm, where the volume forces are predominant, the masses of transported liquid are approximately proportional to the inverse of the viscosity. This can be noticed from the values to which the rates of flow tend in systems 1 and 2, or in systems 3 and 2. In these cases, the ratio of the viscosities is 1 : 2.

— the downwards rates of flow Q_+ are affected by the ascendent liquid as well as by the range in which the two flows coexist. We attribute to these effects the difference between curves 1 and 3, dealing with systems in gravity flow is realized with liquids of identical viscosities. For system 1 (curve 1), at $h > 2$ cm the upward rate of flow is practically zero. Consequently although the viscosity of the corresponding liquid which ascends the inclined plane is much greater ($\mu_{01} = 1$ cP, $\mu_1 = 6$ cP), it does not influence the magnitude of the downward rate of flow. In the case of system 3, at $h > 2$ cm the rate of flow Q_- is appreciable (see Fig. 3) and the competition between the antiparallel flows is evidenced. It is to be supposed that, at large level differences, $h \gg 4$ cm, the value of the rate of flow for system 3 tends towards that one corresponding to system 1, due to the identical viscosities of the descending liquids and to the cancelling of the upward flows in these two systems.

The way the fluids viscosity intervenes in the flow processes is rediscovered by theoretical means, namely by solving the model of a pellicle with triangular transverse section with the aid of the finite element method in the Simplex form. The results, obtained by simulation on computer, are presented in Fig. 5. One finds that the ratio of the rates of flow at one and the same

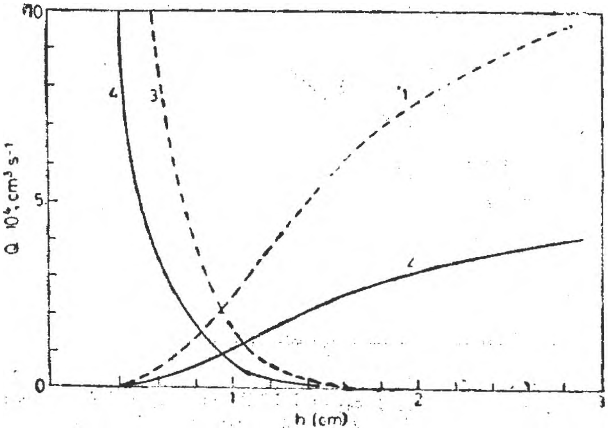

Fig. 5. Theoretical curves $Q_+ = f(h)$, curves 1 and 2; $Q_- = f(h)$, curves 3 and 4 for $\Delta\sigma = 8.82$ mN/m. $\mu_1 = \mu_3 = 0.004$P, $\mu_2 = \mu_4 = 0.01$ P.

level difference, is proportional to the inverse ratio of the viscosities. For the system considered the calculus gives:

$$\frac{(Q_-)_1}{(Q_-)_2} = \frac{(Q_+)_1}{(Q_+)_2} = \frac{\mu_2}{\mu_1} = 2.5$$

The finite element method has allowed us, to obtain the velocity profiles for the liquid flow through a canal of triangular (transverse) section ($\delta = 2.99 \times 10^{-2}$ cm; $a = 4.19 \times 10^{-2}$ cm), at different relative depths $Z = \frac{z}{\delta}$ of the pellicle. Corresponding to two viscosities, at constant surface tension gradient and level difference, the shape of the profiles is given in Fig. 6. It can be see that the flow velocities are negatives at the interface ($Z = 1$) curves 1, 1′ and in its immediate neighbourhood ($Z = 0.9$) curves 2, 2′. At a larger profundity, curves 3, 3′, the velocities have values of both signs; while, as the depth continues to increase, curves 4, 4′, the velocities become exclusively positive, the drawing by surface tension forces being here much reduced. In all situations it has been ascertained that the velocities corresponding to the liquid with high viscosity ($\mu' = 0.010$ P) — the continuous lines — are smaller than those of the liquid with low viscosity ($\mu = 0.0065$ P) — the dotted lines.

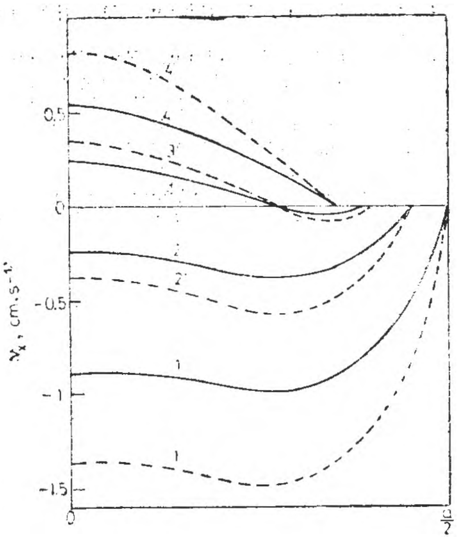

Fig. 6. The dependence of the velocity profile — projected on the xOy plane — upon the relative depth of the pellicle Z; $\Delta\sigma = 3.53$ mN/m. Curves: 1,1′ for Z = 1; 2,2′ for Z = 0.9; 3,3′ for Z = 0.8; 4.4′ for Z = 0.7.

The theoretic foresights agree with the experimental results, by indicating diminution of the flow rates and velocities when the viscosity of the liquid has large values. The influence of the viscosity is however, more complex, because this parameter can also be affected by the competition between the two types of flow.

REFERENCES

1. E. Chifu, E. Gavrilă, M. Sălăjan, *Rev. Roumaine Chim.*, **39**, 697 (994)
2. Y. Kamotami, S. Ostrach, S. Lowry, *Material Processing in the Reduced Gravity Environment of Space*, G. E. Rindone, edit., Materials Research Soc. Proc., vol. 9, 1–12 (1982).
3. F. Bauer, *Wärme und Soffübertragung*, **16**, 229 (1982).
4. T. J. McNeil, R. Cole, R. S. Subramanian, *J. Colloid. Interf. Sci.*, **98**, (1), 210 (1984); *J. Amer. Ceram. Soc.*, **68** (5), 254 (1985).
5. A. Cloot, G. Lebon, *J. Physique*, **47**, 23 (1986).
6. E. Chifu, *Roum. Chem. Quart. Rev.*, **1** (1), 33 (1993).
7. E. Chifu, I. Albu, *Studia Univ. Babeş-Bolyai, Chem.*, **1**, 99 (1968).
8. E. Chifu, I. Albu, C. I. Gheorghiu, E. Gavrilă, M. Sălăjan, M. Tomoaia-Cotişel, *Rev. Roumaine Chim.*, **31**, 105 (1986).

9. E. Chifu, I. Stan, M. Sălăjan, E. Gavrilă, *Rev. Roumaine Chim.*, **34**, 79 (1989).
10. E. Chifu, I. Stan, *Rev. Roumaine Chim.*, **27**, 703 (1982).
11. E. Chifu, C. I. Gheorghiu, I. Stan, *Rev. Roumaine Chim.*, **29**, 31 (1984).
12. J. T. Davies, E. K. Redeal, *Interfacial Phenomena*, Academic Press, New York and London, 1963, p. 261; *Surface and Colloid Science*, vol. 5. Ed. E. Matijevic, John Wiley and Sons, 1972, p. 128, 129.
13. E. Chifu, C. I. Gheorghiu, I. Stan in VI. *Internationale Tagung über Grenzflächenaktive Stoffe*, Akademie Verlag, Berlin, 1987, p. 211.
14. E. Chifu, C. I. Gheorghiu, *Rev. Roumaine Chim.*, **32**, 945 (1987).

STUDIA UNIV. BABEŞ-BOLYAI, CHEMIA, XXXIX, 1–2, 1994

COMPARATIVE STUDY OF SOME CHROMATOGRAPHIC RESPONSE FUNCTION (CRF) USED IN LC AND TLC OPTIMIZATION. A NEW WEIGHTED MULTIPLE CRF USEFUL FOR TLC

HOREA I. NAŞCU*, TEODOR HODIŞAN, CLAUDIA CIMPOIU****

ABSTRACT. A new weighted chromatographic response function (CRF), containing first and second degree terms, have been proposed and its application for the optimization of a ternary solvent system: benzene — petroleum ether — chloroform mixture, used for the separation of a five component pesticides mixture, was demonstrated. The comparation with some other CRFs was made. Including a greater number of features of a good chromatogram the proposed function seems to be a safer one.

Introduction. From the beginning of using chromatography as an analytical tool for separation and determination of multi-component mixtures, a great effort were made in the field of the optimization of the separation process. Because of specific problems encountered in the fields of TLC an LC, the subject of optimization is treated separately by many workers and only by few as a general case. With the widespread availability of computers in analytical laboratory, the topic became more and more preferred and today several reviews can be consulted both for LC [1—5] as well as for TLC [6, 7] and very few for more general cases [8]. A great numbers of software packages have been developed to help the chromatographer in the optimization of the separation parameters values, more frequent for solvent optimization and some books may be consulted related this subject [2—4]. Some programs were incorporated into the software of liquid chromatograph [9].

To reflect the quality of a chromatogram in a single number, in order to reduce the optimization strategy to a software, a function must be selected and this is the chromatographic response function (CRF). This function becomes in the optimization process the "objective function" so the conditions for the separation (particularly the solvent composition) are selected in such a way that its numerical value become a maximum (or possibly a minimum).

Chromatographic Response Function. While no one CRF will ever be entirely satisfactory in all cases and for all chromatographers a great number of CRFs have been designed and tested. A list of them is presented in the table 1, without the pretention to be exhaustive. Some CRFs attempt to catch in its value a single essential quality of the whole multicomponent separation while others combine several desired qualities into a weighted sum (see Table 1). We are thinking that studies of the kind of the present paper will be helpful in the designing of expert systems as well as for the software in the chromatographic instrumentation.

---

* *Technical University of Cluj-Napoca, 1, C. Daicoviciu, 3400—Cluj-Napoca, ROMANIA.*
** *„Babeş-Bolyai" University, 3400—Cluj-Napoca, ROMANIA.*

Table **1.**

Some chromatographic response functions found in the literature.

No	Field	Name of The Function	Equation	Author	Yr 19..	Li
1	GC	Total Overlapping	$\Phi = \Sigma\exp(-2Ri)$	Giddings	60	10
2	LC	Chromatogr. Response Function	$CRF = \Sigma\ln(n_i)$	Morgan	76	11
3	TLC	Trennungszahl (Sep. number)	$TZ = 2L_{chr}/(\sigma_s + \sigma_f) - 1$	Kaiser	75	12
4	TLC	Amount of Information	$I = -\Sigma(n_k/n)\lg_2(n_k/n)$	Souto	70	13
5	TLC	The hi Squared Function	$x^2 = \Sigma(O_i - E_i)^2/E_i$	Massart	73	14
6	TLC	Discrimination Power	$DP = 1 - ((2m/n(n-1))$	Massart	75	15
7	TLC	Performance index	$I_p = \sqrt{\Sigma(\Delta hRf,i - \Delta hRf,t)^2/}$ $/n(n+1)$	Gocan	81	16
8	TLC	Information Power	$I.Rs_{mean} = I.\Sigma R_i/n$	Nascu	82	17
9	TLC	Informational Energy	$EI = \Sigma p_k^2$	Sârbu	90	18
10	TLC	Information Power	$P_{inf} = \Sigma^2\log S_i$	Smits	75	19
11	LC	Chromatographic Response Function	$FCR = \Sigma\log_e n_i$	Morgan	75	20
12	LC	Chromatographic Response Funtion	$CRF = \Sigma\ln(n_i/n_d) + a(t_m - t_n)$	Watson	79	21
13	LC	Sparation Number	$SN = \Sigma\log_2 S_i$	Spencer	82	22
14	LC	Chromatographic Response Function	$COF = \Sigma a_i\ln(R_i/R_d) +$ $+ b(t_m - t_1)$	Glajch	80	23
15	LC	Resolution Product	$\Pi RS = \Pi R_i$	Schoenmakers	82	24
16	LC	Chromatographic Response Function	$CRF = 1/n\ \Pi f_i/(g_i + 2h_i)$	Wegscheider	82	25
17	LC	Fraction of the overlaped aria	$A_0 = P_c/(A_s\ 2\pi\sigma_c^2)\cdot$ $\cdot\ \exp(-y^2/2\sigma_c^2)\,dy$	Knoll	82	26
18	LC	Evaluation Function	$CrF = \Sigma a_i + 1/(n-1)\cdot\Sigma b_j P_i$	Vajda	82	27
19	LC	Chromatographic Response Function	$CRF = \Sigma R_i + n_a - b(T_m -$ $- T_1) - c(T_0 - T_1)$	Berridge	82	5
20	LC	Chromatographic Response Function	$CRF = \Sigma\ln(f_i/g_i) + 100(m-n)$	Nickel	83	29
21	LC	Objective Function	$F_{obj} = \Sigma 100e(1,5 - Ri) + (t_m - t_n)^3$	Dunn	83	30
22	LC	Objective Function	$F_{obj} = \Sigma[10(1,5 - R_i)]^2$	Kester	84	31
23	LC	Separation Degree	$Y = n/m$	Doudi	87	32
24	LC	Chromatographic Response Function	$CRF = \Sigma R_i + n - (t_m - t_n)$	Wright	87	33
25	LC	Figure of Merit	$Fmer = \Sigma 1/x^5(\exp(/gx) - 1)$	Howard	89	7
26	LC	Relative Resolution Product	$RRP = \Pi Ri/(\Sigma Ri/(n-1))n-1$	Warren	91	9

In the Table 1, R_i is the resolutions of every pair of the n − 1 adjacent peaks, n — the number of peaks/investigated compounds, m — number of peaks expected, t_0 — void volume, t_1 — retention time of the first peak, t_m — desired retention time of the whole chromatogram, O_i — statistical frequencies observed within a "group", E_i — theoretical frequency for an ideal distribution, I — amount of information, p_k — probability of finding a poak in a group, p_i — actual peak separation, p_d — desired peak separation, S_i — peak overlap, L_{chr} — the lenght of chromatogram, σs and σf the standard deviation of the first and the last peaks, a, b, c — selectable weightings, f_i, g_i, h_i, peak separation factors, ΔhR_f,i — measured intervals between two adjacent peaks, ΔhR_f,t — theoretical intervals between any two adjacent peaks in the case of an ideal separation. (For other symbols see the original source)

In practice to can say that a given chromatogram is "the optimum" it must fulfil the following conditions:
1) The number of separated components must be maximum.
2) The peaks width must be as low as possible.
3) The separation coordinates (retention time, retention value, Rf, hRf etc.) of all individual peaks must be as uniform as possible distributed throughout the chromatogram.
4) The separation of all the pairs of adjacent peaks must be the best, in average, even if the separation is not perfect.
5) The solvent system and the stationary phase used must have a maximum separation potential (optimum selected concerning its selectivity).
6) The separation time must be the shortest.

Therefore, on our opinion, the preferred CRF is the one which contain all these qualities into a weighted sum. Let us see some of the above mentioned qualities preferentially evidenced by some functions.

The number of components entirely separated, n is a useful quality (see ref. [28] and [33]). But if the separation is not "uniform" i.e. the peaks a not equal distributed concerning their retention time coordinate, the column must be longer and the separation time consequently higher. This number alone in not entirely satisfactory.

The sharpness of the zones, best evaluated by Kaiser's "trennungszahl" [12], reflects in its value the maximum of medium width peaks theoretically admitted in a given chromatogram. This value says nothing about relative position of different zones and therefore practical unused in optimization purposes.

The uniform distribution of peaks in any of the "separation coordinate" (retention time, retention volume, migration distance, hRf etc.) is well evaluated by a hi squared function [14] or one of the form: $a\Sigma(R_i - R_t)^2$ [16], where R_i is the retention coordinate of the components sorted in their increasing order and R_t are the ideal (theoretical), previously established, tailored according a particular purpose of the analyst, value and a is a numerical constant This equation, proposed by Gocan and coworkers [16], had very limited utilization, although it proved very useful. So, R may differ for the same mixture but for other application. For instance Gocan and coworkers, who first time used such an equation for TLC [16], prefer as ideal Rf values for a 4 components mixture the row: 0.2, 0.4, 0.6, 0.8 (assuming that no component remain at the starting point). For the application of TLC as a solvent selection tool, for a LC separation, the Rf values must lie between 0.2 and 0.3. Therefore, for the same four-component mixture, in this hypothetical case, the R values must be: 0.2, 0.33, 0.67, 0.3. This equation (see equation number 7 in Table 1) reflects the uniformity of the separation but the same quality of separation may be reached by using other functions, too.

The overall separation of all pairs of adjacent peaks was estimated sometimes by using the mean resolution of all consecutive peaks [24, 48] or by calculating a product of this function with the amount of information [17] The product of resolutions have been used also, alone [24] or in a combined function with the mean resolution [9]. The amount of information, I [13] and the informational energy, IE [18] illustrate the multi-component separation using discontinuities of probabilities related with some arbitrary "groups" of retention parameter values. They are not affected by peak widths and therefore not very sensitive especially when a small number of peaks are concerned. Functions of the differences between 1.5 (an ideal value for two peaks) and individual resolutions of the same adjacent peak were also successfully used [30, 31] (see tab 1 for all of this). The "figure of merit" [7], a special very sensitive function, was also tested but its great numerical value make sometimes difficulties in using the computer.

The optimization of the separation potential of solvent system used was taken into account in the papers of Nyredy and coworkers (see [6]) and this must be the first step in any optimization procedure. But once solvent nature was selected the CRF became necessary.

The sixth quality in our above-mentioned list was estimated with $t_m - t_1$ terms (see equations 22, 23, 25 in tab. 1). But, in the present paper case the corespondent of this difference was neglected because of its little effect in TLC. In adition, if the separation is uniform i. e. the peak are equidistant on the chromatogram, the column my be shorted in only one step.

Based on our previous experience [35] the objective function tested in the

$$F_{obj} = a \cdot n + b \cdot I \cdot \overline{R_s} + c \cdot 10/IE + d/(I_p + \varepsilon)$$

where *a, b, c, d* are arbitrary weging factors, *n* — number of components observed as peaks (zones), *I* — the amount of information (position no. 6 in tab. 1) R_s — the mean resolution of all adjacent peaks (see equation under no. 10 in tab. 1), *IE* — informational energy (see no. 11 in tab. 1), *I* — performance index (see no. 9 in tab. 1) and ε a very small, arbitrary value (10^{-5}). In the present work *a, b, c* and *d* were all taken as unity.

Experimental. The CRF proposed in the present paper was tested on the optimization of the separation of a five pesticide mixture: wofatox (1), fosfalon (2), phosmet (3), azinphosmethyl (4) and pirimiphosmethyl (5) presented as chemical structural formulae in Fig. 1. They were used as 0.1% solution in ethyl ether and applied, for every solvent tested, onto the start of a flexible, aluminum foil, this layer chromatographic, ready made, plate (E. Merck, Darmstadt) using a capillary pipet. All the plates were 250 µm thick.

The first composition of the solvents tested were selected through preliminary tests. This The TLC silica plates, after running a sufficient time to migrate in a N — chamber about 15 cm with every solvent system from table 2, were then examined and read in UV light. For every spot, applied individual and in a mixture, with all the other studied components, their length and width, in the same direction with the elution, were recorded.

The measured data were input data for the calculation in the PROGFOB2 program, presented as listing in the present paper. It was written in QBASIC language and is presented below.

```
'"PROGFOB2" A PROGRAM FOR COMPUTING THE OBJECTIVE FUNCTION
DECLARE SUB weigh (a!, b!, c!, d!)
DECLARE SUB order (n AS INTEGER, ro(), sr()   )
DECLARE SUB info (no AS INTEGER, n AS INTEGER, ei!, hi!, RsM!, ro(), sr(), p(), pind!
INPUT "Number of test =", ntest
INPUT "Number of comp. = ?", n: DIM SHARED r (1 TO n) AS SINGLE DIM SHARED)
s(1 TO n) AS SINGLE, ro (1 TO n) AS SINGLE, sr (1 TO n) AS SINGLE
INPUT "Length of chromatographic run (cm) =", length: length = 10 * length
INPUT "Number of intervals = 20 ? (Y/N)", y$
IF y$ = "n" THEN INPUT "Number of groups are (10 or 20) =", no ELSE no = 20
```

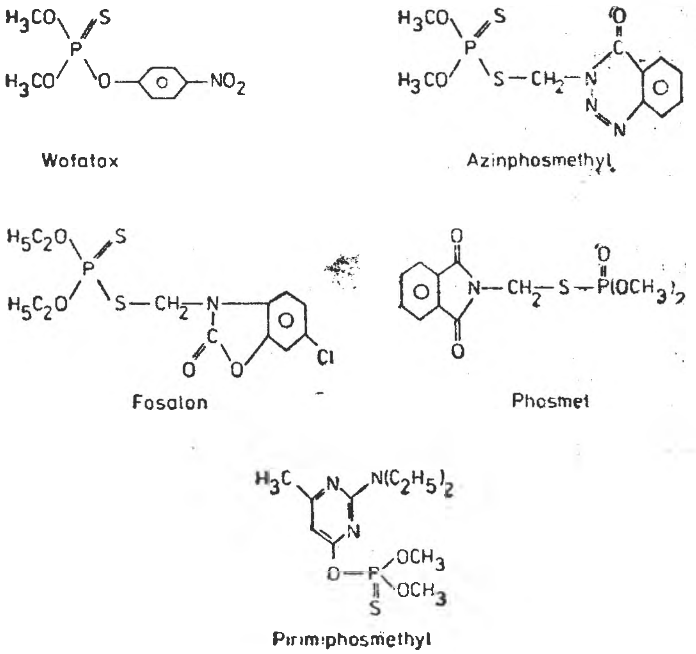

Wofatox

Azinphosmethyl

Fosalon

Phosmet

Pirimiphosmethyl

Fig. 1. The structure of the five — component mixture used in the TLC separations.

Table 2.

Solvents used in practical optimization during the utilization of the SIMPLEX algorithm.

Solvent	Benzene-Petroleum ether-Chloroform mixture compositions (v/v)	Fobj calculated with "PROGFOB2"
1	60 : 20 : 5	9.7571
2	75 : 20 : 5	12.5359
3	55 : 15 : 30	11.9625
4	71 : 1 : 28	12.8819
5	90 : 6 : 4	12.7075
6	78 : 12 : 10	13.8606
7	60 : 7 : 33	13.1791
8	66 : 18 : 16	12.5714
9	70 : 5 : 25	16.9933

```
DIM SHARED p(1 TO no) AS SINGLE
 ant = 100 / no
 FOR i = 1 TO n
PRINT "peak position  (cm) ("; i; ") = ": INPUT  lungime:  lungime = lungime ∗ 10:  r(i) =
= lungime ∗ 100 / length
ro (i) = r (i)
 FOR j =  1 TO no
          IF r(i) > = (j − 1) ∗ ant AND r(i) < j ∗ ant THEN p(j) = p(j) + 1 / n
 NEXT j
PRINT "peak width (cm)("; i; ") = ?: INPUT  s(i): s (i) = s(i) ∗ 10:  s(i) = 100 ∗ s(i) / length
sr(i) = s(i): smed = smed + s(i)
 NEXT i
 CLS: smed = smed / n
 CALL order ((n), ro(), sr())
CALL info ((no), (n), ei!, hi!, RsM!, ro(), sr(), p(), pind!)
 LET sum = 1
 FOR i = 1TO n − 1
          IF ABS (ro(i) − ro(i + 1)) < = smed THEN
                      sum = sum + 1
          END IF
 NEXT i
 INPUT "Weighing ? (Y/N)", y$
 IF y$ = "Y" OR y$ = "y" THEN
          CALL weigh (a!, b!, c!, d!)
          ELSE a = 1: b = 1: c = 1: d = 1
 END IF
LET Fobj = a ∗ sum + c ∗ 10 / ei + b ∗ hi ∗ RsM + d ∗ 1 / (pind + 10   −5)
 PRINT "Fobj = "; Fobj, "Medium peak width ="; smed
 PRINT "Peak no. = "; sum; " "; "a = "; a; " "; "a. Peak no. = "; a ∗ sum
 PRINT "IE = "; ei; " "; "c = "; c; " "; "c. 10/IE = "; c ∗ 10 / ei
PRINT "Cant. inf. = "; hi; " "; "Medium Rs = " RsM; " "; "b = "; b; " ";
PRINT "Cant. inf. RsM = "; b ∗ hi ∗ RsM
PRINT "Perf. ind. = ";pind; " "; "d = "; d; " "; "d/Perf. ind ="; d ∗ 1 / (pind + 10   −5)
 CLOSE
 OPEN "b:/H1.DAT" FOR APPEND AS #5
 PRINT #5,
 PRINT #5, "Number of test ="; ntest
 NEXT i
 PRINT #5, "Fobj = ; Fobj; " "; "Peak no. ="; sum; " "; "a ="; a; " "; "a. Peak no. =";
 a ∗ sum
 PRINT #5, "IE ="; ei; " "; "c ="; c; " "; "c. 10/IE ="; c ∗ 10 / ei
 PRINT #5, "Cant. inf. ="; hi; " "; "Medium Rs ="; RsM; " "; "b ="; b; " ";
 PRINT #5, "Cant. inf. RsM ="; b ∗ hi ∗ RsM
PRINT #5, "Perf. ind. ="; pind; " "; "d ="; d; " "; "d. Perf. ind ="; d ∗ pind
CLOSE #5
'Subroutine "Info" calculates Amount of Information, Informational Energy
'Medium Resolution, Relative Resolution Product and Performance Index (Ip).
 SUB info (no AS INTEGER, n AS INTEGER, ei!, hi!, RsM!, ro(), sr(), p(), pind!)
 FOR j = 1 TO no
          IF p(j) > 0 THEN
                 ei = ei + p(j) ∗ p(j)
               hi = hi − p(j) ∗ (LOG(p(j)) / LOG(2))
          END IF
 NEXT j
 ri = 100 / (n + 1)
 FOR i = 1 TO n − 1
         Rsi = 2 ∗ ABS(ro(i) − ro(i  + 1) / (sr(i) + sr(i + 1))
         RsM = RsM + Rsi
         sigma = sigma + ((ro(i + 1) − ro(i)) − ri) · 2
```

```
NEXT i
RsM = RsM / (n − 1)
pind = SQR(sigma / (n * (n + 1)))
END SUB
SUB order (n AS INTEGER, ro(), sr())
o = 1
FOR i = 2 TO n
        k = i
200 kl = k − 1
        IF o * ro(k) <= o * ro(kl)THEN
                GOTO 300
        END IF
n = ro(k) : ro(k) = ro(kl) : ro(kl) = n
u = sr(k) : sr(k) = sr(kl) : sr(kl) =
        IF k = 2 THEN
                GOTO 200
        END IF
        k = k − 1 : GOTO 200
300 NEXT i
END SUB
'Input for the weighings.!)
SUB weigh (a!, b!, c!, d:
PRINT "The equation is  Fobj = a.n + b.inf.RsM + c/EI + d.s"
INPUT "The value of a= ?"; a
INPUT "The value of b = ?"; b
INPUT "The value of c = ?"; c
INPUT "The value of d = ?"; d:CLS
END SUB
```

After writing (or opening) it, by stroking RUN (on an IBM compatible PC), the computer ask for data. The program, presented here, stores the final data, as a file with the name H1.DAT, on a flexible disk (the disk with the name *b*: in our case). The file is created automatically on disk by this program.

In the Table 3 the successive experiments (solvents used) were presented. They were obtained graphically, from a bi-dimensional diagram, as may be seen from Fig. 2. In the same table, to-

Table 3

The abandoned solvents and the new simplexes used during the optimization experiment.

The eliminated slovent (the worst, according the data recorded table 2) from the preceding simplex.	The new simplex	Remarks
—	1, 2, 3	The first simplex
1	2, 3, 4	—
3	2, 4, 5	The new point, opposed to the point 2, fall outside of the experimental field. The contraction leads to solvent 6
2	4, 5, 6	—
5	4, 6, 7	—
4	6, 7, 8	—
8	==> 9 OPTIMUM SOLVENT	The reflection leads to the solvent 4 again. Therefore we made a new contraction i.e. solvent 9

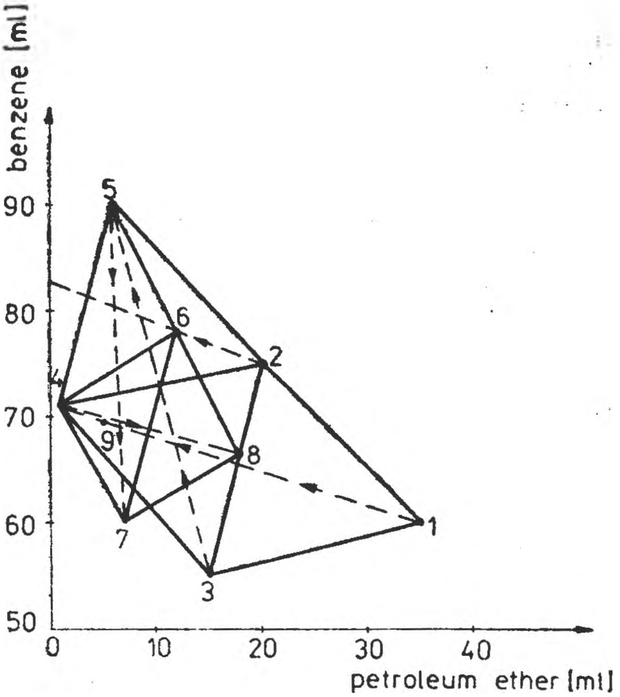

Fig. 2. The compositions of solvents selected by using the simplex method.

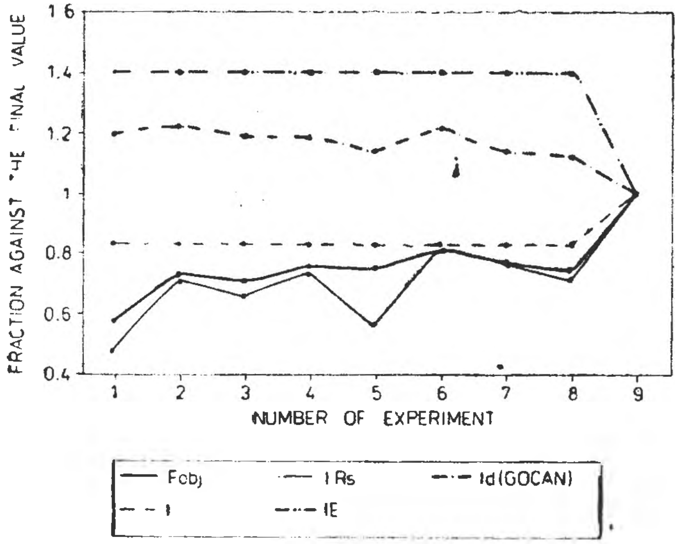

Fig. 3. The plot of some individual functions together with the droposed objective function vs. the number of experiment.

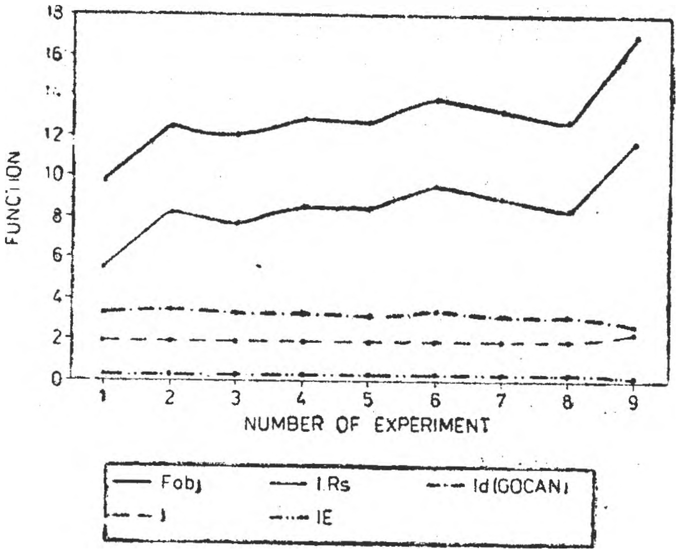

Fig. 4. The plot of the fraction against their final (optimum) value of functions from Fig. 3 vs. the number of solvent tested.

gether with the solvents of the individual simplex, the CRF value and the abadnoned solvent, from the previous simplex, have been presented. The simplex optimization ewas stopped when the last solvent change falls within the range of instrumental error of the volume measurement tool (a glass pipet in our case) used.

The plot of numerical values calculated for several CRF using PROGFOB2 versus the number of experiment are presented in Fig. 3. It can be seen that F_{obj} leads through the optimization steps to its maximum values and this is the best value for all the other functions recorded. Some of them (IE and I had a minimum optimum value but the terms in which thay are factors became maximum. Because of differences in their absolute values comparisons are difficult to be made. In Fig. 4 it can be better seen the evolution of individual functions to their final limit by representing the fraction against their final value, during the optimization.

Discussion. The most sensitive function proved to be in the present work, the mean R (and the product $I.R_s$, consequently) together with the I_p values. The R_s and I_p functions had reverse fluctuations but finally the trend was to the same "optimum". In the present case I and *IE* values seemed to be insensitive, having therefore a smoothing action. But their final confirmatory action proved helpful in making the final decision.

From Fig. 2 it can be seen that with the only exception of the *I* and *IE* functions the tested objective function leads to the same result by using the simplex method. We are thinking that this two functions become insensitive only when a small number of components are present in the mixture. Therefore we believe that not the sensitivity (the slope) of the function is essential, as was stated by some workers, but the ability to give strictly different values for different solvents during the optimization steps. This condition may be realized through very different ways.

Conclusion. The objective function proposed in the present paper, containing more than one term and even a second degree term, was compared with other similar functions. The final result was very similar with that obtained using other simple objective functions, already used in TLC but the introduction of a greater number of factors, associated with a "good" separation, seemed to make safer the final result. The function is not perfect because it is not indicating if the composition of the solvent system used has, through its nature, a maximum separation capacity and does not considering the time factor.

REFERENCES

1. H. J. G. Debets, Optimization Methods for HPLC, *J. Liq. Chromatogr.*, **8** (15), 2725 1985).
2. J. C. Berridge, *Techniques for the Automated Optimization of HPLC Separations*, Wiley, New York, NY, 1985.
3. P. J. Shoemakers, *Optimization of Chromatografic Selectivity*, Elsevier, Amsterdam, 1986
4. L. R. Snyder, J. L. Glajch and J. J. Kirkland, *Practical HPLC Method Development*, Wiley, New York, N.Y., 1988.
5. J. C. Berridge, *J. Chromatogr.*, **485**, 3 (1989).
6. Sz. Nyiredy, Karin Dallenbach-Tolke and O. J. Sticher, *Planar. Chromatogr.*, **1** (Dec), 336 (1988).
7. A. G. Howard and L. A. Bonicke, *Anal. Chim. Acta*, **223**, 411 (1989).
8. Elaine Heilweil, Cap. 3 in *Mobile Phase Design and Optimation*, 37—49.
9. F. V. Jr Warren, C. H. Jr Phoebe, M. Webb, A. Weston, and E. A. Bidlingmeyer, *Int. Lab.*, **5** (Jul/Aug), 14 (1991).
10. J. C. Giddings, *Analyt. Chem.*, **32**, 1707 (1960).
11. S. L. Morgan and S. N. Deming, *Sep. Puriff. Methods*, **5**, 333 (1976).
12. R. Kaiesr, Euroanalysis, II-nd Conference, Budapest, 1975.
13. J. Souto and A. G. de Valesi, *J. Chromatogr.*, **46**, 274 (1970).
14. D. L. Massart, *J. Chromatogr.*, **79**, 157 (1973).
15. D. L. Masart, A. Dijkstra and R. Smits, Euroanalysis, II-nd Conf., Budapest, 1975.
16. S. Gocan and Maria Mihaly, *Stud. Univ. Babeş-Bolyai, Chemia*, **1**, 18 (1981).
17. H. Naşcu, C. Sârbu, Elena Moraru and T. Hodişan, *Rev. Chim.*, **33**, (6), 550 (1982).
18. C. Sârbu and H. Naşcu, *Rev. Chim.* (Bucureşti), **41** (3), 271 (1990).
19. R. Smits, C. Vanroelen and D. L. Massart, *Fres. Z. Anal. Chem.*, **273**, 1 (1975).
20. S. L. Morgan and S. N. Deming, *J. Chromatogr.*, **112**, 267 (1975).
21. M. W. Watson and P. W. Carr, *Anal. Chem.*, **32**, 1835 (1979).
22. W. A. Spencer and L. B. Rogers, *Anal. Chem.*, **52**, 950 (1982).
23. J. L. Glajch, K. M. Kirkland, K. M. Squire and J. M. Minor, *J. Chromatogr.*, **199**, 57 (1980).
24. P. J. Schoenmakers, A. C. J. H. Drouen, H. A. H. Billiet and L. Galan, *Chromatographia*, **15**, 688 (1982).
25. W. Wegscheider, E. P. Lankma and . W. Budna, *Chromatographia*, **15**, **498** (1982).
26. J. E. Knoll and M. R. Midget, *J. Chromatogr. Sci.*, **20**, 221 (1982).

27. J. Vajda şi L. Leisztner, *Proc. Symp. Advances in Loiquid Chromatogr.*, Szeged Hungary, **1982**, p. 103.
28. J. C. Berridge, *Chromatographia*, **16**, 172 (1982).
29. J. H. Nickel and S. N. Deming, LC, *Mag. Liq. Chromatogr. HPLC*, **1**, 414 (1983).
30. D. L. Dun and R. E. Thompson, *J. Chromatogr.*, **264**, 264 (1983).
31. A. S. Kester and R. E. Thompson, *J. Chromatogr.*, **310**, 372 (1984).
32. F. Doudi, Y. D. Kahie, P. Reschiglian, C. Bighi and G. P. Cartoni, *Chromatographia*, **23**, 844 (1987).
33. A. G. Wright, A. F. Fell and J. C. Berridge, *Chromatographia*, **24**, 335 (1987).
34. T. Hodisan, H. Nascu, Claudia Cimpoiu and I. Hopirtean, *Rev. Chim.* (Bucharest), **41**, 85 (1996)

STUDIA UNIV. BABEŞ-BOLYAI, CHEMIA, XXXIX, 1–2, 1994

CADMIUM ION – SELECTIVE MEMBRANE ELECTRODE, CD-ISME

I. Preparation of the active electrode material

ELENA HOPÂRTEAN, VIORICA COSMA

ABSTRACT. The present paper reports some preparation methods for mixtures of cadmium and silver sulphides with Cd^{2+} – selective electrode properties. Natrium sulphide (S), thioacetamide (TA) and natrium thiosulphate (TS) have been used for simultaneous precipitation of CdS and Ag_2S. Sulphide mixtures obtained with TA, thermally treated at 200–250°C, and those obtained with TS exhibit the best electrode properties. The main electrode charcteristics are: Nernstian response in the concentration range of $5 \cdot 10^{-6}$–10^{-1} M Cd^{2+}; optimum pH range 2–5; internal electric resistance below 100 kΩ; response time less than 1 minute.

Introduction. The active electrode material used for the achievement of the cadmium selective electrode consists of cadmium suplhide mixed with other less soluble sulphides (Ag_2S, Cu_2S) [1–12]. Cadmium selenide or cadmium telluride mixed with silver sulphide [13–15] or polycrystalline compounds, for instance those of type $CdM_2(III)X_4$ where M = Zn, Ga, Bi; X = S, Se, Te/16 / may be also used.

This paper reports the elaboration of an optimum method for the preparation and conditioning of CdS-Ag_2S mixture, which was used for obtaining of the Cd^{2+} – selective membrane electrode, Cd-ISME.

Experimental.

Reagents and Solutions: Use has been made of the following reagents of p.a. purity: recrystallized silver nitrate, cadmium nitrate, sodium sulphide, thioacetamide, sodiumthiosulphate, nitric acid, acetone, potassium nitrate, glacial acetic acid and sodium acetate.

The following solutions have been prepared: 10^{-1} M silver nitrate, 10^{-1} M cadmium nitrate, 10^{-1} M sodium sulphide, 10^{-1} M thioacetamide, 10^{-1} M thiosulphate, 0,32 M potassium nitrate, buffer solution (pH = 4,7, acetic acid – sodium acetate), 2M natrium hydroxide and 2M nitrique acid. The checking solution series ranging from 10^{-6} to 10^{-1} M Cd^{2+} hawing pH = 4,7 and J=0,32 (KNO_3 ionic strenght adjustor) was prepared by successive dilutions.

Apparata and working conditions: Digital pH/mV-meter; the measuring cell formed by the Cd-ISME and a double junction saturated calomel reference electrode; PW 4620 Phillips difractometer of CPS 10^3 sensitivity (operating rate: 2°/minute; recording rate: 10 mm/minute; 2θ between 10–60°); Teraohmmeter E6–13A. Electrical resistance of the measuring cell was determined at room temperature in 10^{-3} M Cd^{2+}. Potential measurements were performed at room temperature, under stirring (magnetic stirrer).

Preparation of CdS – Ag_2S Mixture: The simultaneous precipitation method of cadmium and silver sulphides from the solution of the corresponding nitrates (molar ratio 1 : 2) with different precipitants (natrium sulphide (S), thioacetamide (TA), thiosulphate (TS)) was elaborated. The solution of the mixture of cadmium and silver nitrates was added to the precipitant solution. The precipitant solution was used in excess. The precipitations with thioacetamide and thiosulphate were carried out at 70°C and those with sodium sulphide at 20°C and 70°C respectively. The precipitates were washed succesively with acidulated distilled water, then with bidistilled water and finally with acetone.

Some precipitates were thermaly treated at 200,250 and 500°C, in a tube electric owen.

Our patents [17—19] refer to the detailed procedures for obtaining electrode materials and Cd-ISME, respectively

Results and Discussion. Table 1 shows the response characteristics of the electrodes whose membranes were obtained from $CdS-Ag_2S$ mixture in molar ratio 1 : 1 (columns 5 and 6) by using different precipitants under the specified working conditions.

Table 1.

Electrodic behaviour of the $CdS\text{-}AgS_2$ mixture (molar ratio 1 :1), obtained with different precipitants.

Nr. crt.	Precipitation agent	Precipitation temperature °C	Thermal treatment °C	Electrode code	Concentration range of the liniar response M/l	mV/pCd Ratio
0	1	2	3	4	5	6
1	Na_2S, excess 20%	70	—	S—1	$5 \cdot 10^{-4}$ —$5 \cdot 10^{-2}$	25±2
2	Na_2S, excess 40%	70	—	S—2	$5 \cdot 10^{-4}$ —$5 \cdot 10^{-2}$	30±2
3	Na_2S, excess 80%	70	—	S—3	10^{-5} — 10^{-1}	26±2
4	Na_2S, excess 80%	20	—	S—4	10^{-5} — 10^{-1}	25±2
5	Na_2S, excess 80%	20	200	S—5	10^{-6} — 10^{-1}	27±2
6	Na_2S, excess 80%	20	250	S—6	$5 \cdot 10^{-5}$ — 10^{-1}	30±2
7	Na_2S, excess 80%	20	500	S—7	$5 \cdot 10^{-3}$ — 10^{-1}	29±2
8	Thioacetamide, excess 100%	70	—	TA—1	$5 \cdot 10^{-6}$ — 10^{-1}	26±2
9	,,	70	200	TA—2	$5 \cdot 10^{-6}$ — 10^{-1}	28±2
10	,,	70	250	TA—3	$5 \cdot 10^{-6}$ — 10^{-1}	26±2
11	,,	70	500	TA—4	unrecycled (useless)	
12	Thiosulphate, excess 100%	70	—	TS—1	$5 \cdot 10^{-6}$ — 10^{-1}	28±2

From the data given in Table 1, it results:

— By using sodium sulphide as a source of S^{2-} ions, an excess of 80% is optimum (electrode S-3 versus electrode S-1) regardless of the thermal regime of the precipitation (electrode S-3 and S-4).

— The thermal treatement at 200—250°C improves the electrode characteristics both for the sulphides obtained by precipitation with Na_2S (electrodes S-5 and S-6 versus electrode S-4) and for those obtained with thioacetamide (electrodes TA-2 and TA-3 versus TA-1). The thermal treatment at 500°C caused the worsening or even the cancelling of the electrode's response (electrode S-7 and TA-4 respectively) as a result of CdS loss by volatilization.

— The best electrode response was display by the sulphides obtained by precipitation either with thioacetamide and treated thermally at 200°C or with sodium thiosulphate with no thermal treatment (electrodes TA-2 and T1-S).

The following characteristics of the electrode's response were also established: the internal electric resistance with values below 100 KΩ and the response time which is at maximum 1 minute.

It has been established that the optimum pH value for TA-2 electrode ranges from 2 to 5. The change of the pH was obtained by adding 2M HaOH and 2M HNO_3 solutions, respectively.

The stability of the electrode response to Cd^{2+} has been followed for a longer period of time (a year). The standard deviation of the potential for every level of concentration in the range 10^{-2}—10^{-5} M Cd^{2+} was found to be below 4 mV.

The crystalline structure of the electrode materials prepared was analyzed, by recording the X-ray diffraction spectra. By interpreting the spectra one may conclude that the electrode materials obtained are mixture of α-CdS, β-CdS and Ag_2S in different proportions. By correlating the resulting structures with the data given in Table 1 for the corresponding electrodes it becomes obvious that compositions richer in αCdS than β-CdS are preferable (electrodes TA-2 and TS-1).

As a result of the present study, it has been concluded that the optimum electrode material is that one with a molar ratio CdS : Ag_2S = 1 : 1, obtained by precipitation either with TA and thermally treated at 200—250°C or with sodium thiosulphate and no thermal treatment.

The electrodes made of these electrode materials shown the following functional characteristics: a practically Nernstian response to Cd^{2+}(28 ± 2 mV/pCd in the concentration range of 5 10^{-6}—10^{-1}M Cd^{2+} and in the pH range = 2—5); a response time shorter than 1 minute; internal electric resistance below 100 kΩ.

REFERENCES

1. J. W. Jr. Ross, in *Ion Selective Electrodes* cap 2, Washington, D.C. 1969.
2. A. V. Gordievskii, V. S. Shzerman, Ya. A. Syrochenkov, N. J. Sauvin A. F. Zhukov, Yu. J. Urusov, *Zh. Anal. Khim.*, 1972, **27**, 2170
3. M. Semler, B. Manek, *Ion Selective Electrodes* Conference 1977
4. W. E. Van der Linden, G. J. M. Heijne, *Ion Selective Electrodes* Conference 1977. Elsevier, Amsterdam, 1978, p. 445
5. G. Yu. Vlasov, E. Yu. Ermolenko V. V. Kolodnikov, *Zh. Anal. Kim* 1981, **36**, 889
6. W. E. Van der Linden, Oastervink, *Anal. Chim. Acta*, 1979, **108**, 169
7. J. W. Ross, Jr. *Pat. Ger. Offen.* nr. 1942379, 1970
8. H. Hirata, K. Hagashiyama, *Z. Anal. Chem.*, 1971, **257**, 104
9. T. Aniält, D. Jagner, *Anal. Chim. Acta*, 1971, **56**, 477
10. M. Mascini, A. Liberti, *Anal. Chim. Acta.*, 1973, **64**, 63
11. J. D. Czahan, G. A. Rechnitz, *Anal. Chem.*, 1973, **45**, 471
12. H. Hirata, K. Higashiyama, *Talanta*, 1972, **19**, 391

13. K. Higashiyama, H. Hirata, *Pat. Ger. Offen.* nr. 2210531, 1972
14. N. J. Savvin, V. S. Shzerman, A. V. Gordievskii, A. Ya. Syrchenkov, *Zavod Lab.* 1971, **37**, 1025
15. V. P. Delouma, J. J. Fornbon, F. Lancelot, J. Paris, M. Roubin, J. Tacusse, J. C. Verdier, *Pat. Fr.* 2268264, 1975
16. H. Bougognon, J. J. Fambon, F. Lancelot, *Analysis*, 1981, **9**, 385
17. E. Hopîrtean, V. Cosma, *Pat. RSR* nr. 95495, 4 nov. 1988
18. E. Hopîrtean, V. Cosma, *Pat. RSR*, nr. 98786, 28 june 1989
19. H. Lingner, E. Hopitrean, M. Horn, V. Cosma, *Pat. RSR* nr. 87517, 26 fbr. 1985.

UNIV. BABEŞ-BOLYAI, CHEMIA, XXXIX, 1–2, 1994

LA DÉTERMINATION DU FACTEUR D'ACCELERATION A L'ABSORPTION DES GAZ DANS DES SOLVENTS CHIMIQUES

I. SIMINICEANU[*], C. PETRILA[*], C. GHERMAN[**], A. POP[***]

RÉSUMÉ. On établit une nouvelle équation pour la détermination *du facteur d'acceleration* (E) à l'absorption suivie d'une reaction de II-ieme ordre. L'equation est verifiee par la methode numerique. Les valeurs obtenues permettent la concretisation de l'equation cinetique du processus global de la chimisorption en fonction des dimensions experimentales des coeficients partiels de vitesse.

Introduction. Les processus chimiques dans lesquels un composant A de la phase de gaz réactionne après le transfert à l'interface, avec le composant B qui existe dans la phase liquide, ont de multiples applications industrielles autant à la purification des gaz (l'élimination du CO_2 par absorption sélective dans des solutions activés de K_2CO_3) qu'à la synthèse de l'acide atotique, l'obtentation du phénol par l'oxydation de l'isopropyle benzène, la fermentation aérobique. Il y a aussi des processus dans lesquels on absorbe deux oü plusieurs gaz, avec ou sans la désorption simultanée d'un produit. Dans les cas de l'absorption d'un seul gaz on peut distinguer plusieurs cas, ce la en fonction du modèle de la réaction : la réaction irréversible de premier ordre, irréversible de II-ième ordre, irréversible avec les ordres „m" et „n", ainsi que pour, les réactions complexes (réversibles) consécutives, parallèles, séries de réactions.

Cela se rapporte à une réaction irréversible du type :

$$A + \nu_B B = \text{produits}$$

avec une équation cinétique de la forme suivante :

$$r = K \cdot C_A \cdot C_B$$

La macrocinétique du processus

Ces processus contiennent quatre processus en série, avec les vitesses individuelles $v_1 \ldots v_4$.

I. Le transfert du composant A du volume de la phase gazeuse à l'interface (v_1).
II. La dissolution à l'interface gaz—liquide (v_2).
III. Le transfert du composant A de l'interface dans le volume du liquide en même temps que la réaction dans le film de liquide (v_3).
IV. Le réaction chimique dans le volume de la phase liquide (v_4).

Dans le schéma 1 on donne les équations cinétiques des quatre étapes individuelles et aussi les „vitesses virtuelles maximales" correspondantes, dans des conditions limites précisées dans la dernière colonne.

---

[*] *Universitatea Tehnică, Iaşi*
[**] *Grupul Şcolar, Orăştie*
[***] *Univ. „Babeş-Bolyai, Cluj-Napoca*

Tabelle 1

Les équations cinétiques des processus composants.

La vitesse du processus individuel	„La vitesse virtuelle maximale"	Les conditions limites
$v_1 = K_g(p_A - p_A^s)$	$v_1 = K_g \cdot p_A$	$p_A^s = 0$
$v_2 = K_d(p_A^s - C_A^s/H)$	$v_2 = K_d \cdot p_A$	$p_A^s = p_A;\ C_A^s = 0$
$v_3 = E \cdot K_L(C_A^s - C_A)$	$v_3 = E \cdot K_L \cdot H \cdot p_A$	$p_A^s = p_A;\ C_A^s = H \cdot p_A$
$v_4 = \frac{v}{A} \cdot K \cdot C_A \cdot C_B$	$v_4 = \frac{v}{A} \cdot K \cdot C_B \cdot H \cdot p_A$	$p_A^s = p_A;\ C_A^s = H \cdot p_A;$ $C_A = H \cdot p_A$

Car les quatre étapes oposent des résistances en série, la vitesse du processus global d'absorption chimique a l'expression:

$$v = \frac{1}{\sum_{1}^{4} \frac{1}{v_1}} = \frac{P_A}{\frac{1}{K_g} + \frac{1}{K_d} + \frac{1}{EK_LH} + \frac{a_v}{KH \cdot C_B}} \tag{1}$$

Dans l'expression de v_3, K est multiplié avec E la réaction ne pouvant qu'accélérer le transfert de A de l'interface dans le volume du liquide. La détermination du facteur d'accélération E ($E \geqslant 1$) fait l'objet de cette étude.

La détermination du facteur d'accélération

Par l'intégration de l'équation differéntielle de bilan dans le film de liquide, on obtient la relation implicite de E, valable pour l'absorption accompagnée d'une réaction irréversible de II-ième ordre [1]:

$$E = \frac{\mathrm{Ha}\sqrt{1 - \frac{E-1}{b}}}{\mathrm{th}\left(\mathrm{Ha}\sqrt{1 - \frac{E-1}{b}}\right)} \tag{2}$$

oú:

$$b = \frac{D_B \cdot C_B}{v_B \cdot D_A \cdot C_A^s}, \quad \mathrm{Ha} = \frac{\sqrt{K \cdot C_B \cdot D_A}}{K_L} \text{ le critérium Hatta)}$$

En même temps, on éttablit des relations empiriques $E = f$ (Ha, b) qui ayant des formes explicites, sont plus faciles à résoudre. Wellek [2] arrive à la conclusion que la plus précise des équations empiriques est celle établie par Kishinevski [3]:

$$E = 1 + \frac{\mathrm{Ha}}{A}\,[1 - \exp.\,(-0{,}65\ \mathrm{Ha}\ A)] \tag{3}$$

Oú :

$$A = \frac{Ha}{b} + \exp\left(\frac{0{,}68}{Ha} - \frac{0{,}45\ Ha}{b}\right)$$

Dans un ouvrage antérieur on a établi une nouvelle relation pour la détérmination de E, ayant la forme (4) :

$$E = 1 + \frac{1}{\dfrac{1}{\dfrac{Ha}{th\ Ha} - 1} + \dfrac{1}{\dfrac{D_B \cdot C_B}{D_A \cdot H \cdot p_A}}}$$

L'équation (4) a plusieurs avantages. Elle est établie sur des bases rationnelles et, par conséquant, elle est plus générale que les autres, empiriques. Ainsi en remplaçant dans (4) la condition $C_B = 0$ on obtient la rélation simple établie pour les réactions de I-er ordre (4) :

$$E = \frac{Ha}{th\ Ha} \tag{4}$$

L'adéquance de l'équation est verifiée sur l'ordinateur en comparant les valeurs de E avec celles résultées des relations (2) et (3). Les expériments numériques éffectués à cette occasion ont relavé un autre avantaje de l'équation (4), simple et explicite, vis-à-vis de la relation implicite (2) qui présente des difficultés de convergence. Les résultats sont présentés dans le Tabelle 2. Pour chaque Ha, les valeurs correspondant en ordre aux équations (2, 3) et (4).

Tabelle 2

$E = f(Ha, b)$

Ha/b	1	5	10	20	50	100	200	500	700	1000
0.1	1.003	1.003	1.003	1.003	1.003	1.003	1.003	1.003	1.003	1.003
	1.000	1.000	1.000	1.000	1.000	1.000	1.000	1.000	1.000	1.000
	1.000	1.000	1.000	1.000	1.000	1.000	1.000	1.000	1.000	1.000
	1.003	1.003	1.003	1.003	1.003	1.003	1.003	1.003	1.003	1.003
0.2	1.013	1.013	1.013	1.013	1.013	1.013	1.013	1.013	1.013	1.013
	1.003	1.003	1.003	1.003	1.003	1.003	1.003	1.003	1.003	1.003
	1.013	1.013	1.013	1.013	1.013	1.013	1.013	1.013	1.013	1.013
0.5	1.076	1.081	1.081	1.082	1.082	1.082	1.082	1.082	1.082	1.082
	1.061	1.061	1.061	1.061	1.061	1.061	1.061	1.061	1.061	1.061
	1.076	1.081	1.081	1.082	1.082	1.082	1.082	1.082	1.082	1.082
1.0	1.241	1.296	1.304	1.308	1.311	1.312	1.313	1.313	1.313	1.313
	1.276	1.300	1.302	1.303	1.303	1.303	1.303	1.303	1.303	1.303
	1.238	1.294	1.303	1.308	1.311	1.312	1.312	1.313	1.311	1.313
2.0	1.544	1.909	1.986	2.029	2.056	2.065	2.070	2.073	2.073	2.074
	1.681	2.022	2.071	2.095	2.109	2.114	2.116	2.117	2.118	2.118
	1.518	1.884	1.970	2.021	2.052	2.063	2.069	2.072	2.073	2.073
3.0	1.722	2.532	2.749	2.875	2.957	2.986	2.999	3.009	3.011	3.012
	1.876	2.757	2.934	3.027	3.084	3.103	3.113	3.118	3.120	3.120
	1.668	2.436	2.667	2.830	2.937	2.975	2.995	3.007	3.009	3.011

Tabelle 2 (continued)

b	1	5	10	20	50	100	200	500	700	1000
5.0	1.875	3.524	4.143	4.537	4.807	4.902	4.951	4.981	4.986	4.998
	1.976	3.849	4.459	4.825	5.063	5.146	5.187	5.212	5.217	5.221
	1.800	3.222	3.857	4.334	4.704	4.847	4.982	4.969	4.977	4.984
10	1.965	4.832	6.619	8.048	9.149	9.562	9.778	9.910	9.936	9.955
	1.998	5.103	6.942	8.377	9.480	9.893	10.11	10.24	10.27	10.28
	1.900	4.214	5.737	7.207	8.627	9.256	9.621	9.840	9.886	9.919
20	1.991	5.607	8.983	12.80	16.59	18.20	19.07	19.63	19.73	19.81
	1.999	5.795	9.262	13.05	16.82	18.46	19.36	19.94	20.04	20.13
	1.950	4.958	7.552	10.74	14.76	1.696	18.35	19.30	19.50	19.65
50	1.999	5.930	10.55	18.32	31.35	39.28	44.26	47.61	48.28	48.79
	2.000	5.994	10.79	18.67	31.37	39.18	44.26	47.77	48.48	49.02
	1.980	5.537	9.305	15.20	25.75	33.88	40.35	45.62	46.79	47.71
100	2.000	5.982	10.88	20.18	42.13	62.24	78.32	90.59	93.18	95.17
	2.000	5.999	10.98	20.58	42.50	61.90	77.68	90.27	92.99	95.15
	1.990	5.760	10.08	17.64	34.22	50.74	67.22	83.63	87.73	91.08
200	2.000	5.996	10.97	20.78	48.11	83.55	124.0	164.1	173.6	181.1
	2.000	6.000	10.99	20.97	49.01	84.05	122.9	162.5	172.2	180.0
	1.995	5.877	10.52	19.17	40.96	67.55	100.7	143.3	155.9	166.9
500	2.000	5.999	10.97	20.96	50.49	97.22	176.2	309.5	352.7	390.6
	2.000	6.000	11.00	20.99	50.94	98.93	177.9	306.1	348.1	385.7
	1.999	5.955	10.80	20.22	46.44	84.30	143.7	250.7	292.3	333.9
700	2.000	6.000	11.00	20.98	50.74	99.00	186.7	365.0	433.0	496.9
	2.000	6.000	11.00	21.00	50.99	100.4	189.8	363.1	428.3	490.3
	1.999	5.964	10.86	20.44	47.66	88.48	156.5	292.5	350.7	412.4
1000	2.000	6.000	11.00	20.99	50.87	100.0	193.5	414.9	515.2	618.4
	2.000	6.000	11.00	21.00	50.99	100.9	196.9	416.5	512.6	611.5
	1.999	5.975	10.98	20.92	50.50	99.04	193.3	405.5	415.0	534.3

Résultats et discussions. Les résultats du Tabelle 2 sont partiellement présentés dans la figure 1, dans des coordonnées logaritmiques sous la forme des courbes $E = f$ (Ha) pour $b = 1$, $b = 10$, $b = 100$, $b = 1000$, Les valeurs de E obtenues par l'équation (4) sont plus basses sur certains intervalles, mais la concordance est satisfaisante.

En se basant sur les valeurs numériques obtenues, on paut établir avec précision autant le régime cinétique d'un processus réel que l'équation cinétique correspondante en fonction des valeurs des critériums Ha et b. Car, en général, la dissolution est très rapide, trois régimes cinétiques principaux sont possibles (a, b, c). a) Quand $K_g \ll E \cdot K_L \cdot H$; $\frac{v}{A} \cdot K \cdot C_B \cdot H$, K_d, le transfert de A par la phase gazeuse est l'étape déterminante de vitesse ou modèle macrocinétique simple. En tenant compte des conditions ci — dessus, l'équation cinétique (1) devient : $v = v_1 = K_g \cdot p_A$ (5)

b) Si $\frac{v}{A} \cdot K \cdot C_B \cdot H \ll K_g$, K_d, $E \cdot K_L \cdot H$, la réaction devient le plus lente, et l'équation cinétique devient :

$$v = v_4 = \frac{v}{A} \cdot K \cdot H \cdot p_A \qquad (6)$$

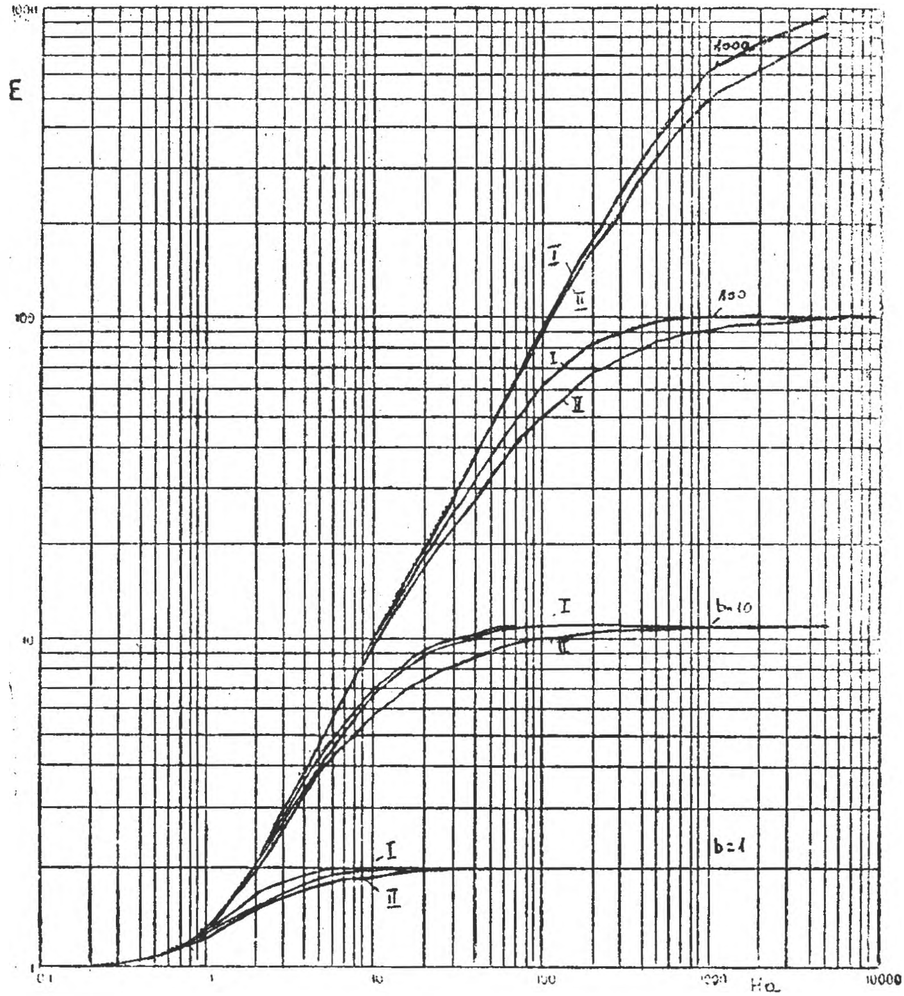

Fig.1. La forme des courbes E=f(Ha) pour b=1, b=10, b=100, b=1000 obtenues par l'equations 2-3(I) et 4(II)

c) Si $E \cdot K_K \cdot H \ll K_g,\ K_l,\ \frac{V}{A} \cdot KC_B \cdot H$ est un modèle macrocinétique combiné. La vitesse est contrôlée aussi bien par la diffusion que par la réaction qui a lieu simultanément dans le film du liquide. En tenant compte desdonnées expérimentales du schéma 2, le cas (c) peut être divisé en trois régimes ciné-
(c.1) Pour $Ha < 0,5$ on observe que le facteur d'accélération varie seulement entre 1,0 et 1,08. Pratiquement, $E = 1$ et l'équation cinétiques est celle de transfert physique par la phase liquide.

$$v = K_L \cdot H \cdot p_A \tag{7}$$

(c.2.) Pour Ha >3 et b $\gg$ Ha on a E $=$ Ha, et l'équation cinétique devient :

$$v = Ha \cdot K_L \cdot H \cdot p_A = H \cdot p_A\sqrt{K \cdot C_B \cdot D_A} \qquad (7')$$

C'est le régime ,,Réaction très rapide'', quand la vitesse globale de l'absorption croit proportionnellement avec Hatta. En employant des solutions activées, K et Ha augmentent aussi.

(c.3.) Pour Ha >3 et b $\ll$ Ha $-$ 1, l'écuation cinétique devient :

$$r = K_L \cdot H \cdot p_A\left(1 + \frac{D_B \cdot C_B}{D_A \cdot H \cdot p_A}\right) = K_L(H \cdot p_A + D_B \cdot C_B/D_A) \qquad (7'')$$

oú $E = 1 + b$

C'est le régime ,,réaction instantanée'', réaction qui a lieu pratiquement à l'interface.

Notations et indices:

— D_A, D_B — *coeficients de diffusion* m^3/s
— K, K_g, K_L, K_d — *coeficients cinétiques de la réaction, du transfert par le gaz, du transfert par le liquide et du la dissolution.*
— H — *la constante de Henry*
— $a_0 = A/V$ — *l'aire de la surface spécifique*, m^2/m^3
— s — *l'indice pour l'interface.*

BIBLIOGRAPHIE

1. I. Siminiceanu, *Studia Univ. Babeş-Bolyai, Chemia* 1—2, 1991, 36, 256
2. R. M. Wellek, R. J. Brunson, F. H. Law, *The Can. Jaurnal of Chem. Eng.* 1978, 56
3. M. K. Kisinevschi, *Theor. und. Chem. Eng.* 1971, 4, 641
4. I. Siminiceanu *Chem. Eng. Process*, 1993, 30, 115

TUDIA UNIV. BABEŞ-BOLYAI, CHEMIA, XXXIX, 1–2, 1994

MASS TRANSFER COEFFICIENTS AT Fe^{2+} OXIDATION TO Fe^{3+}

R. MIŞCA*, AL. OZUNU*, S. DRĂGAN*, ADINA GHIRIŞAN*

ABSTRACT. – This work presents experimental results obtained at Fe^{2+} oxidation to ferric ion in alkaline solution, using an apparatus endowed with an interior contacting coil gas-liquid with autoinduced film. It has determined Fe^{2+} to Fe^{3+} conversion vs. time at different concentrations and mass transfer coefficients at different velocities of oxidant agents (air).

Measurements and results obtained permit to establish the stage determinative of velocity in progress of global process, as well as the intensification factor. In experiment's conditions the values of activation energy are in the range 3300 – 5000 [cal/mol] and the mass transfer coefficient in the range 1 – 8 [g/(m²s)].

Key-Words: Mass transfer coefficients, Oxidation of Fe^{2+}

Introduction. Owing to practical interest wich ancatalytic process of oxidation Fe^{2+} to Fe^{3+} presents, it has tried the study of intensification of the global process through modification's contacting procedure of reaction's phases and work's conditions.

It is known [1, 7, 9] that ferrous ion in alkaline medium reacts cvasisnopshot with oxygen from air, passing in compounds where the iron is threevalent.

By the practical point of view this thing is observed visual through colour's changing of hurried from yellow to black.

Reaction scheme:

$$Fe^{2+} \rightarrow Fe^{3+} \tag{1}$$

$$O_2 + 2H_2O \rightarrow 4HO^- \tag{2}$$

The final product is a coloured hurried with general formula: $FeO(OH)XH_2O$ [1, 9].

The morphology and the colour of hurried depends of obtaining conditions [1, 2, 4, 9].

The apparatus and Works Conditions. The experimental installation is shown in Figure 1. The contacting apparatus that generate an upward film through intermediate oxidant agent [4, 7, 8, 10] has in componence a contacting coil with $S_{int} = 0.014$ m² made from a glass tube with diameter $D_{int} = 4.8 \cdot 10^{-3}$ m, and a recirculation tube of liquid phase with h = 0.12 m.

The reaction substratum was prepared in that way: in aqua solution of ferrous sulphate p.a it was added in bubles under powerful agitation in closed vessel, a NaOH 20% solution, for obtaining an uniform and very advanced degree of dispersion.

The substratum was very quickly poured in the inferior recipient of contacting apparatus, that is immersed in a thermoconstant vessel.

---

* *Department of Chemical Engineering, „Babeş-Bolyai" Univ., Cluj-Napoca, 3400.*

Working parameters were maintained constants in the experiment's time and these values are presented in Table 1.

Determination of ferrous ion concentration at one moment was done by permanganometric method.

Table 1

Parameters	U.M.	Values		
Q — Flow rate	l/h	60	120	180
T — Temperature	°C	20	40	80
c — Concentration	%	2,5	5	10

Results and discursions. Experimental results are shown in Table 2.

The variation of conversions in time vs. velocity are shown in Figure 2.

It is found an expected variation of conversion vs. velocity (flow rate of air). The increase of velocity determine the increase of final conversion and the velocity of touching of higher conversions.

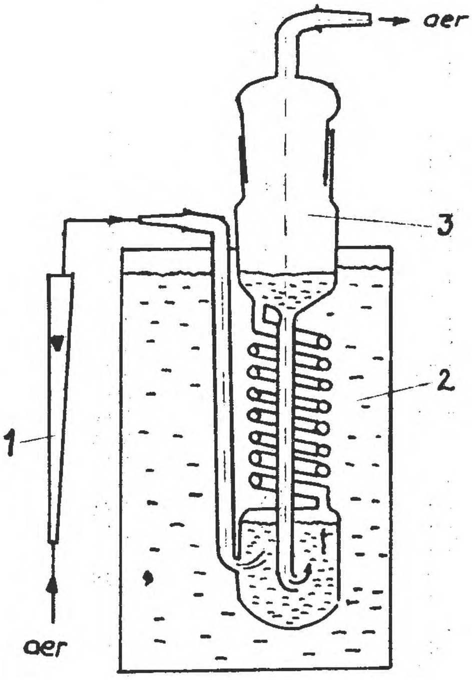

Fig. 1. Experimental installation
1 — rheometer; 2 — thermoconstant vessel; 3 — contacting apparatus

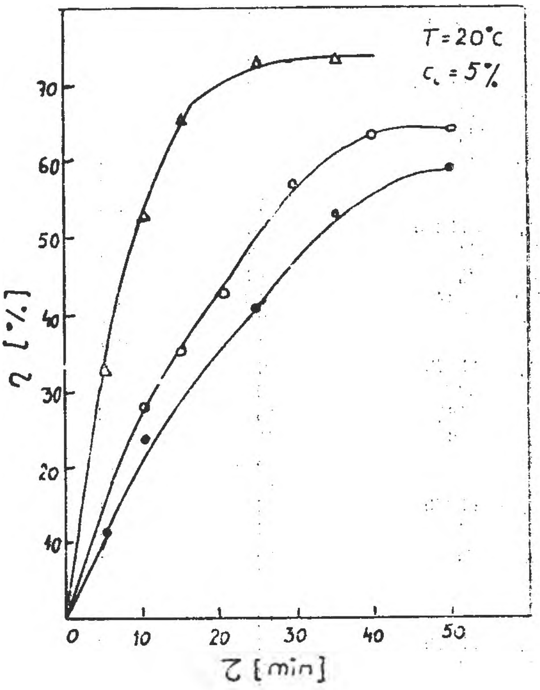

Fig. 2. Conversion's variation vs. time at different flow rates.
Δ: $Q_v = 180$ l/h; o: $Q_v = 120$ l/h; ●: $Q_v = 60$ l/h.

Table 2

Working parameters	τ min	$V_{KMnO_4} \cdot 10^{-6}$ m^3	m_{O_2}(consumed) $\cdot 10^7$ kg	Fe^{3+} %	$K_L \times 10^6$ kg/m^{2}s
$O_v = 60$ l/h	0	3,2	0	0	0
T = 20°C	10	2,2	9,02	31,25	9,24
$c_i = 10\%$	25	1,5	8,92	53,12	0,435
$H_a = 1{,}07$	35	1,2	5,43	62,5	0,265
	45	1,1	1,74	65,62	0,085
	55	0,8	1,43	75,0	0,0036
$Q_v = 60$ l/h	0	2,8	0	0	0
T = 40°C	5	2,4	7,18	14,3	0,986
$c_i = 10\%$	10	2,2	3,59	21,4	0,493
Ha = 7,59	17	1,8	2,18	35,7	0,30
	27	1,7	1,74	39,3	0,32
	37	1,5	0,59	46,43	0,246
$Q_v = 60$ l/h	0	3,4	0	0	0
T = 80°C	5	3,0	7,16	11,76	0,042
$c_i = 10\%$	10	2,4	5,87	29,41	0,033
Ha = 494,6	15	2,3	2,74	32,35	0,005
	25	2,2	1,84	35,29	0,003
	42	2,0	1,64	41,17	0,0025
$Q_v = 60$ l/h	0	1,4	0	0	0
T = 20°C	10	1,0	10,15	28,57	0,99
$c_i = 5\%$	15	0,9	2,5	35,71	0,42
Ha = 16,44	20	0,8	2,1	42,86	0,38
	30	0,6	1,9	57,14	0,21
	40	0,5	0,5	64,28	0,19
$Q_v = 120$ l/h	0	1,7	0	0	0
T = 20°C	5	1.5	4.1	11.76	0.4
$c_i = 5\%$	10	1.3	4.0	23.53	0.39
Ha = 4.7	15	1.0	3.8	41.17	0.32
	25	0.9	2.8	43.1	0.28
	35	0.8	2.6	58.4	0.20
$Q_v = 180$ l/h	0	1.5	0	0	0
T = 20°C	5	1.0	10.15	33.33	0.99
$c_i = 5\%$	10	0.7	6.15	53.33	0.6
Ha = 2.87	15	0.5	4.1	66.67	0.42
	25	0.4	2.05	73.33	0.1
	35	0.4	0	73.33	0
$Q_v = 60$ l/h	0	3,2	0	0	0
T = 20°C	10	2,2	9,02	31,25	1,1
$c_i = 10\%$	15	2,0	3,59	37,5	0,85
Ha = 2,8	25	1,5	7,02	35,12	0,44
	35	1,2	5,33	62,5	0,26
	45	1,1	1,74	65,62	0,18
$Q_v = 60$ l/h	0	1.4	0	0	0
T = 20°C	10	1.0	4.72	28.6	0.46
$c_i = 5\%$	15	0.9	3.05	35.7	0.31
Ha = 5,7	20	0.8	2.05	42.85	0.22
	30	0.6	1.71	57.1	0.19
	40	0.5	0.92	64.28	0.15
$Q_v = 60$ l/h	0	0.7	0	0	0
T = 20°C	5	0.6	2.05	16.66	0.4
$c_i = 2{,}5\%$	10	0.5	1.92	18.62	0.32
Ha = 4,05	15	0.4	1.2	28.42	0.21
	20	0.3	0.9	33.33	0.18
	25	0.2	0.72	35.2	0.17

Conversion's variations vs. temperatures are presented in Figure 4. Here is observed a fast increase of ferrous ion concentrations with temperature's increase.

It was determined relatives constants of velocities, and after that, apparent energy of activation in the purpose to establish the determinative stage of velocity in global process progress.

The values obtained for apparent energy of activation suggest that the determinative stage in global process progress was oxygen transfer from gaseous phase to liquid phase.

In our working conditions the oxygen consumption from reaction medium was momentary. [1, 2, 3, 7, 9].

It has calculated the values of mass transfer coefficients at Fe^{2+} oxidation to Fe^{3+} in alkaline substratum when determinative was oxygen transfer into liquid phase.

The variation of K_L coefficient at different initial concentrations of reaction substratum, shows a diminuation with decrease of concentration in Figure 5.

Variation of K_L coefficient vs. flow rates of oxidant agent, shows that with increases of gass velocity increase the mass transfer coefficients too, like in Figure 6.

With temperature increases, at constants velocity and concentration, it is found a diminuation of K_L coefficient, diminuation that at low temperatures is practicaly linear, and at high temperatures is exponential like in Figure 7.

Exponential diminuation of mass transfer coefficient with temperature's increase should be owed to diminuation of oxygen solubility in solutions of aquas electrolit.

It has calculated Hatta module:

$$Ha = (K \cdot C_B \cdot D_A)^{1/2}/K_L \tag{3}$$

For constants temperature and concentration, the value of Hatta module decreases with increases of air flow rate.

For constants initial concentration and flow rate, the value of Ha increase with increases of temperature.

The variation of Ha suggests informations concerning the kinetic's process. For $Ha > 4$ the reaction take place in liquid film, and for $0.04 < Ha < 4$ the reaction take place in liquid film and in convective zone.

Conclusions. Measurements and calculus efectuated demonstrate that ferrous ion oxidation to ferric ion in alkaline aqua solution, determinative of velocity in global process progress was oxygen transfer through liquid phase.

Mass transfer coefficients in liquid phase are influenced by initial concentration of substratum, by temperature and by oxidant agent velocity, and the intensification of turbulence in liquid phase determines the increase of transfer coefficient.

The value of Hatta modulus determinated in works conditions demonstrated that reaction took place both in liquid film and in convective zone. This justify that determinative in process progress is the transfer through liquid phase.

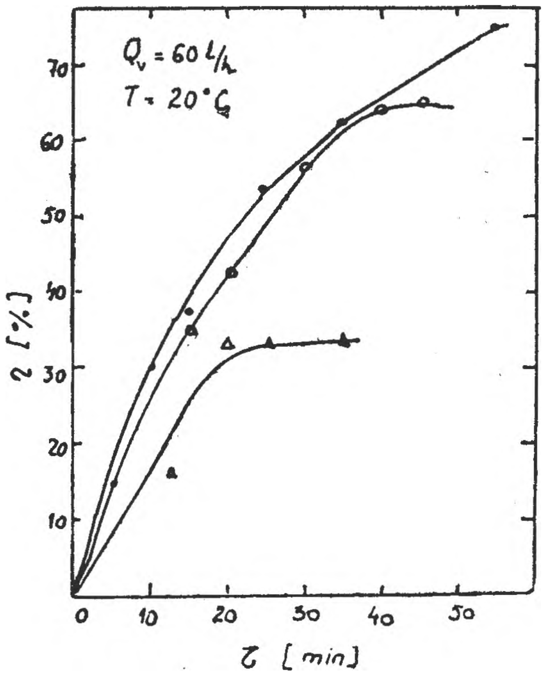

Fig. 3. Conversion's variation vs. time at different initial concentrations
● : c_i = 10% ; o : c = 5% ; Δ : c = 2.5%.

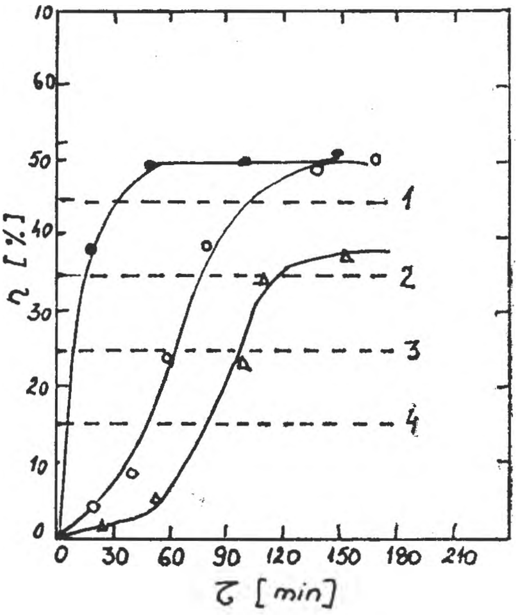

Fig. 4. Conversion's variation vs. time at different tenperatures
● : T = 80ŏC ; o : T = 40° C ; Δ : T = 20°C
1 : η = 45% ; 2 : η = 35% ;
3 : η = 25% ; 4 : η = 15%.

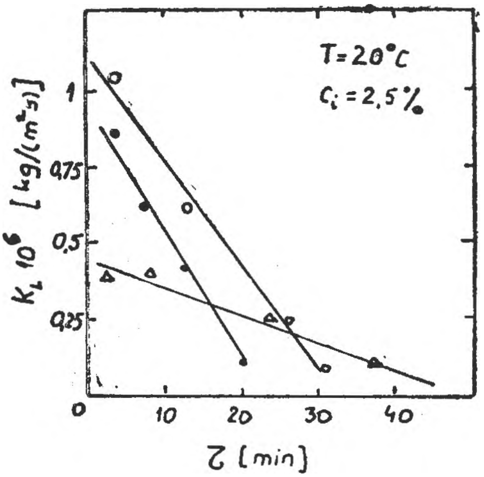

Fig. 5. Variation of K_L coefficient vs. time at different initial concentrations
o: $c_i = 10\%$; ●: $c_i = 5\%$; Δ: $c_i = 2.5\%$

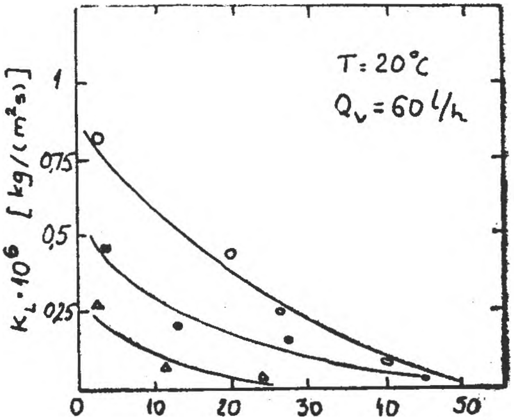

Fig. 6. Variation of K coefficient vs. time at different flow rates
o: Q_v = 180 l/h; ●: Q_v=120 l/h; Δ: Q_v=60 l/h

Fig. 7. Variation of K coefficient vs. time at different temperatures
●: T = 20°C; o: T = 40°C; Δ: T = 80°C.

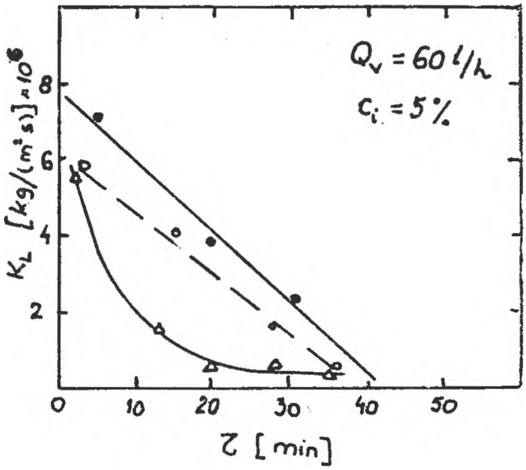

Working conditions (temperature, air flow rate, initial concentration) determine the modifications of morphology and structure shown by hurried colour changing.

Nomenclature:

S_{int} : *interior surface of coil,* m^2
D_{int} : *interior diameter of coil,* m
Qv : *air flow rate,* m^3/s
η : *conversion,* %

Ha : *Hatha modulus*,
K : *relative constant of velocity of reaction*,
D_A : *diffusion coefficient*, m^2/s
K_L : *mass transfer coefficients*, $kmol/(m^2/s)$

REFERENCES

1. P. Spacu, C. Gheorghiu, M. Stan, M. Brezeanu, *Tratat de chimie anorganic ă* vol. III, Ed. Tehnică, Bucureşti, 1978, p. 1104.
2. C. Ionescu, *Chimie-fizică*, Editura Didactică şi Pedagogică, Bucureşti, 1972, p. 142.
3. C. Carloganu, *Introducere în ingineria reactoarelor chimice*, Editura Tehnică, Bucureşti, 1980, p. 160.
4. I. Vodnar, A. Biro, *Tehnologia şi merceologia produselor industriale*, lito, Universitatea ,,Babeş-Bolyai", Cluj-Napoca, 1992, p. 43.
5. F. Albert, A. Iancu, V. Mărculeţiu, *Tabele chimice în practica analitică*, Ed. Tehnică, Bucureşti, 1965, p. 150.
6. O. Floarea, R. Dima, *Procese de transfer de masă şi utilaje specifice*, Editura Didactică şi Pedagogică, Bucureşti, 1982.
7. L. Ifrim, C. Calistru, *Proces unitar adsorbţie-reacţie-formare de germeni*, Institutul Politehnic Iaşi, 1987.
8. I. Vodnar, Brevet RSR, nr. 96372 (1987).
9. C. Calistru, C. Leonte, *Tehnologia substanţelor anorganice*, Editura Didactică şi Pedagogică, Bucureşti, 1972.
10. J. Szekely, J. W. Evans, *Chem. Eng. Sci.*, **26**, (6), 1971.
11. D. Muntean, A. Woinarosky, G. Bogza, *Aplicaţii la calculul reactoarelor chimice*, Editura Tehnică, Bucureşti, 1984.

STUDIA UNIV. BABEŞ-BOLYAI, CHEMIA, XXXIX, 1-2, 1994

AN EXPERIMENTAL TECHNIQUE FOR MEASURING DIFFUSION COEFFICIENTS IN POROUS SOLIDS

R. MIŞCA*, AL. OZUNU*, S. DRĂGAN*, ADINA GHIRIŞAN*

ABSTRACT. — It has tried experimental determination of total permeability of some porous materials at Cu^{2+} flow, and the dependence of the ions flow vs. hydrodinamics caracteristics and the materials voidages who are passing. The technique is appropiate for measuring D_e in the range $0.1-20 \cdot 10^{-6}$. Comparisons between this technoque and other techniques are discussed.

Key-words: Permeability, Effective Diffusivity

Introduction. Problems connected with diffusion of liquids in porous solids occur in many technically important areas. These are within the problems of diffusion of gases. Most of the research both theoretical and experimental, has been concentrated on diffusion in catalysts [6, 7, 8, 9, 10] and molecular sites [11].

Experimental Section: As shown in Figure 1, the apparatus consisted of a hollow, cylindrical chamber [4, 5, 6, 7]. The cylindrical solid sample was placed in the central portion of the chamber. The chamber had a diameter of 35 mm and the cylindrical samples had the size of about 46 mm in diameter and greater than 4 mm in width. The temperature in this work was 20°C, measured constant.

Measurements of Cu^{2+} ions concentration were done with ion selective electrodes in ratio with a standard curve built previously. Pore size distribution of the materials used are shown in Figure 2 and Figure 3.

The values of concentration and flow rates of one side and of the other side of porous wall were performed after steady-state stabilisation. The results are presented in Table 1, Figure 6 and Figure 7.

Results and discussions. This technique employs flows of liquids of different composition over two sides of a cell separated by a porous solid. Composition changes between cell's entering and leaving. It are measured and are related to the mass flux and the diffusion coefficient by using the solution to the governing diffusion equation [2, 3].

Going from general aspects of mass transfer [1, 2] the material flux who is passing the porous bed, without consideration the transport mechanism, one can calculate with general relation [2, 3]:

$$F = -D \cdot S \cdot (dc/dx), \tag{1}$$

Considering that the concentration gradient is established only on a distance equal with the sample width the equation (1) become:

$$F = Q_c \cdot S \cdot [(c_1 - c_2)/1], \tag{2}$$

---

* *Department of Chemical Engineering, „Babeş-Bolyai" University, 3400, Cluj-Napoca, ROMANIA.*

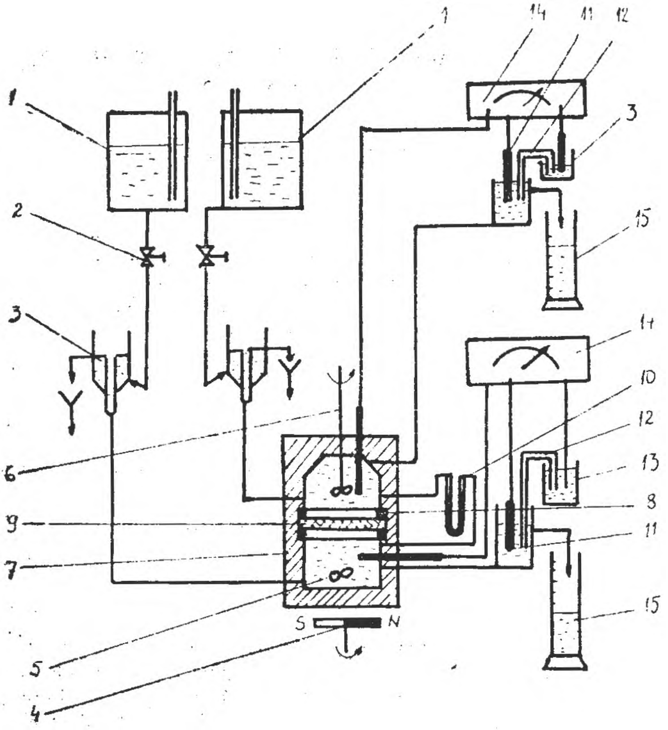

Fig. 1. Experimental installation
1 — Mariotte vessel; 2 — valve; 3 — constant level vessel; 4 — magnetic agitator; 5 — pale of agitator; 6 — mecanic agitator; 7 — measurement cell; 8 — tight rings; 9 — porous bed; 10 — differential manometer; 11 — Cu^{2+} selective electrodes; 12 — electrolitic trap; 13 — calomel saturated electrodes; 14 — measurement apparatus; 15 — cylinder.

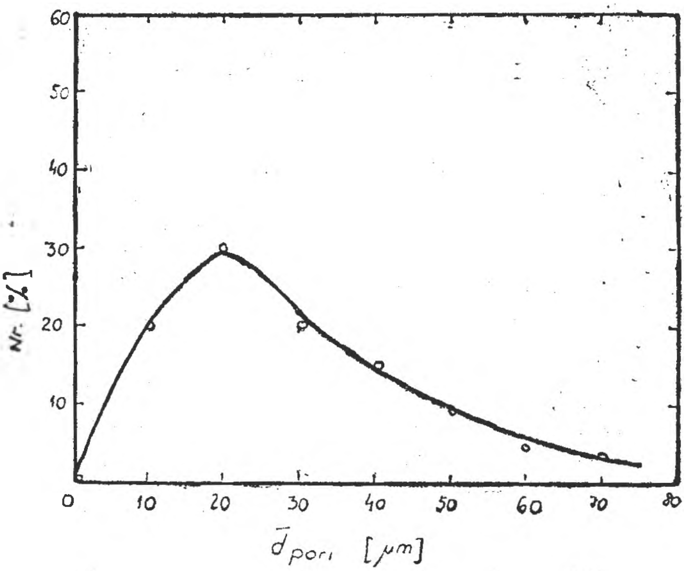

Fig. 2. Pore size distribution
Bz 18% voidages
Dmed = $20 \cdot 10^{-6}$ μm

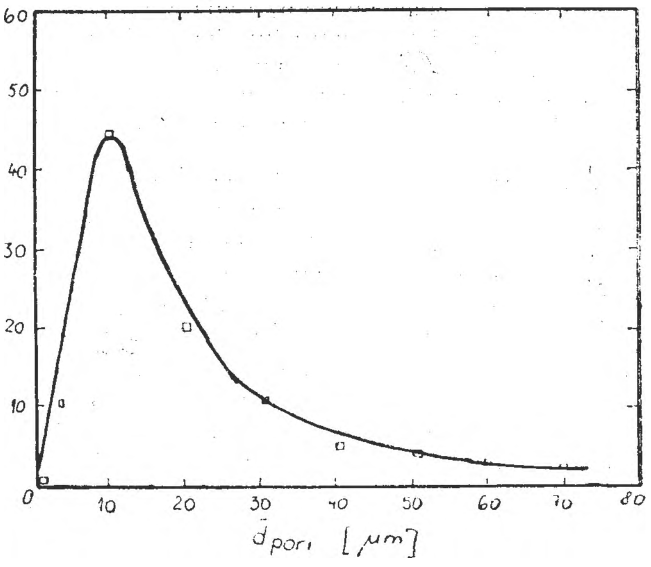

Fig. 3. Pore size distribution
Glass 30% voidages
Dmed = 10 · 10^{-6} µm

This general relation don't presume the knowledge in details of transport mechanism [5], because the permeability coefficient Qc in terms of concentration it will take over the influence of hydrodinamic and morphology structures details of porous bed.

The sample are represented in Figure 4 and the profile of concentration are given in Figure 5.

Like that we mentioned previously, we cannot determine c_1, c_2, c_1^*, c_2^*.

If the separator bed is inert by the pshysical-chemistry point of view given the fluid who are passing, ones can presume disappearing of the terms who involve the absorbtion-desorbtion phenomenom in the separator bed, and

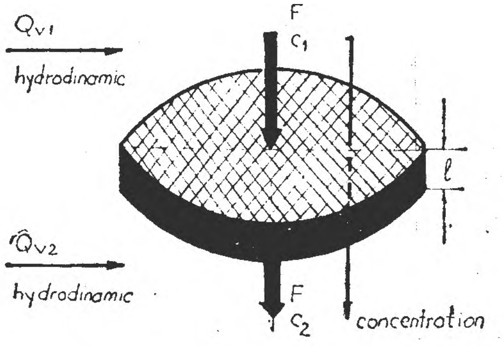

Fig. 4. Schematic representation of porous sample

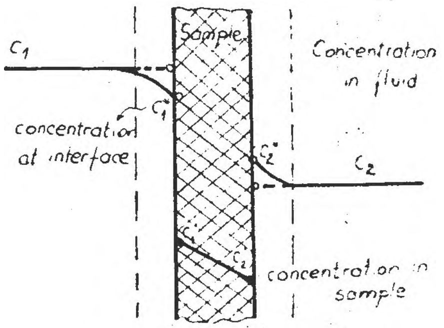

Fig. 5. Profile of concentration through porous material

possible solvation phenomenom, remain in discussion diffusion through pores of material. It is determinate by the gradient of concentration and by the influence of hydrodinamics factors on the separators surfaces and possible macropores who are keeping a convective foreign current, owed to differences of concentrations between two faces of separator bed.

Conclusions. At the constant diameter pores the growing of solution concentration determine a rising of permeability of porous wall.

Big flow rates of fluids who are passing the sample determine a very fast plateformation of concentration's level.

Over diameter of pores like 40 µm at width of sample in the range of 4.5—5.0 mm prevail foreign currents.

The resindence time for steady state stabilisation is about 10—20 minutes for porous walls with the pore diameter in the range 10—40 µm.

The range of permeability 1—18 · 10^{-5} cm^2/s is with two or three dimensions order higher than the autodiffusion coefficients in zeolytics molecular sites [12].

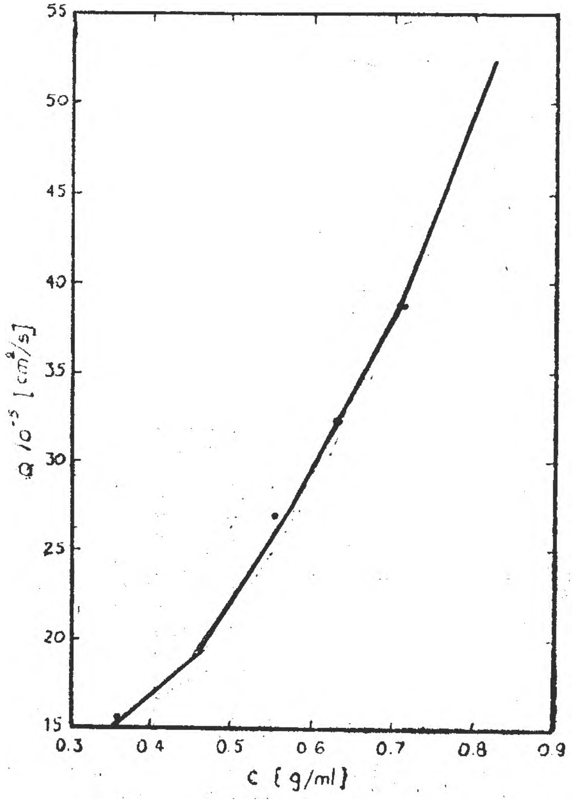

Fig. 6. Profile of effective permeability vs. concentration for a sample of Bz. 18%, Dmed = = 20 · 10^{-6} µm.

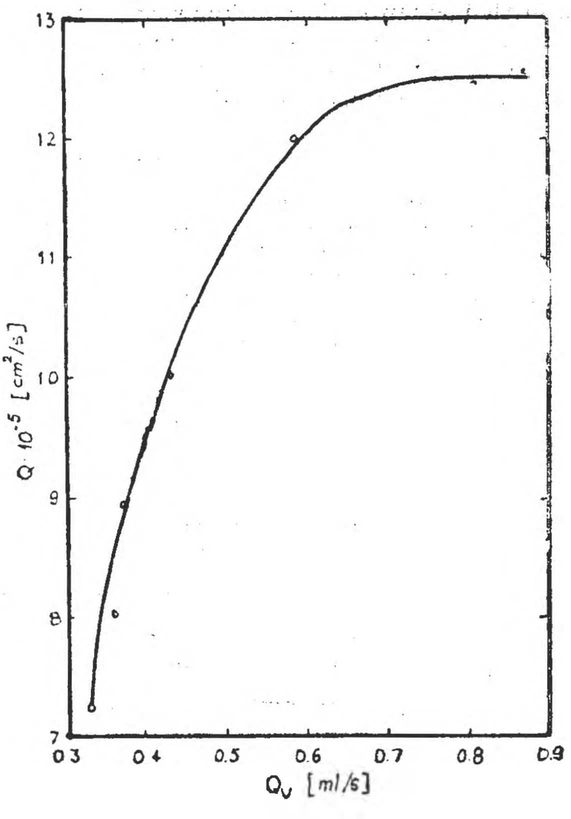

Fig. 7. Profile of effective permeability vs. concentration for a sample of glass 30%, Dmed = $= 10 \cdot 10^{-6}$ μm

Table 1

Experimental and calculated results

$C_{entrance}$ %	C_{exit} %	ΔC %	$\bar{C}$ %	$Q_v \cdot 10^6$ m³/s	$m_{transf} \cdot 10^5$ kg/s	$C_e \cdot 10^2$ %	$\bar{C}_e \cdot 10^2$%	$Q_v \cdot 10^6$ m³/s	$Q_c \cdot 10^2$ cm²/s
1	2	3	4	5	6	7	8	9	10
26	19.5	6.5	22.5	0.33	2.16	10.5	5.25	0.2	0.00742
26	20.5	5.5	23.25	0.694	3.817	18.1	9.05	0.21	0.01285
26	21.75	4.25	23.87	0.879	3.735	1.7	0.85	2.22	0.01221
10.5	5.8	4.7	8.16	0.725	4.35	2.67	1.335	1.63	0.0416
6.6	6.0	0.6	6.3	1.66	0.996	1.63	0.815	0.612	0.0123
2.6	1.9	0.7	2.25	1.02	0.714	0.47	0.235	1.52	0.0247
1.8	0.35	1.45	1.075	0.35	0.07	0.013	0.0065	0.55	0.0054
1.6	0.4	0.2	0.5	0.265	0.33	0.5	0.25	0.66	0.0052
0.85	0.8	0.005	0.825	0.97	0.0487	0.127	0.0635	0.384	0.0047
0.82	0.8	0.02	0.815	1.18	0.093	0.131	0.065	0.71	0.00534
0.45	0.43	0.02	0.44	0.89	0.0178	0.036	0.018	0.49	0.00185
0.35	0.18	0.17	0.265	0.65	0.094	0.05	0.0255	1.82	0.00166

(1—5) concentrated phase characteristics
7—9) diluated phase characteristics (distilated water at 20°C)

Acknowledgements. We acknowledge the helpful discussions and suggestions of Mr. lecturer Iuliu Marian for practical realisation of experimental installation. We thank to staff of S.C. Sinterom S.A., Cluj-Napoca who made and characterized for us porous materials.

Nomenclature:

F: *material flux*, $[kg/s]$;
Qe: *permeability, in terms of concentration*, $[cm^2/s]$;
s: *separator surface*, $[m^2]$;
c_1: *entrance concentration of the fluid, in the superior chamber*, $[kg/m^3]$ *or* $[kmol/m^3]$;
c_2: *exit concentration of the fluid, in the inferior chamber*, $[kg/m^3]$ *or* $[kmol/m^3]$;
l: *width of porous bed*, $[m]$;
De: *effective diffusivity*, $[cm^2/s]$.

REFERENCES

1. S. T. Hwang, K. Kammermeyer, *Membranes in separations*, vol. 7, John Willey & Sons, New York, Sidney, Toronto, 1975.
2. E. M. Bratu, *Operaţii unitare în ingineria chimică*, vol. III, Ed. Tehnică, Bucureşti, 1985.
3. C. Liteanu, Gh. Rădulescu, *Bazele membranologiei*, Ed. Ştiinţifică şi Enciclopedică Bucureşti, 1984, p. 43.
4. L. Ifrim, C. Calistru, *Procesul unitar adsorbţie-reacţie-formare şi creştere de germeni*, IP Iaşi, 1987, p. 174.
5. K. K. Kim, J. M. Smith, *AICh Journal*, 4, 1974, p. 670.
6. I. I. Joffe, M. Pismenet, *Cataliza eterogenă în ingineria chimică*, Ed. Tehnică, Bucureşti, 1967.
7. R. Montarnal, *The fourth international congress on catalysis*, (Moscow, 1968), Simposium II, Novosibirsk, p. 179—203.
8. B. R. Davis and D. S. Scott, *The fourth international congress on catalysis*, (Moscow, 1968), Simposium III, Novosibirsk, p. 239—261.
9. T. Yang Ralph, Rea-Tiing Liu, M. Steinberg, *Diffusion in Carbonaceus Materials*, Ind. Eng. Chem. Fund., vol. 16, no. 4, 1977.
10. Lap-Keung Lee, D. M. Ruthven, *An Experimental Method for the Determination of Macropore Diffusivities for Liquid in Molecular Sieve Pellets*, Ind. End. Chem. Fund., vol. 16, no. 2, 1977.
11. I. V. Simiti, I. Magyarosy, *Materiale poroase sinterizate*, Of. de inf. pt. Ind. Constr. de Maşini, 1992.
12. M. Cruceanu şi colab. *Site moleculare zeolitice*, Ed. Ştiinţifică şi Enciclopedică, Bucureşti 1986.

STUDIA UNIV. BABEŞ-BOLYAI, CHEMIA, XXXIX, 1–2, 1994

STUDY CONCERNING DISC CENTRIFUGAL SEPARATORS. NON-CONVENTIONAL METHOD FOR THE EVALUATION OF SUSPENSION PHASE FLOWING

RADU IATAN*, CĂLIN ANGHEL, GHEORGHE PASAT***

ABSTRACT. The rational use of disc centrifugal separators involve the possibility to determine or to evaluate correctly specific parameters as: flow capacity, critic dimensions for solid particles, the dynamics of solid evacuation etc. The specific parameters are generally evaluated theoretically or based on laboratory models, subsequently followed by the generalisation of the findings. Because of that reason and because the disc centrifugal separator is a closed structure, hard observable, there are very substantial errors introduced. The present work represents an experimental possibility of evaluating working parameters specific to the disc centrifugal separators.

Symbols:

Q — *total flow capacity of suspension, m^3/h*
q — *specific flow capacity for a disc unit, m^3/h*
Z — *number of flowing interstices, number of disc units*
N — *number of discs*
h — *normal distance between two discs, m*
α — *semiangle of disc*
n — *rotation speed of rotor, rpm*
ω — *angular velocity of bowl, s^{-1}*
η — *dynamic viscosity of suspension, cP*
ΔQ — *differential density, kg/m^3*
$\bar{u}_x, \bar{u}_\theta$ — *components of the flow suspension velocity along the disc, respectively, on the tangential one*
R — *current radius, m*
σ — *mechanical stress, MPa*

General aspects. Although, within a period of 100 years, there are a lot of theoretical and experimental works concerning disc centrifugal separators, the technological use of discs separators is, even today, affected by a lot of unknown aspects. One of these, is the total flow capacity-Q, or the specific flow capacity — q, which is decisively conditioning all evaluations regarding the separation capacity of the machine. Disc separators are by construction closed systems and that characteristic makes impossible, in practice, to observe flowing between discs or through the bowl. However, there are some specific methods developed to provide useful informations.

a) Transfer of a pigmented material deposed on discs [1, 2, 5]. It reacts with the liquid or the suspension and it is washed because of the different flowing according with different parts of the bowl. This method can be used directly on industrial installations. The difficulty of the method consists in making photos of the discs and the planimetration of washed area to estimate the real flowing route.

---

* *Politechnical University Bucharest, Dept. of Mechanical Engineering, Techn. equipment for process indurstsei*
** *Babeş-Bolyai University, Dept. of Industrial Chemistry, 3400 Cluj-Napoca, Romania*

b) Visualization of flowing domains through coloured jets which make evident also, the phases stratification [5, 6]. This method can be applied only for models or for special constructions — opened or transparent.

In the present work, we try to eliminate these unknown, related to the suspension flowing, by experimental quantitative determinations based on a method specific for rotor structure resistance, analyse performed with strain ganges.

Theoretical presentation. Usually, any consideration regarding flow suspension velocity $\bar{u}_x$, $\bar{u}_\theta$, the critical dimension of solid particles d_{cr}, thickness of the flowing suspension layer h_s etc. suppose the same specific flow capacity, $q = \text{const}$, for the whole separator. Under these conditions, it was established:

— flow suspension velocity [3]

$$\bar{u}_x = u_1/x\,; \qquad \bar{u}_\theta = v_1/x \tag{1}$$

$$u_1 = Q/2\pi h \sin\alpha \qquad v_1 = Q(1-\lambda)2\pi h \sin\alpha \tag{2}$$

— thickness of the flowing suspension layer [4]

$$h_s == [3Q\eta/2\pi R^2\omega^2 \sin\alpha]^{1\,3} \tag{4}$$

$$\bar{u}_x = [Q^2\omega^2 p \sin\alpha/12\pi^2 R\eta]^{2\,3} \tag{5}$$

where:

$$q = Q/z \tag{6}$$

$$\lambda = h[\omega p \sin\alpha/\eta]^{1\,2} \tag{7}$$

— stability factor of the flowing suspension layer [7]

$$k = \varepsilon(\lambda - 1), \text{ where } \varepsilon = u_x/\omega R \tag{8}$$

The value of the stability factor k, determines, by approximation, the transportation conditions as laminar, when $k < 1$ or turbulent, when $k > 1$ decisively for the rest of hypothesis for calculation.

In context with the previously presented considerations, we have to mention that an important disturbing factor for the separation process, the contraflow between suspension and sediment, is strongly dependent on the flowing regime existent between discs [1, 6, 7]. The laminar flowing regime is favourable to sedimentation and sediment evacuation, but the regime evaluation is not rigorously done because of theoretical considerations. That involves for operation, flow capacity adjustments for feeding which can completely change the sedimentation conditions.

Regarding the resistance analyses of structures, in conformity with mechanics principles, as long as the stress state is kept in the elastic domain, the effects superposition principle can be applied. According with this principle it is possible to analyze separately the effects due to a complex of factors and we can finally write as follows:

$$\sigma_T = \Sigma\sigma_i \tag{9}$$

where:

σ_T — total stress

σ_i — stress due to the solicitation factor, i

The disc centrifugal separators construction belongs to structures with thin or moderate thickness of walls and the discs certainly are axsymmetric structures with thin walls and consequently, for the plane stress state, the equation (9) becomes:

$$\sigma_1 = \Sigma\sigma_{1i}, \text{ respectively, } \sigma_2 = \Sigma\,\sigma_{2i} \tag{10}$$

The main stress, σ_1 — on the annular direction, can be expressed in accordance with the constructive type of separator and the phase of the analysis, as operating unfeeded or with suspension.

Limiting, restricting the analyses only at the discs from the separator set, the relation (10) take the following form:

— for operating empty, without snspension flow:

$$\sigma_{10} = \sigma_1(\omega) + \sigma_1(F_i)$$
$$\sigma_{20} = \sigma_2(\omega) + \sigma_2(Fi) \tag{11}$$

where:

$\sigma_{1,2}(\omega)$ — stress due to centrifugal forces

$\sigma_{1,2}(Fi)$ — stress due to structural connective loading

— for operating with suspension flow:

$$\sigma_1 = \sigma_1(\omega) + \sigma_1(p_s) + \sigma_1(Fi)$$
$$\sigma_2 = \sigma_2(\omega) + \sigma_2(p_s) + \sigma_2(Fi) \tag{12}$$

$$\sigma_1 = \sigma_{10} + \sigma_1(p_s)$$
$$\sigma_2 = \sigma_{20} + \sigma_2(p_s) \tag{13}$$

where:

$\sigma_{1,2}(p_s)$ — streses due to the pressure of the suspension layer flowing on disc.

Based on these simple considerations, it follows the proposal of a possibility to evaluate the suspension flow distribution between discs starting from mechanical measurements of the stress state, using strain gauges.

Experimental. Starting from the idea that for a certain point on the geometry of the disc, but the same one for all measurements, the diffefence between the stress founded for the operation without suspension flow, respectively for the operation with suspension flow, is determined by the local loading of the disc with the flowing suspension layer. Registering the local stress, it is possible to point out more or less loaded areas in the package of discs [fig. 1].

The experiment has been carried out on a relative small centrifuge (fig. 1) type TSL. 4 — Tehnofrig, with Q = 400 l/h at a rotation speed, n = 6500 rpm and N = 40 discs. It was followed and registered the stress state in three points located along the discs, for two basal discs, the median area and the vertex of discs package and numbered Z = 1, 2, 19, 20, 39, 40.

The registration of specific deformation has been realised with a tensometric bridge with 6 channels, type N — 2302 (IEMI, Bucharest), precision 0,3—0,5%.

The experimentation programme supposed the use of two rotation speed levels, at the rotor filling rate G = 0,2.

Strain gauges was constantan wire, type TER.5H.120 (INCERC, Bucharest); recording of strains has been done by strain bridge with 6 channels, type N — 2302 (IEMI, Bucharest).

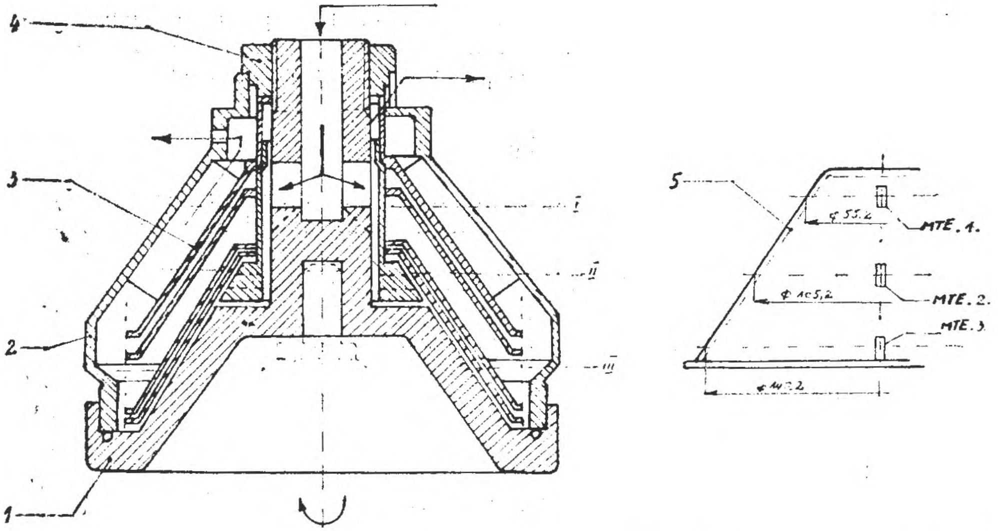

Fig. 1 Rotor agrgegate and disc set: 1 — bottom zone; 2 — head coonical zone; 3 — disc set; 4 — upper ring for assembly; 5 — disc element.

Results and Discussion. After processing primary the specific deformations according with the plane stress state, the dependence of stress upon the rotation speed and the loading of discs is represented in the Table 1.

Analysing the results of the measurements presented in the Table 1, one can clearly observe, from the value of the equivalent stress σ_e, that there is a difference between the situation of discs without suspension flow and with suspension flow, both, between the points of the same disc "1", "2", "3" and between the discs of the set. The values of the equivalent stress does not permit the quantitative identification of the cause, it only signal out the cause. For that reason, we use the components σ_1, σ_2.

From the relation (13), we point out the differences $\Delta\sigma$:

$$\Delta\sigma_1 = \sigma_{1T} - \sigma_{10} = \sigma_1(p_s)$$

$$\Delta\sigma_2 = \sigma_{2T} - \sigma_{20} = \sigma_2(p_s)$$

The values of differences $\Delta\sigma_1$, $\Delta\sigma_2$, for homologous points of the three different discs from the three areas I, II, III, represented in the fig. 1, are very important for the chemical technologist.

In conformity with Table 1, for $\Delta\sigma_1$, $\Delta\sigma_2$, corresponding to discs "2", respectively "39", these are deviations going from 0,5% to 6%, perfectly explicable through measurement errors, experimental reproducibility etc. and between the same discs and the discs from the median zone "20", for the same homologous measurement points, there are deviations going from 40% to 60%. These deviations reflect actually a higher suspension load of discs from the upper zone, respectively the lower zone, in comparison with the discs

Table 1

Experimental stresses at local points

Disc number	Local point	σ [N/mm^2]	$n_1 = 1850$ min^{-1}	$n_2 = 2850$ min^{-1}
		Empty bowl		
,,2''	1	σ_1	−34.65	−42.750
		σ_2	−45.225	−53.770
		σ_e	40.974	49.1946
	2	σ_1	5.400	10.687
		σ_2	−12.710	−32.625
		σ_e	16.104	39.080
	3	σ_1	15.750	22.275
		σ_2	25.200	31.252
		σ_e	22.05	27.869
,,20''	1	σ_1	−34.66	−42.620
		σ_2	−45.34	−54.1015
		σ_e	41.0554	49.372
	2	σ_1	5.388	10.800
		σ_2	−12.700	−32.700
		σ_e	16.085	39.231
	3	σ_1	15.690	22.315
		σ_2	25.300	31.200
		σ_e	22.120	27.8419
,,39''	1	σ_1	−34.600	−42.830
		σ_2	−45.200	−53.910
		σ_e	40.942	49.312
	2	σ_1	5.500	10.880
		σ_2	−12.700	−32.740
		σ_e	21.981	39.325
	3	σ_1	15.815	22.345
		σ_2	25.100	31.360
		σ_e	21.891	27.964
		Flowing conditions		
,,2''	1	σ_1	−34.6418	−42.7279
		σ_2	−44.900	−52.873
		σ_e	40.751	40.601
	2	σ_1	5.4155	10.7273
		σ_2	−11.504	−29.505
		σ_e	14.965	36.035
	3	σ_1	15.7706	22.3283
		σ_2	27.343	36.868
		σ_e	23.772	32.165
,,20''	1	σ_1	−34.6498	−42.7367
		σ_2	−44.913	−53.2318
		σ_e	40.762	48.837
	2	σ_1	5.4095	10.7113
		σ_2	−11.986	−30.753
		σ_e	15.419	37.281
	3	σ_1	15.725	22.307
		σ_2	26.486	34.622
		σ_e	23 071	30.396
,,39''	1	σ_1	−34.640	−42.860
		σ_2	−44.880	−52.650
		σ_e	40.737	48.501
	2	σ_1	5.425	10.900
		σ_2	−11.500	−29.360
		σ_e	14.968	36.057
	3	σ_1	15.800	22.400
		σ_2	27.415	36.920
		σ_e	23.834	32.215

from the central zone. In another way, if it is accepted a medium specific low capacity, q_m — on the interstice, we can suppose:

— in the zones I and III, real flow capacity 1,4 ... 1,6 · q

— in the zone II, real flow capacity q_m

The previous findings are very useful for the chemical technologists, who has to dimension the flows according with its or to cooperate for the rearrangement of the median zone discs to bring its efficacity at the level of the others. These remarks confirmed by scientific works [1, 5, 6]:

in the zones I and III, real flow capacity 1,6 · q_m

— in the zone II, real flow capacity 0,7 ... 1 · q_m

Conclusions. Although the validity of observations is valoric limited at the type of the analyses separator, it can be useful for the chemical technologist in many directions: the correct choose of the separator through flow capacity conditions, evaluation of secondary flowing and of turbulence (through suspension pressure, on each disc, it appears the possibility to determine the thickness of the flowing layer, and the flowing regime u_x, u_θ, form far more exactly than the classic theorectical way). The method can be applied for industrial existing separators to extend the operation field, as well as for experimental necessities, to increase the performances of the centrifugal separator.

REFERENCES

1. K. H. Brunner, O. Molerus, *Chem. Ing. Tech*, 51, 3 (1979), 238—239.
2. K. H. Brunner, O. Molerus, *Chem. Tech.*, 33, 5, (1981), 237—240.
3. V. I. Sokolov, E. V. Semeonov, *Him. promî.*, 25, 6, (1976), 478—485.
4. V. I. Baturov, D. E. Schkoropad, *Chem Tech.*, 26, 11, (1974), 695—696.
5. A. Balla, H. H. Schmidt, E. Fritsche, *Chem. Tech.*, 24, 10, (1972), 621—622.
6. H. Reuter, *Chem. Ing. Tech.*, 39, 5—6, (1967), 310—318.
6. V. A. Balandin, *Him. Neft. Mas.*, 11, (1983), 31—34.

STUDIA UNIV. BABEŞ-BOLYAI, CHEMIA, XXXIX, 1–2, 1994

THE STUDY OF LEAD SULFIDE FILMS. IV. PROTECTION BY OPTICAL LACQUERS

ILEANA POP*, VIOLETA IONESCU*, VALENTINA VOMIR*, CRISTINA NAŞCU*

ABSTRACT. – This study presents photosensitivity and electrical resistance variation of lead sulfide films in presence of humidity. Humidity drastically affects electrical and photoelectrical properties of chemically deposited PbS films. Considering this behaviour, some experiments have been made regarding protection of PbS films by polymer thin film application. Good results have been obtained by protecting with polystyrene, ethylcellulose, novolak, ABS and polymethylmethacrylate films. None of these polymers seriously affects PbS films properties, being suitable for their protection.

Introduction. It is known the fact that PbS films kept in atmosphere have the tendance to adsorb gases like: O_2, CO, CO_2, H_2O.

Berejnaia [2] made a study regarding the influence of O_2 and CO at room temperature, on electrical properties of PbS films. Important modifications of conductivity and mobility of the carriers were observed after 20–30 minutes of exposing PbS films to above mentioned gases action. Hillebrand [3] shows that at 25°C a chemosorption of oxygen takes place, leading to considerable oxidation of film surface in only few minutes time. Water sorption between 25°C–70°C worsens photoresistance quality of PbS films [4].

Considering these, PbS films used as photoresistances must be protected in order to conserve their electrical and photoelectrical properties.

In reference materials are mentioned various compositions based on glass [5, 6] or Al_2O_3, As_2S_3, CdTe, MgF_2, SiO, SiO_2 thin films deposited in vacuum [7, 8]. None of the overcoatings seriously degrade detector properties. Improved detector properties were obtained with As_2S_3.

In present paper, the influence of various optical polymer films on photoconducting and electrical properties of PbS films, was studied.

Experimental. The lead sulfide films obtained by chemical deposition [9] were sensitized by thermic treatment in presence of oxygen. The electrical contacts were realised with chemically deposited gold films through thermal decomposition of terpenesulfide [10]. Polymer films were deposited at room temperature from their's solutions in suitable solvents. Electrical resistance of PbS films was determined with digital multimeter E 0302 (IAEM — Bucharest–Romania). Photoconductivity was estimated through $\Delta R/R_i$ ratio, where $\Delta R = R_{\square d} - R_{\square i}$. ($R_{\square d}$ = electrical resistance in the dark $R_{\square i}$ = electrical resistance at illumination with a 75 watt lamp through germanium filter at 0.25 m distance from the sample).

Results and discussion. As support for PbS films were used optical glass slides (K 515) sized at 6 × 3.5 × 0.8 mm on which preliminary were deposited gold contacts on a 2 × 3.5 mm area from a mixture containing 16% Au and proper fondants for adherence [10]. Golden film's formation temperature

---

* *Institute of Chemistry, 30 Fântânele, str., 3400, Cluj-Napoca*

is 500°C. On thus prepared slides, a PbS film with a thickness of 0.2 μm has been chemically deposited [9]. After by thermal treatment in presence of oxygen the samples were kept in the desiccator on anhydrous $CaCl_2$ (humidity at 25°C is approximately 0.15 mg H_2O/l air). It was noticed that keeping the samples in these conditions the electrical resistance decreases in time consequently with photoconductivity's decrease.

Obtained data are shown in fig. 1 and 2.

These variations can be explained by water adsorption which takes place slow enough. Increasing humidity at approximately 19 mg H_2O/l air — in samples no. 5—7 case hydratation rate is higher — electrical resistance drastically drops (fig. 1) consequently with $\Delta R/R_i$ ratio decreasing (fig. 2).

By thermal treatment at 90°C photoconductivity and electrical resistance increase up to initial values. Therefore the hydratation-dehydratation process is reversible. Our data are in concordance with other's authors data [11] which

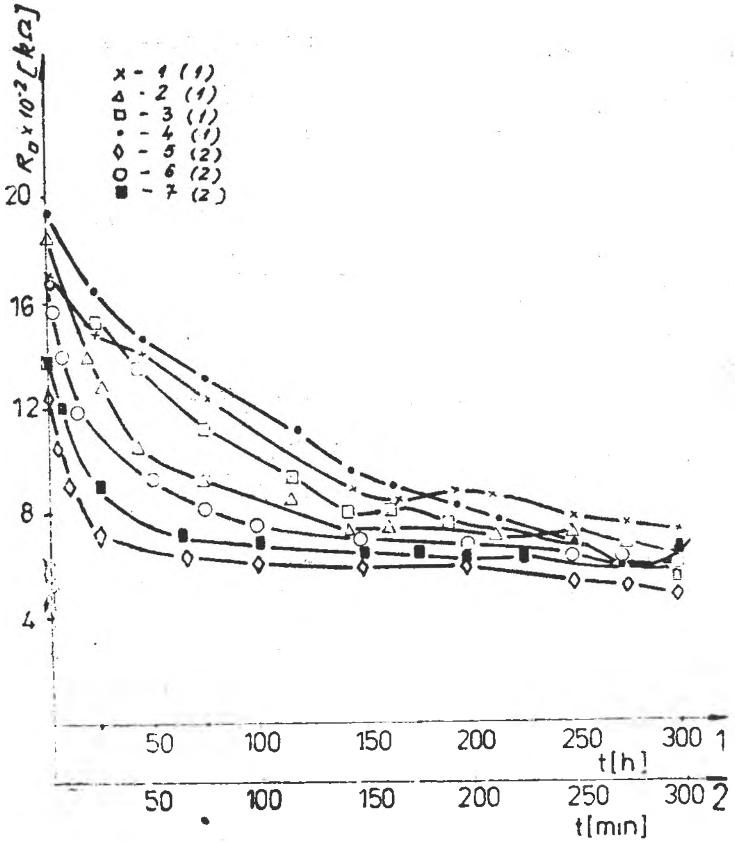

Fig. 1. The variation of electrical resistance $R_\square$ (25°C) with the time. Samples no. 1—4 were kept at the approx. humidity 0.15 mg H_2O/l air. Samples no. 5—7 were treated with air containing approximately 19 mg H_2O/l air.

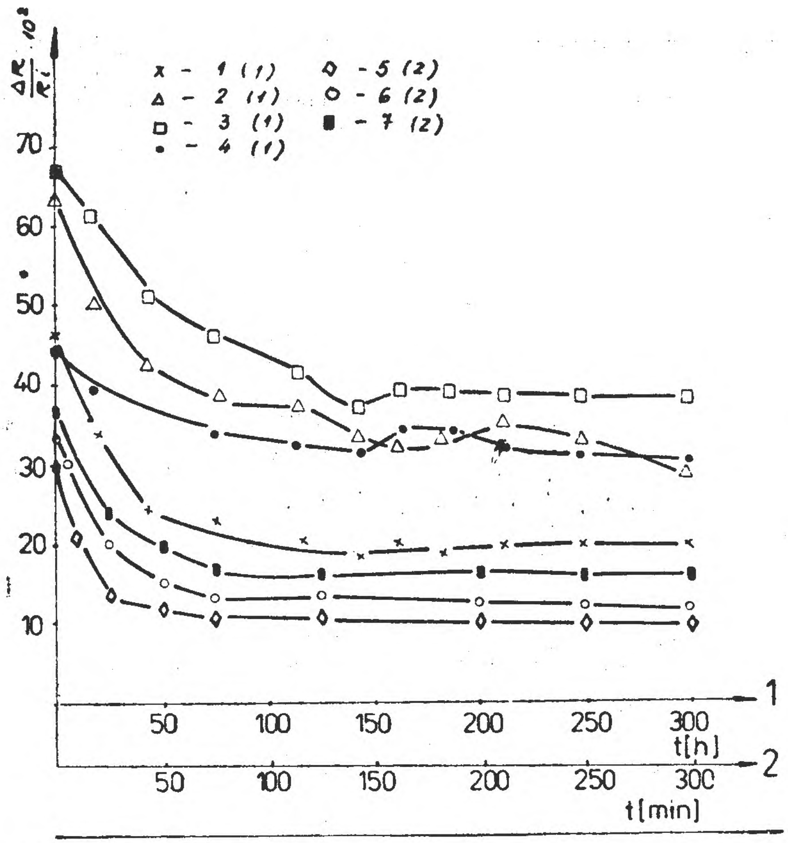

Fig. 2. The variation $\Delta R/R_{\square i}$ with the time for the samples presented in fig. 1.

have established that maximum temperature for PbS films dehydratation treatment is 150°C. Over this temperature oxidizing processes can take place.

To avoid photoelectrical and electrical characteristics'variation in time after reaching imposed parameters it's necessary to protect the photoresistance with optical films.

We experimented in this purpose polymer films selected so that the volume resistivity (at 25°C — RH 65%) to be higher than $10^7 \Omega \cdot \text{cm}$ and to have an IR transmission with maximal spectral response for PbS ($\approx 2.6\ \mu\text{m}$) higher than 70—80%.

Between the polymers that fulfill these conditions and which were experimented by us, we mention: polystyrene, polymethylmethacrylate, ABS, ethylcellulose and novolak [12—15].

Examining transmission spectra in IR [12, 13] were established wavelength ranges in which some polymers can be used as optical lacquers. In table 1 it's shown some usual polymers with the ranges in which they don't have absorption peaks and can be used for protecting optical overcoating.

Table 1

The range in which some polymers can be used as optical lacquer for IR radiation

The polymer	The range in which it can be used as optical lacquer μm
Polystyrene	<3; 3.8–5.0
Ethylcellulose	<3; 4.5–7; 11–15
Nitrocellulose	<5; 13–15
Polyvinylchloride	<3.2; 3.8–5.5
A.B.S.	<4.2; 5–6
Polymethylmethacrylate	<2.8; 3.8–5.2
Polybutadiene	<3; 4.5–6.5
Polyvinylalcohol	<2.7; 4–6

In table 2 it's shown electrical resistance ($R_{\square}$) in the dark and photoelectrical ($\Delta R/R_{\square i}$) characteristics of PbS films, uncoated and coated with polymer thin films deposited from 1–10% solutions in suitable solvents. Films deposition has been made at room temperature by immersion. The measurements were made after 24 hours (after removing solvents) at 20°C temperature.

Table 2

Electrical and photoelectrical characteristics of PbS photoresistances before and after coating with polymers films (u — uncoated; c — coated)

a) Polystyrene in chloroform

Sample no	8	9	10	11	12	13	14	15
$R_{\square d}$ kΩ(u)	483	908	955	970	1002	1063	1560	1620
$\Delta R/R_{\square i} \times 10^2$(u)	84.35	97.39	42.96	86.53	67.22	44.62	134	131.42
$R_{\square d}$ kΩ(u)	470	998	940	1000	1090	1072	1570	1680
Variation %	−2.6	+9.91	−1.57	+3.09	+8.78	+0.84	+0.64	+3.75
$\Delta R/R_{\square i} \times 10^2$ (c)	84.31	102.27	42.42	85.5	66.50	43.5	132	130.20

b) Polymethylmethacrylate in cloroform

Sample no	16	17	18	19	20	21	22	23
$R_{\square d}$ kΩ(c)	488	564	618	666	680	830	908	960
$\Delta R/R_{\square d} \times 10^3$ (u)	122.83	121.17	68.40	75.03	118.64	84.44	97.39	45.00
$R_{\square i}$ kΩ (c)	505	590	640	680	700	850	958	980
Variation %	+3.48	+4.60	+3.55	+2.10	+2.94	+2.40	+8.48	+2.08
$\Delta R/R_{\square i} \times 10^2$ (c)	120.50	119.90	67.2	74.10	116.50	83.5	98.00	46.10

c) A.B.S. in butyl acetate

Sample no	24	25	26	27	28	29	30	31
$R_{\square d}$ kΩ/(u)	394	416	432	460	484	647	727	820
$\Delta R/R_{\square i} \times 10^2$(u)	122.59	144.70	111.56	146.77	145.78	154.72	160.57	130.25
$R_{\square d}$ kΩ (c)	402	430	455	480	495	630	652	805
Variation %	+2.30	+3.36	+5.32	+4.34	+2.27	−2.62	−10.31	−1.82
$\Delta R/R_{\square i} \times 10^2$ (c)	120.30	142.56	99.40	144.22	142.02	149.20	155.20	128.32

d) Ethylcellulose in chloroform

Sample no	32	33	34	35	36	37	38	39
$R_{\square d}$ kΩ(u)	399	406	420	432	434	442	476	486
$\Delta R/R_{\square i} \times 10^2$ u)	150.94	126.81	154.54	154.11	93.72	163.09	117.35	138.23
$R_{\square d}$ kΩ(c)	425	395	410	425	425	465	492	480
Variation %	+6.51	−2.70	−2.38	−1.62	−2,07	+5.20	+3.36	−1.23
$\Delta R/R_{\square i} \times 10^2$ (c)	145.82	125.20	152.20	156.12	94.50	162.32	115.20	136.42

e) Novolak

Sample no	40	41	42	43	44	45	46	47
$R_{\square d}$ kΩ(u)	200	230	237	282	293	310	328	378
$\Delta R/R_{\square i} \times 10^2$ (u)	69.49	49.35	70.50	41.00	66.47	64.89	43.23	78.56
$R_{\square d}$ kΩ(c)	185	245	230	272	295	290	326	400
Variation %	−7.5	+6.52	−2,95	−3.54	+0.68	−6.45	−0.60	+5.82
$\Delta R/R_{\square i} \times 10^2$ (c)	67.20	45.26	67.80	40.5	65.4	63.4	42.50	79.20

Detectivity of experimented samples was approximately 10^{10} W · $Hz^{1/2}$ · cm^{-1}. From table 2 data is find that electrical resistance modifications of films are maximum ±10% after coating with polymer films and photosensitivity modifications are insignificantly. The measurements made at 30 days after protection coating show too insignificantly variations in samples characteristics.

The obtained results agree with optical and electrical properties of tested polymers.

All tested polymers can be applied as protection coatings for PbS films in photoconductivity and electrical characteristics stabilization.

Conclusions. From experimental results presented in this study the following conclusions can be infered:

— PbS films modify fast enough its electrical resistance and photoelectrical properties in humidity presence between 0.16 — 19 mg H_2O/l air.

— This behaviour justify us to affirm that these PbS films can be used as humidity sensors.

— To conserve electrical and photoconducting properties can be used polymer films such as: polystyrene, ethylcellulose, novolak, ABS, polymethylmethacrylate which do not modify the electrical resistance and photoconducting properties of PbS films.

REFERENCES

1. C. Naşcu, I. Pop, V. Ionescu and V. Vomir, Studia Univ. Babeş-Bolyai, **XXXVII** (1—2), 55—59 (1992).
2. I. A. Berejnaia, *J. Phys. Chem.*, **36**, 2763—65 (1962).
3. L. J. Hillebrand, *J. Chem. Phys.*, **73**(9), 2902—8 (1969).
4. V. P. Kovbasyuk and N. S. Chorna, *Ukr. Fiz. Zhur.*, **8**(9), 1030—32 (1963).
5. S. Hera, M. Hanazona and M. Takahoshi, *Pat. Jpn. Kokai Tokkyo Koho* 7973, 815, 13 Jun., 1979; cf. Chem. Abstr. **1979, 91**, 150175 d.
6. S. Masaru, T. Katsuiro and N. Mikiko, *Pat. Jpn. Kokai Tokkyo Koho* 7898, 319, 28 Aug., 1979; cf. Chem. Abstr. **1979, 90** 1312 u.

7. G. H. Blount, M. K. Pleis, R. T. Yamada and R. H. Bube, *J. Appl. Phys.*, **46**(8), 3489—99 (1975).

8. R. B. Scoolar and J. D. Jensen, *U. S. Pat.* 4, 126, 732, 21 Nov., 1978; cf. Chem. Abstr. **1979,** 90, 45506 t.

9. C. Naşcu, V. Vomir, V. Ionescu and I. Pop, Part II of the serie, *Rev. Roumaine Chim.*, 40(2), 127—140 (1995)

10. R. Ripan and Gh. Pop, *Rom. Pat.*, 55816, 12 Nov., 1970.

11. R. I. Muller, A. V. Danilov and Ian In-gui, *Zhur. Prikl. Khim.*, **34,** 71—78 (1961).

12. S. Bădilescu, M. Toader, M. Giurginca and V. Tălpuş, *Spectroscopia în infraroşu a polimerilor şi auxiliarilor,* Ed. Tehnică, Bucureşti, 1982, p. 287—397.

13. B. Werner, *Einfuhrung in die Ultraspektroskopie,* Dr. Dietrich Steinkopff Verlag Darmstadt 1962. p. 400—409.

14. I. Moţoiu and M. Moţoiu, *Răşini sintetice pentru lacuri, vopsele şi cerneluri poligrafic* Ed. Tehnică, Bucureşti, 1972, p. 212, 359.

15. S. Horun, *Memorator de materiale plastice şi auxiliari,* Ed. Tehnică, Bucureşti, 1973, p. 164

STUDIA UNIV. BABEŞ-BOLYAI, CHEMIA, XXXIX, 1–2, 1994

EFFECT OF SOME ADDITIVES ON THE PERFORMANCES OF ZINC ELECTRODES IN Ni-Zn BATTERIES

L. ONICIU*, VIOLETA VOINA**, ELEONORA MARIA RUS*, DELIA CONSTANTIN**, CRISTINA CORĂBIAN**

ABSTRACT. — It have been prepared pressed and sintered zinc electrodes from zinc powder and additives and it have been determined their performances in a Ni—Zn cell. The effect of various additives to the zinc electrode was also investigated on the cell performance.

Introduction. The Zn/NiOOH couple has a high theoretical specific energy (326 Wh · kg^{-1}) that it can be expected to deliver about 75 Wh · kg^{-1} in a monopolar rechargeable battery. High specific energy, excellent power performance (>130 W · kg^{-1}), good performance even during very cold ambient conditions (—20°C), inexpensiv and low-toxicity materials, make the Zn/NiOOH battery a large portable power sources applications [1].

The potential active reaction at the zinc electrode is:

$$Zn + 2\,KOH + 2OH^- \underset{\text{recharge}}{\overset{\text{discharge}}{\rightleftharpoons}} ZnK_2(OH)_4 + 2\,e^-$$

In spite of significant research and development of this battery two important problems remain. One is the high cost of the battery due to the NiOOH electrode. The other important problem is the limited lifetime of this battery; it rarely completes more than 200 full-capacity cycles before failing.

Failure is typically associated with two phenomena: 1) zinc dendrite initiation and propagation, leading to cell shorting; 2) zinc material redistribution leading to gradual capacity loss.

Zinc active material can migrate across the face of the electrode (in a parallel direction to the face of the electrode), into or out of the pores of the electrode (perpendicular to the face of the electrode) and away from the electrode to the NiOOH electrode. These migration processes take place in regions with dense and nodular zinc and in regions which have very little or no zinc. As a result of these processes are: the capacity reduction of NiOOH electrode; the zinc electrode may become the capacity-limiting electrode, and dense areas of zinc can short the cell. Although the cause of zinc electrode shape change is not knowen with certainly, various mechanisms have been proposed to offer an explanation [1].

These mechanisms include: (a) electrolyte flow through ion-exchange separators caused by osmotic pressure gradients in cells; (b) electrolyte concentration gradients caused by the difference between the current density distribution during charge and discharge; (c) natural convenction of the electrolyte

---

* *Babeş-Bolyai University, Dept. of Physical Chemistry, 3400 Cluj-Napoca*

** *Babeş-Bolyai University, Laboratory, of Electrochemistry, 3400 Cluj-Napoca, Romania*

caused by density gradients; (d) autocatalytic zinc dissolution from the periphery of the zinc electrode; (e) lower charge efficiency for the zinc deposition at the electrode periphery caused by nonuniform OH^- ion concentration; (f) oxidation of zinc to soluble ZnO by oxygen that has migrated from the NiOOH electrode (where it is evolved during charge) to the periphery of the zinc.

However, none of these models can not fully account for the shape change phenomenon, particulary the zinc migration either toward or away from the centre of the electrode [1]. However all of the models suggest that if the amount of zinc dissolved in the electrolyte is decreased, therate of zinc redistribution will decrease.

The high solubility of $Zn(OH)_4^{-2}$ ion in alkaline-solutions and the formation of zincate-supersaturated electrolyte solutions during discharge is strongly associated with the shape-change process.

Methods which can to reduce the solubility of zincate ion in the alkaline electrolytes has recongnized [2—7].

Results and discussion. Our intention was to form a relatively low soluble complex with ZnO and there by maintaining much of the Zn in a solid form, but to allow the fast interconversion of Zn to ZnO which permit the cell chargeing and discharging at high rates. Calcium hydroyide is insoluble in alkaline solutions, and would therefore retain a uniform distribution as the cell is cycled [8]. Furthermore $Ca(OH)_2$ is not toxic and is cheap. In the literature it were reported some experiments with other alkaline-earth metal hydroxides as in complexing with zinc species [9].

From the different types of zinc electrodes reported we have chosen the pressed and sintered electrodes [10]. The performances of these electrodes have been examined in a NiOOH-Zn cell, using sintered NiOOH electrodes.

The pressed zinc electrodes were obtained from zinc powder or needles and electrolytical prepared fibres. The sintered electrodes were prepared by sintering of zinc powder. The active material composition of the electrodes is shown in tab. 1.

Table **1**

Electrode	Compozition	Coulombic efficiently for the first ten cycles %
1	ZnO 10%; Zn 85%; $Ca(OH)_2$ 3%; $Bi(NO_3)_3$ 2%	80
2	ZnO 20%; ZnO 75%; $Ca(OH)_2$ 3%; $Bi(NO_3)_3$ 2%	75
3	ZnO 30%; Zn 65%; $Ca(OH)_2$ 3%; $Bi(NO_3)_3$ 2%	80
4	ZnO 40%; Zn 55%; $Ca(OH)_2$ 3%; $Bi(NO_3)_3$ 2%	83
5	ZnO 50%; Zn 45%; $Ca(OH)_2$ 3%; $Bi(NO_3)_2$ 2%	72
6	ZnO 60%; Zn 35%; $Ca(OH)_2$ 3%; $Bi(NO_3)_3$ 2%	55
7	ZnO 75%; Zn 24,4%; HgO 0,6%	68
8	needles and fibres of Zn	65
9	Zn + teflon	50

The mixture of zinc powder and additives was compressed at 500—600 daN/cm^2 on current collectors from nickel mesh, and then was packed in an electrolytic paper, pressed once again at 200—250 daN/cm^2 on nikel reofors and packing in the same conditions.

The sintered electrodes were prepared by pressing of zinc powder with polytetrafluor-ethylene bonded on nickel reofor and sintering in hydrogen atmosphere at 370°C.

The zinc anodes (45 × 102 × 1,5 mm) assembled in a cell, were insulated from the Ni sintered electrodes by polypropylene separators. The electrolyte was 6 N KOH with 35 g/l LiOH saturated in ZnO. The cell was cyclated performed in galvanostatic conditions.

The charge-discharge curves for a cell with pressed anodes (7) are shown in fig. 1.

From zinc anodes prepared by us, the greatest nominal capacity of cell and higher lifetime had the pressed electrodes (tab. 1).

The discharge curves for evaluation of nominal capacity are shown in fig. 2. Also was studied the effect of Pb^{2+} addition to the electrolyte.

The sintered electrodes had a good mecanic resistance, but they lost it during the cycling. These electrodes present a less capacity than the pressed electrodes, because of the decrease specific surface.

The most pregnant electrodes shape change it has been observed for the (6) and (7) composition from the tab. 1. It seams that although it suppress

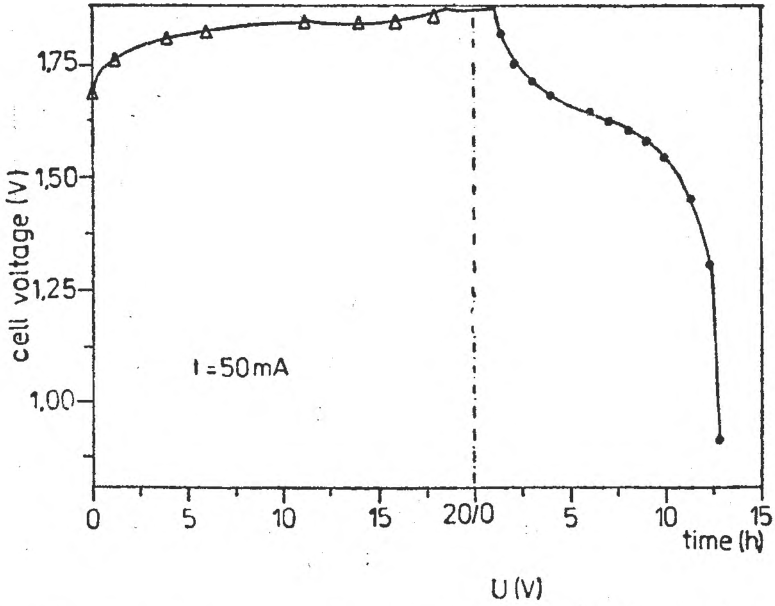

Fig. 1. The charge-discharge curves for a cell with pressed Zn electrodes.

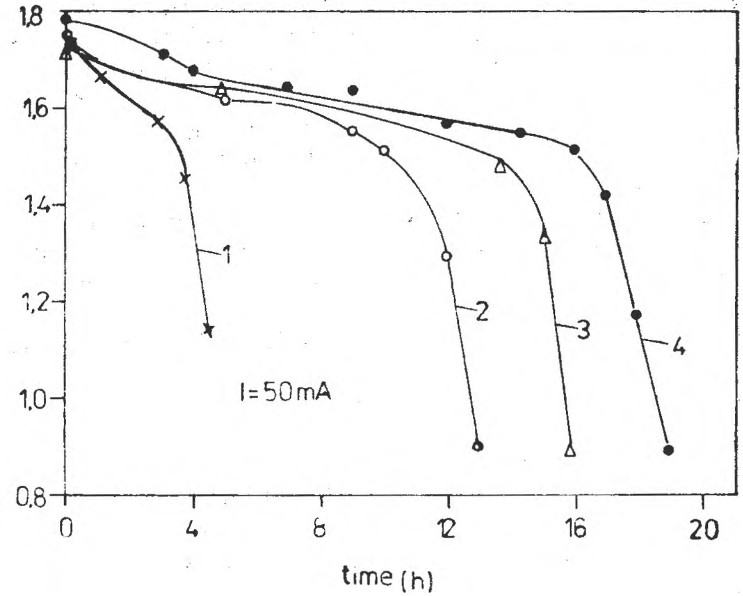

Fig. 2. The discharge curves for a cell with (1), (2), (3), (4) Zn type electrodes.

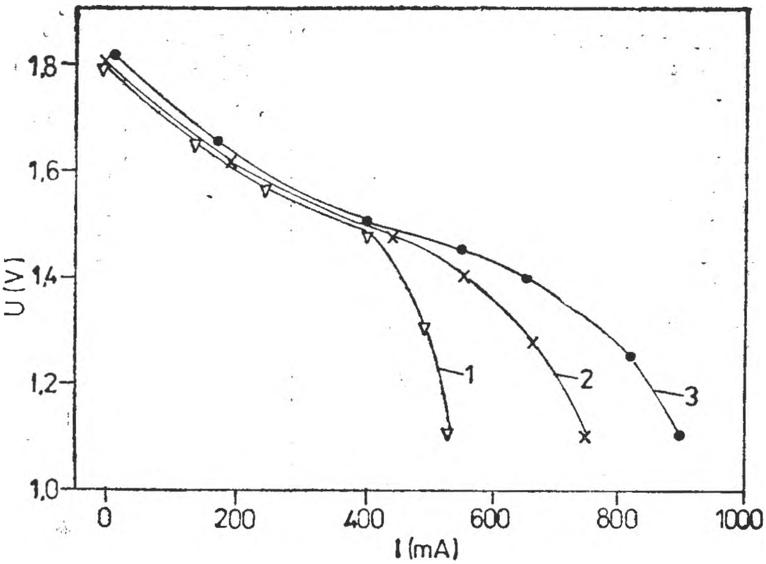

Fig. 3. The polarization curves: 1 — without additives; 2 — with ZnO additive in the electrolyte; 3 — with Pb^{2+} additive in the electrolyte;

the H_2 evolution, (due to the increased overpotential of the rdH on Hg), the HgO determines an acceleration of electrode shape change.

The $Ca(OH)_2$ addition to the zinc electrodes, which forms a calcium-zincate complex, minimizes the active material redistribution. The composition of thus complex is not known with certainly and will be investigated by X-Ray diffraction.

The addition of $Ca(OH)_2$ to the active material and the Pb^{2+} to the electrolyte is beneficial for the zinc electrode functionality and performances.

It has been observed high performances expecially at high current densities (fig. 3).

REFERENCES

1. F. R. Mc Larmon and E. J. Cairns, *J. Electrochem. Soc.*, **138**, 645, (1991).
2. V. V. Romanoff, *J. Appl. Chem.*, **35**, 1246, (1962).
3. N. A. Zhulidov and F. I. Efremov, *Vest. Elektropron.*, **34**, 74, (1971).
4. W. J. van der Grinten, *Abstract* No. 28, 96, *The Electrochemical Society Extended Abstracts*, oct. 15—20, (1967).
5. W. van der Grinten (General Electric Co.), *U.S. Patent*, 3516862, (1970).
6. J. Maki, M. Fujita, H. Takahashi and I. Ino (Hitachi, Ltd. and Tokyo Electric Power Co.), *U.S. Patent*, 3816178, (1974).
7. R. A. Jones (General Motors Corporation), *U.S. Patent*, 4358517, (1982).
8. R. Jaint, T. C. Adler, F. R. Mc Larnon, E. J. Cairns, *J. of Appl. Electrochem.*, **22**, 1039, (1992).
9. G. Kawamura and Y. Maki, *Denki Kagaku*, **48**, 592, (1980).
10. C. Cachet, R. Wiart, J-Zoppas-Ferreira, *Electrochim. Acta*, **38**, 311, (1993)

STUDIA UNIV. BABEŞ-BOLYAI, CHEMIA, XXXIX, 1-2, 1994

THE INFLUENCE OF SOME ADDITIVES ON ELECTROCHEMICAL BEHAVIOUR OF NICKEL ELECTRODES IN ALKALINE BATTERIES

L. ONICIU*, DELIA CONSTANTIN**, ELEONORA MARIA RUS*, VIOLETA VOINA**, CRISTINA CORĂBIAN**

ABSTRACT. — Sintered nickel plates were prepared from nickel powder obtained by thermolysis of $Ni(NO_3)_2$. The influences of $Co(OH)_2$ and $Cd(OH)_2$ in the active material and LiOH in the electrolayte, respectively, on the electrochemical behaviour of nickel electrodes were investigated.

Introduction. The physico-chemical and electrochemical characteristics of a given cathode material have a great influence on the performances of electrochemical power sources.

Nickel hydroxide is a successful cathode material used in Ni—Cd, Ni—Zn and Ni—Fe alkaline batteries, having a large area of applications, and in $Ni-H_2$ batteries, used extensively in aerospace systems [1].

The reaction at the nickel electrode during charge-discharge is:

$$NiOOH + H_2O + e^- \underset{\text{charge}}{\overset{\text{discharge}}{\rightleftharpoons}} Ni(OH)_2 + OH^- \qquad (1)$$

$$\varepsilon^\circ = +0{,}490 \text{ V/NHE}$$

For the one-electron change process, the theoretical charge density of NiOOH cathode is 290 Ah/kg.

Despite the long technological hystory of nickel hydroxide electrode his electrochemistry is not yet fully understood. This is due to the participation of two distinct couples, β-$Ni(OH)_2$ / β-NiOOH and α-$Ni(OH)_2$ / γ-NiOOH, in the potential-determining reactions (2, 3).

The transitions of these couples take place according to Bode scheme [4]:

$$\begin{tikzcd}
\beta\text{-}Ni(OH)_2 \arrow[r, "\text{aging}"] \arrow[d, shift left, "-e^-\ -H^+"] & \alpha\text{-}Ni(OH)_2 \arrow[d, shift left, "-e^-\ -H^+"] \\
\beta\text{-}NiOOH \arrow[u, shift left, "+e^-\ +\text{-}H^+"] \arrow[r, "\text{overcharge}"] & \gamma\text{-}NiOOH \arrow[u, shift left, "+e^-\ +H^+"]
\end{tikzcd} \qquad (2)$$

The discharge of the electrodes containing β-NiOOH proceeds at more positive potentials than that of the electrodes having γ-NiOOH. The discharge capacity is higher for electrodes containing γ-NiOOH due to a nickel oxidation state of 3.7—3.8, while for β-NiOOH it only slightly exceeds 3 [5].

---

* *Babeş-Bolyai University, Dept. of Physical chemistry, 3400 Cluj-Napoca*

** *Babeş-Bolyai University, Laboratory of Electrochemistry, 3400 Cluj-Napoca, Romania*

The existence of α, β, γ species is related to the preparing method of active material, charge-discharge cycling conditions, concentration and composition of the electrolyte.

In the charging process of the active material, at high anodic potentials, oxygen is evolved according to the reaction:

$$4OH^- \rightarrow O_2\uparrow + 2\,H_2O + 4e^- \qquad (3)$$

The addition of some metal hydroxides to the active material and lithium hydroxide to the electrolyte has a great influence on the electrochemical behaviour of the nickel hydroxide electrode [6—11].

Results and discussion. The nickel electrodes were prepared by immersion of sintered nickel supports (35 × 70 × 0.5 mm) in saturated $Ni(NO_3)_2$ solution and followed by anodic polarization in 42% KOH. The sintered nickel plates were prepared with nickel powder obtained by thermic decomposition of $Ni(NO_3)_2$. The impregnated active material was the black nickel oxy-hydroxide.

The electrochemical investigations were carried out in a half-cell containing 6 M KOH and 6 M KOH + 35 g/l LiOH solutions, using a nickel foil counter-electrode and a saturated calomel electrode (SCE) as reference.

The electrode potentials variations with time in anodic (charge) and cathodic (discharge) processes, at constant current were traced.

The effect of 35 g/l LiOH addition to the 6 M KOH electrolyte was investigated by charge-discharge curves, at I = 100 mA (fig. 1).

In the presence of LiOH the conductivity of the electrolyte decreased and, as a result, the charge potential was higher (curve 4) and the discharge potential was lower (curve 2) than for 6 M KOH electrolyte alone (curves 3, 1).

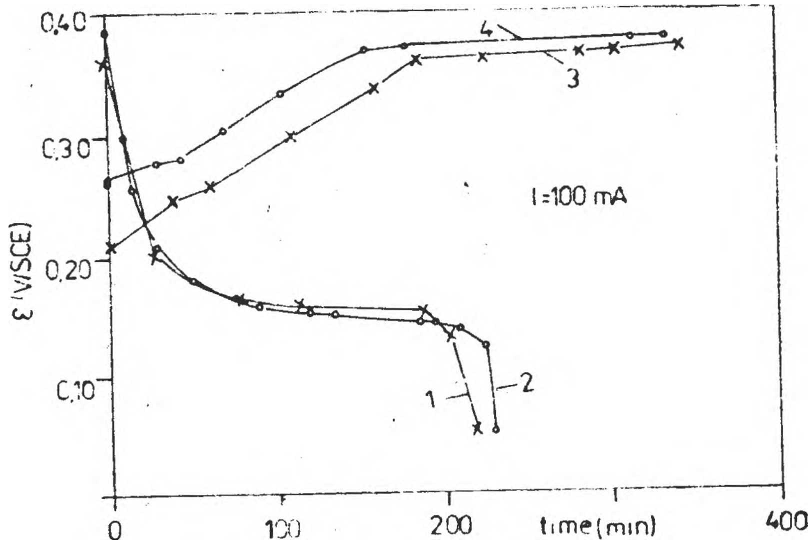

Fig. 1. Charge-discharge curves for nickel hydroxide electrode in 6 M KOH electrolyte (1—3) and 6 M KOH + 35 g/l LiOH electrolyte (2—4).

Table 1

Electrochemical characteristics of nikel hydroxide electrode

Electrode	Electrolyte	I_{charge} mA	t_{charge} h	C_{charge} mAh	$I_{discharge}$ mA	$t_{discharge}$ h	$C_{discharge}$ mAh	r_F %	e_r V/SCE
Ni	6N KOH	100	5,5	550	100	3,5	350	63,63	0,253
	6N KOH+35 g/l LiOH	100	5,5	550	100	3,83	383	69,64	0,273
Ni+Co	6N KOH	100	5,5	550	100	4,44	444	80,73	0.220
	6N KOH+35 g/l LiOH	100	5,5	550	100	4,75	475	86,36	0.241
Ni+Cd	6N KOH	100	5,5	550	100	4	400	72,73	0.261
	6N KOH+35 g/l LiOH	100	5,5	550	100	4,33	433	78,73	0,287

LiOH had a favorable effect by increasing the capacity and the coulombic efficiency of the nickel hydroxide electrode (Table 1).

The reversible potentials (ε) of the nickel hydroxide electrode, in 6 M KOH and 6 M KOH + 35 g/l LiOH, were evaluated from the ε versus lg t data by intersecting the anodic decay and cathodic recovery lines (fig. 2).

The presence of LiOH in electrolyte shifted the reversible potential of $Ni(OH)_2/NiOOH$ couple ($\varepsilon = 0.253$ V/SCE) to more anodic value (0.273 V/SCE) Li^+ ions were quite probably incorporated in the $Ni(OH)_2$ lattice forming an intercalation product such as $(\mathrm{Ni\ III})O^{2-}Li^{+}(OH^{-}))$ [8]. This intercalation

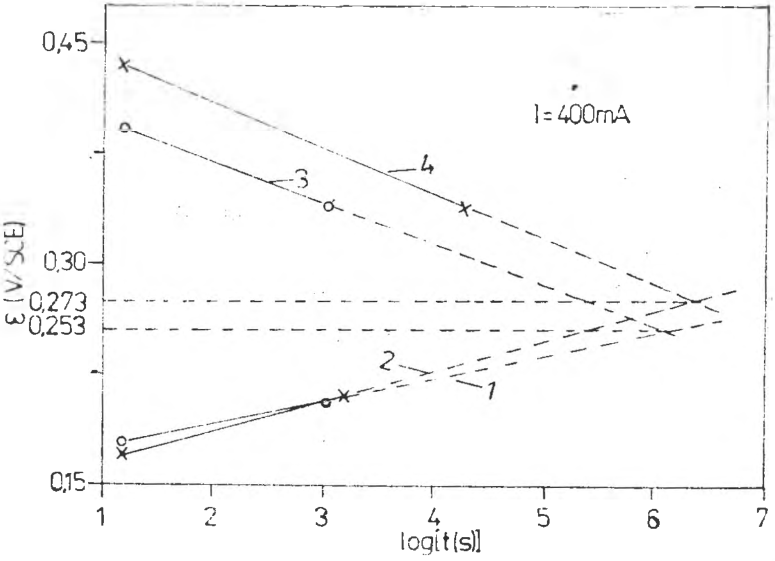

Fig. 2. The ε evaluation for nickel hydroxide electrode in 6 M KOH electrolyte (1–3) and 6 M KOH + 35 g/l LiOH electrolyte (2–4)

compound facilitates the transfer reaction of the proton, involved in the oxidation and reduction processes of nickel hydroxide:

$$Ni(OH)_2 \underset{\text{discharge}}{\overset{\text{charge}}{\rightleftharpoons}} NiOOH + H^+ + e^- \qquad (2)$$

The influence of some metal hydroxides additives in the active material on the nickel hydroxide electrodes performances was investigated. The electrodes were prepared by electrochemical coprecipitation of 10% cobalt hydroxide and 10% cadmium hydroxide, respectively, into nickel hydroxide. The charge-discharge curves of these electrodes, at 100 mA, are shown in fig. 3.

Some electrochemical characteristics of nickel hydroxide electrodes, with and without additives, are shown in Table 1.

The presence of $Co(OH)_2$ and $Cd\ (OH)_2$ in active material increased the capacity and efficiency of the electrodes. The reversible potential of nickel hydroxide electrode was shifted to more cathodic value by $Co(OH)_2$ (0.220 V/SCE) and to more anodic value by $Cd(OH)_2$ (0.261 V/SCE).

The beneficial effect of $Co(OH)_2$ on the nickel hydroxide redox reaction was due to schifting the oxidation reaction to less positive potential (away from the oxygen evolution region).

$Cd(OH)_2$ improved the charging efficiency by increasing the oxygen overpotential.

In conclusion, the addition of 10% $Co(OH)_2$ and 10% $Cd(OH)_2$ to the electrode and 35 g/l to the 6 M KOH electrolyte have been shown to increase the

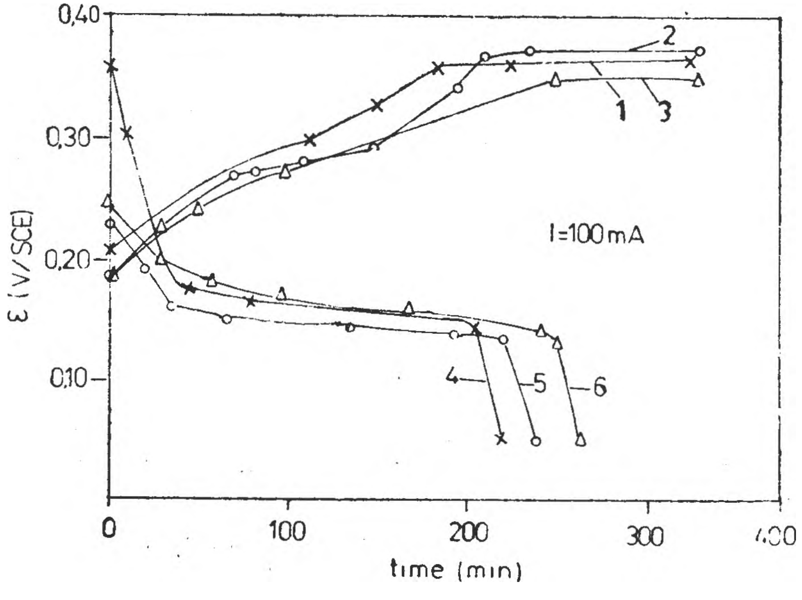

Fig. 3. Charge-discharge curves for nickel hydroxide electrode (1—4), nickel hydroxide + $Cd(OH)_2$ electrode (2—5) and nickel hydroxide + $Co(OH)_2$ electrode (3—6) in 6 M KOH electrolyte

capacity and efficiency of nickel hydroxide electrode by improving the utilization of active material and by minimizing the parasitic oxygen evolution process.

REFERENCES

1. L. Oniciu, E. M. Rus, *Surse electrochimice de putere*, Ed. Dacia, Cluj-Napoca, 1978
2. J. Desilvestre and O. Haas, *J. Electrochem. Soc.*, **137**, 5c, 1990.
3. R. Barnard, C. F. Randell, F. L. Tye, *J. Appl. Elecotrochem.*, **10**, 109, 1980.
4. H. Bode, K. Dehmett, J. Witte, *Electrochim. Acta*, **11**, 1079, 1966.
5. B. B. Ezhov, O. G. Maladin, *J. Electrochem. Soc.*, **138**, 885, 1991.
6. B. C. Cornilsen, X. Shan, P. L. Loyselle, *J. of Power Sources*, **29**, 453, 1990.
7. L. Oniciu, E. M. Rus, P. Ilea, V. Voina, D. Constantin, *Rev. Chim.*, (Bucureşti), **36**, 340, 1985.
8. M. E. Unates, M. E. Folquer, J. R. Vilche, A. J. Arvia, *J. Electrochem. Soc.*, **139**, 2697, 1992.
9. D. A. Corrigan, R. M. Bendert, *J. =Electrochem. Soc.*, **136**, 723, 1989.
10. P. V. Kamath, M. F. Ahmed, *J. Appl. Electrochem.*, **23**, 225, 1993.
11. L. Demourgues-Guerlou, C. Delmas, *J. Electrochem. Soc.*, **141**, 713, 1994.

STUDIA UNIV. BABEŞ-BOLYAI, CHEMIA, XXXIX, 1–2, 1994

DIE THERMISCHE ZERSETZUNG DER SALPETERSÄUREESTER VON STEROLEN, ANWENDUNGEN IN DER KONFORMATIONS-UND STRUKTURANALYSE

MIRELA MIHĂEŞI*

ABSTRACT. Following spectrometrically the thermal sleavage of the ONO_2 group in a series of relatively simple sterol mononitrates, correlations could be established between the measured half times and steric (structural) factors. Thus in a conformer pair the thermal decomposition of the axial nitrate group proceeds faster than that of the equatorial one. The steric hirdrance, as well as a homoallylic double bond, increases the decomposition rate considerably.

Die kinetischen Untersuchungen der thermischen Zersetzungsreaktionen von Salpetersäureestern wurden vor allem auf einfachen Vertretern dieser Substanzen durchgeführt. Die Untersuchungsergebnisse der Salpetersäureester von niedrigen Alkylalkoholen (Methyl-, Äthyl-, und Isorpropylalkohol) gestatten zwei allgemeine Feststellungen: erstens, den ungefähren Charakter der Ermittlung verschiedener kinetischer Faktoren einschließlich der Reaktionsordnung und zweitens, die Variation der Reaktionsordnung zwischen den Grenzwerten 0,5 und 1. Von den Faktoren, die in bestimmten Fällen die Annäherung der Reaktionsordnung an den Grenzwert 0,5 [1] und in anderen Fällen an den Grenzwert 1 [2], [3], [4] verursachen könnten, wird in der Fachliteratur nur die Temperatur erwähnt. Das Steigen der Temperatur gibt der thermischen Zersetzung den ausgeprägten Charakter einer Kettenreaktion und damit die Annahme einer Kinetik der Ordnung 0,5 [1].

Unsere kinetischen Untersuchungen an Salpetersäureestern der Sterole wurden in der Schmelze auf Mengen von 5–10 mg durchgeführt. Die Voruntersuchungen haben gezeigt, daß die Mehrheit der Monoester gute Ergebnisse bei 185°C liefert. Im Falle einiger schneller Zersetzungen, die von einigen im Rahmen der vorliegenden Arbeit diskutierten Faktoren verursacht worden sind, wurden die Zersetzungsreaktionen bei einer Temperatur von 170°C durchgeführt.

Das Verschwinden der ONO_2 — Gruppe wurde durch die Abnahme der Extinktion der drei sehr starken spezifischen Hauptbanden um die Werte 860, 1270 und 1630 cm^{-1} verfolgt.

Die Verarbeitung der erhaltenen experimentellen Daten wird am Beispiel des Salpetersäureestres des 5 α-Cholestan-3β-ols (I) erläutert.

Zuerst wurde die Gültigkeit des Beer-Lambert-Gesetzes für jede der drei Absorbtionsbanden eines jeden untersuchten Salpetersäureesters untersucht, indem die Variation des Extinktionslogarithmus als Funktion der Konzentration aufgezeichnet wurde.

---

* *Universitat „Ovidius", Constanța, B-dul Mamaia 124, Rumanien*

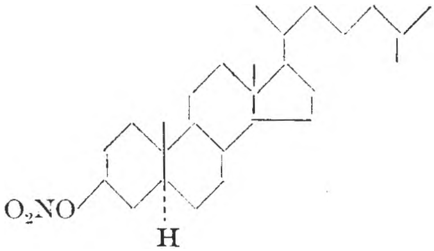

Die so erhaltenen Geraden konnten als Standard — Geraden verwendet werden. Um eine größere Genauigkeit zu erzielen, wurden aufgrund der erhaltenen experimentellen Punkte unter Auslassen der Punkte, welche die Bedingung einer 0,95 — Sicherheit nicht erfüllten, die Gleichungen der drei Geraden errechnet. Im Falle des Salpetersäureesters von 5α-Cholestan-3β-01 (I) wurden folgende Gleichungen ermittelt:

$$y = 0{,}0713\,x + 0{,}06745004 \qquad (860\ \mathrm{cm}^{-1})$$
$$y = 0{,}0937\,x + 0{,}09324200 \qquad (1270\ \mathrm{cm}^{-1})$$
$$y = 0{,}1479\,x + 0{,}58725392 \qquad (1630\ \mathrm{cm}^{-1})$$

wobei:

$$y = \log \frac{P_0}{p} = A \text{ und } x = \text{Konzentration (mg/ml)}$$

Diese Gleichungen dienten der Konzentrationsermittlung während der thermischen Zersetzung des untersuchten Salpetersäureesters. Die als Zeitfunktion graphisch dargestellten erhaltenen Werte führten zu einer Hyperbel-Kurve (Abb. 1). Diese führten dann zur graphischen Ermittlung der mit t_{05} bezeichneten Halbwertszeit.

Um die Reaktionsordnung ermitteln zu können, versuchten wir Linearsierungen, indem wir $\log c = f(t)$ und $\sqrt{c} = f(t)$ darstellten. Im Falle der Substanz I entsprach die Linearität der Gleichung $\log c = f(t)$, und somit hat die Reaktionsordnung den Wert 1 und nicht 0,5 (Abb. 3).

Mit der nun bekannten Linearitätsbedingung konnte die Gerade-Gleichung errechnet werden und daraus ergab sich ein genauerer Wert für die Halbwertszeit, die dann mit $t'_{0,5}$ bezei-

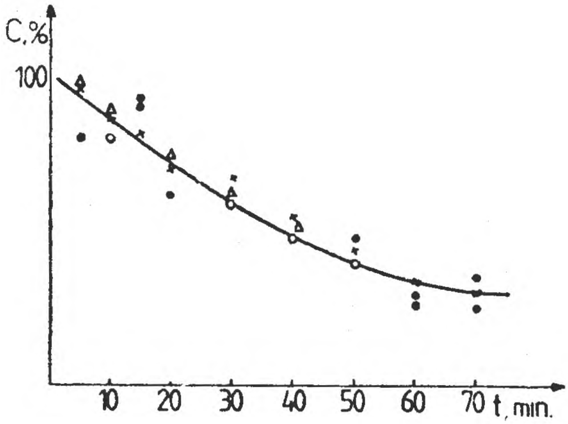

Abb. 1

Abb. 1. Die kinetische Kuve der thermischen Zersetzung des Salpetersäureesters von 5α-Cholestan-3β-ol (I)
x — die Punkte fur 830 cm^{-1}
Δ — die Punkte fur 1270 cm^{-1}
o — die Punkte fur 1630 cm^{-1}
● — ausgelassene Punkte

chnet wurde. Unter einer weiteren Bedingung der Linearitätsrespektierung mit einer Sicherheit von 0,95 wurden alle Punkte die diese Bedingung nicht erfüllten, eliminiert, und so wurde eine neue Gerade-Gleichung und ein neuer Wert für die Halbwertszeit $t''_{0,5}$ erhalten. Unter Verwendung des Wertes $t''_{0,5}$, der genauer als $t_{0,5}$ bzw. $t'_{0,5}$ ist, wurde die Geschwindigkeitskonstante für die Zersetzungsreaktion 1. Ordnung berechnet.

Die Ergebnisse der bei 185°C durchgeführten kinetischen Bestimmungen sind in Tabelle 1, die der bei 170°C durchgeführten in Tabelle 2 enthalten.

Tabelle 1

	$t''_{0,5}$	$t'_{0,5}$	$t_{0,5}$	Reaktions ordnung	$K \cdot sec^{-1}$
1. Salpetersäureester des 5α-Cholestan3-β-ols	39,5	39,5	37,1	1	$0,2924 \times 10^{-2}$
2. Salpetersäureester der Cholesterols	21,5	21,5	19	0,5	
3. Salpetersäureester des 5α-Androstan-3β-ol-17-ons	32,5	32	34	0,5	
4. Salpetersäureester des 5α-Androstan-3α-ol-17-ons	25,5	24,5	24	05	
5. 3α-OAc-6β-ONO_2-5β-methylcholanat	16,5	16	17,5	1	$0,7000 \times 10^{-3}$
6. 3α-OAc-6α-ONO_2-5β-methylcholanat	32,5	31,5	33	1	$0,3553 \times 10^{-3}$
7. 3β-OAc-6β-ONO_2-5α-cholestan	9,5	9,5	10	1	$1,2157 \times 10^{-3}$
8. Salpetersäureester des Methyllitocholats	28,5	28	30	1	$0,4052 \times 10^{-3}$
9. 3α-OAc-7α-ONO_2-methyl-chenodesoxicholat	9	8	10	1	$1,2833 \times 10^{-6}$
10. 3α-OAc-12α-ONO_2-methyl-desoxicholat	10,5	9,5	11	1	$1,1000 \times 10^{-3}$
11. 3α, 12α-Di-ONO_2-methyl-desoxicholat	16,5	16	16	1	$0,7000 \times 10^{-3}$
12. 3β, 4β-Di-ONO_2-cholestan	4	4	4	1	$2,8875 \times 10^{-3}$
13. 3α, 7α, 12α-Tri-ONO_2-methylcholat	11	11	11	1	$1,0500 \times 10^{-3}$
14. 11β-ONO_2-21-OAc-pregnen-(4)-dion-(3,20)+	4,5	4,5	4,5	1	$2,5666 \times 10^{-3}$
15. 17β- ONO_2-5α-Androstan++		6	6		
16. 6β, 7β-Di-ONO_2-3α-OAc-methylcholanat+++		7	7		

+ -- Die gefundenen experimentellen Punkte unterscheiden sich in den verschiedenen Frequenzen der Absorbtionsbanden in den verschiedenen Erequenzen der Absorbtion
banden. Aufgeführt wurden die Ergebnisse für ν = 860 cm^{-1} und ν = 1270 cm^{-1}. Nach den erhaltenen Punkten für ν = 1670 cm^{-1} ist $t_{0,5}$ = 25 Min.

++ -- Da die Reaktion sehr schnell verläuft, konnte nur eine kleine Anzahl von experimentellen Punkte ermittelt werden, so daß keiner davon eliminiert wurde.

+++ -- Wegen der Streuung der Punkte bei der Linearisierung wurde die beobachtete Halbwertszeit genommen.

Tabelle 2.

	$t''_{0,5}$	$t'_{0,5}$	$t_{0,5}$	Reaktions ordnung	$K \cdot sec^{-1}$
1. 3β-OAc-6β-ONO_2-5α-Cholestan	14	41	39	1	$0,2817 \times 10^{-3}$
2. 17β-ONO_2-5α-Androstan	16	16	18,5	1	$0,7218 \times 10^{-3}$
3. 3α-OAc-7α-ONO_2-Methyl-chenodesoxi-cholat	40,5	39,5	41	1	$0,2851 \times 10^{-3}$
4. 3α-OAc-12α-ONO_2-Methyl-desoxicholat	60	61	58,5	1	$0,1925 \times 10^{-3}$
5. 3α, 12α-Di-ONO_2-methyl-desocxicholat+++	98,5	97,5	99	1	$0,1172 \times 10^{-3}$
6. 3α, 7α, 12α-Tri-ONO_2-methylcholat	66	67	65,5	1	$0,1747 \times 10^{-3}$

Wie aus den Tabellen 1 und 2 hervorgeht, sind die Werte für $t'_{0,5}$ und $t''_{0,5}$ in vielen Fällen identisch, und nur in einigen Fällen betragen die Unterschiede 1 Minute. Die Fehler, mit denen die $t'_{0,5}$ —, Werte behaftet sind, sind sehr klein und in den meisten Fällen sogar zu vernachlässigen, da bei der Berechnung eine Sicherheit von 0,95 gestellt wurde. Die $t_{0,5}$ — Werte — ausschließlich graphisch ermittelt — unterscheiden sich von den $t''_{0,5}$ — Werten um einen Betrag von höchstens ±2,5 Minuten. Infolgedessen könnten die graphisch ermittelten $t_{0,5}$ — Werte für praktische Zwecke verwendet werden, wenn man die Unterschiede, die ±3 Minuten überschreiten, berücksichtigt. Übrigens verursachen die strukturellen und sterischen Faktoren Reaktionsgeschwindigkeitsänderungen, welche die erwähnten Fehler mehrfach überschreiten, so daß diese zu keiner nennenswerten Fehlinterpretation führen können.

Bevor man nun zur Diskussion der Ergebnisse übergehen kann, muß noch erwähnt werden, daß nur in sehr wenigen Fällen nicht alle drei Hauptabsorbtionsbanden der ONO_2-Gruppe gleichzeitig verwendet werden konnten. Einen solchen Fall bildet das 11 α-ONO_2-21-OAc-Pregna-4-en-3,20-dion, bei dem nur die Banden um 860 und 1270 cm^{-1} übereinstimmende Ergebnisse liefern; die Bande um 1630 cm^{-1} liefert einen unverhältnismaßig hohen $t_{0,5}$-Wert, den man nicht berücksichtigen kann. Die Erklärung dafür ist, daß Zersetzungsprodukte entstehen, die im Bereich 1600—1700 cm^{-1} absorbieren. Die bei 170°C durchgeführten Untersuchungen lieferten auch keine verwertbaren Ergebnisse, da die $t_{0,5}$-Werte für jedwede Bande stark verschieden waren. Ein ähnloches Verhalten zeigte bei 170°C auch das 3β, 4β-Dinitroxi-5α-cholestan.

Im Bezug auf die Reaktion zwischen den bei 185°C ermittelten kinetischen Daten und den sterischen bzw. konformationellen Faktoren kann folgendes festgestellt werden:

Die Halbwertszeiten $t_{0,5}$ der äquatorialen ONO_2-Gruppen an C_3 in den gesättigten Steroiden liegen um den Wert 35 Minuten (Abb. 2).

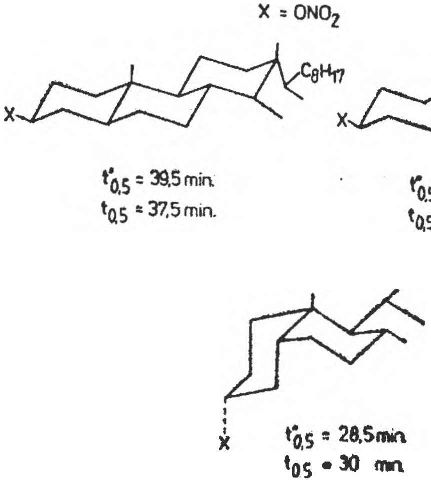

Abb 2

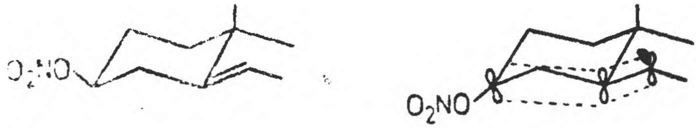

$t_{0,5}$ = 21,5 min
$t_{0,5}$ = 19 min

Abb 3

Man kann eine Verschiebung zu kleineren Werten feststellen, wenn man statt eines Sterolderivates mit gesättigter Seitenkette ein Derivat mit einer Ketogruppe in der 17-Stellung untersucht. Diese Erscheinung kann durch die Fernzwischenwirkung der Substituenten erklärt werden, wie es in der Fachliteratur in vielen ähnlichen Fällen festgestellt und beschrieben worden ist [5]. Eine noch größere Verschiebung verursacht die Anelierungsänderung der A/B-Ringe, und der Vergleich der Halbwertszeiten kann dazu dienen, die Zugehörigkeit zur 5α-bzw. 5β-Reihe im Falle von Isomerenpaaren zu bestimmen.

Das Vorhandensein einer 5,6-Doppelbindung wird von einer noch stärkeren Steigerung der Zersetzungsreaktion begleitet (Abb. 3). Diese Wirkung kann man einer „konformationellen Übertragung" zuschreiben, da bekannt ist, daß eine Doppelbindung im Steran-Skelett die Reaktionsgeschwindigkeiten am Niveau entfernterer Zentren beeinflussen kann [5]. Die Stabilisierungswirkung einer 5,6-Doppelbindung auf ein Radikal an C-5 darf aber nicht Vernachlässigt sigt werden (Abb. 3), da eine solche Wirkung die Bildung eines solchen Radikals und damit die Zersetzung des Esters nach folgender Gleichung begünstigt:

$$\rangle\overset{\circ}{C}-ONO_2 \longrightarrow \rangle-C=O+NO_2$$

Die axialen ONO_2-Gruppen zersetzen sich viel schneller als die äquatorialen. So weist das 3α-Nitroxi-5α-androstan-17-on eine unvergleichbar kleinere Halbwertszeit als jegliche äquatorialen Ester an C-3 in den beiden Reihen 5α und 5β auf. Die Erscheinung könnte als eine durch die nichtgebundene Zwischenwirkung der axialen Substituenten hervorgerufene sterische Beschleunigung betrachtet werden (Abb. 4). Eine bedeutende Minderung der sterischen Kompression findet vor allem infolge von Eliminierungsreaktionen statt, wenn die nichtgebundene Zwischenwirkung der axialen Substituenten hervorgerufene sterische Beschleunigung betrachtet werden (Abb. 4). Eine bedeutende Minderung der sterischen Kompression findet vor allem infolge von Eliminierungsreaktionen statt, wenn die sp^3-Hybridisierung durch eine sp^2-Hybridisierung ersetzt wird. Es ist bekannt, daß derartige Reakti-

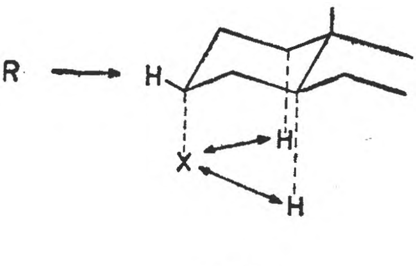

Abb. 4

onen von der axialen Konformation des Substituenten begünstigt sind, wie es auch im Falle der thermischen Zersetzungsreaktion von Salpetersäureestern festgestellt werden konnte.

Andererseits wäre auch die sterische Begünstigung der Zersetzung nach der erwähnten Gleichung: $\rangle\overset{\circ}{C}-ONO_2 \rightarrow \rangle C = O + NO_2$ zu berücksichtigen.

Tatsächlich ist die Bildung eines Radikals an C—3 durch die äquatoriale Orientierung des 3β-H-Atoms erleichtert, da dieses einem Radikalangriff bedeutend zugänglicher ist (Abb. 6).

Die Zersetzungsgeschwindigkeiten der 7α-ONO_2-bzw. 12α-ONO_2-Derivate können bedeutend größer als die im vorhergehenden Fall gemessene Geschwindigkeit sein. Die Erscheinung kann der Steigerung der ungebundenen Zwischenwirkung in solchen Substanzen im Vergleich zu 3α-Nitroxi-5α-androstan-17-on zugeschrieben werden. In einem 7α-Nitroxiderivat der 5ß-Reihe tritt neben zwei 1 :3-diaxialen Zwischenwirkungen mit H-Atomen auch eine Zwischenwirkung mit einer Methylengruppe (C-4) auf. In einem 12α-Nitroxiderivat der Gallensäure ist nicht nur der Einfluß der drei axialen C-9-, C-14-und C-17-H-Atome sondern auch der Einfluß der Seitenkette wirksam, denn in solchen Substanzen erhält die Seitenkette eine Orientierung, die den Substituenten in 12α überlappt (6) (Abb. 5). Leider standen keine Substanzen wie z.B. ein 7α-Nitroxiderivat der 5α-Reihe bzw. ein 12α-Nitroxiderivat ohne Seitenkette an C-17- zur Verfügung, mit denen diese Erwägungen experimentell überprüft werden konnten

Interessant ist auch das Verhalten der 6-Nitroxiderivate. Das äquatoriale 6α-Nitroxiderivat ergibt eine Halbwertszeit, die mit der der äquatorialen Salpetersäureester am C-3 übereinstimmt.

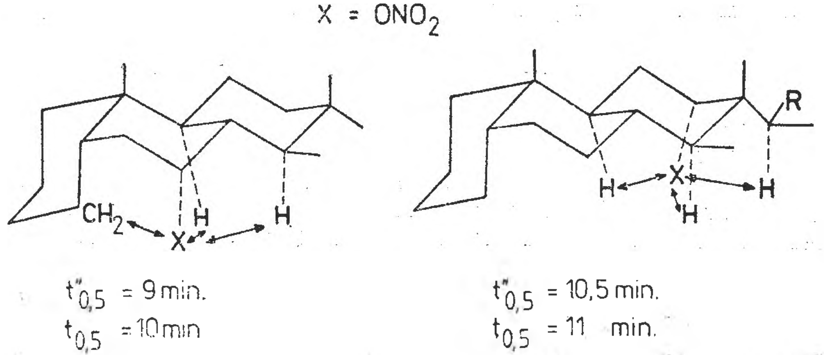

Abb. 5

Erwartungsgemäß zersetzen sich die axialen 6β-Nitroxiderivate unvergleichlich schneller. Entscheidend dafür ist die strenge Zwischenwirkung zwischen der Nitroxi-Gruppe und der Methylgruppe an C-10 (Abb. 6). Aber zwischen den Halbwertszeiten der 6β-Nitroxiderivate in Abhängigkeit von der Konfiguration an C-5 ist ein bemerkenswerter Unterschied zu beobachten; es besteht eine stärkere Zwischenwirkung 6β-ONO_2 :10-CH_3 in der Reihe 5α als in der Reihe

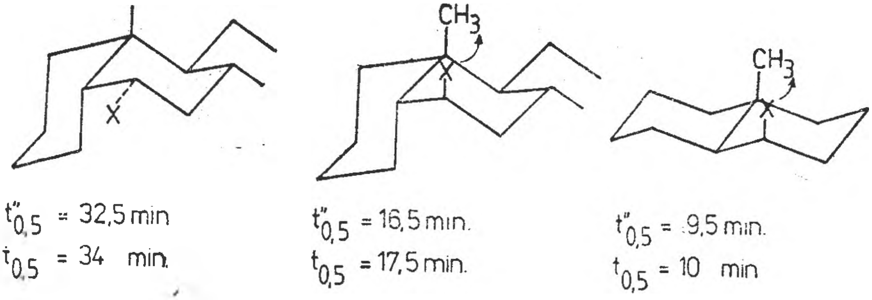

Abb. 6

5β. Diese Feststellung stimmt mit den NMR-Ergebnissen überein; diese Ergebnisse bestätigen eine kleinere Überlappung der 10-CH_3-Gruppe durch 6β-Substituenten der 5α-Reihe als durch die der 5 β-Reihe.

Eine Erklärung dafür könnte die größere Leichtigkeit sein, mit der durch die konformationelle Distorsion des B-Ringes eine Minderung der Verspannung zustande kommt und infolgedessen hat man es nur mit den Überlappungen der C_5-H- und der C_6-X-Bindung zu tun. Gleichzeitig ist eine solche Distorision in der 5α-Reiche weniger günstig, sie würde zur Überlappung der C_4-C_5 und der C_6-X-Bindung führen (Abb. 7).

Die Übereinstimmung unserer Ergebnisse mit den NMR-Daten unterstützt unsere Auffassung über die sterische Natur der Beschleunigung der untersuchten Zersetzungsreaktionen (7).

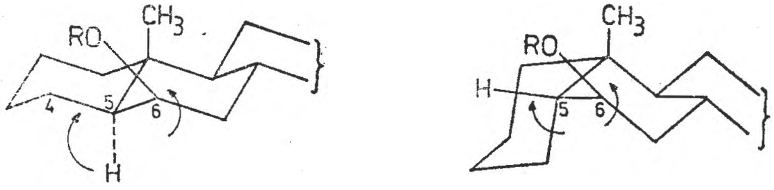

Abb. 7

Die sehr kurzen Halbwertszeiten im Falle der 11β-bzw. 17β-Salpetersäureester können gleichfalls auf von den CH_3-Gruppen verursachte sterische Verspannungen zurückgeführt werden (Abb. 8).

Reaktionsgeschwindigkeiten in derselben Größenordnung erhält man im Falle der vicinal-Diester (3β, 4β-bzw. 6β, 7β-Di-ONO_2-Derivate) infolge der gegenseitigen Wechselwirkung zwischen den benachbarten ONO_2-Gruppen. Solche Wechselwirkungen konnten spektral nachgewiesen werden. Es gibt auch chemische Beweise, daß zwei vicinale ONO_2-Gruppen sich gegenseitig stark

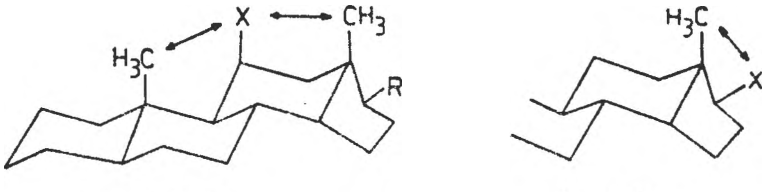

$t_{0,5}$ = 4,5 min. $t_{0,5}$ = 6 min

Abb 8

beeinflussen. Solche Substanzen setzen — zum Unterschied von Substanzen mit isolierten ONO_2-Gruppen — aus einer wässrigen angesäuerten Kaliumjodid-Lösung in der Kälte Jod frei, und sie zersetzen sich unter der Einwirkung von Trifluoressigsäure, indem Nitrosegase entweichen.

Die Substanzen, die bei 185°C eine zu große Zersetzungsgeschwindigkeit aufwiesen, wurden bei 170°C untersucht. So konnte man eindeutig zwischen den 7α-ONO_2-, 12α-ONO_2- und 17β-ONO_2-Derivaten unterscheiden. Im Falle des untersuchten 11α-Salpetersäureesters führte die Verfolgung des Verschwindens der ONO_2-Gruppe mittels Spektralanalyse zu keinen verwertbaren Ergebnissen, da die erhaltenen Werte je nach der verwendeten Absorbtionsbande sehr unterschiedlich waren und außerdem weit streuten. Es besteht die Möglichkeit, daß die Zersetzungsreaktion stark von der Temperatur beeinflußt wird. Es scheint, daß die durch Erniedrigung der Temperatur verursachte Reaktionszeitverlängerung das allgemeine Zersetzungsbild durch Auftreten von Nebenreaktionen kompliziert und damit jegliche Möglichkeit für Schlußfolgerungen zunichte macht.

Aus dem Dargelegten geht hervor, daß die bei 185°C mit Hilfe der IR-Spektrometrie verfolgte Zersetzungsgeschwindigkeit der Sterol-Salpetersäureester eine bequeme Methode für die Konformations und Strukturanalyse darstellt und eine Reihe von Grundproblemen in dieser Substanzenklasse lösen kann. Da die Salpetersäureester in einfacher Weise aus den entsprechenden Alkoholen zugänglich sind, kann die von uns vorgeschlagene Methode zur Untersuchung der sowohl in der Natur vorkommenden als auch der als Zwischen- bzw. Endprodukte auftretenden OH-Steroiden dienen.

LITERATUR

1. Thomas J. Houser, Betty M. H. Lee, *J. Phys. Chem.*, **71**, 3422, (1967).
2. Joseph B. Levy, *J. Am. Chem.*, **76**. 3254 (1954).
3. G. K. Adams, G. E. H. Bawn, *Trans. Faraday Soc.*, **45**, 494 (1949).
4. L. Phillips, *Nature*, **165**, 564 (1950).
5. E. L. Eliel, N. L. Allinger, S. T. Angyal şi G. A. Morrison, *Conformation Analysis*, 1966, Interscience Publishers, New York, S 345, 350.
6. L. Fieser şi M. Fieser, *Steroids*, 1959, Reinhold Publishing Corp. New York S 222.
7. Norman S. Bhacca, Dudley H. Williams, *Applications of N.M.R. spectroscopy in organic chemistry*, London 1964, S 26.

STUDIA UNIV. BABEŞ-BOLYAI, CHEMIA, XXXIX, 1–2, 1994

IN MEMORIAM

RALUCA RIPAN

S-a născut la Iaşi, în 27 iunie, 1894.

O găsim studentă a Facultăţii de Ştiinţe, secţia fizică-chimie, la Universtitatea din Iaşi, între 1914 şi 1919.

A avut dascăli, printre alţii, pe Petre Bogdan (cu studii la Berlin şi Leipzig), pe Nicolae Costăchescu (cel dintâi doctor în chimie din ţară), pe Anastasie Obregia (cu doctorat luat la Zürich).

După susţinerea examenului de licenţă, în 1919 este reţinută preparator la Laboratorul de Chimie Minerală şi asistent la Laboratorul de Chimie fizică al universităţii ieşene.

La numai un an, 1920, Raluca Ripan este transferată la Universitatea Daciei Superioare proaspăt înfiinţată la Cluj, ca şef de lucrări la catedra profesorului Gheorghe Spacu, venit şi el cu un an în urmă, de la Iaşi.

De numele Ralucăi Ripan se leagă priorităţi demne de semnalat:

— 1922 susţinerea tezei de doctorat şi obţinerea celui dintâi titlu de doctor în chimie de către o femeie, în România;
— 1948 alegerea celei dintâi femei-membru al Academiei Române;
— cea dintâi femeie rector a Universităţii din Cluj (1952–1956);
— cea dintâi femeie decan al Facultăţii de Chimie de la universitatea clujeană (1947–1951);

În 1942 este promovată profesor titular, şef al catedrei de Chimie anorganică şi analitică.

În 1949 s-a înfiinţat filiala Academiei Române de la Cluj, condusă de Raluca Ripan între 1957 şi 1975, iar doi ani mai târziu s-au pus bazele Institutului de Chimie de pe lângă filiala clujeană a Academiei Române; a condus acest institut până la pensionarea în 1970.

Activitatea ştiinţifică este concretizată în peste 300 de articole publicate în reviste de specialitate din ţară şi din străinătate şi o serie de manuale şi tratate universitare, destinate studenţilor pe care i-a iubit şi îndrumat permanent. Activitatea ştiinţifică a Ralucăi Ripan se înscrie în domeniul Chimiei coordinative şi în cel al Chimiei analitice, reflectând 55 de ani de căutări neobosite.

Multe aspecte, legate de structura şi comportamentul compuşilor coordinativi, dar şi multe metode de analiză calitativă şi cantitativă constituie rodul muncii sale de cercetare. Trebuie remarcată şcoala creată în domeniul hetero- şi izopolicombinaţiilor unor metale (azi numite polioximetalaţi).

Dascălul Raluca Ripan

Avea ţinuta academică atât în conţinut cât şi în formă, însuşită de la iluştrii săi profesori. La curs era urmărită cu interes, se impunea prin stil şi răspândea o atmosferă de căldură şi fineţe sufletească.

Avea un farmec personal irezistibil, avea un accent moldovenesc prin nimic strident, se bucura de stimă şi dragoste din partea colegilor de muncă şi a studenţilor. Exigentă la examene şi în activitatea desfăşurată de colaboratori, demonstra spirit în intervenţiile sale şi o uşoară notă de ironie când situaţia o cerea. Era neobosită şi pasionată pentru profesiunea sa, pe care o practica fără economie de efort şi dăruire. Iubea frumosul în toate formele lui de manifestare şi demonstra un rafinament inegalabil în aprecierea acestuia.

Dorinţa de a afla noul şi de a-l împărtăşi celor din jurul său se surprindea prin informaţia conţinută în prelegerile sale care nu erau monotone ci dimpotrivă, pline de relief ştiinţific remarcabil. Expunea liber, convingător, lăsându-se antrenată şi fascinată de ineditul noutăţii ştiinţifice comunicate.

Activitatea desfăşurată de Raluca Ripan a fost apreciată nu numai în ţară ci şi în străinătate. I s-a tradus în limba rusă Chimia metalelor, i s-a decernat titlul de Doctor Honoris Cauza de către Universitatea ,,Nicolaus Copernicus'' din Torun (Polonia), a fost aleasă membru de onoare al Societăţii Industriale de Chimie din Franţa şi membru al Societăţii Germane de Chimie.

Întrunind reale calităţi de educator cu vocaţie, având un aport remarcabil în cercetarea ştiinţifică din domeniul polioxometalaţilor şi cel al chimiei analitice, participantă activă la activitatea socială şi militantă neobosită pentru promovarea femeii în diversele sectoare ale economiei, Raluca Ripan constituie un exemplu demn de urmat. Mesajul care se desprinde din exemplul oferit de viaţa sa este clar şi se defineşte cu deosebită pregnanţă: lupta neîntreruptă pentru afirmarea adevărului ştiinţific, pentru educarea tinerilor în spiritul probităţii ştiinţifice şi pentru instruirea lor în tainele chimiei.

De aceea comemorarea celor 100 de ani care s-au scurs de la naşterea Ralucăi Ripan este un act de cultură de înalt conţinut ştiinţific, valoric, având reverberaţii benefice pentru generaţiile de tineri de ieri, de azi şi de mâine.

LIVIU ONICIU

STUDIA UNIV. BABEŞ-BOLYAI, CHEMIA, XXXIX, 1–2, 1994

RECENZII

Cs. Várhelyi, I. Gănescu, D. Oprescu, A. Popescu **The pseudohalides in the co-ordination chemistry of chromium,** (Pseudohalogenurile în chimia coordinativă a cromului, Editura Meridian, Craiova, 1993, 224 p.)

The book is a review based on a number of over 850 references. The autors are known specialists of this field, in which they published almost 120 papers.

The monography is dedicated to various problems connected with the pseudohalido-complexes of chromium.

Chapter 1 is dealing with the formation and structure of pseudohalides az CN^-, CNX^- ($X = O$, S, Se, Te), N_3^-, NO_3^-.

Chapter 2 shows the co-ordination possibilities of these anions, being able to play the role of monodentate, ambidentate, or even bidentate (bridging) ligands.

Chapter 3 gives a classification of the pseudohalido-complexes containing NCX^- type ligands.

Chapter 4 is a short presentation of complex forming properties of chromium.

Chapter 5 is the most extended one (over 100 p). It begins with the classification of chromium(III) complexes. A special interest is poid to the Reinecke salt, containing the $[Cr(NH_3)_2(NCS)_4]^-$ complex ion, as well as to the analogous compounds in which the NH_3 ligands are substituted by organic N-bases.

Preparation of these derivatives is described for various types of N-bases as aliphatic and aromatic mono- and diamines, heterocyclic mono- and diamines and even for phosphines. The thermal decomposition, IR spectra and electronic spectra of these compound are presented based mainly on the results of the authors Further the kinetics of the solvation o $[Cr(NCS)_4A_2]^-$ type complexes is discussed. In these solvation reactions, thoroughly studied by the authors, the substitution of both NCS and A ligands by solvent molecules is ethanol--water and aceton-water mixtures, leads to a complicated frame-work of successive and parallel reactions. In this chapter also the $[CrX_6]^{3-}$ type hexaacido complexes are described.

Chapter 6 deals with the polynuclear complexes of chromium with bridging pseudohalide anions.

In chapter 7 the chelate compounds of Cr(III. are shortly reviewed.

The last chapter is dedicated to the application of pseudohalido-chromium complexes in the analytical chemistry.

The book gives a detailed review of en interesting field of co-ordination chemistry. It can be useful chemists, engineers, students postgraduate students and research workers interested in co-ordination chemistry.

JÁNOS ZSAKÓ, FERENC MAKKAY

Hellmut York, Werner Funk, Walter Fischer, Hans Wimmer
Thin – Layer Chromatography: Reagents and Detection Methods

Volume Ib. Physical and Chemical Detection Methods: Activation Reactions, Reagent Sequences Reagents II. VCH Verlagsgesellschaft mbH, Weinheim–New York–Basel–Cambridge–Tokyo, 1994.

Thin-Layer Chromatography is the most frequently used separation and detection technique of substances an it will remain identically actual, because it is extremely simple. The technique requires an equipment that can be manufactured or acquired at a low cost price.

The progress of this method consists in the improvment of technology for obtaining chromatographic plates and of detection method "in situ" for enlargement detectability and sample identification. The progress consists too in the elaboration of new strategies for optimization separation systems on TLC plates.

This present book deals with the physical and chemical detection methods of the separated substances by thin-layer chromatography.

The book is divided into two parts: the first part contains the specific detection methods and the second part comprises the detection reagents in alphabetical order.

The specific detection methods are arranged according to the activation mode of reaction (photochemical, thermochemical and electrochemical activation, respectively) for simplifying very much the chromatographist work.

The first part includes in two chapters the recognition reagents of functional groups and the types of reactions that take place between the detection reagent and the separated substance (electrophilic substitutions, oxidations and reductions, azo coupling, metal complexes, etc.)

The second part of this book contains the monograph of 65 reagents arranged in alphabetical order. For every reagent is given the preparation mode, the reaction between the reagent and the separated substance, the mode of working and the exemplification of one chromatographic separation and identification with this reagent

An important achievement of this book consists in the introduction by the authors of some solour photos according to the original chromatogram.

At the end of this book, the list of companies that produce equipment and chromatographic materials, the reagent names and reagent acronyms and the collective index to volumes 1a and 1b are presented.

This book is an exceptional realization of the authors, highly specialized, and of the valuable publishing house VCH.

The book addresses to specialists, researchers, university teaching staff and students who can recieve information concerning the separation and detection of substances by thin-layer chromatography.

CONSTANTIN MĂRUȚOIU

Tehnoredactare: FIAT FLORIN

Volum editat cu sprijinul financiar
al Fundației Soros pentru o
Societate Deschisă

Tiparul executat la Imprimeria „ARDEALUL“ Cluj
sub comanda 60135/1996.

În cel de al XXXIX-lea an (1994) *Studia Universitatis Babeş-Bolyai* apare in următoarele ii:

matematică (trimestrial)
fizică (semestrial)
chimie (semestrial)
geologie (semestrial)
geografie (semestrial)
biologie (semestrial)
filosofie (semestrial)
sociologie-politologie (semestrial)
psihologie-pedagogie (semestrial)
ştiinţe economice (semestrial)
ştiinţe juridice (semestrial)
istorie (semestrial)
filologie (trimestrial)
teologie ortodoxă (semestrial)
educaţie fizică (semestrial)

In the XXXIX-th year of its publication (1994) *Studia Universitatis Babeş-Bolyai* is issued the following series:

mathematics (quarterly)
physics (semesterily)
chemistry (semesterily)
geology (semesterily)
geography (semesterily)
biology (semesterily)
philosophy (semesterily)
sociology-politology (semesterily)
psychology-pedagogy (semesterily)
economic sciences (semesterily)
juridical sciences (semesterily)
history (semesterily)
philology (quarterly)
orthodox theology (semesterily)
physical training (semesterily)

Dans sa XXXIX-e année (1994) *Studia Universitatis Babeş-Bolyai* parait dans les séries suivantes:

mathématique (trimestriellement)
physique (semestriellement)
chimie (semestriellement)
géologie (semestriellement)
géographie (semestriellement)
biologie (semestriellement)
philosophie (semestriellement)
sociologie-politologie (semestriellement)
psychologie-pédagogie (semestriellement)
sciences économiques (semestriellement)
sciences juridiques (semestriellement)
histoire (semestriellement)
philologie (trimestriellement)
theologie orthodoxe (semestriellement)
éducation physique (semestriellement)